UNIVERSITY OF SOUTHAMPTON
FACULTY OF ENGINEERING AND APPLIED SCIENCE
School of Engineering Sciences

# Aerodynamic Interaction of an Inverted Wing with a Rotating Wheel

by

**Martinus Anthoon van den Berg**

Thesis for the degree of Doctor of Philosophy

March 2007

Dedicated to my parents, Cees and Cora,
who have always had a never-ending belief in
- and support for - all of my choices.

UNIVERSITY OF SOUTHAMPTON

ABSTRACT

FACULTY OF ENGINEERING AND APPLIED SCIENCE

SCHOOL OF ENGINEERING SCIENCES

Doctor of Philosophy

# AERODYNAMIC INTERACTION OF AN INVERTED WING WITH A ROTATING WHEEL

by **Martinus Anthoon van den Berg**

This research contributes to the knowledge on aerodynamic wing - wheel interaction. Hereto an experimental and computational study has been performed, during which the wing ride height and the wing - wheel overlap and gap have been considered as the primary variables. The wheel drag for the combined configuration is generally lower at low ride heights and higher at high ride heights compared to the case without wing. This results primarily from changes in the flow separation over the top of the wheel - partly induced by the wing circulation - from the channel flow along the inside of the wheel and from the vortex interaction in the wheel wake. The wing downforce increases at low ride heights due to the wheel presence, but reduces at high ride heights. The modified channeling effect, vortex and separation effects govern the wing flow field, although the wheel circulation acts as an additional mechanism for downforce enhancement and limitation.

The wing - wheel interaction has been studied extensively for a baseline configuration, using forces, on-surfaces pressures for the wing and wheel, oil flow and PIV data. A reduced set of data has been obtained for alternative overlap and gap settings. An increase in overlap generally leads to a reduction in wheel drag and wing downforce. A larger gap setting has relatively little influence on the wheel drag at low ride heights, but shifts the higher ride height part of the curve to lower values. The wing downforce is generally slightly lower when the gap increases. An analogy between the wing - wheel configuration and a multi-element airfoil has been used to partly explain the aerodynamic interaction between the components, based on the cross flow along the flap trailing edge.

The application of a steady RANS computational approach with Spalart Allmaras turbulence model has been assessed for a baseline configuration over a range of ride heights. Qualitatively, the flow field is predicted fairly accurately, but the flow quantities correlate less satisfactory with the experiments. The downstream interaction is underpredicted, resulting in lower values for the wheel drag, in particular at high ride heights. The use of non-conformal zones around the wing is one of the causes for this discrepancy.

# Contents

## Appendices

# List of Tables

# List of Figures

# Acknowledgements

The following work would not have been possible without the help and advice of a multitude of people. Professor Zhang needs to be acknowledged for his faith in my abilities and for letting me find my own way. Of course I would also like to thank him for all the time he has invested in this project as a supervisor.

Many thanks to Honda Racing F1, former BAR, for the industrial support and advice. In particular David Jeffrey, Jonathan Zerihan, Neil Carlisle and Willem Toet need to be mentioned. ACFD has been very helpful on the CFD side by providing training, advice and resources; for which I would especially like to thank Bill Pearson, Rob Lewis and Philip Postle.

The supporting staff at the University of Southampton have proved to be indispensable in the process as well, including the wind tunnel team, consisting of Mike Tudor Pole, Mike Thomas and Charlie Williams - who will be remembered - and the AFM and Astro group secretaries. I also very much appreciate all the help of and discussions with my fellow PhD students and especially all the efforts by Steve Mahon and Jim McManus with respect to the experimental models and equipment that I inherited from them.

Finally, my parents, brothers, family and friends - both here in the UK and in the Netherlands - have always supported me enthusiastically and given me the energy and motivation to pursue my dreams.

# Nomenclature

$a$ : Channel width

$b$ : Wing span

$c$ : Wing chord

$C_D$ : Drag coefficient, $C_D = \frac{Drag}{q \cdot S}$

$C_L$ : Downforce coefficient, $C_L = \frac{Downforce}{q \cdot S}$

$C_M$ : Moment coefficient, $C_M = \frac{Moment}{q \cdot c \cdot S}$

$C_P$ : Pressure coefficient, $C_P = \frac{p - p_\infty}{q}$

$C_Y$ : Side force coefficient, $C_Y = \frac{Sideforce}{q \cdot S}$

$D$ : Diameter of cylinder or wheel

$f$ : Frequency

$G$ : Gap between wing and wheel in streamwise direction

$h$ : (Wing) ride height or gap between cylinder and ground

$I$ : Turbulence intensity level

$L$ : Length scale

$O$ : Overlap between wing and wheel in spanwise direction

$p$ : Pressure

$q$ : Dynamic pressure, $q = 1/2\rho V^2$

$Q$ : Second invariant of the velocity gradient tensor $\nabla u$

$\overline{Q}$ : Non-dimensionalized version of $Q$, using $U_\infty$ and $c$

$R^2$ : Coefficient of determination of a trendline

$Re_L$ : Reynolds number based on characteristic length $L$, $Re = \frac{\rho \cdot U_\infty \cdot L}{\mu}$

$S$ : Surface area or wing planform

$\mathbf{S}$ : Symmetric components of the velocity gradient $\nabla u$

$St$ : Strouhal number, $St = \frac{f \cdot L}{U_\infty}$

$t$ : wing element thickness

$U_\infty$ : Free stream Velocity

$V_r$ : Rotational velocity

$y^+$ : Non-dimensional distance perpendicular to the wall in law of the wall

$\mathbf{\Omega}$ : Asymmetric components of the velocity gradient $\nabla u$

$\lambda_i$ : $i$th Eigenvalue of a matrix or dynamic system

$\rho$ : Density

$\mu$ : Viscosity

# Glossary

ACFD : Advantage CFD
AR : Aspect Ratio
BAR : British American Racing
BL : Baseline
CAD : Computer Aided Design
CFD : Computational Fluid Dynamics
CoP : Centre of Pressure
CWW : Combined Wing - Wheel
DES : Detached Eddy Simulation
DNS : Direct Numerical Simulation
FIA : Federation Internationale de l'Automobile
GCI : Grid Convergence Index
LDA : Laser Doppler Anemometry
IWh : Isolated Wheel
IWi : Isolated Wing
LES : Large Eddy Simulation
PIV : Particle Image Velocimetry
RANS : Reynolds Averaged Navier-Stokes
RMS : Root Mean Square value
RNG : Renormalisation Group theory (k - $\epsilon$ turbulence model)
RSM : Reynolds Stress transport Model (turbulence model)
SA : Spalart Allmaras model (turbulence model)
SST : Shear Stress Transport (k - $\omega$ turbulence model)
SRANS : Steady Reynolds Averaged Navier-Stokes
URANS : Unsteady Reynolds Averaged Navier-Stokes
ZOC : Zero Operate Calibrate (pressure scanner)

# Chapter 1

# Introduction and Literature Review

This chapter provides an introduction to the research topic. This will first be achieved in a global way, by discussing the background and context, and then in more detail via a review of the relevant literature. The literature review is divided into three different parts, covering the wheel, the wing and additional literature. After this the research questions will be formulated, based on the hiatuses in the knowledge that is available in open literature. Finally, to conclude the chapter, the structure of this thesis report will be presented.

## 1.1 Introduction

The introduction consists of a short look at the history of motorsport and the relevance of racing car aerodynamics in the pursuit of performance. Following this the study will be placed in context with previous projects at the University of Southampton and with academical research in general. Finally, the motivation for the current research will be presented as part of this discussion.

### 1.1.1 Background

The external design of an open-wheel racecar is primarily dictated by aerodynamic considerations. Large gains in laptime performance can be achieved by streamlining the car body and by fitting downforce producing parts. The rules for open-wheel racecars however state that the wheels have to be exposed to the flow and the presence of these rotating bluff bodies can contribute to up to 40% of the total drag of the complete car [1,2]. Furthermore the wheels produce lift as well, which is very difficult to measure experimentally. The disturbed flow field, that is induced by the wheels, also interacts with the other components of the car and this leaves these parts subjected to sub-optimal flow conditions. Therefore it can be concluded that the aerodynamic performance of an open-wheel racecar is largely affected by the wheels, which incidentally are the parts of the car that are probably least understood from an aerodynamic point of view.

Formula 1 traditionally represents the pinnacle of open-wheel motorracing and racecar development. From the beginning of the first Formula 1 championship in 1950 up to 1967, aerodynamic principles were mainly applied to streamline the competing cars and to provide adequate cooling. The transformation in engine layout from the front of the car to the rear, which took place around 1955, did not alter this approach significantly. The bodywork was still draped closely around the chassis and engine, while the four wheels remained completely exposed. It was not until the mid sixties that the constructors started realizing that the laptimes could be improved far more significantly by producing downforce than by reducing the drag [3]. The increased cornering speeds, acceleration and braking performance due to aerodynamically enhanced wheel grip easily outshone the advantageous top speed on the straights that resulted from drag reductions. Thus inverted wings started appearing on open-wheel racecars in imitation of prototype race classes, where this new application of aerodynamic principles had been pioneered.

In 1969 the technical regulations in Formula 1 changed in reaction to structural failures of wing mountings with disastrous consequences [1]. Aerodynamic devices that were adjustable during the race were prohibited and aerodynamic components could no longer be connected to the unsprung part of the car. However in 1977 Lotus made a big step forward by using the full plan area of the car to generate downforce. The entire car body operated as a wing ‘in ground effect’ and flexible side skirts were added to seal the accelerated low pressure flow underneath the car from the outer flow. Since then the regulating body of the sport has continuously rewritten the rule book in order to limit the (cornering) speeds, while the designers keep pushing the boundaries for additional downforce. Side skirts, flat underbodies, extractor fans and full body diffusers have all been banned in response.

The aerodynamic configuration of a racecar is generally modified for the specific track on which it will race. Depending on the race course characteristics, such as number of corners, average speed through them and length of the straights, a trade-off will be made between downforce and drag, expressed as the aerodynamic efficiency of the car (the ratio of downforce compared to drag). Aerodynamic stability is the other critical factor that defines the aerodynamic configuration. A relatively constant centre of pressure location throughout the range of orientations and ride heights that the car will experience will help the driver to perform to his best abilities [2]. More background information on the aerodynamics of racecars can be found in two recent reviews [4, 5].

### 1.1.2 Context and motivation

The review of racecar ground effect aerodynamics by Zhang et al. [4] presents an overview of the research that has previously been conducted. Up till now most attention has been fixed on isolated components in ground effect. Single [6–11] and double element wings [12, 13], diffusers [14–16] and wheels [17] have all been studied in undisturbed flow conditions. However in real life situations, as discussed previously, none of these components operate in isolation and interaction plays an important role in the overall effectiveness. This research forms the logical next step in trying to increase the understanding of racecar aerodynamics and hereto two largely influential components will be studied simultaneously. The flow resulting from the front wing and wheels affects all downstream parts of the car, but the aerodynamic behaviour of each of these components themselves changes as well due to the presence of the other component. The previous research of isolated components presents a solid base from which this new exploration can be started. This study will thus continue in the footsteps of the work by Zerihan [8] and Mahon [12] on isolated wings and of McManus [17] on isolated wheels.

Several motivations can be given for extending the research domain from the isolated wing and wheel to the combined case. First of all, conclusions about the aerodynamic characteristics of these parts based on research in isolation may be incorrect for the complete car. Most studies of isolated wheels, for example, have shown that a wheel on its own produces lift, whereas the wheel on a car in general generates less lift, or sometimes even downforce. Secondly, components that have been optimized in isolation do not necessarily produce optimal performance when put together, due to (non-linear) interaction effects. Finally, it is expected that the additional insight into the flow phenomena can be used to harness the negative interaction effects and to utilize the positive effects.

The complicated endplate shapes that are being used on current F1 cars show that the constructors are constantly looking for gains resulting from the interaction of wing and wheel flow. However some of the design changes are made quite ad hoc and the physical principles behind them are not always understood. Furthermore, with the exception of using two smaller instead of one normal size wheel [1], not much can be done to limit the wheel drag directly. However when the relative wing position and the wing endplate design are taken into consideration as well, it is very well possible to reduce the wheel drag indirectly.

The obvious area of application for this research is (open-wheel) racecar aerodynamics. Nevertheless similar kind of configurations can be found in aircraft landing gear designs, where upstream parts influence the wheel flow as well and vice versa. Therefore the findings of this study could also be useful to this field. The obtained knowledge and understanding of the flow behaviour is however applicable to a much wider range of flow problems, since interaction effects occur in many situations.

## 1.2 Wheel literature review

The literature review is divided into three components. This section deals with wheel flow, but relevant topics such as cylinder aerodynamics and bluff body aerodynamics are included into the discussion as well. The next section then focuses on wing aerodynamics; both in freestream and in ground effect. The final section with additional literature looks mainly at vortices and interaction phenomena, before summing up the available literature on combined wing - wheel flows. These review sections give a broad overview of relevant topics, for more specific results and discussion of the isolated wheel and wing flow is referred to chapter 3.

### 1.2.1 Cylinder flow

A cylinder and a wheel share many flow features as a result of their geometrical similarities. Therefore it is illustrative to start a study of wheel aerodynamics with a summary of cylinder flow characteristics, especially since a lot of fundamental aerodynamic research has been accomplished in this subject area. Zdravkovich [18,19] has given a comprehensive overview of literature on cylinder aerodynamics and the following discussion will be loosely based on his work.

**Two dimensional flow characteristics** The flow characteristics for an infinite 2D cylinder result primarily from its blunt body geometry and from the absence of sharp edges. Typically this shape causes a large separated wake zone behind the cylinder, high form drag compared to the viscous drag and intrinsic unsteady flow patterns, such as vortex shedding [18]. Alternate shedding from the top and bottom of the cylinder, due to cyclic opposite movement of the separation lines, can result in the formation of a Von Karmann vortex street. Traditionally, cylinder flows are subdivided in regimes that are defined by the topological region in which flow transition takes place; this is either in the wake, the shear layers, the boundary layers, or upstream. Each of these regimes features its own unique flow topology and combination of drag coefficient ($C_D$) and Strouhal number ($St$).

For ideal undisturbed flows the transition location - and therefore the regime boundaries - only depends on the $Re$-number, however in practical cases it is also influenced by various other parameters. These usually start of as small disturbances, but once they exceed a certain threshold they replace the $Re$-number as governing parameter and become the dominant factor of influence. Examples of these parameters are:

- Aspect ratio, $L/D$, or 3D aspects, which lead to the introduction of 'end effects'.
- Ground clearance and wall proximity (also called wall or tunnel blockage), $h/D$.
- Rotation of the cylinder, $V_r/U_\infty$.
- Freestream turbulence level intensity, $I$ (see for example Zdravkovich [18]).
- Surface roughness (see for example Ribeiro [20, 21]).
- Vibrations and oscillations of the cylinder; i.e. due to the finite rigidness of the experimental set-up (see for example Zdravkovich [19]).

Next, the first three parameters will be discussed in more detail, because of their relevance to wheel aerodynamics.

The different regimes for undisturbed cylinder flows are summarized in table 1.1. The boundaries of the regimes, expressed by the $Re$-number, are purely indicative and are influenced by the values of the other parameters as well. Finding exact regime boundary values for specific conditions remains one of the major research topics of cylinder flows. One of the most famous results of cylinder flow research is the discontinuous drop of the drag value during the critical regime, for increasing $Re$-number. Table 1.1 shows that this happens in regime Tr-BL1 and Tr-BL2. The cause of this phenomenon is the movement of the transition position in the (free) shear layers. In the critical regime the transition location moves upstream of the separation position. The resulting turbulent attached shear layers can withstand the adverse pressure gradient better than the laminar shear layers and the separation positions thus move downstream. The reduction in wake size causes the form drag to reduce more than the viscous drag increases due to the turbulent boundary layers and therefore the total drag decreases.

**Effects of low aspect ratio** Three major differences are apparent when the flow around a wheel is compared to that around an infinite 2D cylinder. First of all the sides of the wheel give the flow a 3D character. The extent of the influence of 3D effects on the flow is usually expressed with the aspect ratio, $L/D$, which presents the ratio of the relevant length scales. The other two differences are ground contact and rotation and these will be discussed at a later stage. The free ends of a finite 3D cylinder (i.e. a wheel shaped body) introduce new topological features to the flow and lead to changes in the quantitative characteristics as well. The flow topology for a cylinder with two free ends has been described by Zdravkovich [22], whereas that for a semi-infinite cylinder with one free end can be found in the work of Roh [23]. Notable differences with respect to the 2D cylinder flow are the inflow into the wake region (also called the secondary flow) and the four vortices that start from the two corners of each of the free ends. The 3D effects also change the appearance of the separation lines, which turn into bow-shaped curves when the aspect ratio is reduced.

The topological differences are reflected in changes in the drag coefficient and Strouhal number. The secondary flow into the near-wake around the free edges induces a higher base pressure, which implies that the end effects result in a lower drag coefficient. Zdravkovich [19] mentions a $C_D$ of 1.2 for a 2D cylinder at $Re = 10^5$, whereas its finite equivalent with $L/D = 2$ only has a drag coefficient of 0.7. The shape of the free ends becomes a governing parameter for cylinders with $L/D < 5$ and for example the use of hemispherical ends instead of flat ends has led to a further drag reduction of 19% in a typical case [22]. Vortex shedding does still occur for finite cylinders, but it becomes irregular, spreads over a wider frequency band and interrupts intermittently [22]. The concept of a universal Strouhal number is therefore no longer applicable to highly 3D cylinder flows [24]. Ayoub [24] concluded that the shedding regime in the tip region near the free ends corresponds to a value of the $Re$-number that is lower than the nominal one. In particular, he found that a subcritical regime type of vortex shedding in the tip region may just as well coexist with a supercritical flow on the main portion of the cylinder.

The secondary flow introduces three additional aspects to the flow. The acceleration required to turn the flow around the sides into the near-wake leads to low pressure regions near the free ends. Furthermore the separated shear layers from the sharp edges are modified into a top and bottom counter-rotating swirling vortex pair for each free end. The final aspect is a displacement of the vortex formation region in downstream direction, due to the inflow. This leads subsequently to an additional drag decrease on top of the contribution due to the higher base pressure and also to a lower frequency of vortex shedding as a result of the widening of the shear layers before roll-up.

For disc-like cylinders, with $L/D < 1$, the flow is dominated by the separation from the sharp edges at both free ends. The flow characteristics are therefore more determined by the secondary flow than by the primary. Three types of separation can be distinguished for such a flow [25]: primary separation from the sharp edges, secondary separation of the reversed flow along the flat sides - often followed by reattachment - and finally normal separation from the cylinder circumference due to the adverse pressure gradient. The latter is no longer over the full span of the cylinder, but in the form of separation islets at centre span. Zdravkovich [25] states that these separation islets present intrinsic aspects of the low aspect ratio cylinder flows, caused by the disruption of the separation lines by the flow along the edges. In his experiments the 3D flow phenomena changed the separation lines, located at approximately 86° of the stagnation line, into separation islets at 96° for $L/D < 0.39$. Lazos [26, 27] demonstrates the complexity that the flow topology on an isolated wheel in freestream conditions can have, including many of the features for a finite cylinder.

**Effects of ground contact** The governing parameter for flows around a cylinder in the vicinity of a wall is the gap to diameter ratio, $h/D$. Ground contact can be seen as a special case of asymmetrical blockage, for which this parameter is equal to zero. Apart from the $Re$-number, $h/D$ and the parameters presented for the 2D cylinder flow, this type of flow is also influenced by the relative boundary layer thickness and the state of the boundary layer (laminar or turbulent) along the wall. The flow characteristics change drastically when the gap is decreased below a critical ratio, $h/D_{crit}$. The actual value of this critical gap ratio is again dependent on the conditions defined by the other parameters. Three different flow regimes can be distinguished based on $h/D$, these are:

1. The wide-gap regime, $h/D > h/D_{crit}$; the flow patterns are topological similar to those for a cylinder in free flow and feature regular vortex shedding.
2. The narrow-gap regime, $h/D < h/D_{crit}$; below the critical gap ratio the gap induces

a jet-like flow along the boundary (a wall jet) and the contraction between the cylinder and the boundary produces a locally favourable pressure gradient. This results in a separation bubble in front of the cylinder, reattachment due to the favourable pressure gradient and a second separation caused by the wide-angle diffuser downstream of the minimum gap. The regular vortex shedding first disappears from the side closest to the boundary and then stops completely when the gap is further reduced.

3. The contact regime, $h/D = 0$; the cylinder appears to be an obstacle on the boundary when in contact with the ground and the flow is forced to pass around it on the other side. This causes large scale separation both up- and downstream of the cylinder and the resulting asymmetric flow patterns lead to a significant mean lift force. The stagnation point does no longer reach $C_P = 1$ for this case, because its original position is totally absorbed in the separated - lower total pressure - flow upstream of the cylinder. No regular vortex shedding is present for this case.

The contact regime features the highest possible lift coefficient and the lowest drag coefficient within the $h/D$-range, according to Zdravkovich [19]. In general, vortex shedding stops completely once the cylinder is in contact with the ground, however Sumer [28] was able to generate vortex shedding from the top of the cylinder by forcing the cylinder to move in an oscillatory way and Bearman [29] still found weak shedding from the top for very small $h/D$-values. Research of the flow around a half cylinder in ground effect showed that for this configuration the vortex shedding stops abruptly below a critical gap ratio, which goes hand in hand with a significant reduction of the drag force due to the reduced base suction [30].

The previous discussion should be kept in mind when some of the earlier articles on wheel aerodynamics are studied. Technical limitations at that time forced the researchers to use stationary grounds and / or small gaps between the wheels and the ground. It can now be concluded that the first simplification leads to an incorrect prediction of the force coefficients as a result of the (thicker) boundary layer along the ground, whereas the use of gaps induces a wall jet through the gap, resulting in an underprediction of the lift and an overprediction of the drag.

**Effects of rotation** The final aspect that is of fundamental importance to wheel aerodynamics is rotation of the body. The governing parameter for rotating cylinder flows is the spin factor, defined as the ratio of the peripheral cylinder surface velocity compared to the freestream velocity ($V_r/U_\infty$). For non-slipping rotating wheels this parameter has a value of one. The effects of rotation on cylinder flows have been studied extensively; mainly triggered by the occurrence of an additional aerodynamic force, which is named after its discoverer Gustav Magnus. This Magnus effect force is directed perpendicular to the cylinder axis and perpendicular to the freestream velocity and acts towards the downstream moving cylinder side [19]. Most research into rotating cylinders has focused on the wake development [31], the vortex shedding [32] and the Magnus effect [19], because of the complicating factor that the cylinder surface rotation introduces. On-surface methods, such as oil flow visualization, can not be used for a rotating cylinder and measurement of the on-surface pressures requires a much more complex measurement system.

The rotation of the cylinder wall generates a boundary layer of rotating flow with a velocity similar to that of the cylinder. This layer thickens with increasing spin factor. The locations of the stagnation point and of the separation points change, because one side of the cylinder moves downstream in the same direction as the free flow, while the other moves upstream - in the opposite direction. The stagnation point is slightly displaced opposite to the rotation direction, whereas the separation points are postponed and promoted proportionally to the rotational speed for respectively the side that moves downstream and for the upstream moving side. For the latter side the flow has to reverse direction and relatively high momentum transfer conditions prevail in this region. As a result - for spin factors up to a value of one - boundary layer separation and vortex shedding are slightly suppressed from the downstream moving side compared to the other side. Hence the wake is deflected in the direction of the side with the contrasting surface and freestream velocities. Furthermore the near-wake and vortex formation region are also shortened and compressed as a result of the rotation. The last topological change due to rotation is that the boundary layer origin is displaced as well. With rotation it is located in the position where the surface velocity is equal to the surrounding freestream velocity - or in other words at the point of zero relative velocity - and is thus moved in the rotation direction; opposite to the stagnation point movement.

Although the Magnus effect force is a result of the asymmetric pressure distribution due to rotation, it can also be explained from the perspective of circulation. From the cylinder side with the contrasting surface and freestream velocities originates a strong vortex, which induces a circulation around the cylinder in opposite direction to this eddy. It is this circulation that is the cause of the Magnus effect. In general the vortex shedding frequency - and thus the Strouhal number - rises slightly for increasing spin factors (see

Diaz [32]). However for spin factors above one the Von Karman vortex street starts to disappear and the eddy shedding becomes more random. For spin factors above a *Re*-dependent critical value the periodic shedding and meandering of the vortex street ceases completely [31].

**Relevance to wheel aerodynamics** The individual influences of the three discussed effects on the force coefficients and Strouhal number for a 2D cylinder in free stream have been summarized in table 1.2. However for a realistic wheel flow all of these three effects act simultaneously. Unfortunately hardly any literature is available on the interaction between these effects when two or three of them co-exist in a flow situation[1]. Besides the total effect can not simply be determined by adding the individual effects together, as for most non-linear phenomena. Stationary wheel flows and juncture flows could provide further insight into the interaction of two of these effects.

Wheels typically operate in the *Re*-range of $10^5 - 10^6$ [34]. Purely based on the *Re*-number this would place the conditions around the critical regime at which the discontinuous fall of the drag coefficient is experienced. However it is expected that the ground effect, rotation and end effects in particular have taken over the role of governing parameter from the *Re*-number. Nevertheless some conclusions for cylinder flows can still be applied to wheel aerodynamics. The wheel flow field will be characterized by large separated flow regions, because the wheel is essentially a bluff body, just like a cylinder. Regular vortex shedding has probably ceased as a result of the ground contact, but there may be some irregular shedding from the sharp edges at the sides. The low aspect ratio of a racecar wheel, with usually $L/D \approx 0.5$, implies that the secondary flow (the inflow from the sides into the near-wake) is at least as important as the 2D-type cylinder flow over the top and a complex pattern of separation and reattachment on the sides of the wheel can be expected. Finally rotation as well as ground contact are the reasons for the complete disappearance of flow symmetry between the top and the bottom of the wheel.

### 1.2.2 Bluff body flow

Wheels and cylinders are specific cases of bluff bodies. Apart from the cylinder flow features that have been discussed previously, a wheel has additional characteristics in common with bluff body flows as well. These will be discussed in this section together

---

[1] Kano and Yagita [33] describe the combination of rotation and ground effect, although the 2D cylinder is never tested in contact with the ground.

with the implications for CFD simulations of bluff body flows. Furthermore juncture flows will be examined in particular, because of the relevance to (stationary) wheel flows. The application of diffusers to bluff bodies will also be introduced, since the wing flow shows similar characteristics for the lower ride heights.

**General characteristics** Bluff bodies can be characterized as objects that generate a large region of disturbed flow downstream of the object. The term bluff body is not necessarily equivalent to non-streamlined, because airfoils can behave like bluff bodies as well, whenever subjected to high angles of attack that result in stall conditions. The common feature for bluff body flows is the formation of similar flow structures in the separated region behind the object. The separated flow is usually unsteady in character and its behaviour and extent is influenced by the presence - or absence - of sharp edges on the object. In general, recirculation regions and large-scale turbulent or vortical structures with high rates of dissipation can be identified in the wake of a bluff body. The boundary layers separate at some location from the bluff body surfaces, i.e. the sharp edges, but additionally it is also possible that the bluff body causes flow separation from a nearby wall, when placed in close proximity to it [35].

The Morel [36] and Ahmed body [37] have been studied intensively as representative shapes for a generic automobile body. The governing flow structures and resulting drag value are dependent on the slant angle of the upper surface. The large wake behind a bluff body causes a low base pressure[2], which in turn leads to a high value of the pressure (or form) drag. At higher $Re$-numbers the aerodynamic pressure drag is therefore predominant and the friction drag is negligible in comparison [18]. From an industrial perspective, pressure drag reduction has always generated a lot of interest in bluff body research. One approach is to streamline the afterbody, but alternatively, if the physical shape can not be changed, turning vanes, vortex generators, strategical positioning of an upstream object [39] and splitter plates [40] can also be used. The latter two solutions may be more relevant to wheel aerodynamics, since the wheel shape presents few opportunities for alterations for aerodynamic purposes. The front wing could play a major role in influencing the wheel drag using any of the previously mentioned methods to alter the flow around the wheel.

---

[2] Since the wake has a finite length and closes on itself, the base pressure is significantly lower than the freestream pressure [38].

**CFD simulations** Computational simulations of bluff body flows are much more complicated than those for attached flows, because the results are very much dependent on the prediction of the separation position. Furthermore turbulence and unsteady features play an essential role in the considered flow phenomena. Steady RANS simulations do not resolve the time-averaged contribution of the fluctuating pressures to the drag value. However even unsteady RANS simulations are hampered by the fact that the applied turbulence closure models, which are based on statistical models, can not cope with the large-scale 3D eddy structures that dominate the turbulence transport and therefore they still predict incorrect mean drag values [41, 42].

However if a RANS simulation is used nevertheless, then usually a form of the second order k-$\epsilon$-turbulence model is implemented [43], because of its superior performance in separated flows compared to the SA model. The production of turbulence in the stagnation flow is considerably overpredicted in RANS k-$\epsilon$ simulations, resulting in a strong underprediction of the periodic motion in the wake. Methods that resolve the large scale unsteady motions instead of modeling them, such as DES, LES and DNS, perform better in bluff body problems, but at considerable higher computational costs [41]. Within an industrial context useful solutions can be obtained using RANS, as long as the hypotheses behind the method are kept in mind [44]. The wheel flow and combined wing - wheel simulations in this report are therefore primarily RANS-based, because of the lower computational costs.

**Juncture flow** The flow around a bluff body placed on a flat surface is also referred to as a juncture flow. This kind of geometry bears resemblances with a stationary wheel that is in contact with the ground. The majority of papers published on juncture flows feature a finite cylinder with its axis perpendicular to the flat plate [45–47]. This is in contrast to the wheel orientation, where the axis is placed parallel to the ground. However horseshoe-shaped vortices around the object occur for many different juncture flow configurations (i.e. for a wall mounted cube [41]) and their presence has been suggested for (stationary) wheel flows as well [48].

The horseshoe vortex is created in the following way. A boundary layer forms along the ground, which separates in the proximity of the obstacle due to the induced adverse pressure gradient [46] in front of the object. Subsequently the separated boundary layer rolls up and bends around the cylinder in the shape of a horseshoe vortex. Depending on the flow conditions (primarily the *Re*-number) either a single horseshoe vortex or an array of vortices can be identified. The primary vortex rotates in the opposite direction to the vortices that would be present at the free ends of a 3D cylinder in free flow. For the case of a stationary wheel in ground contact it is therefore expected that the free end vortices at the contact side are replaced by the opposite rotating legs of the horseshoe vortex. It is at this moment unknown whether similar vortices exist for the rotating wheel in ground contact. Even though the moving ground would eliminate most of the boundary layer along the ground, velocity differences due to the presence of the wheel could still lead to the creation of a local boundary layer. However the strong acceleration of the flow just in front of the contact patch - propelled by the moving surfaces - will influence the adversity of the pressure gradient as well and promote the flow to stay attached to the ground. The effect of the horseshoe vortex - if any exists at all - for the rotating case will thus most likely be negligible.

**Diffusers** The application of a diffuser to a bluff body in order to increase the camber and thereby to generate (additional) downforce forms an essential part of the bluff body aerodynamics field. The main reason for discussing diffuser flow in this literature review is that the wing displays certain flow physics that are similar in character, especially at low ride heights. Senior [14] reports the force behaviour of a bluff body equipped with diffuser in ground effect for varying ride height and discusses the flow mechanics with the help of on-surface pressure and oil flow data. The generated downforce is first enhanced and then limited with reducing ride height, in a similar way as for a wing in ground effect. The mechanisms for downforce enhancement are a channeling effect due to increasing diffuser area ratio between the outlet and inlet and increased suction resulting from the edge vortices. Downforce reduction on the other hand is a result of vortex dilution and asymmetric breakdown, as well as from flow separation. A large discontinuous change in downforce occurs when the flow field in the diffuser changes from two symmetric vortices with attached flow to one large diluted asymmetric vortex with large scale flow separation.

The strength and state of the edge vortices have a large influence on the diffuser flow and Zhang et al. [16] have conducted an off-surface study into the characteristics. One relevant conclusion from their work is that the downforce is being enhanced exponentially when the vortices are strong and concentrated with a high axial velocity at the core, whereas this enhancement mechanism disappears when the vortex core slows down, resulting in enlarged weaker vortices that move away from the diffuser ramp surface. Ruhrmann [15] performed a parametrical study of diffuser flows and found that the area ratio and the diffuser ramp angle are two major factors that define the flow behaviour. The maximum downforce is always generated at a similar value of $h/(d \times \theta) \approx 0.7$, where $h$ is the ride height, $d$ half the diffuser width and $\theta$ the diffuser ramp divergence angle in radians. A final noteworthy detail of diffuser flow is that the largest suction peak always occurs at the diffuser inlet [14].

### 1.2.3 Wheel flow

The amount of literature available on wheel aerodynamics is limited compared to that on cylinder flows. Nevertheless, recently the interest in this area has grown, as can be concluded from the list of publications over the last five years [17,49–54]. The lack of similarity between the used models, configurations, test conditions and measurement strategies presents a major difficulty when constructing an overview of previous wheel aerodynamic research. Direct comparison of results is severely hampered by the absence of a generic model and it is therefore almost impossible to judge whether the conclusions are generally applicable or only valid for the studied case. This section first takes a look at the various approaches that can be taken to research wheel aerodynamics, followed by a discussion of respectively the previous experimental and computational studies. In this process the literature will be introduced in almost chronological order based on the progress made in finding solutions for the encountered research complications.

**Various approaches to aerodynamic wheel research** The flow around a wheel is influenced by a large variety of parameters, just like in the case of a cylinder. Furthermore, modeling of the exact configuration and flow conditions still often proves to be complex despite the current technological possibilities. In experiments the combination of correct tyre geometry (contact patch deformation and side wall profile due to set-up camber) and wheel rotation as well as ground movement impose compromises on testing; whereas CFD is mainly limited by the capabilities of the solvers to model both the large and small scale turbulent structures at affordable computational costs. In practical research applications this implies that choices have to be made with respect to simplifications of the problem and modeling assumptions.

Over the years wheel aerodynamic research has been modeled using a large variation in approaches. Differences can be distinguished in:

- The modeling of the wheel: deformable vs. non-deformable, but also in aspect ratio and detailing of the rim, grooves and side profile.

- Wheel exposure: isolated and fully exposed, within a fairing, or modeled on a complete car model.
- Simulation of the ground contact: in direct contact with the ground, with a gap between the wheel and the ground, or with a sealed gap.
- Model dynamics: a rotating or stationary wheel and a moving or stationary ground.
- General flow conditions: $Re$-number, aligned with the flow, or under yaw conditions.
- Previously mentioned factors such as freestream turbulence level, tunnel blockage, surface roughness, model support influence etc.

The prevailing conditions for each of the articles that will be discussed later on are summarized in table 1.3 and 1.4 for respectively the experimental and computational studies.

Apart from these variations in general approaches, a few choices that are specific to experimental or CFD research have to be discussed as well. Two opposing methods can be applied to gather quantitative data in the form of aerodynamic forces and moments acting on a wheel. The first one, the 'Direct Method', makes use of load cells and balances (internal or external); the second, the 'Indirect Method', derives the loads by integrating the pressure distribution over the surface of the body. Disadvantages of the indirect method are that the viscous drag[3] is omitted from the final drag value and that the accuracy is dependent on the spatial resolution of the pressure measurements. On the other hand a major advantage of the indirect method is that the pressure distribution can also give insight in the (local) on-surface flow features, whereas the direct method only gives an integrated (global) overview. Separating the aerodynamic forces from the reaction forces due to the ground contact is the main problem facing the direct method.

Currently the choice of force measurement method limits the selection of the wheel model. The indirect method has mainly been applied to non-deformable tyres made of - for example - carbon fibre or aluminum[4], because deformation in the contact patch region creates additional problems for the on-surface pressure measurement systems. Deformable rubber tyres have been tested in a direct method approach, however due to wear issues

---

[3] However in section 1.2.2 it has been discussed that the viscous drag component is negligible compared to the pressure drag for a bluff body at high $Re$-numbers and therefore the penalty of using this method is small.

[4] With the exception of Mears' experimental set-up, which measures the pressure on the surface of a pneumatic Go-Kart tyre [52, 55, 56], however the tyre was not preloaded and did therefore not deform during the experiments.

and heat production this requires a steel moving ground. Unfortunately, having to use a non-deformable tyre has some modeling disadvantages compared to the deformable tyre approach. First of all the contact patch will not be modeled accurately, because it is represented as a line instead of as a finite area. However also the difference between the undeformed upper and deformed lower side profiles of the tyre can not be modeled when a non-deformable tyre is being used. These effects will all be magnified when the actual tyre is run with a camber-inducing suspension system, which can only be modeled with a permanent conical wheel shape for the case of a non-deformable tyre.

In CFD it is possible to deform the contact region and side profile of the tyre locally, without having to compromise the complete geometry by using the same deformed geometry at the top of the wheel as well. However the application of CFD faces other difficulties, which in turn require simplifications of the problem. The wheel geometry needs to be adapted slightly to assure satisfactory cell quality in the contact wedge region when using a structured mesh approach. Either an elevated ground plane or a (vertical) plint between the wheel and the ground are essential for managing cell skewness in this region (see figure 2.13). Furthermore, only LES or DNS related methods can simulate both the large and the small scale turbulent flow structures accurately, but this imposes impractical requirements on the grid refinement and therefore on the number of cells. Using (steady) RANS solvers is an effective and often used approach to reduce the computational costs, however it needs to be remembered that not all of the physics are modeled correctly in that way. Next it will be discussed how the researchers have dealt with all of these considerations in their studies.

**Experimental studies** The first experiments in wheel aerodynamics followed the direct method route. However the technological possibilities at that time restricted the measurements to rotating wheels located above a stationary ground with a small gap separating them. Under these conditions Morelli [57, 58] found that his isolated rotating wheel model produced downforce and an extra 7-10% drag compared to the stationary wheel case. His results also indicated that fairing of the rim with cover discs led to a drag reduction of approximately 25%. Later on it was proven that the negative lift was caused by accelerating flow in the gap underneath the wheel [58] and that an isolated rotating wheel in ground contact should in fact produce an upwards directed lift force [34].

After this Stapleford [59] studied the influence of ground clearance on the results and the effect of closing the gap between the wheel and the road. His test facilities featured a moving ground, but due to the gap sealing with paper strips and blocks of foam he could not apply wheel rotation and ground movement at the same time. The wheel was attached to a cylinder-shaped racecar body and - in contact with the ground - produced a moderate positive lift. The lift value was considerably lower than for the stationary wheel, since the flow over the top of the wheel got slowed down by the advancing surface of the wheel. The aerodynamic drag of the exposed wheel was found to increase both with rotation and with ground proximity. Stapleford concluded that a correct simulation of the flow problem required wheel rotation and ground contact, but that a moving ground surface did not lead to significant improvements. Cogotti [60] used a similar experimental set-up; featuring a rotating wheel in contact with a stationary ground, however he tested also under yaw conditions.

The next big step was made by Fackrell [34,61,62], who proved that ground contact and ground movement are both essential for the accurate simulation of wheel flows. Fackrell used the indirect method to determine the forces on the wheel, hereby circumventing the problem of having to separate the aerodynamic forces from the reaction forces that are inflicted by the ground. The technical progress since Morelli's experiment had made it possible for Fackrell to measure the pressure from inside the wheel with a microphone-based system and to transport the data out of the wheel with the help of a slip ring. The moving ground system solved the inaccuracies in modeling that resulted from a stationary ground. These are the occurrence of viscous side lobes and vorticity smearing in the wheel wake. Both discrepancies, compared to a full moving ground simulation, could not be resolved by applying boundary layer blowing either, as is discussed by Hackett et al. [63]. Fackrell's research set a new standard, resulting in a wider use of the indirect method. His results are still the benchmark in this subject area, although recent unpublished tests by McManus could provide further insight into wheel aerodynamics due to improved spatial and frequency response of the measurement system.

More recently, Mears [52, 55, 56] was the first to combine the indirect measurement method with a deformable tyre model, although he did not preload the tyre itself. He tested his isolated wheel under yaw conditions as well, leading to a reduction in lift and an increase in drag at 5° yaw angle. Purvis [53] tested a simplified deformable tyre of his own design to study the influence of the contact patch size on the wake development. Although this foam tyre did not have an accurate side profile and suffered from (asymmetric) wear, he concluded that the contact patch primarily influences the lower part of the wake and that the width of the wake increases with contact patch size. In contrast to these studies, Wäschle [54] recently returned to the direct measurement method, but for the first time in combination with proper ground contact, rotating wheel and moving ground. The lift and drag values that he reports are in line with indirect measurement results, even though Wäschle only used a small wheel rotation unit instead of a full rolling road. Finally a few studies of wheels fitted to cars [48, 63–65] have resulted in additional information concerning non-isolated wheel aerodynamics.

Fackrell [34] integrated the measured pressures over the wheel surface. The resulting lift and drag values were $C_L = 0.76$ and $C_D = 0.77$ for the stationary wheel and $C_L = 0.44$, $C_D = 0.58$ for the rotating case. Rotation of the wheel thus decreases both the lift and the drag compared to the stationary case, when a correct ground simulation is applied. The centreline pressure distribution showed two characteristic features for the rotating wheel. These are the high pressure peak, with $C_P > 1$, in front of the contact patch and the earlier separation from the top of the wheel due to the rotation. Fackrell attributed the pressure peak - with values exceeding stagnation conditions - to the introduction of energy to the flow by the moving boundaries. The squeezing of the flow into the contact wedge by the moving ground and by the rotating wheel resulted in the occurrence of a viscous jet, pointed upstream, that would account for the energy increase. This principle is similar to the effect of a pump. Fackrell predicted a negative pressure peak on the downstream side of the contact patch as well, however he reckoned that lifting of the moving belt in this location prevented the occurrence of this feature in his results.

Similar pressure distributions have been found by other researchers as well - both experimentally [51, 52] and computationally [50, 66, 67] - whereas Mears [52] even discovered the negative peak experimentally. However the discussed phenomena are still not completely undisputed and certainly not correctly quantified or understood. A major concern with respect to the pressure peaks in Mears' results and to a lesser extent in Fackrell's is the fact that they are followed by oscillations, which could be of an instrumental kind. This explains the continuing effort in trying to find a universally accepted pressure distribution, among others by McManus [68].

Additional information on the flow field has been derived with the use of tufts [49, 59, 64], smoke visualization [69], total pressure wake measurements [34, 53, 55], LDA [51, 54, 70] and PIV [56, 68]. In general it has been concluded that rotation of the wheel leads to a higher and wider wake at the upperside, while in contrast the lower contours near the road are narrower than for the stationary case. Mears [55] describes that the upper vortices are closer to one another and in a slightly higher position for the rotating wheel, whereas the stationary case is characterized by stronger vortices in the wake, which corresponds to higher energy absorption and thus to a higher drag. Purvis [53] mentions that his total pressure contours in the wake confirm the presence of streamwise vortices emanating from the front of the contact patch. The concept of these so-called jet vortices was introduced by Fackrell [34] and they seem to replace the horseshoe vortex that exists for a stationary wheel. The variations in results for the different experiments show that the side profile shape of the wheel has a large influence on the flow characteristics. Fackrell's comparisons of wheel shapes [34] present the best discussion of this aspect. The effect of wheel camber has been studied by Knowles [70], who noticed a 12% increase in drag coefficient for the cambered wheel (4° camber).

**Computational studies** The first application of CFD to wheel aerodynamics in 1998 by Axon [66] was primarily aimed at validating the usability of this technique. He modeled a simplified version of Fackrell's geometry to study how accurately CFD could predict the experimental data. In general most researchers using CFD have so far either tried to recreate Fackrell's experimental results - or their own in some cases - in simulations [49, 50, 66, 67] and / or studied the influence of variables such as solver settings and turbulence models on the final outcomes [50, 54, 67]. Kellar [69] on the other hand applied CFD simulations to visualize the flow around the front quarter of a racecar, while Knowles [51] tried to determine the support sting effects by modeling the isolated wheel with and without sting.

Table 1.4 summarizes the simulation characteristics for the various CFD studies on wheel aerodynamics. Fully structured grids have only been applied to simplified models that consist exclusively of an isolated wheel. As soon as extra geometries, such as the support sting, are added it proved too difficult and cell consuming to use any other method than a hybrid or even fully unstructured grid. Almost all studies use the same boundary conditions; a velocity inlet, pressure outlet and symmetry on the sides and top of the domain. The ground and wheel are modeled as respectively translating and rotating smooth no-slip surfaces[5]. Knowles [51] and Wäschle [54] model the flow in the rim with sliding meshes, which is also the standard in the motorsport industry, all others use flush cover discs to close the cavities. The contact patch in all of the simulations is modeled by

---

[5] Except for Skea [67] who applies a symmetry condition at the ground instead of a moving wall. His conclusion that a moving wall forces air into the ground - wheel crevice seems correct, however this should actually confirm rather than reject the motivation to prefer the use of a moving wall over a symmetry condition.

elevating the ground plane (see the left figure of 2.13) in order to ensure acceptable cell quality.

Steady RANS solvers with (RNG) $k-\epsilon$ turbulence models are most widely used, with the exception of Wäschle [54], who applies an unsteady RANS solver and presents averaged results, and Basara [50], who presents unsteady RANS solutions. The latter results showed substantial differences in pressure distribution - and to a lesser extent in force coefficients - compared to the steady solutions, however the unsteady results seem to be even more dependent on the turbulence model that has been used. Steady solver results show reasonable agreement with experiments in the prediction of the force coefficients ( [51, 66] came to within a 10% difference). However the flow fields differ qualitatively in specific places compared to the experimental results. Areas where SRANS particularly struggles are separation prediction, transition of boundary layers, base pressure and unsteady phenomena. Causes for this are the incompatibility of trying to solve an intrinsic unsteady flow with a steady solver and the use of turbulence closure models, which are not validated for separated flows and have problems in modelling the transport of large turbulent structures. Obviously mesh quality plays a role as well and obtaining mesh- and solver-independent solutions therefore forms a major difficulty in applying CFD to wheel aerodynamics.

Basara's study [50] showed that unsteady solver simulations produce better agreement than steady[6]. Some of the differences - and sometimes even false agreement - between CFD and experimental results are however also caused by inaccurate modeling of the experimental geometry. All of the researchers have made modifications to the geometry in order to simplify the mesh generation. Side profiles of the wheels have regularly been changed and hubs have been covered with flush discs. This prompted McManus [68] to model Fackrell's exact geometry and to simulate the flow using RANS, URANS and DES. His URANS [17] results are promising and show good agreement. The changes in force coefficients from the stationary to the rotating case are similar to the experimental trend. However the computational lift is predicted to be nearly half of the experimental value, which McManus mainly attributed to incorrect experimental pressures[7] near the line of contact. His unpublished DES results showed similar pressure distributions and force

---

[6] His RNG $k-\epsilon$ URANS simulation produced lift and drag values that differed only respectively 1% and 5% from the experimental values; where the larger discrepancy in the lift coefficient can primarily be explained by a 10° earlier flow separation prediction from the top of the wheel.

[7] In particular an overprediction of the width of the positive pressure peak and omitting of the negative pressure peak, which reaches to $C_P = -1.5$ in McManus' CFD simulations.

coefficients as the URANS simulations, whereas the wake was predicted better with the DES simulations, as expected.

## 1.3 Wing literature review

The literature that is relevant to the wing flow has previously been reviewed by Zerihan [8] and Mahon [12]. Therefore it has been decided to refer to these works, instead of to review this topic as extensively as the wheel literature. The equivalent to tables 1.3 and 1.4 can be found in Mahon's thesis [12], summarizing the experimental and computational literature for inverted wings in ground effect. Furthermore it is worth mentioning that the typical flow features and mechanisms that occur for the specific isolated wing that has been used within the current research are analyzed in section 3.2 of this thesis.

### 1.3.1 General wing characteristics

Since it is impossible to look at all subject areas concerning wing flow, only some specific topics will be covered. General knowledge of wing aerodynamics is assumed and further information can be found in [8, 12]. Multi-element wings can be used to increase the generated lift and / or to postpone stall to a higher angle of attack. Smith [71] defined five effects of slots for multi-element wings that influence the pressure distribution over the elements. A multi-element wake is characterized by confluent boundary layers, where the wake of the upstream element interacts with the downstream element boundary layer on the suction side. Several 2D numerical studies have been performed to analyze this viscous feature [12]. Petrov [72,73] found that bursting of the wake of an upstream element could lead to a stable off-surface separated region, which limits the lift of the downstream element(s). This lift limiting mechanism creates a gradual stall with increasing incidence, in contrast to the more violent leading edge stall. Mahon [12] concluded that this 2D mechanism also limited the downforce experienced for a wing in ground effect with ride height reduction. He could however not find any conclusive experimental proof for this statement.

Reynolds effects play an important role in multi-element airfoil aerodynamics. In general an increase in Reynolds number will lead to beneficial separation characteristics, because the boundary layers become more resistant to adverse pressure gradients. However for multi-element wings adverse Reynolds effects may occur, which are a result of the reduction in boundary layer thickness with increasing Reynolds number and lead to a disadvantageous increase in the effective slot gap between the elements [12]. Mahon's table of previous numerical studies of multi-element airfoils and wings reveals that both RANS and URANS methods have been used in combination with a large variety of turbulence models. A final aspect of wing aerodynamics that is essential to the subject of wing - wheel flow interaction are the tip vortices that result from the finite pressure differences between the wing (and endplate) surfaces. A large amount of literature is available on the characteristics and downstream development of these tip vortices (i.e. see [74]); further discussion of vortices in general can be found in section 1.4.1.

### 1.3.2 Inverted wing in ground effect

Racecar (front) wings usually consist of multiple elements in combination with components to control the flow, such as endplates, endplate feet and in some cases Gurney flaps. The suction surfaces of the elements are directed downwards in order to create downforce. Endplates [75] provide a means to maximize the wing performance for fixed wing dimensions by separating the suction and pressure surfaces of the wing at the tip. This results in a finite pressure difference between the top and bottom at the spanwise extremities of the wing and thus increases the downforce [12]. Endplate feet, which are outward horizontal extensions at the bottom of the endplate, introduce an additional downforce enhancing mechanism in the form of an extra vortex underneath each of the feet, while the other lift enhancing mechanisms get magnified as well [12]. Finite trailing edges [12] and / or Gurney flaps [76, 77] can be used to generate more downforce by creating a finite pressure difference over the trailing edge. The latter is a short strip fitted perpendicular to the pressure surface along the trailing edge of a wing element. Alternate vortex shedding can occur behind the blunt trailing edge or Gurney flap, however this phenomenon ceases to exist when separation from the suction side starts taking place [77].

Several options are available to model a wing in ground effect. However only the use of a moving ground installation will lead to correct results [8], while the other possibilities of using a fixed ground with or without suction or blowing, and the reflection method using mirrored models, all have their shortcomings. A wing in ground effect can produce significantly higher downforce compared to when it is placed in freestream conditions. The downforce increases with reducing ground clearance until it reaches a maximum value after which flow separation occurs. Zerihan [8] introduced the analogy between a wing in freestream with increasing incidence and the same wing in ground effect with reducing ride height. The trend with parameter variation is qualitatively very similar for both situations, although the suction peak and resulting downforce reach higher values for the ground effect case. The main difference is that the freestream stall occurs more abruptly due to the instabilities caused by the separation from the trailing edge moving upstream, whereas the ground effect stall is more gradually. The constraining of the flow by the moving ground prevents the separated region to move upstream and therefore separated regions can be sustained in a more stable way in ground effect. Therefore separation is not the sole downforce limiting factor for wings in ground effect, in contrast to for wings in freestream, whose maximum downforce occurs in general just before flow separation takes place.

Flow field studies of the wing tip vortices [10, 12] revealed that another governing force enhancement mechanism for a wing in ground effect is related to the generation, dilution and breakdown of the wing tip vortices. The presence of a wheel downstream of the wing, during the current research, will influence the path and state of the tip vortices and therefore the downforce that the wing produces. The wake and vortices, that are induced by the wing, will on the other hand influence the pressure distribution on the wheel as well. Understanding of the interaction between these flow fields will be essential in obtaining insight into the aerodynamics of the combined components.

Wings in freestream can experience hysteresis effects, which make the flow features depending on the direction of the parameter change. An abruptly stalled wing will for example not immediately return to the attached flow case when the angle of attack is reduced. Further reduction of the incidence is required before the pre-stall flow is restored. In a similar way a diffuser body in ground effect displays hysteresis effects with ride height reduction [14]. Mahon [12] was the first to discover hysteresis effects for the wing in ground effect, showing that the force coefficients at low ride heights were dependent on the direction of ride height change. It is important to realize that this hysteresis effect is not a time dependent, dynamic result, like the downforce changes due to instantaneous movement of the wing as simulated by Moryossef [78], but a sustainable difference between the increasing and decreasing ride height variation. For the hysteresis results the measurements have been taken after a settling period at a static constant wing ride height.

The summary of numerical simulations for wings in ground effect by Mahon [12] shows that only a limited number of results is available in literature. Most of these studies concern 2D airfoils, including the recent contribution by Mahon [11]. Although Mahon also did some preliminary simulations for a 3D wing in ground effect [12], these results have not been published. From this it can be concluded that there is a severe lack of literature on 3D wing in ground effect simulations, especially with respect to the influence of the ride height on the flow features and mechanisms. Such a study could result in better understanding of the flow physics for a wing in ground effect and would add to the knowledge available from 2D simulations, in which the tip effects are not simulated [9,11]. Finally it needs to be mentioned that Guilmineau [79] successfully simulated hysteresis effects resulting from deep dynamic stall for a 2D wing in freestream using a URANS approach.

## 1.4 Additional literature review

To complete the literature review this final part deals with additional relevant subjects such as vortices, flow interaction and combined wing - wheel aerodynamics.

### 1.4.1 Vortices

In the previous section it has been discussed that endplate vortices from the wing form an important aspect of the wing in ground effect flow field. Furthermore these vortices will be the primary factor of influence on the aerodynamic behaviour of a downstream located wheel. In general, aerodynamic design of racecars is very much orientated towards using vortices to control the flow and to generate or enhance downforce [80]. Therefore this section summarizes a few relevant aspects of vortex flows. First the general characteristics will be discussed, followed by the identification and visualization of vortices and finally the dynamics and interaction with for example the surrounding flow field or with a ground plane will be reviewed.

**Characteristics** The vortices that are most relevant to the current problem result from flow separation at sharp edges of the geometry due to a pressure difference between both sides of the object. Longitudinal vortices originate from edges that are more or less aligned with the flow [10,16], while transverse vortices result from edges perpendicular to the flow, such as blunt trailing edges [7] and Gurney flaps [77]. The endplate vortices are of the first type and play an important role as downforce enhancing and limiting mechanism for wings in ground effect. The pressure difference, which causes endplate and wing tip vortices, induces a circulation around the edge, which in turn leads to divergence of the streaklines on the pressure side relative to the edge, while the streaklines on the suction side converge towards the edge. At the tip of the wing the combination of the pressure difference and the opposing flow direction causes the flow to swirl and detach from the wing, thus forming a vortex with its axis aligned with the flow in streamwise direction.

The second type of vortices result from the pressure difference between the upper and lower side of the element, which causes the boundary layers to separate at the sharp trailing edge and can result in alternate vortex shedding from the top and bottom of the element [7]. The axis direction is in this case parallel to the trailing edge and normal to the freestream flow direction. A final type of vortices are those that result from a delta wing under incidence [81]. These vortices are responsible for generating the main part of the lift force on a delta wing and develop in streamwise direction. Their axial velocity is in general higher than for longitudinal tip vortices [10].

Vortices can thus be described as having a swirling motion around an axis. Devenport [74] discusses the structure and development of a tip vortex from a rectangular wing under incidence. The vortex core along the axis can be distinguished from the outer rotating flow. In general vortex cores are characterized by having a low pressure. Within the vortex, the centrifugal force generates a strong radial pressure gradient, with the minimum pressure occurring in the core. The tangential velocity in the core centre is zero and reaches a maximum at the edge of the core after which it reduces to the outer flow value. Devenport [74] describes how a vortex shed from a wing in turbulent flow produces no turbulence and thus evolves to a laminar state. The velocity fluctuations experienced in the laminar core are inactive motions, which are produced by buffeting of the core due to the surrounding wake.

**Identification and visualization** A practical problem in studying vortices is the identification and visualization of the vortical structures. Objective comparison of the strength and size of a vortex is a very helpful tool in analyzing the influence of the vortex effect for a wing in ground effect. Jeong et al. [82] reviewed several identification methods based on curvature of the streamlines or pathlines, local pressure minimum, vorticity magnitude and / or components of the velocity gradient tensor $\nabla u$. Each method has its limitations, but their preference goes out to a definition based on the $Q$-criterion. $Q$ is the second invariant of $\nabla u$, defined as $Q = 1/2(||\mathbf{\Omega}||^2 - ||\mathbf{S}||^2)$, where $\mathbf{S}$ and $\mathbf{\Omega}$ are respectively the symmetric and antisymmetric components of $\nabla u$; i.e. $\mathbf{S}_{ij} = 1/2(u_{i,j} + u_{j,i})$ and $\mathbf{\Omega}_{ij} = 1/2(u_{i,j} - u_{j,i})$ [82]. In a plane the $Q$-criterion is equivalent to the $\lambda_2$-criterion and a vortex core is subsequently defined as a connected region with two negative eigenvalues of $\mathbf{S}^2 + \mathbf{\Omega}^2$ [82].

The $Q$-criterion, or $\lambda_2$-criterion, can not only be used as a vortex core identification method, but also to visualize vortices. Iso-surfaces give an overview of vortical structures, even in turbulent (wall) shear layers, but the choice of the visualization threshold - the magnitude of the $Q$-iso-surface - is still arbitrary [83]. This has to be kept in mind when analyzing iso-surfaces of $Q$, because for example a lower value could show vortex merging while this phenomenon can not be distinguished for a higher value of $Q$. The iso-surfaces in the figures are non-dimensionalized with $U_\infty$ and $c$ resulting in $\overline{Q}$. Alternatively, vortices can also be visualized using helicity iso-surfaces [84]. The advantage of this method for a 3D flow field is that it can differentiate between primary and secondary vortices and mark their separation and reattachment lines, as well as trace the vortex core streamlines.

**Dynamics and interaction** Wing tip vortices are complex in structure, contain inherent instabilities and show unsteady behaviour. The latter may result in wandering of the vortex core. Investigations have related this wandering to free stream turbulence levels, or to Kevin-Helmholtz instabilities in the shear layer that are absorbed into the vortex [8]. The various stages in the ‘life’ of a vortex generally involve the formation, the roll up in the near-field region, the development and the final breakdown. The roll up into an axi-symmetric vortex can be completed within two chord lengths from the trailing edge.

Vortex breakdown is another dynamic process, just like wandering. Under the influence of an adverse pressure gradient, a vortex may slow down and fall apart. Dilution of the vortex core and the presence of a stagnation point on the axis of the vortex are distinctive features of vortex breakdown [12], but the breakdown is usually initiated and recognizable by a change in the characteristic ratio of the tangential compared to the axial velocity components. Delery [85] discusses in his overview that the breakdown location moves upstream with increasing $Re$-number, increasing swirl number (swirl velocity divided by axial velocity) and with an increasingly adverse pressure gradient. Vortex breakdown can take on various forms and Lucca-Negro [86] offers a comprehensive overview. Examples are a double helix, a spiral and an axi-symmetric bubble form. The type and mode of vortex breakdown depends primarily on the $Re$-number and the swirl intensity of the vortical flow.

When vortices interact with each other they can either merge and form a stronger vortex or repel each other, depending - amongst others - on the swirl direction and vortex strength. The interaction of a vortex with a moving ground plane has been studied experimentally by Harvey [87]. The resulting rebound of the primary vortex and creation of a secondary vortex are relevant to the wing - wheel interaction. The mechanism behind this interaction is as follows: while the vortex moves closer to the ground it induces a cross flow along the floor with an attendant suction peak below the core. The boundary layer resulting from this cross-flow has to negotiate an adverse pressure gradient once it has passed underneath the vortex. When the vortex is sufficiently close to the ground, the pressure gradient causes separation of the boundary layer and a bubble forms with vorticity of the opposite sense as the main vortex. Progressing downstream, this bubble grows rapidly to the point where it detaches from the floor as a secondary vortex, fed by a vortex sheet from the separation point. This leads to the rebound of the primary vortex. The vortex trajectories for this problem have been simulated in 2D by Barker [88], whereas Puel [89] has also looked at the 3D characteristics using CFD.

### 1.4.2 Flow interactions

The aerodynamic behaviour of two or more objects that are placed in close proximity to each other is different than that for the geometries in isolation. The previously discussed wing near a ground plane presents a good example of the interaction of such flow fields, just like the currently studied wing - wheel flows. Due to the non-linear character of flow dynamics it is impossible to superimpose the individual flow fields in order to simulate the total effect and careful analysis of the total configuration aerodynamics is required. This section discusses some flows around multiple objects to get a first idea of what influence interaction phenomena may have.

Katz and Dykstra [90] looked at the interaction of the rear wing flow with that around a car body. They found that a wing that was designed in isolation could produce quite different results when it was placed on a car. The local shape of the car body could for example affect the wing performance via the induced flow field, depending on the position of the wing. Alterations to the local angle of attack have the same effect as wing twist and can lead to higher lift induced drag, when the spanwise loading deviates from an elliptic distribution. Soso [91] showed that a wing placed in the wake of an idealized car model loses downforce and produces more drag[8], partly due to the upwash that was induced by the upstream model. Furthermore the transition on the downstream wing is also influenced by the wake of the upstream model. The downstream wing loses relatively more downforce at higher than at lower ride heights and the downforce of the wing sections close to the

---

[8] This increase in drag is in contrast to the general expected trend that slipstreaming would lead to a drag reduction, making it easier to overtake, as described by Dominy [92].

centre span reduced more than proportionally.

Dominy et al. [92] studied the interaction of the flow around two slipstreaming sports prototype cars. The wake of the leading car is a complex combination of regions with low total pressure and high vorticity. The following car would in general experience less downforce and less drag, which would enable overtaking of the upstream car. The drag reduction was found to be approximately proportional to the area of the car that is exposed to the wake flow. A final interaction example is that of a cylinder behind an airfoil [93]. It was found that the *Re*-number and the vertical offset distance of the cylinder downstream of the airfoil have a large influence on the vortex shedding from the airfoil and / or the cylinder and therefore on the unsteadiness of the aerodynamic loading on the cylinder. The fluctuations of the force coefficients would be largest for the case when the cylinder was directly behind the airfoil, in its wake. It needs however to be remembered that this study concerned a 2D flow field, whereas it is expected that tip effects for both the wing and wheel will play a large role in wing - wheel interaction.

### 1.4.3 Combined wing - wheel flows

Aerodynamic wing - wheel interaction is a novel research subject and no publications for this area could be found in open literature. Neither Mahon [12] nor McManus [68] have looked at interaction effects. Some researchers mention the importance of the problem, but they do not include any results. For example, Agathangelou et al. [2] conclude: “The performance of the front wing is also strongly dependent on the presence of the front wheel. A rotating wheel produces strong crosswise flow areas close to the ground in front of the wheel due to a squeezing or jetting effect. These jet vortices are highly influential in understanding the form of the front wing wake, and their effect changes with the steering angle of the front wheel. This is still a little understood transient aerodynamic effect, which is difficult to reproduce accurately in a wind tunnel test.” While recently Katz [5] referred to the wing - wheel interaction in the following way: “Most open-wheel racing regulations allow a wing span wider than the distance between the front wheels. However, earlier (unpublished) studies show an unfavourable interaction between the wing tip-vortices and the wheels, clearly favouring the narrower wing span design.”

The research that probably comes closest in intention to the current study is the one performed by Kellar [69]. He studied the front-end quarter of an open-wheel racecar both with experiments and CFD. However significant discrepancies between the experimental and computational model harmed comparison of the results. Furthermore his experimental set-up did not include ground movement, whereas in contrast to this the wheel was not rotating in the CFD simulations. Recent publications by Diasinos [94,95] do not do justice to the complexity of the problem, because wing tip vortices and wheel end effects have been ignored completely by using a 2D approach. Therefore it can be concluded that there is little understanding of the flow interaction phenomena and mechanisms that govern the combined wing - wheel flow. Furthermore no insight is available into the influence of configuration parameters, such as wing - wheel overlap and gap or wing ride height, on this interaction.

## 1.5 Research objectives

The previous literature review sections have introduced the topic area of aerodynamic wing - wheel interaction by discussing relevant subjects. One important conclusion is that hardly any research has been conducted into this interaction - despite its major influence on the wing and the wheels as well as on other (downstream) parts of a racecar. As a result of the novelty of this topic, many different aspects can be analyzed and a selection of parameter combinations has to be made. This section sets the research goal and derives several research questions that will be examined in the thesis study.

The aim of this research is to contribute to the knowledge on (front) wing - wheel interaction. Hereto a combined experimental and computational study has been performed to answer the following research questions:

1. What is the influence of an upstream-mounted wing on the aerodynamic characteristics of a wheel and vice versa?
2. How does the aerodynamic interaction between these components of the configuration depend on vertical, streamwise and spanwise position variations of the wing relative to the wheel?
3. Which flow mechanisms and phenomena cause the observed behaviour and what would be the main factors of influence for these physics?
4. Would it be possible to reproduce the qualitative (flow features and phenomena) and quantitative (correlation with experimental results) aspects of wing - wheel interaction with the use of current, ‘state-of-the-art’ CFD simulations?

Apart from the above mentioned primary objectives three additional goals can be defined to have a fundamental relevance to this research. These are first of all to improve on the correlation of the isolated 3D wing in ground effect simulations as achieved by Mahon [12]. Secondly, to find experimental (and / or numerical) evidence for the off-surface separation phenomenon described by him as one of the lift limiting mechanisms and at last to determine any fundamental differences between the aerodynamics of a cambered and a non-cambered (as used by McManus [68]) wheel. Finally this chapter concludes with a summary of the thesis structure.

## 1.6 Structure of report

This PhD thesis consists of another four parts. The next part starts off by discussing the problem in more detail. Hereto chapter 2 focuses on the research methodology, looking at how the problem will be modeled and simulated both experimentally and with the use of computational methods. The following part, in chapter 3, will summarize the results for the isolated wheel and wing cases for reference purposes. These previous two parts are not essential for an understanding of the current topic, but present background knowledge. After this the research questions will be answered in the subsequent chapters, 4 to 8, which form the main body of this thesis. The last two research questions will be dealt with in reversed order, to ensure that relevant results of the computations can be included in the discussion of the flow physics as well. Finally chapter 9 will complete this thesis by summarizing the conclusions and by presenting recommendations for future work.

| **STATE** | | **REGIME** | | $Re$-**RANGE** | $L_W$, $L_F$ | $C_D$ |
|---|---|---|---|---|---|---|
| L | Laminar | 1 | No-separation | 0 to 4-5 | none | $\downarrow$ |
| | | 2 | Closed wake | 4-5 to 30-48 | $\uparrow$ | $\downarrow$ |
| | | 3 | Periodic wake | 30-48 to 180-200 | $\downarrow$ | $\uparrow$ |
| Tr-W | Transition in wake | 1 | Far-wake | 180-200 to 220-250 | $\downarrow$ | $\uparrow$ |
| | | 2 | Near-wake | 220-250 to 350-400 | $\uparrow$ | $\downarrow$ |
| Tr-SL | Transition in shear layers | 1 | Lower | 350-400 to 1k-2k | $\uparrow$ | $\downarrow$ |
| | | 2 | Intermediate | 1k-2k to 20k-40k | $\downarrow$ | $\uparrow$ |
| | | 3 | Upper | 20k-40k to 100k-200k | same | same |
| Tr-BL | Transition in boundary layers | 0 | Precritical | 100k-200k to 300k-340k | $\uparrow$ | $\downarrow$ |
| | | 1 | Single bubble | 300k-340k to 380k-400k | unkn. | $\downarrow\downarrow$ |
| | | 2 | Two bubbles | 380k-400k to 500k-1M | unkn. | $\downarrow\downarrow$ |
| | | 3 | Supercritical | 500k-1M to 3.5M-6M | none | $\uparrow$ |
| | | 4 | Postcritical | 3.5M-6M to unkn. | unkn. | same |
| T | Fully turbulent | 1 | Invariable | unkn. to $\infty$ | unkn. | same |
| | | 2 | Ultimate | | unkn. | unkn. |

Table 1.1: Summary of disturbance free flow regimes for cylinders. '$L_W$' is the length of the near-wake (only for L2 regime), '$L_F$' is the length of the eddy formation region (from L3 to T2 regimes), $\uparrow$ is increase, $\downarrow$ is decrease, $\downarrow\downarrow$ is rapid decrease compared to the previous regime, 'unkn.' means unknown; table after Zdravkovich [18].

| | **Coefficients** | | |
|---|---|---|---|
| **Effects** | $C_D$ | $C_L$ | $St$ |
| 3D, end effects | $\downarrow$ | same | $\downarrow$ |
| Ground contact | $\downarrow$ | $\uparrow$ | none |
| Rotation (anti clockwise) | $\downarrow$ | $\downarrow$ | $\uparrow$ |

Table 1.2: Influence of end effects, ground contact and rotation on $C_D$, $C_L$ and $St$ for cylinder flows. For a 2D cylinder in freestream conditions typical reference values are $C_D = 0.6 - 1.2$, $C_L = 0$ and $St = 0.2 - 0.4$, depending on the flow parameters ($Re$ in particular). $\downarrow$ means a decrease, $\uparrow$ an increase, 'same' is no influence and 'none' that no vortex shedding exists for ground contact.

| **AUTHOR** | **REF.** | ***Re*-NUMBER** | $L/D$ | **WHEEL** | **TYRE** | **GROUND** | **CONDITIONS** | **MEAS.** |
|---|---|---|---|---|---|---|---|---|
| *Experimental* | | | | | | | | |
| Morelli | [57, 58] | $1.34 \times 10^6$ | 0.35 | I,IF | D | G | RW,SR | DM |
| Stapleford | [59] | $2.16 \times 10^5$ | $0.33 - 0.66$ | OC | D | G,GS | RW,SW,SR,MR | DM,IM |
| Fackrell | [34] | $5.3 \times 10^5$ | 0.61, 0.66 | I | ND | C | RW,SW,SR,MR | IM,WM |
| Oswald | [64] | $0.2 - 1.2 \times 10^6$ | 0.3 | OC | D | C | RW,MR | IM |
| Cogotti | [60] | $6 \times 10^4 - 2 \times 10^6$ | 0.28 | I,OC | D | G,GS | SW,RW,SR | DM |
| Hackett | [63] | - | - | OC | ND | G,C | RW,SW,SR,MR | DM,WM |
| Mercker | [48] | - | - | OC | D | G,C | RW,MR | DM,WM |
| Wickern | [65] | - | 0.31 | IF,OC | D | C | SW,RW,MR | DM |
| Skea | [49] | $5.51 \times 10^5$ | 0.125, 0.5 | I,IF | D | C | RW,MR | IM,WM |
| Kellar | [69] | $2.5 \times 10^4 - 6.5 \times 10^5$ | - | OC | - | G | RW,SR | IM,DM |
| Knowles | [51, 70] | $3.69 \times 10^5$ | $\approx 0.44$ | I | ND | C | RW,MR | DM,WM |
| Mears | [52, 55] | $2.5 \times 10^5$ | 0.53 | I | D | C | RW,MR | IM,WM |
| Purvis | [53] | $5.54 \times 10^5$ | 0.48 | I | D | C | RW,MR | WM |
| Wäschle | [54] | $5.37 \times 10^5$ | 0.37 | I | D | C | RW,SW,SR,MR | DM,WM |

$L/D$ is aspect ratio; WHEEL is either isolated (I), isolated and faired (IF) or on car (OC); TYRE is deformable (D) or non-deformable (ND); GROUND contact can be gaps (G), gaps sealed (GS) and contact (C); CONDITIONS refers to stationary wheel (SW), rotating wheel (RW), stationary road (SR) and moving road (MR); MEAS. refers to direct (DM), indirect (IM) or wake measurements (WM).

Table 1.3: Summary of relevant factors in experimental research for wheel related articles.

| **AUTHOR** | **REF.** | ***Re*-NUMBER** | $L/D$ | **WHEEL** | **TYPE** | **CELLS** | **SOLVER** | **TURB.** |
|---|---|---|---|---|---|---|---|---|
| *CFD* | | | | | | | | |
| Axon | [66] | $5.3 \times 10^5$ | 0.61 | I | Struct. | $5.4 \times 10^5$ | Steady RANS | RNG $k - \epsilon$ |
| Skea | [49, 67] | $6.9 \times 10^5$ | 0.5 | I,IF | Struct. | $3.6 \times 10^5$ | Steady RANS | (RNG) $k - \epsilon$ |
| Kellar | [69] | $2.5 \times 10^4 - 6.5 \times 10^5$ | - | OC | Unstr. | $3.4 \times 10^5$ | Steady RANS | $k - \epsilon$ |
| Knowles | [51] | $3.69 \times 10^5$ | $\approx 0.44$ | I | Hybr. | $9.3 \times 10^5$ | Steady RANS | $k - \omega$ |
| Basara | [50] | $5.04 \times 10^5$ | 0.79 | I | Struct. | $3.9 \times 10^5$ | Unsteady RANS | (RNG) $k - \epsilon$, RSM |
| Wäschle | [54] | $5.37 \times 10^5$ | 0.37 | I | Hybr. | $6.7 \times 10^6$ | (Un)steady RANS | (RNG) $k - \epsilon$ |

$L/D$ is aspect ratio; WHEEL is either isolated (I), isolated and faired (IF) or on car (OC); TYPE is Structured (Struct.), Unstructured (Unstr.) or Hybrid (Hybr.); CELLS is the number of grid cells; SOLVER refers to the used solver method, Turb. refers to the applied turbulence models.

Table 1.4: Summary of relevant factors in CFD research for wheel related articles.

# Chapter 2

# Research Description

After setting out the goal of this research in the previous chapter, this chapter will take a look at how the wing - wheel interaction has been modeled to study the problem systematically. The general methodology will be discussed and the test configuration will be introduced, after which the general framework of the research will be explained. Finally the experimental and computational research parts will be discussed in more detail in separate sections.

## 2.1 Research methodology

This description of the research methodology comprises three different aspects. First the general approach will be outlined, then the sequence in which the experimental tests have been conducted, and in which the results will be implemented, will be discussed and finally the role of CFD within the research programme will be explained.

### 2.1.1 General approach

Since this is the first study of its kind, it is the intention to conduct a broad initial examination of aerodynamic wing - wheel interaction. Furthermore the resulting knowledge should be generally applicable to different configurations and conditions. A few simplifications have to be made and requirements have to be fulfilled in order to achieve this.

First of all the test model has to be simplified to assure general applicability, because too much detail in the geometry will obscure the global trends with model specific physics. Therefore generic wing and wheel models, which are representative for open-wheel racecars but do not feature all the car specific details, have been used during this research. The wheels have been supplied by Honda Racing F1 and are non-deformable cambered tyres of which the hubs have been covered, whereas the wing is a non-twisted double element constant chord configuration with simple flat endplates that has been constructed by Mahon [12]. Both will be described in more detail in section 2.3.2.

Secondly, for a comprehensive understanding of the interaction it is important that the phenomena can be studied over a wide range of parameters. This research is set up as a parametrical study with three main variables. The wing ride height influences the vertical position of the wing flow field, but also at the same time its characteristics, such as the vortex strength and the induced flow field, via the ground effect. The wing - wheel overlap and gap change respectively the spanwise and streamwise location of the wing flow field without having a similar direct influence on its characteristics. Therefore by varying these three parameters it is possible to alter the wing induced flow field location relative to the wheel in 3D space, as well as its characteristics without having to change the wing settings[1]. Since the position of the wing is fixed by the support structure and the wing span is determined by the size of the model, the wing - wheel overlap and gap are changed by repositioning the wheels relative to the wing; effectively changing the front wheel track and length of the car in this way.

The third requirement is that reference cases and baseline conditions have to be defined to allow a relative comparison of the interaction. Because the characteristics of the wing flow field can be influenced directly by varying the wing ride height, as has been discussed previously, it has been decided that the wing would be kept in a baseline configuration throughout testing. Therefore all interaction tests have been performed at constant wing settings, which are equivalent to the optimal settings defined by Mahon [12]. Furthermore the tests have been performed under similar conditions for both the isolated components and for the combined configuration, wherever possible. The majority of tests have been conducted at a dynamic pressure equivalent to a velocity of $30m/s$ under standard conditions; a summary of the test conditions can be found in section 2.3.3.

Combining the strengths of various analysis methods is another essential requirement to improve the understanding of the flow interaction. Each of the experimental methods, that can be applied to the problem, will shed a different light on the flow phenomena. For general insight into the interaction it is necessary to study the on- and off-surface features, next to the global force behaviour. In addition to using various experimental methods to

---

[1] Wing settings refer here to variables such as the gap and overlap of the flap relative to the main element, as well as the angle of attack of the elements and the use of endplate feet and / or trip strips.

examine the flow, CFD can also help to improve the understanding by providing its own advantages compared to experimental tools. Therefore this research combines a variety of experimental methods with CFD simulations to obtain the best results. Absolute quantitative results have not been pursued during this research, since the goal of this work is to derive qualitative trends and to explain the governing physics. The choice of experimental methods and equipment reflects this priority of relative differences over absolute values. Appendix B.2 presents more information on the accuracy and uncertainty levels for the used methods.

Finally, in any novel subject area it is possible to continue in many different directions and study a variety of factors of influence at different levels. To preserve the character of an initial study, it has been decided to start with the basic level and leave certain details for future research. Therefore the majority of results have been averaged over time, presenting steady flow characteristics. Unsteady features form an intriguing aspect and may be necessary to explain specific flow phenomena, but for an initial understanding it is more time-efficient and productive to focus on the time-averaged results. Also the flow has been considered to be symmetrical with respect to the vertical symmetry plane of the wing in streamwise direction (the $x$-$z$ plane, see figure 2.3). Although differences in the flow could occur between the domains at both sides of the symmetry plane at any given time, considerable savings can be made by using this assumption, for example by allowing to mesh only half the flow domain in CFD simulations. Oil flow results (see chapter 5) indicate that the symmetry simplification is valid for nearly all of the studied cases[2].

### 2.1.2 Test program

The previously defined 3D parameter domain consisting of wing ride height, overlap and gap can still be explored by means of different routes. It has been decided to use a 'three layer approach' to do this in a systematic and efficient way. First the global flow behaviour has to be studied within the practical boundaries of this domain, using integral parameters that will give a clear general overview. Hereto force measurements on the wing and wheel have been performed in order to reveal regions with similar, continuous, force coefficient characteristics. Assuming that the force regions have been defined with sufficient parameter resolution, it can be concluded that the flow features within each of these regions are consistent and comparable. This implies that during the next steps of

---

[2] Some sort of asymmetry can be distinguished in separated flow regions on the wing for specific cases, but this should only have minor influence on the results.

the study one typical setting per region can be chosen to examine the characteristics of the flow features.

An upward and downward cycle through the ride height range has been performed for a number of overlap and gap combinations during this first step. Due to the longer set up time required for overlap and / or gap changes, it is inevitable that the parameter domain has been resolved most accurately in ride height direction. The most extensive examination has taken place for baseline overlap and gap settings of both $20mm$, whereas each of the other setting combinations have been studied with a reduced ride height list. In line with Mahon's measurements [12], analysis of hysteresis effects over the ride height range has been included by performing an upward cycle immediately followed by a downward cycle. With the current set-up it is impossible to test for hysteresis effects due to overlap or gap changes, but such results would have little relevance to practical applications anyway.

Next, the second step looks at how these variations in force behaviour are occurring. On-surface measurement methods have been applied to realize this task. Although these methods, such as pressure measurements and oil flow visualization, produce more detailed information on the flow than the integral force coefficients, it would be harder to derive the flow regions directly from these results. Therefore selecting the test setting combinations during this step has been based on the regions defined during the previous step. The measurement methods during this second step do in general require more time than a force measurement run and only a much smaller part of the parameter domain could be covered as a result. The baseline overlap and gap setting has been studied in some detail over the ride height range, whereas a limited set of data is available for the alternative settings.

The goal of the final step is to improve the understanding of the interaction by deriving why the flow behaviour variations are happening and which phenomena cause the on-surface features discovered during the second step. The on-surface results can give an indication of the location in the flow domain where the relevant flow phenomena take place and this information has been used to choose locations for PIV and hot-wire measurements. Nevertheless the numerous combinations in setting possibilities have to be multiplied by the possible variations in measurement location during this third step and therefore only a small part of all potential measurements could be completed. Again data has primarily been collected for the baseline overlap and gap setting in order to be able to explain the flow phenomena that occur over the ride height range. As a final thought it can be added that CFD could fulfill all of the previous steps at once and the next section will thus look at the role of CFD within the current research.

### 2.1.3 Role of CFD

Within this research CFD has been considered to be an ‘off-the-shelf’ tool that can be used to improve the understanding of the flow interaction. Commercially available codes for mesh creation and numerical solving have therefore been used for this purpose. The application principles are similar to those used in an industrial environment. The only exception to this rule is that the used grids are more labor-intensive to create than for most industrial purposes, as fully structured boundary layer resolving modules are being used.

The role of CFD within the research changes as a result and depends on the phase of the study. Initially the CFD method has been validated by correlating the results with experimental data, while improvements to both numerical grids and solver settings have been implemented during this process. The data that has been gathered during this phase consists of the same flow quantities and representation surfaces as in the experimental outcomes. Therefore CFD does not offer any additional information at this stage. However after this initial phase the true potential of this method can be explored. In the remainder of the research CFD has been applied as a method in its own right. Within the accuracy determined during the validation phase the computational results could now be used to visualize alternative flow quantities on other surfaces and in that way contribute to the goal of this research. Due to the limitations of the numerical schemes and turbulence models it is inevitable that the correlation will show weaknesses in the CFD results - especially in separated regions behind bluff bodies such as the wheel - however CFD has proved crucial in linking all the (experimental) data together.

A final role that is performed by CFD is to compare different approaches for the computational analysis. On the one hand simulations have been performed with techniques that are similar to those used at the industrial partner of this project, while on the other hand more elaborate grids and solver methods, such as DES, have been used for better understanding. This makes it not only possible to correlate computational with experimental results, but also to look at how different approaches perform relative to each other. Furthermore simulating a range of parameter cases, such as for varying wing ride height, can give an indication on how well CFD resolves the occurring flow features, giving better insight into the strengths and weaknesses of this method.

## 2.2 Framework outline

After the discussion of the methodology in the previous section, the attention will now focus on the research context. First the restrictions and simplifications, which have shaped the way the research has been conducted, will be summarized, then the geometries of the test configurations will be described and finally some general definitions will be given that will be used throughout this thesis.

### 2.2.1 Restrictions and simplifications

The scope of any research is realistically determined by imposed constraints, such as available facilities, technological possibilities and requirements from the interested parties. It is important for transparency that these restrictions are stated before the beginning of the discussion. Therefore this section will explain how certain decisions have resulted from constraints, whereas others have been made as simplifications in order to limit the research to workable proportions.

The wind tunnel and the test models are the main factors that have defined the approach to this research. The first is a permanent facility with fixed dimensions and performance, which has previously been used for the research on the isolated wheel [68] and the isolated wing [12]. The latter have been chosen for research continuity and for time considerations, especially with respect to the necessity of conducting reference tests for isolated models and to the time required for model manufacturing. The geometry of the non-deformable wheels is typical for F1 applications and the experimental models have been provided by the industrial partner. The reason that the wheels are cambered, in contrast to those used by McManus [68], is that the initial pressure measurement system was permanently fitted to a cambered wheel so that all other tests had to be performed with cambered wheels as well for consistency. However at a later stage, after it was decided to use McManus' wheel pressure measurement system instead, a large quantity of tests had already been completed and this made it necessary to continue with cambered wheels[3]. The wing models and tunnel model support structure are inherited from Mahon's

---

[3] Disadvantages of wheel camber are that it complicates the setting up process and the understanding of the flow physics, because the camber angle adds another factor of influence. Furthermore cambered wheels are also more prone to irregular behaviour, such as bouncing, because most of the wheel is constantly slipping due to the varying radius over the contact patch. This can be understood by considering that a comparable cone (without a top), which rolls over a flat surface, will follow a curved trajectory instead of a straight and is thus more likely to bounce when forced to move along a straight line.

research [12], whereas the wheel mountings have been made specifically for this purpose.

Apart from these general constraints, several simplifications have been made as well. Although some of these have already been mentioned in the previous sections, they are again included in the following summary for clarity:

- The focus will be on steady phenomena, using time-averaged results.
- The flow is considered to be symmetric with respect to the $x$-$z$ plane.
- All tests have been performed under straightline conditions; although wheel steer angle will influence the results, it is not possible to perform tests in yaw and / or with steered wheels with this tunnel and rolling road installation.
- The wheel hubs have been covered to simplify the flow field (this prevents cross-flow through the hub as well as cavity effects); an additional advantage of this is that no 'sliding meshes' have to be used in CFD to simulate the flow around the rotating spokes of the rim in the wheel hub.
- The wing has been tested in a baseline configuration without endplate feet[4].
- All other surrounding car components, such as the nose cone, suspension parts, the barge boards and the undertray, have been omitted in order to focus on the wing - wheel interaction.

To put these restrictions and simplifications in perspective it is important to realize that they have the following combined consequences:

- Due to the model scale and the maximum wind tunnel velocity it is only possible to test at approximately a quarter of the Reynolds number that will be experienced on the track. Appendix C gives an indication of the influence of Reynolds effects on the results.
- The wheel side profile has been designed as an averaged mix of the deformed and undeformed tyre shape, because the wheels are non-deformable[5]; furthermore the contact patch with the ground is a line instead of a proper imprint.

---

[4] An endplate foot is the horizontal flat surface extending outwards from the lower edge of the endplate.

[5] Nevertheless, even if deformable tyres had been available, it would still be impossible to use them in preloaded condition on the belt of the current moving ground installation.

- The wheel lift can only be measured via the indirect method, because the tunnel is not fitted with wheel balance pads below the rolling road. Using the pressures on the wheel to determine the lift does however have the additional advantage that the on-surface pressure distribution can also be used to get a better insight into the flow features.

- The wind tunnel configuration has to consist of two wheels to create the symmetric flow conditions; unfortunately this induces a higher tunnel blockage for the flow. The complete wind tunnel model has a relative high blockage factor in the tunnel facility, as discussed in appendix B.1. However, although this is just below the limits for which blockage corrections become difficult, the consistency in configurations should guarantee that accurate qualitative trends can be derived.

### 2.2.2 Dimensions and definitions

For clarity and reference, this section will summarize the dimensions of the models as well as present definitions and abbreviations that will be used repeatedly in this thesis. The wing and wheel models are 50% scale with the main characteristic dimensions being 284$mm$ for the total wing chord (main element and flap chords combined), 580$mm$ for the wing span, 313.9$mm$ for the wheel diameter and 172.8$mm$ for the wheel width. Table 2.1 gives an overview of additional dimensions and parameters, whereas the wing has also been described extensively in Mahon's thesis [12]. The wing design has been based on the 2002 FIA technical regulations, but features the possibility to run 55$mm$ wide endplate feet without exceeding the maximum allowable wing span. The profiles are developed by the industrial partner[6], while the endplates are simple flat plates of which the leading, trailing and upper edges have been rounded with a fillet radius of 2.5$mm$. The undersides of these endplates are parallel to the ground and they protrude 2.5$mm$ upstream of the leading edge of the main element and 5$mm$ downwards of the lowest point of the main element. Figure 2.1 shows the element profiles and wing geometry.

The wheel model that has been used for the majority of the tests is from the 2005 season (BAR 050-W0-056 series, Honda Racing F1 Team internal designation) and is an accurate representation of the actual geometry. The only concession that has been made is that the wheel represents a cambered shape due to being made out of non-deformable carbon fibre. It has been common practice in F1 to give such wheels profiles that form a

---

[6] The main element profile has the Honda Racing F1 Team internal designation FM9 and the flap FF08, both are cambered profiles with trailing edges of finite thickness.

blend between the deformed and non-deformed geometry and to add a camber angle to the wheel axis to mimic the aerodynamically important orientation of the wheel on a real car. The main consequence of this is that, whereas the real wheel would have a non-deformed profile for most of the circumference, the cambered model wheel features the same angle of the tyre tread at both the contact patch and at the top of the wheel. Figure 2.2 shows the tyre profile of the wheel. The model wheels have a camber angle of 2.4°, which is defined as the angle between the wheel axis and the ground, or as half the cone angle. The camber has a complicating effect on the analysis, as the wheel radius varies over the tyre tread. The reported wheel diameter of $313.9mm$ is based on the maximum radius, whereas the rotational velocity in the CFD simulations has been derived from the average radius. The characteristic kink in the side profile is located at approximately $21mm$ from the side of the wheel (see figure 2.2). Four longitudinal grooves along the tyre tread are included in the model according to the regulations; these are each $7.5mm$ wide and $1.25mm$ deep. The tread parts between the grooves are each $17.5mm$ wide.

The coordinate system that will be used throughout this work is indicated in figure 2.3. The positive $x$-axis is directed in the downstream direction, the positive $z$-axis upwards and the positive $y$-axis, according to the right hand rule, to the starboard side of the tunnel. The origin is located in the symmetry plane on the ground, whereby the $x$-position is chosen to be underneath the most upstream point of the leading edge of the main element of the wing. Both the location of the origin and the orientation of the coordinate axes differ from those used by Mahon [12] to be more in line with the current application.

Figure 2.3 also shows the definitions of the three primary variables in this research: the wing ride height, the wing - wheel overlap and the wing - wheel gap. The first of these, $h$, is defined in consistency with Zerihan's [8] and Mahon's [12] work as the vertical distance between the ground and the lowest point on the wing main element[7]. Two alternative measurements of the wing ride height - to the flap trailing edge ($h_{Fte}$) and to the top of the endplate ($h_{EPt}$) - are also shown in figure 2.1. The wing ride height can be adjusted automatically with the model in situ within a range from $15mm$ to $180mm$.

The wing - wheel overlap, $O$, is defined as the distance in spanwise $y$-direction between the inside of the wheel - the side closest to the symmetry plane - and the outside of the endplate, consistently measured in a plane at 150mm from the ground plane. The overlap

---

[7] Since the wing orientation is not changed within this research this point is always located at $x = 31.4mm$ from the leading edge of the main element; the lower edge of the endplate is the actual lowest point of the total wing configuration and located $5mm$ below this point.

value is positive when the wheel is physically positioned behind the wing when looking at the configuration in the downstream direction, whereas a negative overlap implies that the wing and wheel have no overlap in this way. The overlap can be varied by hand within a range from $+50mm$ to $-50mm$, but requires relocation and realignment of the wheels. During the experiments the overlap has been changed from $+50mm$ to $-15mm$, which corresponds to an overlap of respectively 30% and $-9\%$ of the wheel width.

The wing - wheel gap, $G$, is defined as the distance in streamwise $x$-direction between the most downstream point of the endplate (at $x = 272.5mm$) and the most upstream point of the wheel, consistently measured in a plane at $150mm$ from the ground plane. Gap values from $10mm$ to $55mm$ have been used within this research. Changing the gap again requires relocation and realignment of the wheels.

The last two definitions both feature a plane at $z = 150mm$, due to the way in which the wheels have been set up. Hereto two metal rulers have been placed on $150mm$ high metal blocks, one parallel to the flow to define the overlap and one perpendicular to the flow to dictate the gap. Figure 2.4 shows a picture of the setting up process with the cover panel of the tunnel side fillet removed. The height of the set-up plane is close enough to the height of the wheel axis on the inside of the wheel to assure that the most forward position of the wheel has been selected.

The definitions of the directions of the aerodynamic loads are also included in figure 2.3. Positive wing and wheel drag both act downstream, in positive $x$-direction. Because this study concerns racecars with downforce producing inverted wings, a positive downforce on the wing is directed downwards, in negative $z$-direction. The pitching moment of the wing is positive if it causes a nose down rotation, so if the moment is directed along the negative $y$-axis. The pitching moment is resolved around the load cell resolution point, but transfered to an arbitrary point at $(53mm, 0, 0,)$ in line with Mahon's results [12]. The quarter chord point for this configuration is at $x = 71mm$ and the pitching moment around this point has also been calculated.

Finally this section will conclude with a few abbreviations that will be used regularly. IWi and IWh refer to respectively the Isolated Wing and the Isolated Wheel, whereas strictly speaking the latter refers to a configuration without wing but still with two wheels in symmetric set-up. CWWxxyyhzz means combined wing - wheels configuration with an overlap of xx $mm$, a gap of yy $mm$ and a ride height $h$ of zz $mm$. Unless stated otherwise, the terms overlap and gap will always refer to the wing - wheel overlap and gap in the rest of this thesis and not to the overlap and gap of the flap relative to the main element.

## 2.3 Experimental research

The test facility, experimental models and measurement methods and equipment will be introduced successively in this section. The data sampling characteristics and postprocessing methods will also be discussed for each of the measurement techniques.

### 2.3.1 Test facility

The experimental tests for this research have all been conducted in the $7 \times 5$ wind tunnel facility of the University of Southampton. This conventional tunnel features a closed test section with a closed return channel. The name refers to the cross sectional dimensions of the test section in feet. The cross section measures $2.1m \times 1.7m$ and has 45° side fillet panels mounted in each of the four corners (see figure 2.5). At the top corners these panels are $0.45m$ wide and at the bottom $0.35m$. The test section is approximately $4.4m$ long.

The wind tunnel has been fitted with a rolling road of the moving belt type for racecar test purposes. The belt is manufactured from two ply teraline of $1.5mm$ thickness with a smooth surface. The usable belt area is approximately $1.45m \times 3.5m$. A four roller system is used to drive the belt, to keep it under tension and to track it so that it stays in the middle of the tunnel. Low pressure above the surface induced by the flow around a model can cause the belt to lift; this is prevented by using suction on the underside of the belt. The heat generated by the friction between the belt and the suction platen is compensated by a cooling system underneath.

The boundary layer at the start of the rolling road is removed by a two stage process. Most of it is scooped away with a duct, while the remainder is removed via suction. The combination of the rolling road and boundary layer removal system produces a velocity profile in vertical direction that is within $\pm 0.2\%$ of the free stream velocity at $2mm$ above the belt [96]. The wind tunnel does not feature any system to keep the temperature in the test section constant and - despite ‘warming up’ running of the tunnel to mix the warmer air in the test section with the colder air in the return channel - the temperature does in general rise with the ambient temperature during the day.

### 2.3.2 Test configuration

The test configuration is designed in such a way that the wheels and wing can be tested independently, but also in combination over a range of parameter settings. Figure 2.5 shows a typical set up for the combined wing - wheel case. Ideally all tests would be performed with the same models to prevent any discrepancies in geometry, however from a practical point this is not always possible. For example, force measurements on the wing can not be combined with pressure measurement for the current configuration, because the pressure tubes would bridge the force balance by connecting the 'live' and 'earth' side of the load cell. Also the pressure measurement system for the wheel limits the operational velocity due to the instability generated by the mass of the internal components and therefore other tests should be performed without the pressure system in the wheel. Finally oil flow and PIV tests can damage the delicate systems or block pressure tap holes, whereas these holes would also disturb the flow visualization.

Two wing models have been used to allow testing with all the intended measurement techniques. A clean wing was required for the force measurements and for all other methods, except for the pressure measurements. The latter have been performed with a pressure tapped wing containing 180 different surface pressure tappings. Both wings were based on the same design and featured the same configuration, however the endplates of the pressure tapped wing were differently shaped on the outside to accommodate the pressure tubing from the flap element to pass through them. Figure 2.6 shows the pressure tapped wing and it can be noticed that the outsides of the endplates are partly covered by a $2mm$ thick extension. The pressure channel tubing is then directed through the support pillars and exits in the shroud where the ZOC measurement system is located.

During the research three different wheel models have been used; the standard 050 dummy wheels without any systems inside, a 'one-off' 050 wheel with a Chell 64-channel pressure measurement system inside and a 020 wheel in which McManus' pressure measurement system [68] was fitted. All wheels are shown in figure 2.7. The Chell pressure measurement system has been used in the early stages of the research, but temperature drift, operational problems and insufficient accuracy meant that no usable data has been collected with this system. The wheel with McManus' system is of an older generation than the 050 wheels[8], but has a comparable tyre profile, dimensions and camber angle. The wheel hub cover discs were manufactured from $1mm$ thick plastic and taped in place with aluminum tape. This solution provided a continuous change from wheel to cover disc without compromising set-up possibilities or influencing the flow field. The wheels were stable in operation and did not show any sign of bouncing, except for the McManus' pressure system wheel. Despite limiting the test velocity to $20m/s$ for this wheel, some irregular bouncing was still noticeable, however applying silicon spray to the contact patch

---

[8] The dummy wheels are labeled as 050-W0-065, while the McManus' pressure wheel is 020-W6-006.

did make the wheel run smoother.

The wing is supported by two vertical pillars on the pressure side of the main element, where the aerodynamic influence is minimal and in similar fashion as to on the real car. These pillars are connected to the 'live' part of the load cell, which is fitted to a sturdy strut with the 'earth' side. The strut is mounted to the PI-system, which hangs from the wind tunnel ceiling. This system allows automatic adjustment of the wing ride height within the specified range, while the tunnel is in operation. Both the strut and the PI system are shrouded by aerodynamic covers (see figure 2.5). The wing is located approximately $1.5m$ from the start of the rolling road.

The wheels are supported from the sides of the tunnel, in a similar way to during 'wheels off' testing for a complete model car. Either a 1-component load cell or a dummy load cell connects the wheel to a Y-shaped carbon fibre wheelarm. This wheelarm is mounted to a vertical pillar with a streamwise orientated hinge. The pillar rests on a ground plate of which the position can be varied independently in streamwise and spanwise direction. Figure 2.8 shows this specifically designed ground plate and it can be seen that a slot and clamp construction is used to adjust the position. Wheelarms and pillars feature a symmetric wing profile to limit the aerodynamic interference. The 'live' part of the wheel load cell is completely enclosed within the wheel hub and covered by the cover disc, however $22mm$ of the cylindrical 'earth' side of the load cell is exposed to the flow as if it were a wheel axis. New tunnel side fillet panels have been manufactured to cover the holes required for setting up.

The setting up process is illustrated in figure 2.4. First the wing is aligned to the flow to within a $\pm 0.1°$ accuracy. The ride height is set to within $\pm 0.05mm$ by sliding a high precision slip gauge between the lowest point of the wing and the ground. Next the wheels are positioned using two metal rulers in a plane at $150mm$ from the ground. The streamwise ruler is being used to align the wheel with the flow and to fix the $y$-position relative to the wing, whereas the spanwise ruler determines the $x$-position of the wheel. Although being quite time-consuming, this process allows positioning of the wheel relative to the wing with an accuracy of up to $\pm 0.5mm$.

### 2.3.3 Test conditions

All experimental tests, with the exception of the wheel pressure measurements, have been performed at a constant dynamic head of $56.19mm$ of water. Considering the lack of temperature control for the tunnel, setting the dynamic head provides the best way to manage the test conditions. The specified dynamic pressure is equivalent to a free stream velocity of $30m/s$ at sea level under standard atmospheric conditions. The influence of the atmospheric conditions on the actual test speed can be derived from $V = \sqrt{(\frac{2\times 287\times p_{dyn}\times T}{p_{stat}})}$. After setting the air speed in this way, the road velocity is matched to the actual flow velocity for the prevailing temperature and static pressure.

The Reynolds number for the tests varies due to the changes in atmospheric conditions; experienced variations in $Re$ based on the total wing chord ranged from $5.71\times 10^5$ to $5.92\times 10^5$. The wheel friction drag has been determined from trundle runs at $2.5m/s$, during which the wind was switched off and only the road moved. The turbulence intensity level of the $7\times 5$ wind tunnel has been determined experimentally using hot-wire equipment. The turbulence intensity and the length scale at $30m/s$ free stream velocity have been quantified as 0.3% and $0.039m$ respectively. No transition fixing has been applied during the tests and all results shown are for a clean wing configuration.

### 2.3.4 Force measurements

During experimental testing the configuration could be fitted with a 1-component load cell to measure the wheel drag of the port side wheel and a 3-component load cell to acquire wing downforce, drag and pitching moment (see figure 2.9). The wheel drag could be measured via the direct method with this load cell[9], because the wheel friction drag and reaction force has been determined with a low velocity trundle run and is subtracted afterwards. The signal from the 1-component strain gauge load cell was amplified via one channel of a full bridge Vishay 2120A amplifier and then read into a computer using a National Instruments data acquisition card. The amplifier also provided the power for the load cell. Data sampling took place in 30 blocks of 1000 samples each, at a sampling frequency of $1kHz$. The load cell was recently manufactured and calibrated and a static calibration check before testing showed less than 0.25% difference between the applied load and the calculated load. The original calibration data has therefore been used during these tests.

The wing loads were measured in a similar way, using three additional channels of the same amplifier. All three components of the load cell[10] were treated completely independently after running through a specially designed splitter box and correction for the cross terms was included in the postprocessing. The same load cell has been used as

---

[9] Wheel drag has been measured with a load cell from Aerotech, serial no. 0551.

[10] The wing loads have been measured using another Aerotech load cell, serial no. 0487.

during Mahon's tests, but the data acquisition, calibration and postprocessing have been completely changed after a component failure of the previous data acquisition system. Appendix A discusses the changes that have been made and the influences these have had on the results that were presented by Mahon. The wing loads are sampled with the same settings as the wheel drag and acquired at the same time, although the channels are acquired consecutively within each individual time step[11].

The adjustment of the wing ride height and the data acquisition could unfortunately no longer be combined in the same system and the sampling process took longer as a result. In general a force test run consisted of taking pre-run load cell zero's, starting the tunnel at a low ride height, acquiring data of all connected channels for 30 seconds, recording the atmospheric conditions and moving the wing to the next ride height with the help of the PI system. This process continued up to the highest ride height, followed by a downward cycle and finished with another reading of the load cell zero's. The tunnel was stopped for intermediate load cell zero's in case the whole test would require more than 20 minutes and subsequently restarted at the lowest or highest ride height, depending on the cycle in which the measurement process was stopped. The load cell zero values have been used to correct the results for the influence of temperature drift on the amplifier and load cell outputs. Linear time interpolation of the zero values over approximately 20 minutes intervals proved sufficiently accurate for the current purposes of deducing qualitative trends.

The acquired data has been postprocessed with a specifically written program. This program interpolates the zero values, subtracts them from the signals, applies the calibration matrices, corrects for the cross terms, subtracts trundle values from the wheel drag and tare values[12] from the wing loads, derives the force coefficients based on the frontal area $A_{wheel}$ and the wing planform $S$ (see table 2.1), calculates the $Re$-number for each ride height based on the atmospheric conditions and finally outputs the coefficients versus the ride height either after averaging the upwards and downwards cycle values when no hysteresis effects take place[13], or in an increasing and in a decreasing ride height file. Appendix B.1 discusses the influence of blockage effects on the results.

---

[11] This feature of the data acquisition system, which means that the four channels are sampled at slightly different times in succession, implies that the data can - strictly speaking - not be used for cross correlation between the channels, nor for unsteady analysis.

[12] Tare measurements are used to determine the loads that act on the support structure when the model is not in situ, in this case only the two vertical pillars contribute to the tare readings.

[13] Hysteresis has been chosen to occur for any ride height where the upward and downward cycle result differ more than 2.5%.

The size of the load cell (see figure 2.9) made it impossible for Mahon to design the wing in such a way that the load cell would be contained inside the wing model. The pitching moment is therefore measured around a point above the wing (around the load cell resolution point) and afterwards transfered to a point on the wing. In Mahon's results this point has no particular meaning except for that it is conveniently located relative to the support structure. Figure 2.3 shows this point as $C_{M53mm}$, being located at centre span ($y = 0$) at the same $z$-position as the leading edge of the main element ($h + 11.1mm$), but $53mm$ downstream of it. In this thesis the pitching moment will - apart from the $C_{M53mm}$ point - also be transfered to the more conventional quarter chord point ($C_{M1/4c}$), with an $x$-position of $71mm$ from the leading edge of the main element and the $z$-location chosen at the same height again. Since the support structure is not infinitely stiff, deformation will however have an effect on the results and it is expected that especially the pitching moment and the drag to a lesser extent will be affected.

### 2.3.5 Pressure measurements

The testing configuration could also be equipped with pressure measurement systems, both for the wheel (starboard side) and for the wing. Figures 2.7 and 2.6 showed the respective models that have been used for this purpose. In the end McManus' wheel pressure measurement system has been given preference due to its superior accuracy and all results presented in this thesis have thus been acquired with this system. However as a consequence of this choice the results are mainly indicative for the current set-up and do not present absolute accurate quantitative values. First of all the wheel model in which the system has been fitted has a slightly different geometry than the other wheels and a thicker wheelarm has been used to reduce the bouncing. Furthermore the tests have been performed at a lower velocity equivalent to $20m/s$, because of bouncing of the pressure tapped wheel. Finally, the low resolution along the profile in spanwise direction means that the acquired data is insufficient to integrate the pressure distribution into a lift coefficient via the indirect measurement. Nevertheless the provided results are very useful for correlation of the CFD results and give insight into the flow features on the wheel surface.

McManus' pressure measurement system contains only one pressure sensor, which has to be moved by hand in order to acquire data at different tap locations. This is the main reason for the low resolution in the spanwise direction. However, on the other hand, the sensor is a high quality Kulite and the resolution in the rotational direction is higher than for the Chell system. The intermediate bouncing and slipping due to the wheel camber made it difficult to capture the pressure peaks near the contact patch. However careful use of silicon spray and a thicker, more sturdy wheelarm did improve the results. The pressure signal is stored inside the wheel and after initial post processing transfered to a computer via radio transmission. In general the results represent the time-average of 250 cycles and corrections for centrifugal forces on the diaphragm and reference pressure, dependent on pressure tap location and orientation, have been applied. The results have also been filtered for a natural vibration frequency of $750Hz$ and the cycles without peaks, as a result of bouncing, have been omitted.

A wheel pressure measurement sequence consisted of preparing the wheel for a certain tap location, measuring for the isolated wheel and for a CWW case at various ride heights and - for certain tap locations - a repeat of this for different overlap and gap settings. This process was repeated for all the required tap locations and as a result of the considerable time required to change the pressure sensor locations and to a lesser extent to change the wing - wheel settings only five tap locations could be finished with four or five ride heights per case. The main data was acquired for CWW2020, with some additional results for CWW2050 and CWW3520[14]. The tap locations are approximately separated by $50mm$ from each other and the middle tap (P1) is located at the centre of the middle tread; figure 2.2 shows the five locations and naming of the taps.

The pressure tapped wing and measurement system have been described in Mahon's thesis [12]. Each of the taps can be connected to a Scanivalve ZOC2B (zero, operate, calibrate) pressure transducer in combinations of 32 at a time (see figure 2.9 for the system and connectors). A dual switch could double this amount, but proved to be not functioning at the time of testing. Each of the 32 sensors has a scanning rate of $20kHz$ with a pressure range of 0 to $5PSI$. The ZOC system performs three steps during each measurement; first the initial zero readings are taken in wind-off conditions, then the sensors are calibrated against an input pressure of known magnitude ($4PSI$) to derive the gains and offsets for each sensor and finally the pressure is measured in a wind-on condition for each of the sensors. Zero reading and calibration takes place at the beginning of each test run to compensate for variations in atmospheric conditions and sensor drift. The signals are read into the PI system and written to an output file presenting the pressure coefficients for each of the sensors. Except for getting the output in the desired format,

---

[14] Due to having to use an alternative more sturdy wheelarm, it was impossible to test in the more frequently used CWW5020 configuration.

no additional post processing is required.

Not all of the 180 taps have been measured due to time constraints, especially the malfunctioning of the dual switch proved to harm the required time, since twice as many measurement runs had to be conducted and retubing was necessary between each run. An analysis of Mahon's data suggested that the chordwise pressure distributions provided the most interesting information and therefore these were selected in a reduced form. On each of the elements 32 taps were selected, both at centre span and at the tip (at $y = -0.265m$, $0.025m$ inside of the port side endplate), implying that four different runs had to be performed for each individual setting. Figure 2.10 visualizes the pressure tap locations, as used during this research, while the tables 2.2 and 2.3 summarize the pressure tap locations for respectively the main element and flap element. Again the main set of data was acquired for the CWW2020 settings, with some additional data for the tip of the wing in CWW5020 settings.

### 2.3.6 Oil flow tests

Oil flow visualization provides on-surface data in the form of surfaces streaklines. The time-averaged streakline pattern can show transition and separation locations as well as vortex imprints. Prior to oil flow tests the model would be prepared in such a way that the surfaces were as smooth as possible; for example black fablon was used to cover any irregularities on the endplates. The oil flow method can only be applied to stationary surfaces, such as the wing elements and endplate. For reference, one wheel and the road have also been analyzed with oil flow for the IWh and CWW2035 case, but the relevance of these results is limited since wheel rotation and ground movement had to be omitted.

A solvent based suspension, in this case a liquid suspension of titanium dioxide ($TiO_2$) in paraffin, was applied to all the surfaces of interest. By running the tunnel at the intended conditions the solvent would evaporate, leaving contrasting streaklines on the surface. Due to the large surface area that had to be covered it proved important to apply the visualization liquid as quickly as possible to prevent drying before the tunnel had started. Once the surface would have dried enough, usually taking about half an hour, the surface streaklines would be captured with a digital camera for further analysis.

### 2.3.7 PIV tests

Off-surface flow data has been gathered using PIV (Particle Image Velocimetry) equipment. Correlation of flow particle positions between two successive images presents the possibility to derive instantaneous and time-averaged velocity data in a plane. Depending on the focal length of the camera lens and on the distance of the camera to the plane, a rectangular field of view with maximum dimensions of up to $240mm \times 300mm$ could be covered. The main advantage of the PIV method is that it is a non-intrusive technique and therefore does not influence the results, while still providing the opportunity to get qualitative and quantitative off-surface data.

A few things have to be considered when analyzing the PIV data. First of all the results in a 2D plane can be quite misleading, because they represent the projection of velocity vectors onto this plane - not necessarily particle trajectories - and in this process one component has been omitted. This also leads to the introduction of perspective errors, resulting from inaccuracies in measuring in-plane displacements due to out-of-plane motion. In a similar way parallax effects, a perspective shift caused by looking at an object under an angle, can introduce increased areas of blocked view, especially when the angle of view is large. When measuring a cross-flow, with the largest velocity component perpendicular to the plane, the accuracy decreases because the particles travel a smaller distance in the plane for a given time, making the results more prone to (resolution) errors. This also applies to bigger field of views. However within these limitations, PIV proves to be an excellent tool to analyze the flow field characteristics and an adequate technique for obtaining quantitative velocity data (also see appendix B.2).

The PIV system consists of a Gemini PIV 15 laser, containing two Tempest Ng:YAG lasers of $125mJ$/pulse at a wavelength of $532nm$, and a $1280 \times 1024$ pixels Dantec HiSense CCD camera (type 13 gain 4), as well as the computers for control and postprocessing. Water based smoke particles of approximately 1 micron in diameter are generated by a smoke generator that was located downstream of the test section. A double laser sheet with a combined thickness of 2 to $3mm$ was created to illuminate the field of view and the images were recorded with a time interval in the order of $20\mu s$ to $50\mu s$. Nikkor lenses of $24mm$, $60mm$ and $105mm$ focal length have been used to adapt the size of the field of view, depending on the location. The wing was fitted with a polycarbonate transparent endplate of identical design for surveys underneath the wing elements. An overview of all the planes that have been studied is given in figure 2.11.

Two aspects proved particularly important for obtaining good results. These were the seeding, which had to be at the right amount because both more or less led to deterioration of the correlation, and the alignment of the laser and the camera. Extra attention was therefore paid to the set-up process. First the laser sheet would be located and orientated in the region of interest, then the camera would be squared up to the laser plane with all three directions being perpendicular up to within ±0.1°. To achieve this - and to create an unobstructed field of view - it was sometimes necessary to position the camera or laser in the tunnel, which led to an increase of tunnel blockage. A typical example of such a set-up is presented in figure 2.12, which shows the case for acquiring data in a vertical streamwise plane over the top of the wheel, requiring both laser and camera to be located inside the tunnel.

Data was recorded in samples of 500 double images using the Flowmanager software. The instantaneous images were subjected to adaptive cross-correlation, in which the second interrogation window is offset by a 3-step iterative process, using interrogation areas of $32 \times 32$ pixels with a 75% overlap of the windows in the horizontal and the vertical direction. Erroneous vectors were removed using a range validation, where the maximum allowed velocity magnitude would depend on the specific field of view, however no further filtering has been apllied to avoid blurring of velocity gradients. The resultant vector fields would be averaged over the amount of data samples in order to analyze the statistic values.

### 2.3.8 Hot wire measurements

Finally one-component unsteady velocity data have been acquired for the isolated wheel with a single component hot wire system. This system consists of a single $2.5\mu m$ Platinum plated Tungsten wire and operates via the Constant Temperature Anemometry principle. A Newcastle bridge amplifier is used to condition the signal. Acquiring data and post-processing takes place with the help of a National Instruments data acquisition card and Enflow software respectively. The low pass filter of the Newcastle bridge amplifier was set to $1.6kHz$ and data sampled at $5kHz$ for 25 blocks of 4096 points. Postprocessing in the form of a 4096-points FFT using a Hamming window without overlap yields the velocity spectra.

The hot wire has been positioned at five different positions behind, around the top and at the side of the wheel. Hereto the hot wire was connected to a metal rod that was supported from the side of the tunnel. Regular calibration and checks of the hot wire were performed in free stream flow conditions, but noticeable drift was still experienced. This does not affect the qualitative aspects of the velocity spectra, but the mean and the instantaneous velocities need to be treated with care. The hot wire was always aligned in the vertical plane, which makes it most receptive to fluctuations in the horizontal plane. The results of the hot wire measurements will not be presented explicitly in this thesis, because of the limited relevance of the results.

## 2.4 Computational research

This section deals with all stages of the computational research, ranging from the numerical method and grid generation to solver settings and convergence criteria. The CFD simulations were performed in 3D to capture the essential flow features. A 2D simulation would not do justice to the complex interaction phenomena and misses out on both the dominating end effects at the sides of the wheel, as well as on the wing tip flow features.

### 2.4.1 Numerical method

Simulations of the combined wing - wheel geometry have been performed using a commercial RANS finite volume method solver on a linux based cluster. The governing equations, consisting of the conservation equations for mass, momentum and energy [97], are solved in a segregated form for each iteration, either in a steady or unsteady formulation. The majority of the results presented here concern steady simulations, DES results for the wheel being the only exception to this. The use of Reynolds-averaged equations implies that a turbulence model is required to obtain an equal number of equations compared to the number of variables. Within this research a variety of turbulence models have been tested ranging from the one-equation Spalart Allmaras model (SA), via several two-equation models and variants to the seven-equation Reynolds Stress transport Model (RSM). A further introduction to the applied turbulence models can be found in section 2.4.7.

Throughout the research the same software versions of the solver and grid generating programs have been used consistently[15]. Two aspects play a decisive role in the quality and accuracy of CFD simulations. First of all the computational mesh - including cell quality, distribution and domain extents - has a major impact on the outcome and secondly the solver method and settings, such as boundary conditions, turbulence models and discretization schemes. The discussion of the computational research will be continued by looking at the grid generation process first.

---

[15] Fluent 6.2.16 has been used as solver, whereas the computational meshes have been made with Gridgen 15.08.

### 2.4.2 Grid strategy

This section will start off with some general considerations for grid construction followed by design criteria that have specifically been derived for the current grids. The basic principles behind grid generation are more restrictive than would be expected considering the unlimited possibilities to vary aspects of a numerical mesh. From a topological point of view it can be concluded that grids constructed according to similar design choices resemble each other on a fundamental level, even though they might look quite differently. A good example of this is the modeling of the contact patch for a tyre in the symmetry plane with a structured hexahedral grid; in essence only either a ‘wedge’ with highly skewed cells near the contact line, or a (vertical) ‘plint’ - a curtain between the wheel and ground - that avoids the actual occurrence of the sharp angled wedge can be used (see figure 2.13).

The fundamental choices, which shape a grid, have to be made carefully, because it is very difficult or even impossible to alter the consequences of each choice at a later stage. This decision process can be considered to follow a cascade, where each option restricts the possibilities at the next level. In descending order these choices concern:

- The type of grid: structured (hexahedral cells in 3D), unstructured (tetrahedral cells in 3D) or hybrid (a combination of these and / or prisms in 3D).
- The conformity of the grid: using non-conformal zones or only one-to-one interfaces.
- The grid block topology: including non-regular nodes, which have less or more connectors than required for a regular hexahedral mesh, grid wrapping around boundaries and grid line ending on boundaries and at the domain extremities.
- The connector dimensions: the number of cells per connector; for a fully structured grid the total number of cells in the grid are determined at this level.
- The cell distribution: allowing for local refinements and to limit skewness, grid line discontinuities and / or abrupt cell volume changes.

Aspects that make a good grid include regular cells, little skewness of the cells, aspect ratio near to unity, grid line continuity, grid line alignment with the flow, local refinement wherever required and gradual cell volume changes. Satisfying these conditions will result in a mesh that resolves the gradients of the flow quantities in the best way and these requirements have to be kept in mind therefore, while making the previous choices. Any grid irregularities can dampen the flow physics and must thus be used in areas away from the critical regions.

A grid design strategy has been derived based on the previously mentioned considerations. It has been decided to use high quality structured hexahedral grids, as it is deemed essential in studying aerodynamic interaction effects that flow quantities, such as vorticity, are conserved as much as possible and not dampened by grid features. If required, non-conformal zones will be used instead of unstructured tetrahedral 'glue' zones, because the cell quality of the latter is much harder to control with the grid generation program that has been used. The use of irregular nodes is unavoidable because of the complex geometrical shapes of the models. Furthermore irregular nodes will be used to limit the influence of high density boundary layer blocks on the far field number of cells and to simplify the block topology towards the outer domain extents. Boundary layer wrapping around the geometry and grid line ending on the geometry and on the ground will also be used for these reasons. The irregular nodes will be located outside the boundary layer blocks, whenever possible.

All boundary layers on the models and on the ground will be created with an initial cell spacing that results in $y^+$-values[16] of the order 1. This ensures that the boundary layers are fully resolved towards the walls, instead of using the 'law of the wall' near the surface [97] to approximate the boundary layer development. The minimum skewness angle will not exceed 50° and the block topology as well as the cell distribution will be used to achieve this. The total number of cells for an isolated wheel or wing grid will be kept to around 4 million cells and 5 million for the combined configuration to ensure workable computational times and case sizes that allow postprocessing with the available programs. Finally, for efficiency it has been decided to create one separate mesh module for the wheel and one for the wing, which form simple blocks that can easily be combined and repositioned relative to each other. The wing ride height can be altered by moving the wing mesh module in the vertical direction, whereas the overlap and gap are changed by moving the wheel mesh module in respectively the spanwise and streamwise direction. The complete mesh can then be constructed by filling the rest of the domain with cells. Next these two mesh modules will be discussed in more detail.

---

[16] The quantity $y^+$ is a geometry and flow field dependent parameter that is used as coordinate perpendicular to a wall to describe the velocity profile of the boundary layer in a non-dimensional form.

### 2.4.3 Wheel mesh module

Generating a mesh is generally an interactive process, where each of the simulation solutions will indicate subsequent changes that could lead to improvements. The computational mesh evolves as a result, sometimes requiring alterations at a high level of the decision cascade, which will lead to a completely different grid from a topological point of view. The grids presented here have all changed considerably over time; however only the end results will be included. Explanations of the modifications will be given if required to understand the final choices.

A wheel mesh module has been created based on the geometry of the standard dummy 050 wheel. The 'plint' option in the contact patch region has been used from the beginning to ensure satisfactory cell quality. McManus [68] used a similar solution for his isolated wheel simulations and since the tyre is deformed in the contact region anyway this simplification seems justified. The plint is $0.1mm$ high and $11.1mm$ wide in the streamwise direction at the 50% model scale, which has also been used for the simulations (see figure 2.14 for an indication of the shape of the contact patch region, being the non-meshed rectangle with chamfered ends). This corresponds to a revolution angle of 4° of the wheel circumference. In a first grid all cells from the wheel boundary layer and from the ground boundary layer ended on the plint, but an alternative block structure has been invented subsequently to save cells and to improve the cell quality. This new block topology makes good use of boundary layer ending on geometrical surfaces. Figure 2.14 shows how the wheel boundary layer is partly ended on the ground, whereas the ground boundary layer is partly terminated on the wheel surface. The grid has an area-weighted average of $y^+$ of slightly less than one over the complete wheel surface and is therefore fully boundary layer resolving.

The block topology has also been simplified towards the outer domains, as can be seen in figure 2.15. If the domains on the wheel surface and those depicted in orange would just have been extruded in the spanwise direction, then this would result in quite a complicated domain topology, consisting of several irregular nodes. In contrast some blocks have been added to transform the complicated structure in a simple zone existing of only regular nodes (the yellow grid). Apart from making it easier to include the wheel mesh module into a completely structured grid, this has also led to improved cell quality and a saving in the total number of used cells. The wheel mesh module incorporates a flat vertical plane at the upstream end for simple connection to the wing mesh module - with or without the use of an additional hexahedral filler block and / or non-conformal zones.

### 2.4.4 Wing mesh module

The wing mesh module has also gone through many evolutions in order to improve the correlation with the experimental results. The simulations by Mahon [12] have been used as a starting point, however Mahon already stated that his 3D study was still at an early stage. Initial improvements involved a larger computational domain (upstream and downstream) and the use of more structured mesh blocks, especially in the critical region underneath the wing towards the ground. Since the correlation did not improve sufficiently, other aspects had to be checked as well. Accurate measurements of the wind tunnel model revealed that the profile geometry differed slightly from the CAD design drawings. The trailing edges of both elements were thicker for the actual models than in the CAD design ($1.6mm$ instead of $0.9mm$). This was a result of the production process, during which the wing was constructed from an upper and lower carbon fibre skin, which were bonded together. The combined thickness of the skins at the trailing edge was larger than intended and the actual profile was therefore deformed as if it was stretched open at the back and rotated relative to the joining point at the nose.

One simulation based on a grid that incorporated these reversed engineering insights by adjusting the geometry in a similar way showed improved results. This grid - as well as several others during the development stage - made use of infinitely thin endplates for which the endplate inside and outside coincided in the same plane. These promising results prompted a further investigation into the existence of geometrical anomalies and the complete pressure tapped wing was 3D laser scanned with a 30,000 points cloud to obtain a CAD representation of the actual physical model. CFD simulations using these new data showed that global dimension and orientation differences, extracted from the scanned data, had much more influence than local geometrical discrepancies. The final wing mesh module has thus been based on a selection of the scanned data, capturing the essential differences compared to the design CAD data, without using all the data points.

Figure 2.16 shows the final wing mesh module in the form which has been used for the presented simulations. Seven streamwise stations were created for which the scanned data was used to determine the continuous profiles at each location (the blue connectors in streamwise direction in figure 2.16); the wing surface between these stations was obtained through linear interpolation. This practice limited the complexity of the geometrical data, while discrepancies in dimensions and orientation were still captured at regular intervals. The grid was constructed in such a way that the boundary layer would be resolved on both elements as well as on all sides of the endplate. The area-weighted average of $y^+$ is slightly below one on the elements and around three for the endplate. The boundary layer blocks were wrapped around the elements (see figure 2.17) and endplates (see figure 2.18) in order to save cells in the far field. The connector dimensions have been chosen in such a way that all opposite outer domains of the module feature the same amount of nodes, which allows for straightforward creation of a fully structured grid from the module.

The final wing mesh module is an accurate representation of the pressure tapped wing elements combined with the less complicated endplates of the force wing. Endplate thickness and fillet radii on the upstream, downstream and top edge of the endplate are the same as for the real force wing model. The endplate of the final wing mesh module evolved from an infinitely thin flat endplate, via a $5mm$ thick rectangular endplate with sharp corners into the realistic endplate with $2.5mm$ fillet radius. Since these changes have been made one at a time, while keeping the rest of the grid the same, it is possible to derive the influence of each step. The infinitely thin endplate baseline case underpredicted the downforce by 8.1%, adding thickness to the endplate, reduced this underprediction to 7.2% and finally using fillets on the edges brought the correlation to within 6.3% of the experimental value. The respective suction peak on the main element went from 8.0% underpredicted, to 7.9% and finally to 6.9% compared to the experimental results. The wing drag was overpredicted by 1.8% for the first case, 3.7% for the thick endplate and 2.1% for the final version. From this it can be concluded that the realistic geometry of the endplate has a noticeable positive influence on the correlation.

Finally, it needs to be mentioned that the wing mesh module incorporates laminar zones[17] for the main element and for the flap, just like in Mahon's simulations [12]. Mahon performed a correlation study between oil flow results and a numerical simulation based on the Orr-Sommerfield equation to show that the transition position can be derived from the experimental oil flow data. This same reasoning and method has been used within the current research.

The laminar zones are included to model the laminar flow along the elements near the leading edges, for better correlation. The locations of these zones have been derived from oil flow visualizations by looking at the transition position. Transition in the simulations is enforced instantaneously at the boundary between the laminar and turbulent zones, in contrast to in the experiments where transition takes place over a certain interval. The

---

[17] Ideally a method predicting transition would be used like described by Czerwiec et al. [98], however for the applied solver such a function is not available and therefore laminar flow has to be modeled in zones with an instant transition into turbulent flow at the zone boundary.

laminar zones were kept constant in spanwise direction, as in Mahon's simulations, and the length was based on that occurring in the symmetry plane. The transition regions in the oil flow experiments were found to be curving downstream towards the wing tips for the higher ride heights, but it proved difficult to include this in the grids. The length of the laminar zones were varied in the simulations depending on the wing ride height, in line with the experimental oil flow data. The computational laminar zones extended all the way upstream to the velocity inlet, which gave slightly better results than Mahon's localized laminar zones, because the current solution meant that no upstream turbulence quantities were transported through the laminar zone, giving the turbulent boundary layer a fresh start at the end of the laminar zones.

### 2.4.5 Complete computational grids

The wheel and wing mesh modules were used to construct three different types of grids, for simulations of the isolated wheel, the isolated wing and for a combined set-up. A symmetry plane was used for all grids to limit the amount of required cells and the isolated wheel case therefore actually modeled two wheels in a symmetrical set-up, similar to the experimental configuration, when two wheels have been used for 'isolated tests' as well. The grids for the isolated geometries were fully structured; hereto the sides of the modules were extruded towards the domain boundaries.

The upstream boundary was located 6.4 wheel diameters upstream of the wheel centre, while the outlet boundary was at $14.7D$ downstream. The computational domain was $5.0D$ high and $3.4D$ wide, in accordance with the cross sectional dimensions of the used wind tunnel. The side fillets of the wind tunnel were not modeled in any of the grids for simplicity. The wheel was located $2.0D$ from the port side of the tunnel. The mesh was refined towards the ground to resolve the boundary layer on this surface; the area-weighted average of $y^+$ on the ground was well below 1 (of the order 0.1) for all complete grids, due to the lack of a velocity gradient between the moving ground and freestream flow for most of the ground surface. The isolated wing grid extended 5.0 total wing chords upstream of the leading edge of the main element and $15.0c$ downstream. The computational domain was $3.7c$ wide and $5.3c$ high.

Both the isolated wheel and wing grids featured a specific wake block downstream of the module to allow for grid refinement, better grid line alignment and high cell quality in these critical areas. Neglecting the coarse and fine grid for the grid sensitivity study, only one wheel grid had to be created, however for the wing different grids for different ride heights were required. Hereto the grid was designed in such a way that the basic central part was the same for all ride heights, whereas extrusion of the lower boundary to the required ride height and construction of an upper block to fill the remaining domain height would lead to the complete grid. In this way a selection of grids all through the ride height range could be constructed fairly straightforwardly and in a short time span. The only final required adjustment after this was a change of the laminar zone extents according to the oil flow results for the lower ride heights.

The domain extents of the combined wing - wheel configuration grids were the same as those used for the isolated cases. Since the number of cells on the backside of the wing module differed from that on the frontside of the wheel module, it was impossible to connect the two modules with a one-to-one structured hexahedral block. Instead non-conformal zones were used to create the combined grid. The ride height could again be changed in a fairly simple manner by putting the wing in a 'non-conformal box' (see figure 2.19), which only required local changes. However altering the overlap and / or gap would involve more time consuming repositioning of the wheel module and was therefore not tested within this research. The total grid once more included a wake block downstream of the wheel module.

### 2.4.6 Solver settings and case setup

The generated cases have all been solved with the help of a segregated RANS solver in implicit form, using the SIMPLEC scheme for the pressure - velocity coupling (see [97]). The gradient option was set to node based and the solver was run with double precision. All differential schemes were second order accurate, with the momentum and turbulence quantity equations being resolved with upwind discretizations. The governing equations were used in the incompressible form[18], because the free stream Mach number was below 0.1, making compressibility effects negligible. In general the flow field was initialized with the freestream conditions, but the turbulent dissipation was set higher to prevent excessive growth of the turbulence quantities in the first stages of the simulation. The Spalart Allmaras simulations would converge directly from this initialization, but some of the other turbulence models needed to be started from previous SA solutions and / or with first order discretization. The DES simulations were also started from steady RANS solutions.

A velocity inlet boundary condition was used with the velocity set to the freestream

---

[18] The conservation of energy equation does not have to be solved in the incompressible form.

value of $30m/s$ and the turbulent viscosity ratio to $10^{-7}$. If the applied turbulence model required a turbulence intensity value on the boundary, then this was set to $I = 0.3\%$ in accordance with the experimental test conditions. A pressure outlet condition was chosen for the downstream boundary using the same turbulence viscosity ratio for the backflow and with the outlet pressure set to the reference pressure. The ground was modeled as a smooth moving wall with a translational velocity of $30m/s$ in $x$-direction. The symmetry plane was given a symmetry boundary condition, just like the port side wall and the roof, so that no boundary layer refinement had to be included towards these walls. This is in line with previous studies [12,68]. The wing surfaces were modeled as smooth non-moving walls, whereas the wheel surface was presented as a rotating smooth surface. The axis of the cambered wheel was chosen as rotation axis, while the rotational velocity was set to $193.63rad/s$. This value was based on the average wheel radius given in table 2.1 and it is thus assumed in the simulations that the wheel rotates around the spanwise middle of the wheel. This is a sensible choice considering that the experimental wheel set-up was checked by sliding a piece of paper between the wheel and road at both sides of the contact patch to centre the contact region. The boundary conditions for a combined wing - wheel case are visualized in figure 2.19.

### 2.4.7 Turbulence models

For the current purpose of using CFD as a research tool it is not required to completely analyze the physics of the turbulence models that are available within the numerical solver program. Nevertheless it is useful to know the strengths and weaknesses of each of the models in order to justify the final choice. This section summarizes the available models, partly using information provided in the manual [97], while the final evaluation of the various models can be found in section 3.1.3 and 3.2.3 for respectively the isolated wheel and isolated wing simulations.

The majority of the turbulence models employ the Boussinesq hypothesis [97] to relate the Reynolds stresses to the mean velocity gradients. This limits the amount of variables that need to be solved and requires only one or two equations for ‘closure’ of the problem, making these methods relatively computational cost efficient. The SA model uses one additional transport equation to calculate the turbulent viscosity, while the k-$\epsilon$ and k-$\omega$ models incorporate two transport equations; one for the turbulent kinetic energy k and one either for the turbulent dissipation rate $\epsilon$ or for the specific dissipation rate $\omega$. The turbulent viscosity is subsequently derived as a function of the two extra variables.

Alternatively all terms of the Reynolds stress tensor can be solved, which - including an additional scale determining equation - leads to the 7-equations RSM model. The advantage of this method is that the turbulent viscosity is no longer modeled as an isotropic scalar quantity, but this advantage rarely outweighs the extra computational costs of this method.

The SA model [99] is known for its robustness and is specifically implemented for aerospace applications with wall-bounded flows. Its strength lies in solving flows with boundary layers under adverse pressure gradients, but the method performance deteriorates when these boundary layers change into free shear flows after separation, because of the quickly changing length scales [97]. The standard k-$\epsilon$ model is the most basic two-equations model and is derived from phenomenological considerations and empiricism. Improvements on this model have been made using the statistical technique of renormalization group theory, creating the more accurate and reliable RNG k-$\epsilon$ model. The Realizable k-$\epsilon$ model incorporates a new formulation for the turbulent dissipation and a new transport equation for the turbulent dissipation rate. This version of the model is consistent with specific mathematical constraints on the Reynolds stresses and should provide better performance for flows involving rotation, boundary layers under strong adverse pressure gradients, separation and recirculation. Finally, the standard k-$\omega$ model is specifically implemented for wake simulations, showing good agreement of the shear flow spreading rates with experimental results. The Shear-Stress Transport (SST) version of this model is a blend of the k-$\omega$ model in the wake with the k-$\epsilon$ characteristics near the wall, improving the performance for adverse pressure gradient flows compared to the standard model.

### 2.4.8 Convergence and correlation

Isolated wing simulations for the higher ride height cases ($h/c = 0.319$ and higher) converged completely to constant force coefficient and scaled residual values. In such a situation convergence could simply be achieved by iterating till the scaled residuals had dropped at least three orders of magnitude and till the force coefficients and residuals were no longer changing. However for flow cases that involved bluff bodies and large separated zones, these criteria could not be applied so straightforwardly. For such cases the residuals and force coefficients would be oscillating irregularly. The solution was considered to be converged when the upper and lower limit of the force coefficient and residual values did not alter any more, or - in other words - when the values stayed within a range band. The mean values after stabilization were then taken as the force coefficient values for the simulation. The convergence behaviour of the isolated wing cases for the lower ride heights showed a combination of both characteristics; initially converging to a steady solution after which the residuals would start rising again and the force coefficient values oscillated irregularly. This appeared as if the flow tried to converge to a state that proved no longer sustainable, leading to large scale flow separation and / or vortex breakdown when the values lost their consistency.

How accurately the computational results correlate to the experimental data can be judged in several ways. In this research force coefficients have been used for a first integral overview, however it needs to be realized that two wrongs can add up to a seemingly correct answer under certain circumstances. Therefore on- and off-surface data have been evaluated as well. Wing and wheel pressure measurements and wake data (from Mahon's tests), as well as PIV flow field data, have all been used for this purpose. A satisfactory level of correlation for the wing at higher ride heights would be to predict the force coefficient and suction peak $C_P$'s to within 10% of the experimental values; this would be an improvement on Mahon's results (downforce underpredicted by 11% drag by 3% and suction peak by 17%), but still presents a realistic goal. Correlation for cases with the bluff body wheel included and / or large separation at lower ride heights is harder to quantify, especially when steady state RANS simulations have been performed with a one-equation turbulence model. In this situation more attention will be paid to the on- and off-surface characteristics to see whether all the features have been captured.

| Wing | | | |
|---|---|---|---|
| main element chord $c_m$ | $139mm$ | total chord $c$ | $284mm$ |
| flap element chord $c_f$ | $145mm$ | spanwidth $b$ | $580mm$ |
| main element thickness $t/c_m$ | 0.14 | wing planform $S$ | $0.16472m^2$ |
| flap element thickness $t/c_f$ | 0.09 | aspect ratio $AR$ | 2.04 |
| main element angle of attack $\alpha_m$ | +4° | flap overlap | $10mm$ |
| flap element angle of attack $\alpha_f$ | +24° | flap gap | $12mm$ |
| endplate size l×b×h | $275 \times 5 \times 115mm$ | | |
| endplate edge fillet radius | $2.5mm$ | | |

| Wheel | | | |
|---|---|---|---|
| maximum radius $r_{max}$ | $156.9mm$ | diameter $D_{wheel}$ | $313.9mm$ |
| minimum radius $r_{min}$ | $152.9mm$ | maximum width $w$ | $172.8mm$ |
| average radius $r_{av}$ | $154.9mm$ | frontal area $A_{wheel}$ | $0.05201m^2$ |
| cover disc diameter $D_{CovD}$ | $185mm$ | aspect ratio $AR$ | 0.55 |
| wheel camber angle | 2.4° | | |
| grooves width×depth | $7.5 \times 1.25mm$ | | |

Table 2.1: Characteristic dimensions and parameters of the wing and wheel model geometries.

| Suction Surface | |
|---|---|
| $x[mm]$ | $x/c$ |
| 0 | 0.000 |
| 2 | 0.007 |
| 4 | 0.014 |
| 6 | 0.021 |
| 8 | 0.028 |
| 10 | 0.035 |
| 15 | 0.053 |
| 20 | 0.070 |
| 25 | 0.088 |
| 30 | 0.106 |

| Suction Surface | |
|---|---|
| $x[mm]$ | $x/c$ |
| 35 | 0.123 |
| 55 | 0.194 |
| 65 | 0.229 |
| 75 | 0.264 |
| 85 | 0.299 |
| 105 | 0.370 |
| 115 | 0.405 |
| 125 | 0.440 |
| 130 | 0.458 |
| 135 | 0.475 |

| Pressure Surface | |
|---|---|
| $x[mm]$ | $x/c$ |
| 2 | 0.007 |
| 4 | 0.014 |
| 6 | 0.021 |
| 10 | 0.035 |
| 15 | 0.053 |
| 35 | 0.123 |
| 55 | 0.194 |
| 75 | 0.264 |
| 95 | 0.335 |
| 115 | 0.405 |

| Pressure Surface | |
|---|---|
| $x[mm]$ | $x/c$ |
| 130 | 0.458 |
| 135 | 0.475 |

Table 2.2: Locations of the chordwise pressure taps on the main element; at the centre $(y = 0mm)$ and at the tip $(y = -0.265mm)$.

| Suction Surface | |
|---|---|
| $x_f[mm]$ | $x/c$ |
| 0 | 0.454 |
| 2 | 0.461 |
| 4 | 0.468 |
| 6 | 0.475 |
| 8 | 0.482 |
| 10 | 0.489 |
| 12 | 0.496 |
| 14 | 0.504 |
| 18 | 0.518 |
| 20 | 0.525 |
| 25 | 0.542 |

| Suction Surface | |
|---|---|
| $x_f[mm]$ | $x/c$ |
| 30 | 0.560 |
| 36 | 0.581 |
| 45 | 0.613 |
| 55 | 0.648 |
| 75 | 0.718 |
| 85 | 0.754 |
| 95 | 0.789 |
| 105 | 0.824 |
| 115 | 0.859 |
| 125 | 0.894 |

| Pressure Surface | |
|---|---|
| $x_f[mm]$ | $x/c$ |
| 2 | 0.461 |
| 4 | 0.468 |
| 6 | 0.475 |
| 8 | 0.482 |
| 10 | 0.489 |
| 20 | 0.525 |
| 36 | 0.581 |
| 55 | 0.648 |
| 75 | 0.718 |
| 95 | 0.789 |
| 115 | 0.859 |

Table 2.3: Locations of the chordwise pressure taps on the flap element; at the centre $(y = 0mm)$ and at the tip $(y = -0.265mm)$; $x_f$ is the streamwise distance from the leading edge of the flap element nose, $x/c$ is the global non-dimensional coordinate.

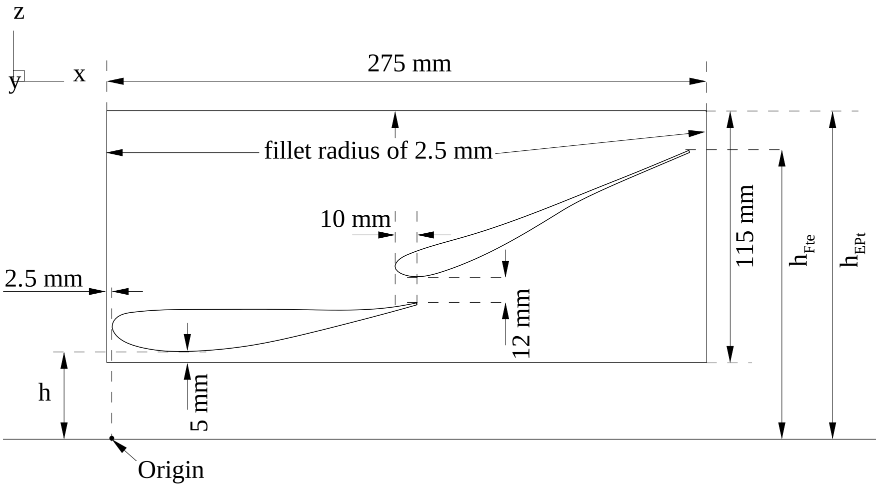

Figure 2.1: Scale drawing of the wing element profiles and endplate showing characteristics and the main dimensions.

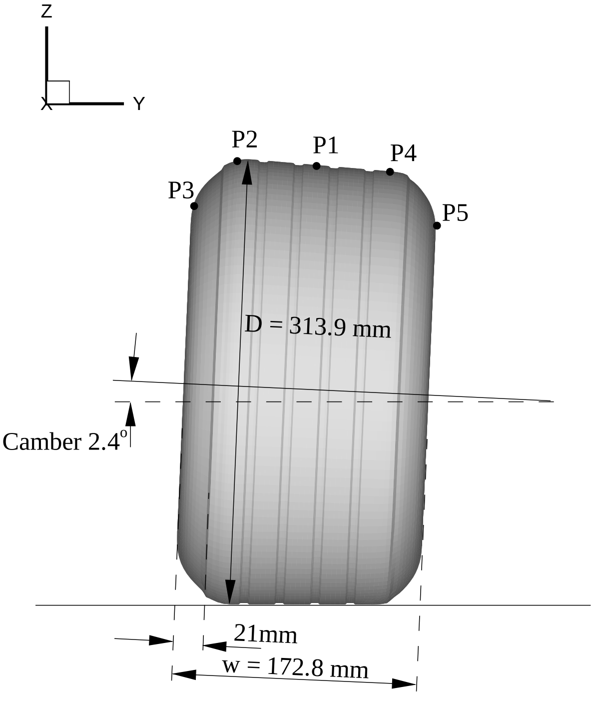

Figure 2.2: Scale drawing of the port side wheel showing the tyre profile, pressure sensor locations (P1 - P5) and the main dimensions.

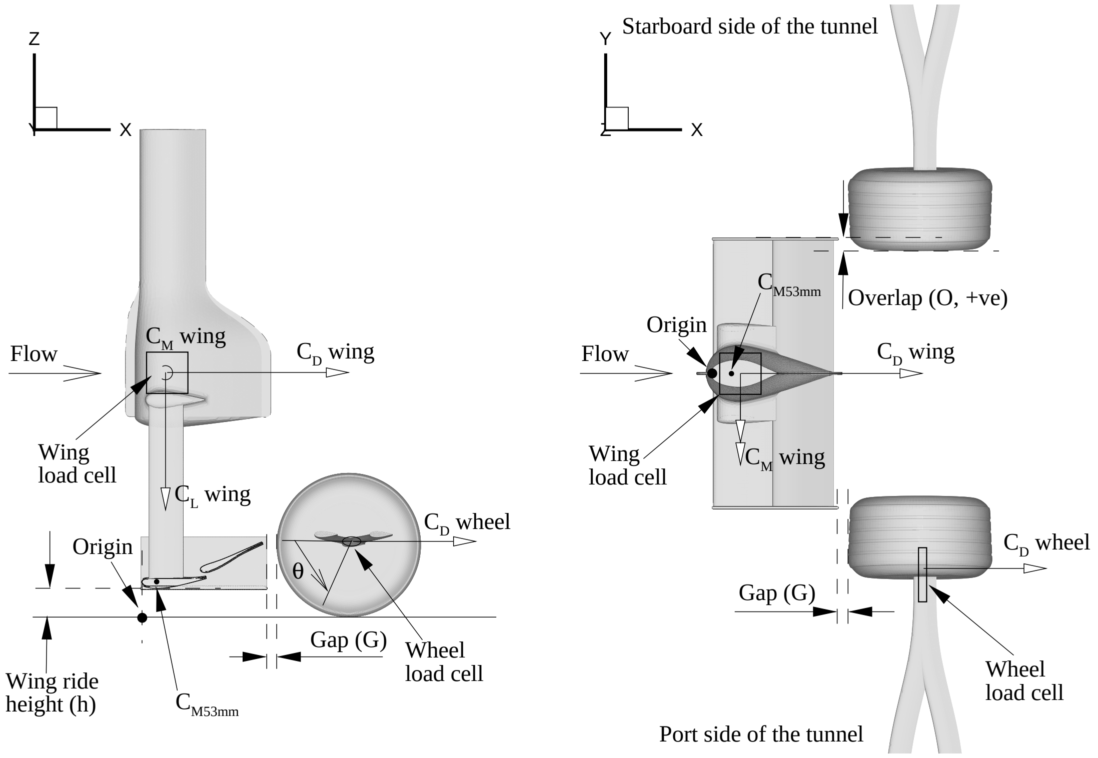

Figure 2.3: Sideview (left) and topview (right) presentation of the combined configuration, showing load cell locations, positive load directions, pitch load resolving point ($C_{M53mm}$) and definitions of wheel angle $\theta$, ride height, gap and overlap.

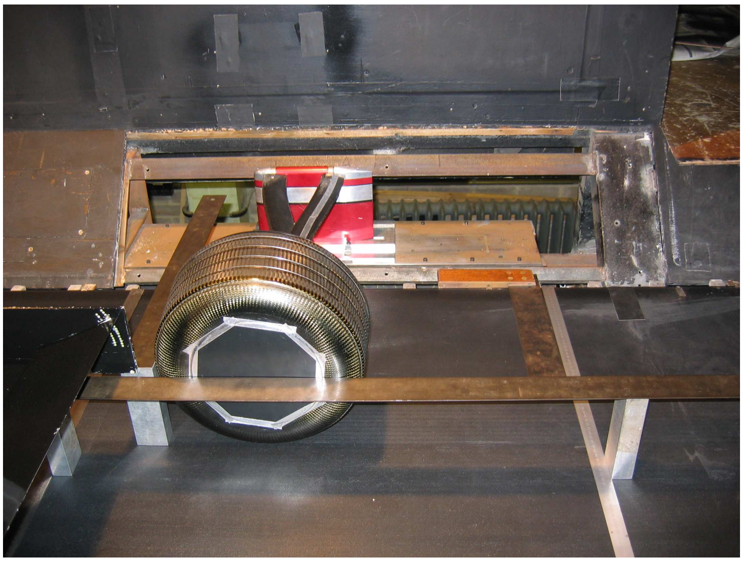

Figure 2.4: Picture showing the setting up process of the wheel relative to the wing; flow direction from left to right.

Figure 2.5: Picture of the 7 × 5 wind tunnel facility with the complete configuration in place, consisting of the force wing model and two 050 dummy wheels.

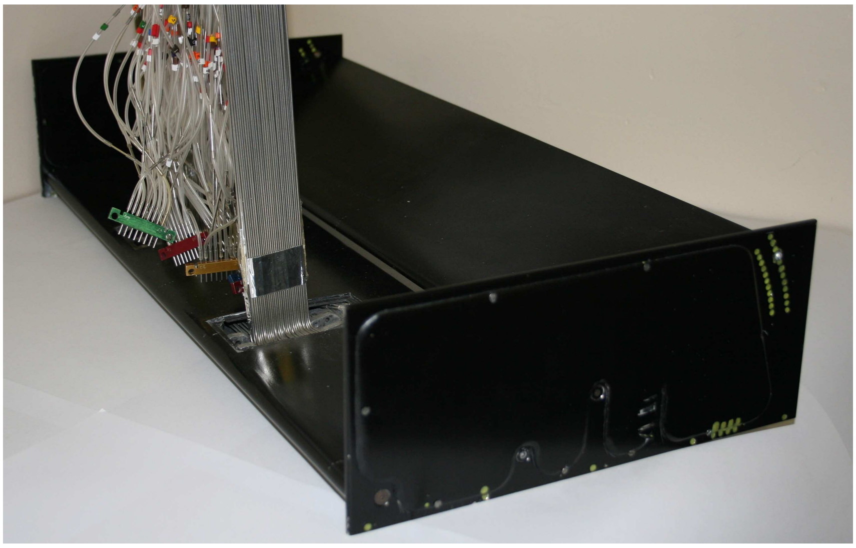

Figure 2.6: Picture showing the pressure tapped wing model without vertical support pillars; the tubing and connectors for the ZOC system are also visible.

Figure 2.7: Picture showing the three different used wheel models; 020 with McManus pressure system (left), 050 dummy (middle) and 050 with Chell pressure system (right).

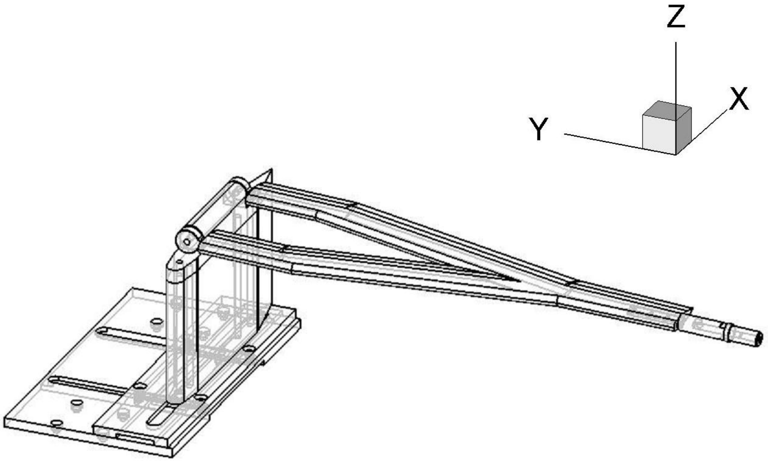

Figure 2.8: Design drawing of the starboard side wheelarm with inserted load cell, support pillar and adjustable ground plate.

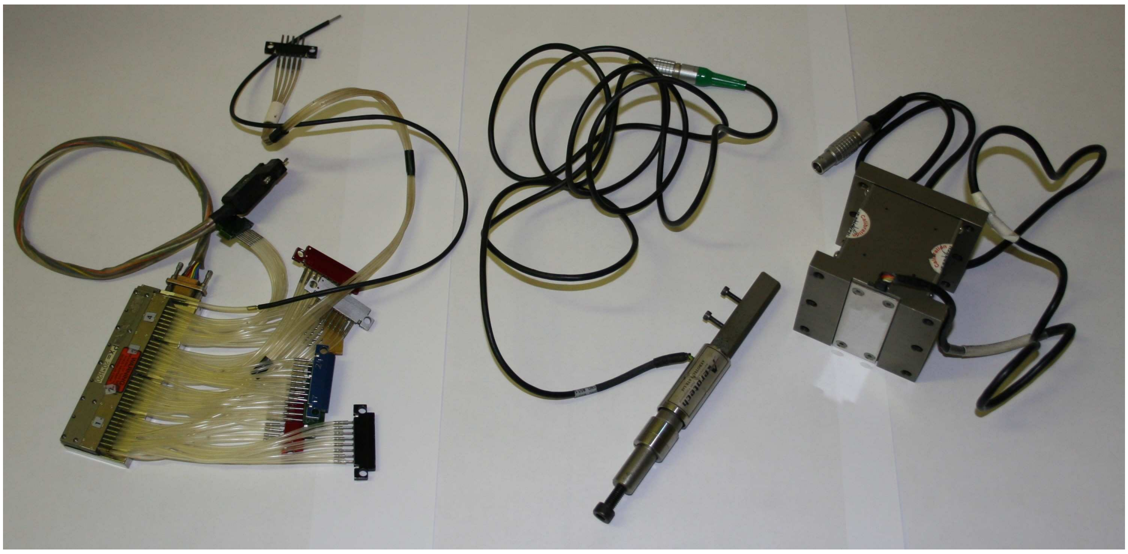

Figure 2.9: Picture showing experimental equipment; ZOC2B wing pressure measurement system (left), Aerotech 0551: 1-component wheel drag load cell (middle) and Aerotech 0487: 3-component wing balance (right).

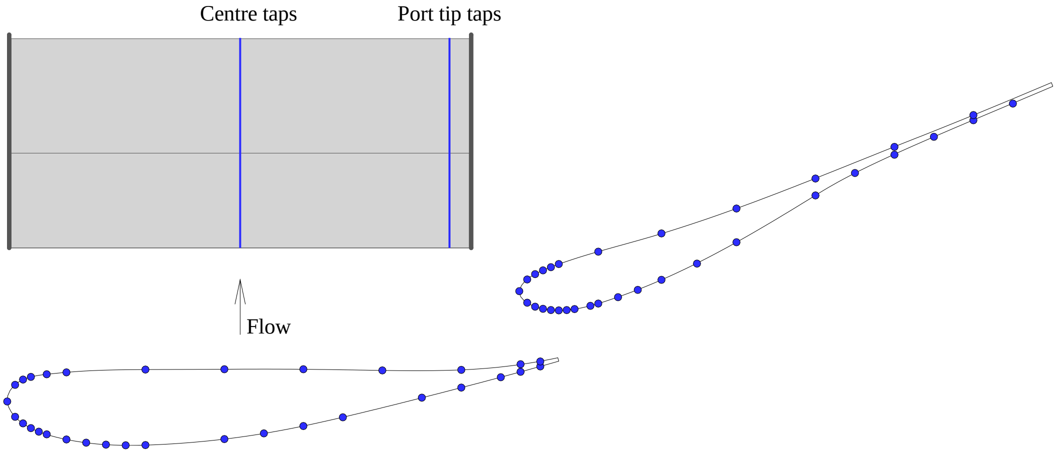

Figure 2.10: Figure showing the pressure tapping locations on the wing; the centre and port tip positions (see top left corner of figure) both feature the same pressure tap distribution as shown on the wing profiles, each blue circle represents a pressure tapping.

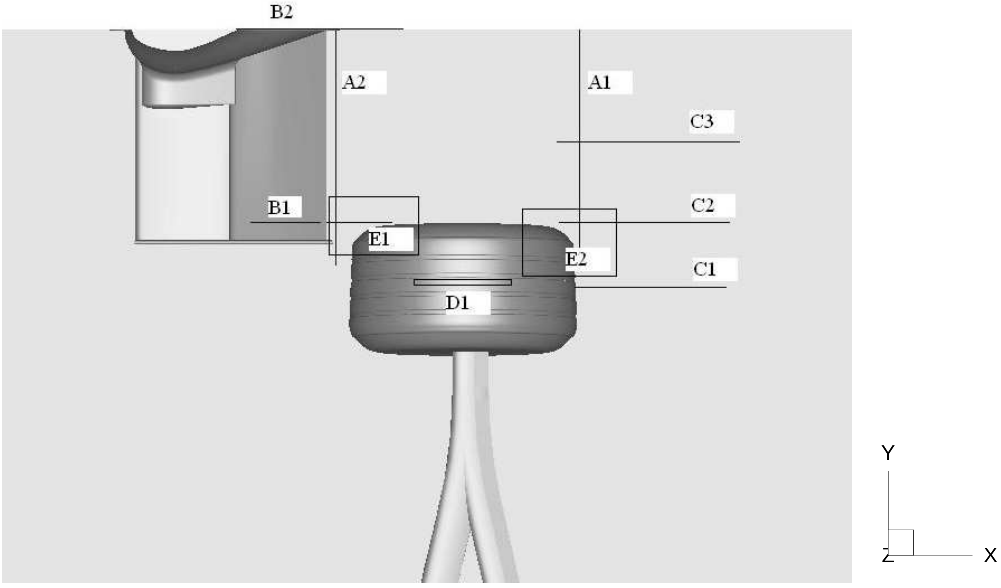

Figure 2.11: Presentation of the PIV planes that have been studied during the research; A to D are vertical planes and E are horizontal planes.

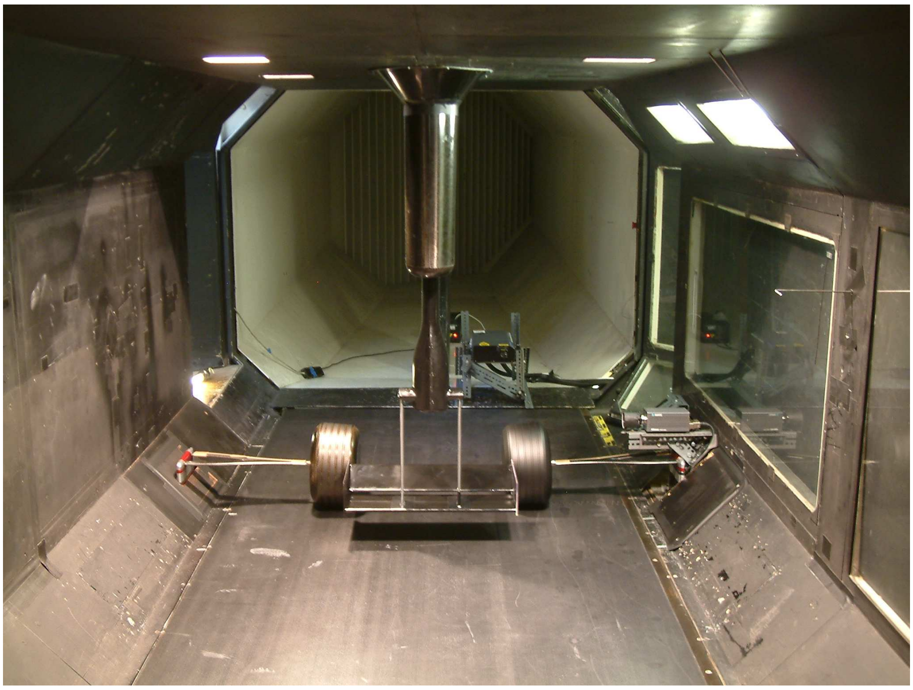

Figure 2.12: Picture of a typical PIV set-up for a vertical streamwise image over the top of the port side wheel; the camera is located above the respective wheelarm, the laser downstream of the rolling road and the smoke generator behind this.

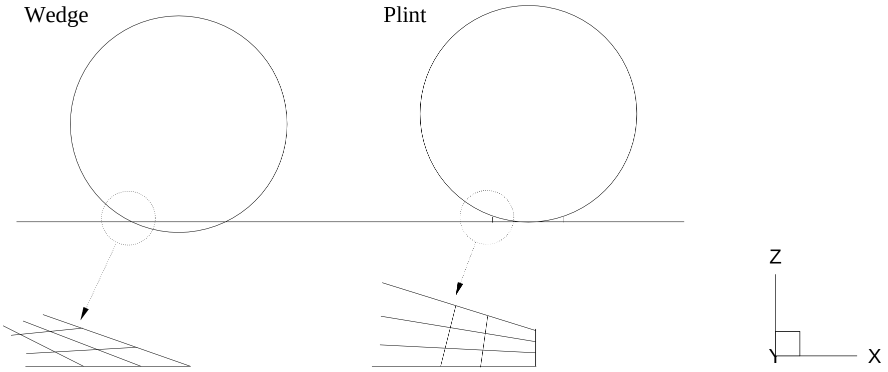

Figure 2.13: Schematic sketch of two wheel contact patch options: 'wedge', due to a sunken wheel (left) and 'plint' with a curtain between the wheel and ground (right).

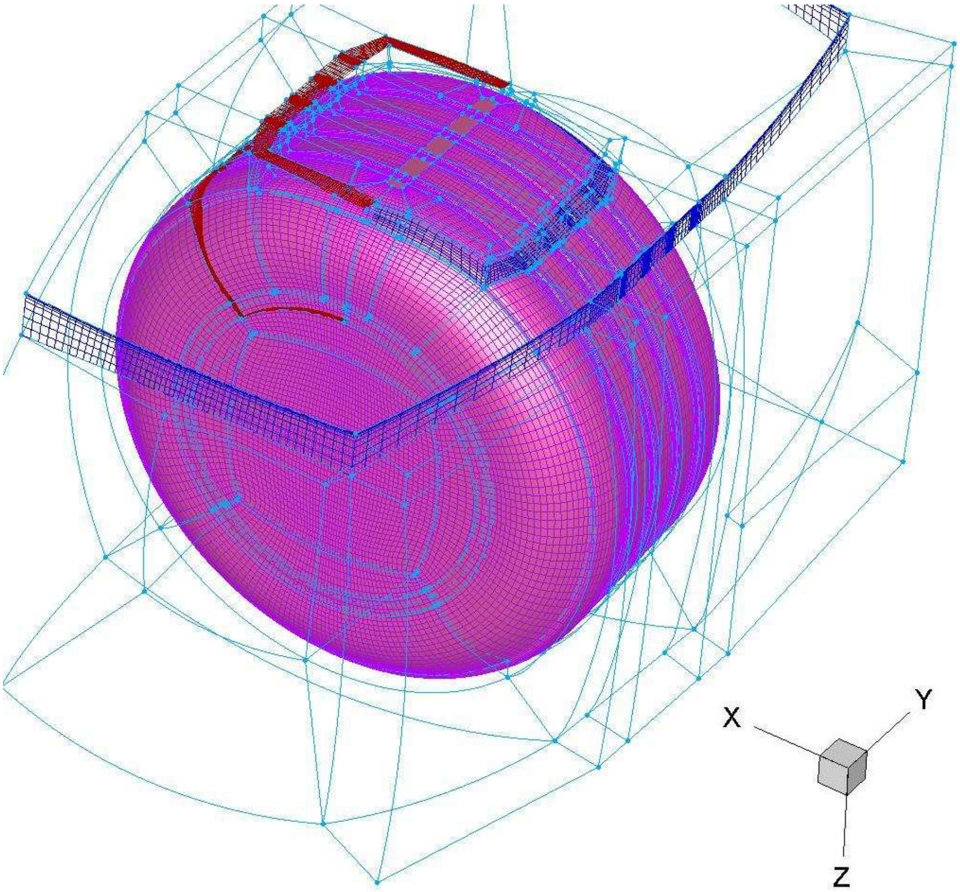

Figure 2.14: Presentation of the wheel mesh module; showing how the wheel boundary layer (red) partly ends on the ground, whereas the ground boundary layer (blue) partly ends on the wheel surface; looking from underneath, through the ground plane.

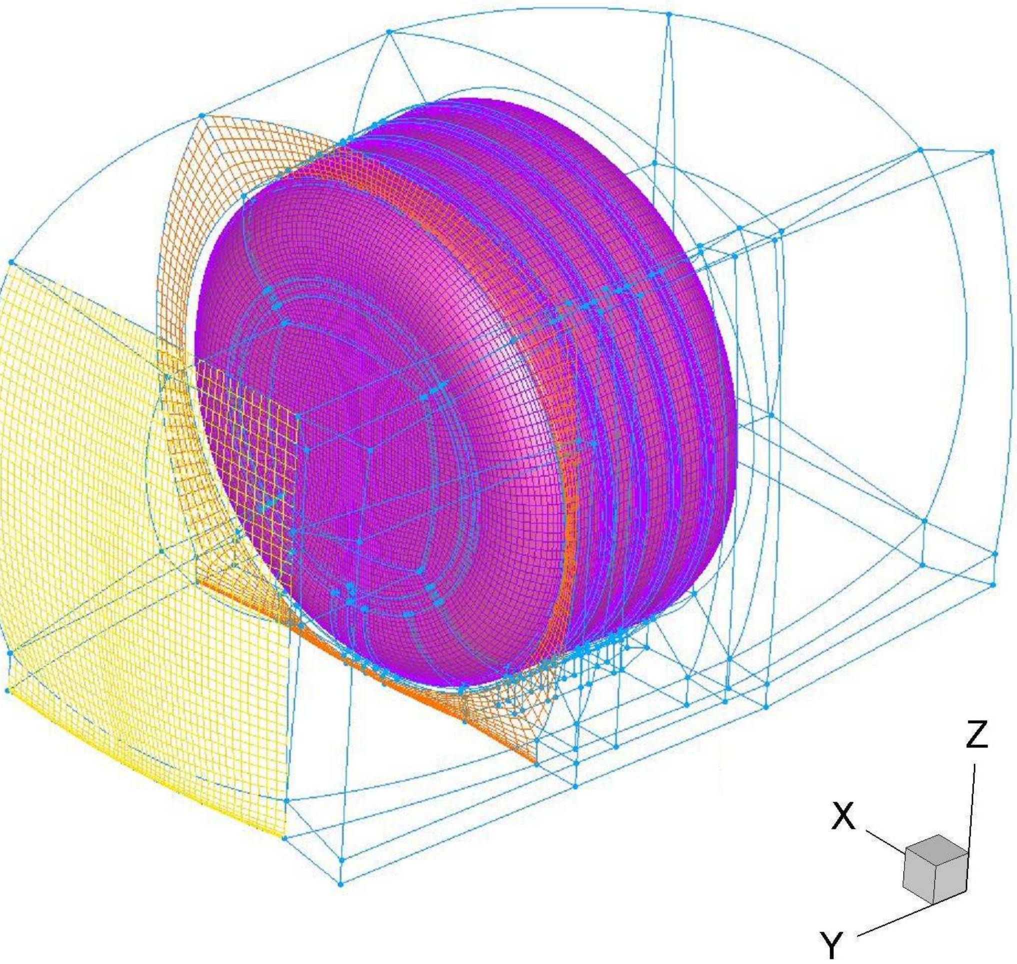

Figure 2.15: Presentation of the wheel mesh module; showing how the complex side mesh (orange and purple on wheel surface) is changed into a regular mesh (yellow) away from the wheel.

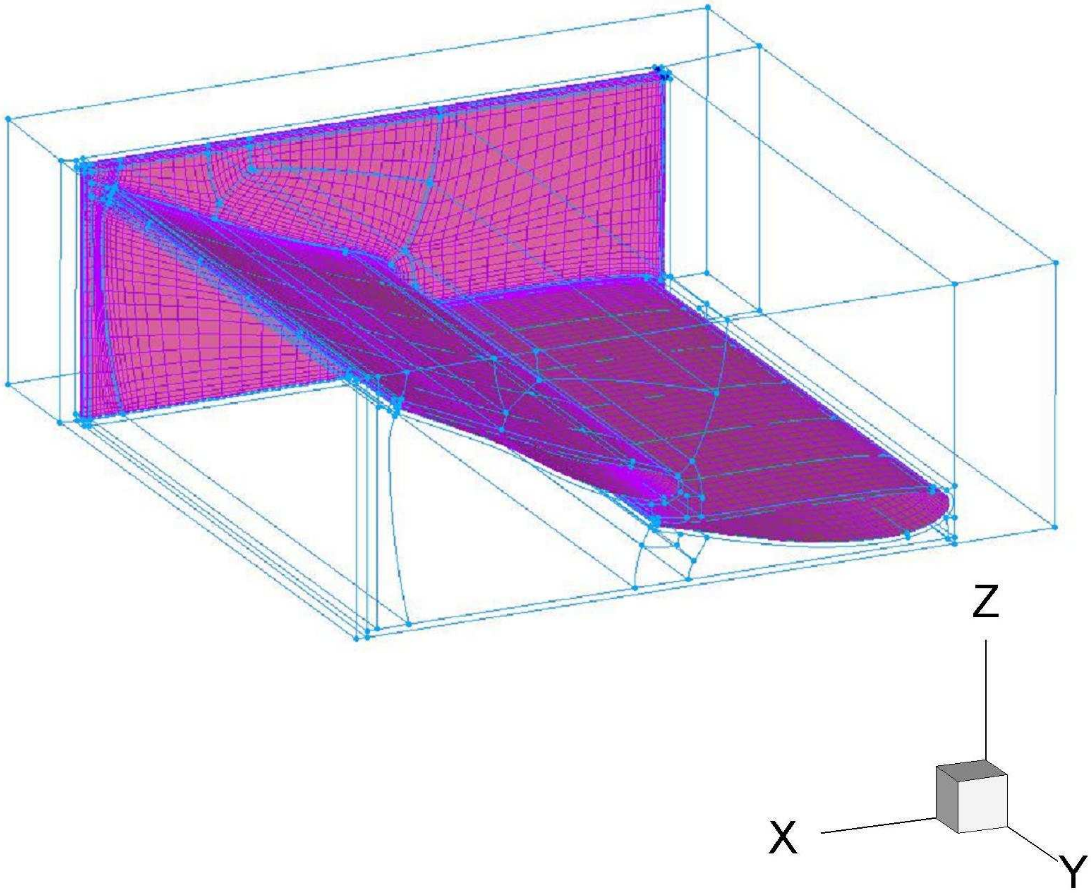

Figure 2.16: Presentation of the complete wing mesh module; showing the geometry surfaces and the on-surface mesh.

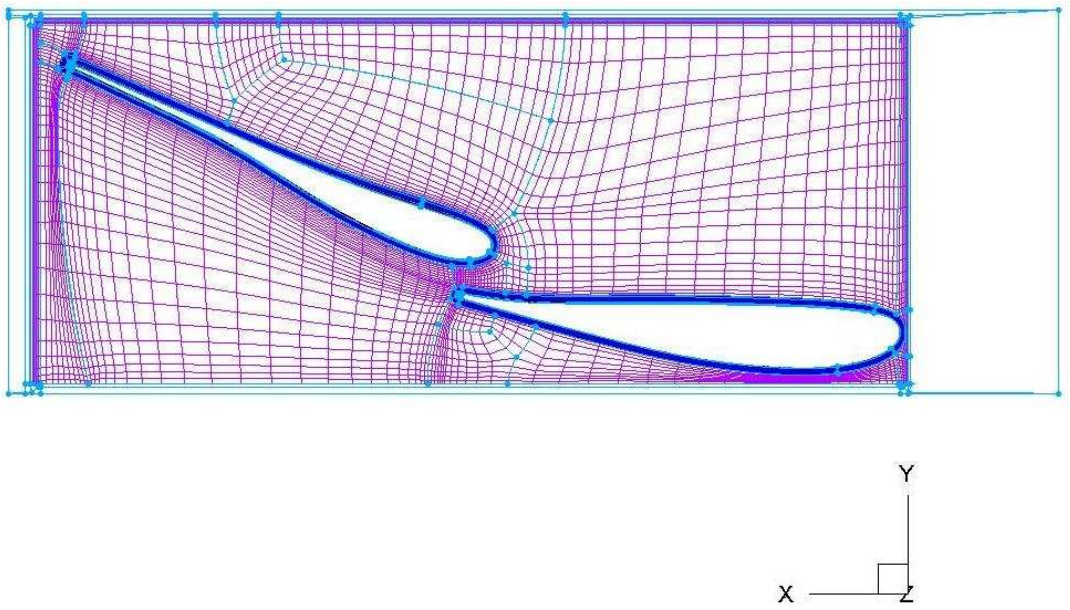

Figure 2.17: Illustration of boundary layer wrapping applied to wing mesh module; boundary layers in blue are wrapped around the main element and flap.

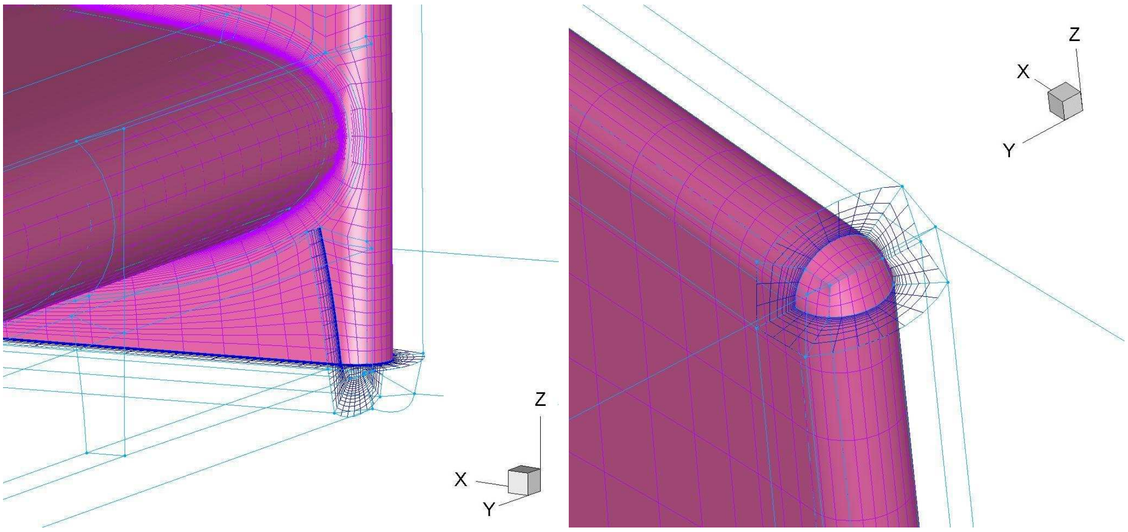

Figure 2.18: Wing mesh module grid details; lower upstream endplate corner (left) and upper upstream corner (right), showing the boundary layer (in blue) wrapping around the endplate.

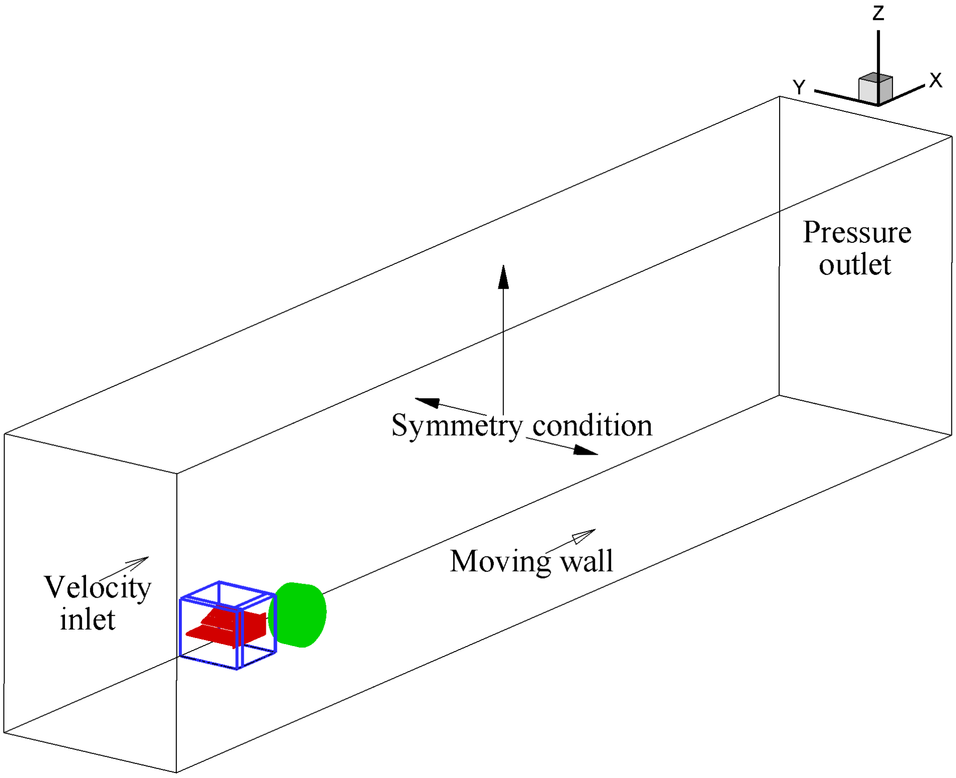

Figure 2.19: Presentation of the complete grid for a combined case (CWW20202h90), showing the wheel (green), wing (red), non-conformal connecting zones (blue boundaries) and the boundary conditions on the domain surfaces.

# Chapter 3

# Reference Results

It is essential to understand how the flow behaves for the isolated components in order to be able to study the interaction phenomena. This chapter will introduce the isolated wheel and isolated wing cases as references for the combined wing - wheel case. Hereto this chapter summarizes previous results by McManus [68] and Mahon [12] for respectively the wheel and wing. Also new and updated results are shown, which were obtained during the current research, such as revised force coefficients, new PIV data and comprehensive CFD results for the wing as well as data for the cambered wheel, including the experimental drag force coefficient. This chapter is divided into two parts, the first part deals with the isolated wheel results and the second with those for the isolated wing.

## 3.1 Isolated wheel

Since the wheel model that has been used during the current research differs from the one in McManus' experiments [68] and because it is not possible to refer to all of the results that have been obtained previously at the University of Southampton, this section will give an overview of the flow field for this specific wheel. The wheel model distinguishes itself from, for example, Fackrell's model [34] by the realistic side wall shape, the grooves and the camber angle. Furthermore it needs to be remembered that the experimental data presented in this chapter has not strictly been acquired in isolation, since a second wheel was placed in a symmetric set-up (see figure C.6), similar to the combined wing - wheel case when the wing would be removed. This condition is reproduced in the CFD by using a symmetry plane. All presented results are for the port side wheel.

The first two subsections will summarize the experimental data for the isolated wheel. After this the correlation of the CFD results with the experimental data will be assessed and subsequently the data of both these approaches will be used to discuss the isolated wheel flow. Finally, this section will be concluded with a short examination of the influence of wheel camber angle on the results.

### 3.1.1 Integrated and on-surface results

The current experimental set-up allows direct measurement of the drag force for the wheel. However the lift has to be derived from integration of the experimental pressures or via CFD computations. The superior resolution of the computational grid along the wheel width, in comparison to the five experimental pressure locations in this direction, should guarantee more accurate results for the second method, but this all depends on the ability of the SA SRANS solver to simulate the flow physics accurately.

The postprocessed drag coefficient values for the rotating and stationary case can be found in table 3.1. The results for the rotating wheel have been corrected for rolling resistance by using trundle runs, as explained in section 2.3.4. The same table also contains the force coefficients for a variety of CFD simulations. The computational solver produces these values by integration of the pressures in the surface cell nodes over the complete geometry of the wheel. A negative downforce $C_L$, or in other words lift, is directed upwards in accordance with the definition in figure 2.3. Furthermore the experimental pressure distributions around the wheel for the five different pressure sensor locations (see figure 2.2 for their positions) are shown in the figures 3.1 to 3.5. It needs to be kept in mind that this data has been obtained at $20m/s$ instead of $30m/s$ and for a slightly different wheel geometry, as has been discussed in section 2.3.5. CFD data for the standard test conditions, at $30m/s$, has been included in these figures as well. The 3D on-surface pressure contours for the wheel, as derived from a steady RANS simulation, are presented in figure 3.7 for reference and to get better insight in the spatial structures behind the experimental pressure distributions.

Although the resolution of the pressures along the wheel width is not fine enough to obtain an accurate wheel lift coefficient value, it is still instructive to integrate these pressures in rotational direction in order to obtain 2D sectional force coefficients for each of the sensor locations. The results of this exercise are summarized in table 3.2; again also for a selection of the simulations. Comparison of these values can give an idea of the regions on the wheel surface where the CFD has problems to capture the physics. The influence of $Re$-effects on the experimental wheel drag coefficient has been determined and is reported in appendix C. The results show that changes in the $Re$-number have hardly any effect on the outcomes[1], indicating that the flow is dominated by end and ground contact effects instead of 2D cylinder characteristics. Finally appendix C.2 presents a picture of oil flow data for the stationary isolated wheel case.

### 3.1.2 Off-surface measurements

Experimental PIV data has been obtained for three different planes in order to investigate the flow patterns. The same planes have also been analyzed with CFD and the results are presented in figure 3.6. These figures use an alternative origin for the axes system, since the wing is not present. The origin is still located on the ground in the symmetry plane, but the $x$-coordinate is now equal to that of the wheel axis. The geometries in the PIV results are projections on the field of view and can be slightly distorted due to parallax effects. The geometries in the CFD figures on the other hand are cross sections of the model at the corresponding plane. The two figures for the top of the wheel, 3.6 (a), also contain red curves, which depict the location where the flow reverses. These are derived from the condition $U = 0 m/s$. A part of the field of view close to the wheel has been blocked in this picture due to the wheel camber, since the PIV camera was positioned on the outside of the wheel. Therefore an additional curve has been included in the CFD representation, which represents the extreme diameter of the wheel model, as seen by the PIV camera. It can be concluded from a comparison of these two figures that the separation position can not be determined exactly from the PIV data as a result of the field of view blockage.

To get a better idea of the steady 3D flow features, figure 3.8 shows an iso-surface of $Q$ for the baseline CFD simulation. This figure provides insight into the vortical structures that can be found for a wheel flow. However it has to be remembered that these results are obtained with a steady solver and are not necessarily equivalent to the time-averaged results for an unsteady simulation or experiment. Finally, hot wire data has been obtained for the isolated wheel as well. However no clear shedding peak occurred in the spectra and therefore it has been decided not to include these data here. A very broad local top was discovered with the hot wire directly behind the wheel for the frequency range 20 to $80 Hz$, which was not present if the hot wire was located outside the wheel wake. Nevertheless all that this proves is that the rotating - and even the stationary - wheel case show no form of 2D cylinder type flow vortex shedding and that the separation from the wheel

---

[1] In a velocity range from 10 to $35 m/s$ the drag coefficient varies less than 1.5%, thus justifying the use of experimental pressure data obtained at $20 m/s$ in a comparison with other results at $30 m/s$.

sides produces no periodic shedding either. Despite this lack of periodic flow features in the wheel wake, the broadness and shape of the spectra does indicate that the wheel wake is highly unsteady nevertheless.

### 3.1.3 CFD correlation comparison

In the literature review it has been argued that steady - and even unsteady - RANS simulations can not reproduce all flow features for an unsteady bluff body flow with large scale 3D eddy structures in the wake. Nevertheless, in industrial applications it is in general not feasible to construct a grid that is fine enough for LES and / or to run a DES or LES simulation with a small enough time step. Therefore, despite its shortcomings, SRANS methods are still used to predict wheel flow aerodynamics and to get an idea of the resulting force coefficients. The industry standard seems to be to use the SA turbulence model, because of its robustness, whereas academia prefers to apply a version of the k-$\epsilon$ model (see table 1.4), because of the claimed better performance in separated flow regions [17, 97]. Due to the sheer extent of the current research, which involves three geometrical parameters to vary ($h$, gap and overlap), it has been decided to limit the computational research to SRANS simulations. This section will first discuss the grid sensitivity of the results and after this a number of the turbulence models will be compared for the isolated wheel flow.

**Grid Sensitivity** The simulation for the baseline grid with a SA SRANS solver produces a difference in drag force coefficient between computations and experiments of -6.6%. Table 3.1 shows that coarsening (13.3% in cell dimension per direction) and refinement (13.6%) of the grid do not result in a consistent trend in the changes, since both cases yield a slightly lower drag value. The Fine grid case drag is 1% less than the Baseline case, but moves away from the experimental value. The other characteristics in table 3.1 do however display consistent trends with grid refinement. The wheel lift increases with refinement, the separation from the top of the wheel at the centreline moves downstream and the positive and negative pressure peak near the contact patch grow in magnitude as the number of cells increases. The prediction of the centreline stagnation position is mainly dependent on the local grid resolution[2] and is in line with the experiments for all

---

[2] The grid resolution angle at the stagnation point is reported in table 3.1 for the various cases. The dimension of the cell in which the highest stagnation pressure occurs is twice the mentioned variance; so 2.4° for the Baseline case.

cases.

In order to get a better understanding of the dependency of the flow features on grid refinement, the figures 3.1 to 3.5 also show the pressure distributions for the Fine case. The Coarse case shows similarity to both the Baseline and Fine cases and is not included. Comparison of the centreline pressure distributions, figure 3.1, reveals that the largest difference between the Fine and the Baseline cases arise around the separation region and in the recovery from the negative pressure peak at the contact patch towards the wake. The Fine grid captures more suction over the top of the wheel before separation; the local extreme is $C_P = -0.521$ for the Fine case compared to $-0.493$ for the Baseline and $-0.520$ for the coarse grid. A same trend can be found for the other tyre tread locations (P2 and P4), whereas on the wheel sides (P3 and P5) refinement has most influence on the suction experienced around 0° and 180°, resulting in a slightly better capturing of the local acceleration experienced in the experiments. Intriguingly, the Coarse case predicts these phenomena in the same way as the Fine case, giving the impression that the effect of cell distribution overrides the influence of cell refinement, since refinement repositions the nodes. However the Coarse case predicts a little bit less suction in the wake than the other cases and than the experiments.

In an attempt to promote uniform reporting on the quantification of uncertainty in CFD simulations Roache [100,101] has introduced a Grid Convergence Index (GCI) [3]. This index makes it possible to estimate the error of the numerical outcomes as a result of the grid size and allows comparison between simulations. For the isolated wheel simulations the GCI values based on the Fine grid are $GCI_{C_D} = 2.8\%$ and $GCI_{C_L} = 4.3\%$. The Baseline grid will be used in the remainder of this work, because the final outcome seems to be relatively insensitive to grid refinement.

**Turbulence models** Next, a number of turbulence models have been tried out for the baseline grid using a SRANS solver. The results for the realizable k-$\epsilon$ and k-$\omega$ SST model have been included in the tables and figures, whereas none of the other models provided

---

[3] The Grid Convergence Index is based on the theory of generalized Richardson extrapolation [100] and can also be used for non-integer grid refinements, implying that the grid does not have to be doubled or halved exactly. The basic idea is to approximately relate the results from any grid refinement test to the expected results from a grid doubling using a second-order method. The index is defined as $GCI = 3|\epsilon|/(r^p - 1)$, where $\epsilon = (f_2 - f_1)/f_1$ is the normalized error of the coarse solution $f_2$ with respect to the fine solution $f_1$, $r$ is the quotient of the fine grid size divided by the coarse grid size and $p$ is the accuracy order of the code, in this case 2. The factor 3 is added by Roache as a safety factor for the error estimate and the GCI is usually presented in a percentage by multiplying the value with 100%.

in the software would converge to a solution. The general problem was related to rapid growth of the turbulent viscosity ratio in a number of cells and further analysis revealed that this occurred only in cells in the outer domain. This is a consequence of the design choice to create a fully structured grid, since this means that the aspect ratio of the cells in the outer regions increases excessively in order to limit the total number of cells. A hybrid approach, which uses the same grid around the wheel and a more equally sized tetrahedral grid in the rest of the domain should solve this problem, but could not be implemented within this research due to time constraints.

Both alternative turbulence models predict a lower drag value and a higher lift than the SA model, see table 3.1. With respect to the pressure distributions it can be concluded that the realizable k-$\epsilon$ case performs better in predicting the suction before separation at $C_P = -0.702$ for the centreline, compared to $-0.836$ in the experiments. This is also true for the other pressure distributions on the tyre tread and for P4 it even matches the experiments. The k-$\omega$ SST performance lies between the baseline and the realizable k-$\epsilon$. Another area where these two models produce better correlation with the experiments than the SA model is the suction region around the corners of the contact patch (see Z in figure 3.7) around $\theta = 80°$ for P2 and P4. On the other hand in the wake region the SA model surprisingly produces better correlation in general. Due to the overall discrepancies in pressure distribution correlation on the side of the wheel, it is difficult to evaluate the models in these areas. Also it is expected that some of these differences result from the use of a slightly different wheel geometry for the pressure measurements compared to the CFD geometry. Considering the results, especially the drag coefficient correlation, it has been decided to use the SA model for all other simulations. The robustness of this turbulence model adds an extra advantage to this choice.

**General correlation conclusions** Finally, to complete this section on CFD correlation, the overall performance of the Baseline SA SRANS simulation will be evaluated. Qualitatively the steady RANS simulation captures most of the time-averaged features shown in the experiments. However a few of them are predicted differently, these are:

- The positive and negative pressure peak in the simulations are larger than those in the experiments (in the order of 75%); the grid refinement study shows that this is primarily resolution dependent, since the peak magnitude increases with refinement. The uniform experimental angular resolution is approximately 1°, whereas the computational resolution near the contact patch is less than 0.3° due to local refinement.

- The local acceleration at $\theta = 45°$ for the centreline pressure distribution is larger in the experiments than in the CFD, which leads to $C_P$-values of 0.61 and 0.71 respectively. This can be traced back to the difference in wheel geometries; the experimental wheel with which the pressures have been measured has a 5.8% lower aspect ratio than the 050 geometry of the CFD model. Thus favouring the secondary flow around the sides and creating larger flow acceleration in this area. A similar result has been found by McManus et al. [17] for a comparison of URANS results for a stationary wheel, where the experimental wheel had a 33% higher aspect ratio, resulting in an approximately 0.2 higher $C_P$-value in this region compared to in the simulations.

- The separation over the top of the wheel is predicted fairly accurately - at most 5° too early - for all three sensor locations on the tyre tread, however the suction at this point is underpredicted. This can also be concluded from figure 3.6 (a), which shows higher velocities over the wheel in the experiments than in the computations. Comparison of the other results in this figure reveals that the PIV velocities are genuinely higher than those in the simulations and it is expected that this is a result of the higher blockage in the tunnel due to the wheel support system, compared to the CFD in which only the wheel has been modeled. The underprediction of the suction at $\theta = 0°$ for P3 and P5 can then partly be explained with the same reasoning. Adding the integrated CFD pressure distributions over the top half of the wheel from $\theta = 180°$ to 360° for the five sensor locations yields a 40% underprediction in lift compared to in the experiments, whereas the lower half only has a 10% lower value. The fact that the CFD does not resolve the broad extreme from $\theta = 325°$ to 210° following the separation (at the centreline) is an additional reason for this dicrepancy in lift prediction. The unsteady flow feature responsible for this will be discussed in the following section.

- The differences in pressure distribution P2 between experiments and CFD can be explained by the difference in wheel geometry; in the experiments this sensor is effectively more on the rounded wheel shoulder and no longer contacts the ground. This leads to the generally higher suction, except for near the contact patch where the flow is no longer forced around the wheel but can pass underneath, inducing less suction at $\theta = 80°$ and explaining the lack of the negative pressure peak behind the contact patch. Similarly the experimental sensor P4 is located closer to the edge of the contact patch, though still contacting the ground, considering the presence of the negative pressure peak.

- Finally, the differences in the flow field behind the wheel are not as extreme as indicated in figure 3.6 (c). The CFD flow field at a slightly higher cross section looks more comparable to the PIV results and figure 3.8 shows that the presented CFD result just misses the arch-shaped vortical structure downstream of the top of the wheel, while the PIV plane still cuts through this feature. Further proof for this can be found in figure 3.5, which shows a high acceleration for the CFD at $\theta = 180°$ due to the turning of the flow into the wake, whereas in the PIV this characteristic is replaced by two much smaller suction peaks and a local $C_P$-maximum around the location of the presented $z$-plane (at $\theta = 187°$).

The limitations mentioned above have to be remembered when analyzing CFD results for the wheel. Furthermore, considering the difference in wheel geometry and test conditions between the experimental and computational pressures, it is suggested to use the pressure data primarily qualitatively. The accuracy is nevertheless high enough to be able to deduce trends and relative changes by comparing different flow situations. Regarding the ACFD case[4], it is remarkable that the force coefficients are very similar, while the ACFD case does not resolve the pressure peaks near the contact patch due to a coarser grid in this region. This shows that such an approach can still result in useful data at much lower labour costs for grid generation and can also be used for comparisons as long as the limitations of the method are kept in mind.

In general it is expected that the computational lift is underpredicted, although no experimental direct lift measurement is available for reference. A comparison of the sectional downforce coefficients in table 3.2 shows that the main differences logically occur on the tyre tread. From the pressure distributions it can be concluded that the underprediction of the suction over the top of the wheel and the lack of the following local suction downstream are the main contributors to this deficiency. If the sectional downforce coefficients for the tyre tread (P1, P2 and P4) are added and compared then it can be seen that the experimental value is 3.3 times as high. Therefore it is expected that the real lift on the wheel is more likely to be between $C_L = -0.09$ and $-0.3$ than the $-0.09$ that follows from

---

[4] This hybrid grid has been created in a similar way as at the industrial sponsor, using wall functions and roughness instead of a $y^+ = 1$ boundary layer resolving grid, a much larger domain. The wheelarm geometry is modeled in this grid.

the computations. Even though there is a large uncertainty involved in the isolated wheel lift, it should still be possible to derive trends as a result of the wing presence at a later stage, as long as the same approach is consistently being used. The difference in drag is much smaller (at 6.6%) and the main contribution to this is the underprediction of the suction on the upstream half of the wheel due to the different wheel aspect ratio.

### 3.1.4 Discussion of flow physics

The general aerodynamics of an isolated wheel in contact with a moving ground have been discussed in section 1.2.3. This section will look at the flow features and physics for the currently used geometry as reference for the combined wing - wheel study. Results from the experimental and computational approach will be combined to give a global overview. The longitudinal tyre grooves only seem to have a local influence and will not be discussed in more detail.

**Contact patch region** The contact patch region, around $\theta = 90°$, is mainly characterized by the positive and negative pressure peaks respectively upstream and downstream of the area of contact. The unusual $C_P$-value above unity for the positive pressure peak can be explained from the fact that the Bernoulli law no longer holds in this region, because the energy is not conserved along a streamline. The energy that is added to the flow by the wheel rotation and ground movement increase the total pressure and this leads to the local high $C_P$-value. A computational simulation in which only ground movement and wheel rotation were modeled, but no flow velocity, showed that the peaks do still appear under these conditions; see table 3.1. This is in agreement with reasoning by Fackrell [61]. In contrast, for the stationary wheel in wind-on conditions the positive peak does not appear and the $C_P$-value does not even reach stagnation conditions due to the total pressure losses as a result of the ground boundary layer; see table 3.1 again.

The viscous action of the two converging surfaces form the flow physics behind this phenomenon that is unique for the rotating wheel. The flow that is drawn into the corner by the moving surfaces is deflected outwards along the sides of the wheel in the form of viscous jets [34]. The rise in pressure has also been compared to a ‘pumping’ action [17]. The negative pressure peak results from the same, but oppositely acting, physical principles and was predicted by Fackrell [34] although it did not occur in his experimental results. The reason for this was suggested to be lifting of the moving ground belt due to the induced low pressure. In the current results the negative peak occurs for both the experiments and the simulations. The low pressure regions just upstream and to the outside of the contact patch (depicted as Z in figure 3.7) as a result of the local acceleration are a secondary characteristic of the contact patch region. These can be recognized in the computations (see figure 3.7) and in the experimental pressure distributions, especially for sensor location P2 (see figure 3.2).

**Stagnation point** The centreline stagnation point appears just below the most forward point of the wheel, near $\theta = 5°$. Fackrell's results [62] indicate that the stagnation point moves closer to the ground due to wheel rotation. No stationary experimental pressure data has been obtained within this research, however the computational results show no effect of rotation on the centreline stagnation position. This is most likely a direct result of the grid resolution in this region. The CFD results predict the global stagnation position to be on the centreline, despite the wheel camber and resulting flow asymmetries.

**Flow separation** Flow separation from the top of the wheel takes place at around $\theta = 275°$ in both the experiments and the simulations. As the flow separates from the top of the wheel in the simulations, the following base pressure in the wake reaches a fairly constant value of around $C_P = -0.4$. In the experiments however the pressure coefficient drops again after the local maximum and can reach lower values for a considerable section of the wheel before it reaches the more constant wake value. This broad second minimum can be distinguished for all of the tyre tread sensor locations and is completely missed by the SRANS simulations, independently of the used turbulence model. A similar second minimum can be distinguished in Fackrell's experimental results for a rotating wheel [34, 62], but seems to occur only for the rotating case and not for the stationary[5].

A physical explanation for this feature can be found by studying the DES results for the isolated wheel. This unsteady simulation captures a second local minimum, even though the magnitude is underpredicted in a similar way as the suction value that occurs upstream of separation. It is therefore expected that this feature is unsteady in nature. However McManus' URANS simulation of Fackrell's geometry [17] does not capture the extra suction that is shown in Fackrell's experimental pressure distribution either. From this it can be deduced that the mechanism behind this flow feature must be related to large

---

[5] The small local minimum for some of the stationary results of Fackrell is most likely the result of a local separation islet on the top of the wheel, as reported by Zdravkovich [25] for low aspect ratio cylinders. This same phenomenon can also be distinguished as the non-dried patch on the top of the wheel in the stationary oil flow results presented in figure C.6.

scale unsteady eddy structures downstream of the separation position. Further analysis of the instantaneous PIV results of figure 3.6 (a), presented in figure 3.9, revealed that the separation process consists of irregular vortical structures that are being shed from the separating shear layer. The additional time-averaged suction that these structures generate compared to the non-vortical recirculation depicted in the CFD results of figure 3.6 (a) is the physical reason behind the occurrence of this flow phenomenon. The statistical modeling instead of resolving of large scale unsteady vortical structures in RANS simulations will thus always lead to an underprediction of the lift for an isolated wheel due to the inability to capture this flow feature.

The CFD simulations show no obvious signs of separation over the sides of the wheel. The relevant pressure distributions, P3 and P5, present a large suction at $\theta = 180°$, indicating attached flow, which curves around the wheel into the wake. The experiments are more ambiguous about side separation, but there is not enough data to come to a decisive conclusion. Figure 3.6 (c) seems to show that the flow has separated and this is partly confirmed by the pressure distribution for P5 in figure 3.2, but on the other hand the sensor location on the opposite side, P3, seems to show only limited separation from $\theta = 230°$ to 190°. No PIV data is available for this side to check whether separation occurs here. Nevertheless it is clear that the complicated interaction of separation and reattachment, which has been described for stationary finite cylinder ends in section 1.2.1, does not occur for the rotating wheel. Finally, McManus et al. [17] also refer to a lower separation region around the front of the wheel close to the ground; in the area where a horseshoe vortex would be located for the stationary case. The current simulations do not show any flow reversal in this area, but a similar shaped 'bow wave' region can be recognized in the $Q$-iso-surface of figure 3.8.

**Wake** Several models have been proposed in literature to describe the trailing vortices and wake for a rotating wheel in ground contact. The majority of these [48, 60, 70] have been of a theoretical nature and are incomplete with respect to the occurring flow features. Recently McManus et al. [17] formulated a new description based on URANS simulations. The time-averaged arch shaped vortex at the top of the wheel, which he discovered, can be recognized in figure 3.8 as well. The flow in the upper near wake rotates around the arch shaped vortex core, instead of in a pair of counterrotating longitudinal vortices as proposed in the previous mentioned theoretical models. The lower extremes of the arch shaped vortex do however turn towards the freestream flow direction, but the vorticity along these legs dies out quickly, within a streamwise distance of $2/3D$.

The lower wake is dominated by two longitudinal counterrotating vortices close to the ground. In figure 3.8 these vortices are represented as the two structures that continue the furthest downstream. The formation of these vortices results from a vortex in the centreline $x$ - $z$ plane, which is bent in an arch shape in a horizontal plane, with the legs formed by the longitudinal vortices. The origin of this vortex in the $x$ - $z$ plane does not occur near the contact patch in the wheel - ground wedge, but more downstream around $\theta = 160°$ at $0.2D$ from the wheel surface. At this location the downstream downwash favours and strengthens this vortex, in contrast to the arch shaped vortex in the upper half of the wake, which is weakened by the local upwash at the downstream side. In figure 3.10 the longitudinal vortices are just being formed and are therefore not yet clearly visible, whereas the ends of the upper arch shaped vortex can be seen as the two local $C_{PT}$-minima around $z = 0.2m$.

### 3.1.5 Influence of wheel camber

The wheel rests more on the side closest to the symmetry plane, due to the wheel camber angle. This implies that the part of the wheel side wall in contact with the ground on this side is larger than that on the other side, as can be seen from the appearance of the positive pressure peak for P4 in contrast to P2. The low pressure regions upstream and on the outside of the contact patch zone are slightly offset as a result as well. However apart from this, the wheel camber does not seem to have a large effect on the pressure contours. The asymmetry in the pressure distribution results in a small aerodynamic side force of $C_Y = -0.05$, directed away from the symmetry plane. The influence of the camber angle on the drag can not be determined, because of the lack of an equivalent non-cambered model. Nevertheless Knowles [70] has done a comparative experimental study using a load cell to measure the drag directly. He found that a wheel with 4° camber angle produced approximately 12% more drag than a similar non-cambered wheel. This difference was explained with wake measurements, which showed larger magnitude vorticity and larger velocity deficits for the cambered wheel.

Due to the wheel rotation around an axis, which is angled relative to the ground, the upstream half of the wheel will experience an effective $y$-velocity away from the symmetry plane, which vanishes at the wheel axis plane and changes into a velocity component towards the symmetry plane for the downstream half. The maximum $y$-velocity component is less than $1.5m/s$ at the most upstream and downstream point of the wheel. The effect of wheel camber on the wake is difficult to distinguish from the influence of the symmetry condition on this. For example figure C.6 shows that the wake is displaced outwards, away from the symmetry plane for the stationary case, but this could be the result of the presence of the other wheel just as well as of wheel camber. From figure 3.10 it can be derived that the asymmetry in the wake is limited at a distance of only $2/3D$ from the wheel axis. In general it can therefore be concluded that the wheel camber does not result in additional flow features and that the asymmetry resulting from the small camber angle of 2.4° has only limited local and no larger global effects.

## 3.2 Isolated wing

Previously, Mahon [12] conducted a comprehensive study of wing in ground effect aerodynamics. Since the same experimental models and configuration settings have been used within the current research, it is possible to refer to his work and to use his results[6]. However the computational side had not been finished completely and additional simulations have been performed during this research. This section introduces the force regions that cover the ride height domain, based on Mahon's definition. The presented force data is quantitatively updated compared to Mahon's results. The reasons for this, as well as the resulting changes, are presented in appendix A. The following discussion of the downforce enhancing and limiting mechanisms and of the flow features is primarily a summary of Mahon's findings, completed with some new results. Next, the new CFD results for the isolated wing will be presented and discussed; first for a baseline ride height and then over the ride height range. Finally, the downstream flow field will be analyzed, because this gives insight into the flow disturbances that the wheel will be subjected to.

### 3.2.1 Definition of force regions

The aerodynamic load coefficients for the isolated wing vary with ride height due to the ground effect. Mahon has distinguished six different flow regions, *a* to *f*, based on the downforce variation within the tested ride height range. Discontinuities in (the slope of) the downforce curve were chosen as region boundaries, because these indicate changes in the flow physics. The results are dependent on the direction of the ride height variation and display hysteresis effects at low ride heights. The force region for the lowest ride

---

[6] The wing has always been kept in the baseline settings during this research, therefore all reference results can be found in chapter 5 of Mahon's thesis [12].

heights has therefore been divided into a branch for increasing and another for decreasing ride height, whereas the other regions are all independent of direction.

Figure 3.11 shows the downforce variation over the ride height range together with the force regions that were defined by Mahon. In a similar way figures 3.12 and 3.13 show the drag and pitching moment behaviour. The latter presents both the moment curve resolved around the $C_{M53mm}$ point, as well as around the quarter chord point of the complete wing ($C_{M1/4c}$). Finally, the location of the centre of pressure has been derived as well, according to equation A.4, and visualized in figure 3.14. The centre of pressure is the point at which the force vector acts that results from integrating the aerodynamic pressure and shear stress distributions over the wing surfaces. The resulting moment around this point is equal to zero and the location of this point is of importance in the context of the stability of the car as a whole.

The six different force regions have the following characteristics:

- Region *a*. This region spans from the highest ride height of $h/c = 0.634$ up to 0.236. In this range the downforce coefficient increases exponentially from 1.60 to 2.26 for decreasing ride height. The drag follows a similar trend, growing from 0.217 to 0.276, while the pitching moment ($C_{M1/4c}$) increases in absolute value from -0.197 to -0.258. The centre of pressure stays close to $x/c = 0.373$, before it moves forward at increasing rate towards 0.364

- Region *b*. From $h/c = 0.236$ down to 0.211 the downforce initially increases to a maximum of 2.29 at $h/c = 0.222$, albeit slower than before, and then decreases to a value of 2.26. The drag and moment show a similar behaviour, reaching extreme values of respectively 0.279 and -0.259 at the same height. The centre of pressure moves continuously forwards with a temporary local minimum of 0.361 at the slightly lower ride height of 0.218.

- Region *c*. Ranging from $h/c = 0.211$ to 0.123, the downforce increases almost linearly to a value of 2.45, while the drag climbs asymptotically to a global maximum of 0.297. The pitching moment grows to a value of -0.255 at $h/c = 0.176$ and then starts reducing again at a rate that becomes larger towards the lower ride height boundary. The centre of pressure keeps moving forward to $x/c = 0.344$.

- Region *d*. From $h/c = 0.123$ down to the hysteresis boundary of 0.081 the downforce increases only slowly and reaches its global maximum value of 2.48 at $h/c = 0.088$. After the global maximum, which was reached at the boundary between *c* and *d*, the drag decreases to 0.288 and the pitching moment to -0.182. The centre of pressure moves forward ever faster to $x/c = 0.324$.

- Region *e*. In the decreasing ride height branch from $h/c = 0.088$ to 0.042 the downforce temporarily increases slightly but then falls rapidly from $h/c = 0.067$ onwards. At the lowest ride height the value has dropped to 2.22. The drag first decreases to 0.280 at $h/c = 0.060$ and then grows linearly to 0.284. The pitching moment continuously falls to -0.146, but at a slower rate from the ride height at which the drag starts increasing again. The centre of pressure initially moves forwards to 0.312 and then downstream again to 0.316.
- Region *f*. The final region has the same boundaries as *e* but covers the increasing ride height branch. The behaviour for the downforce is similar to region *e*, with the exception that the level is offset, as it discontinuously drops to 2.20 at the upper boundary. The value at the lowest ride height is 2.04. The drag decreases continuously to 0.275, while the moment decreases at a constant rate to -0.140. The discontinuous drop in downforce causes an instantaneous shift downstream of the centre of pressure location to $x/c = 0.332$, but afterwards it moves forwards again to a minimum of 0.319.

### 3.2.2 Downforce enhancing and limiting mechanisms

The previously described behaviour of the force coefficients over the ride height range can be explained with the help of downforce enhancing and limiting mechanisms. Zerihan [8] stated that no feature could be singled out to cause the occurrence of maximum downforce, but that a combination of all the mechanisms - both enhancing and limiting - resulted in the outcome via summation of the pressures over the complete wing surface. For a single element wing he mentioned that the global maximum downforce was caused by a balance between disadvantageous lower pressures on the pressure side of the wing, advantageous increased suction on the first part of the suction side due to the ground effect and a disadvantageous rise in pressures on the following part due to boundary layer separation as a result of the adverse pressure gradient. The ground effect can be summarized to cause a larger suction on the side closest to the ground due to the increased circulation. This is caused by the channel between the wing and the ground, which displays a diffuser effect with the largest flow acceleration at low ride heights occurring in the throat formed by the lowest point of the wing with respect to the ground. Finally, the increase and subsequent sudden reduction in tip vortex strength with decreasing ride height influences the force behaviour as well. Zerihan found that the same principles apply to a double element wing, but that the influence of the ground is much more prominent for the main element than for the flap.

Mahon [12] distinguished four mechanisms - two enhancing and two limiting - that cause the particular behaviour in ground effect of the currently studied wing model. The downforce is mainly enhanced by the diffuser-like channeling effect underneath the wing, which increases in strength with reducing ride height. The second downforce enhancing mechanism is the result of lower pressures on the suction side of the flap near to the end-plates due to an increase in lower edge tip vortex strength and therefore of the local flow velocities along the flap surface. On the other hand the downforce is limited via vortex breakdown, which reduces the influence of the second enhancement mechanism. Finally, flow separation also limits the downforce. The separation processes can manifest themselves as normal trailing edge separation (stall) or as off-surface wake bursting according to Mahon [12]. He was the first to state that the bursting of the main element wake is the primary downforce limiting mechanism of a multi-element wing in ground effect. Both downforce limiting mechanisms are the direct result of the adverse pressure gradient that is induced by the stronger suction peak underneath the wing and their influence increases when the pressure gradient grows with reducing ride height. The following paragraphs look in more detail at each of the mechanisms individually.

**Channeling effect** The channeling effect enhances the downforce throughout the ride height domain, for each of the force regions. The channel underneath the wing can be compared to a high aspect ratio diffuser, where the lowest point of the main element resembles the inlet location and the trailing edge of the flap the exit. Decreasing the ride height then leads to an increase in the area ratio and, in accordance with mass continuity, to higher velocities in the channel. Figure 3.15 (a) and (b) show, for example, how the velocities increase from approximately $60 m/s$ to $75 m/s$ when the wing is lowered from $h/c = 0.211$ to 0.106.

The accelerated flow, with $u/U_\infty > 1$, between the lower boundary of the wing (wake) and the ground is described as a wall jet by both Zerihan [8] and Mahon [12] and experimental evidence of this phenomenon has been found by the former. Mahon's experimental results do not show the wall jet, but he attributed this to the used measurement technique. His CFD results did however show the occurrence of a wall jet. A boundary layer is formed on the ground underneath the wing, despite the ground moving with the same velocity as the freestream, because of the velocity difference with the wall jet. The presence of this boundary layer can also be seen in figure 3.15 (a) and (b) and to some extent in figure 3.16 (b). The boundary layer thickness increases with decreasing wing ride height due to the higher velocities in the channel.

The higher velocities underneath the wing lead to lower pressures on the underside of the wing and in particular to a stronger suction peak. Figure 3.17 (a) shows how the suction increases with decreasing ride height, while the pressure side is hardly affected in general. It is interesting to see that the suction peak becomes stronger but stays at the same location of $x/c = 0.021$ until a ride height of $h/c = 0.099$. For this ride height the peak flattens into a kind of plateau. The suction peak moves downstream to $x/c = 0.106$ when the wing is moved even closer to the ground. This location happens to be at the pressure tapping that is closest to the lowest point of the wing. This is reminiscent of diffuser flow for which the suction peak also occurs at the lowest point of the channel.

The oil flow data for the suction side of the wing, see figure 3.18, confirms this as it can be seen that the transition location moves downstream when the ride height is reduced from $h/c = 0.317$ to 0.099. This is a direct result of the advantageous pressure gradient in the part upstream of the lowest point of the main element, which postpones transition. Finally, figure 3.17 (a) also reveals that the channel effect mainly acts on the main element and to a much lesser degree on the flap, which is located further away from the ground. This has previously been discussed by Zerihan [8] and is in line with the general behaviour of the centre of pressure location (see figure 3.14), which moves forward with ride height reduction as a result of the relative increase in main element downforce. The different trends of the pressure distribution at the wing tip, figure 3.17 (b), are caused by the tip vortices, which are discussed in the next paragraph.

**Lower edge vortex effect** The wing is characterized by two vortices per tip, originating from the top and the bottom of the endplates (see figure 3.19). The lower edge vortices are located on the inside of the endplates underneath the flap, while the upper edge vortices can be found outboard at the top of the endplates. These vortices are the result of the finite pressure difference between the inside and outside of the endplate, inducing a flow from the higher to the lower pressure zones. This implies that both vortices at the port side endplate of the wing rotate anti-clockwise, when viewed from behind, whereas those on the starboard side rotate clockwise, in opposite direction. Since the pressure difference between the suction side of the main element and the lower outside of the endplate is larger than that over the top of the endplate, it can be concluded that the upper edge vortices are in general weaker than the lower edge vortices.

The lower edge vortex strength increases with decreasing wing ride height, because the pressure difference grows proportionally to the increase in the suction peak. However the vortex core area also expands due to the adverse pressure gradient. This mechanism acts in force regions $a$ and $b$ until downstream vortex breakdown limits its influence. Table 3.5 gives an indication of the vortex strength (expressed in circulation) and the vortex size (expressed as the maximally connected surface area of the vortex region determined with the $\lambda_2$-criterion [82]). The effect of the increase in strength and size of the lower edge vortex on the force behaviour can be derived from the tip pressure distribution in figure 3.17 (b). Here it can be noticed that the suction on the second part of the main element, from $x/c = 0.25$ onwards, and on the flap increases at the tip, when the wing is lowered from $h/c = 0.317$ to 0.211, but that the suction in these areas decreases again for lower ride heights. This shows that the lower edge vortex increases the suction on these parts at the wing tip as a result of the higher velocities and induced cross flow. The streaklines at the tip in figure 3.18 for $h/c = 0.317$ are curved in these areas, showing the imprint of the lower edge vortex on the suction side wing surface. Finally it needs to be mentioned that figure 3.19 and table 3.5 also show that the upper edge vortex is considerably less affected by the ground effect.

**Vortex breakdown effect** The downforce enhancing influence of the increased lower edge vortex strength diminishes after the vortex starts diluting in force region $b$. Mahon [12] presents smoke visualization pictures, which show the vortex dilution and widening at $h/c = 0.211$. Reductions in ride height cause a larger adverse pressure gradient underneath the wing, which slows the lower edge vortices down in axial direction. However the tangential, or swirl, velocity component still increases upstream of the breakdown location, because the pressure difference between the inside and the outside of the endplate increases. This means that the local swirl number, defined as $\Omega = \Gamma_0/(U_0 \times D_0)$ [85], grows as well, since $\Gamma_0$ increases with the tangential velocity, whereas $U_0$ reduces with the axial velocity. Both the more adverse pressure gradient of the outer flow and the increasing local swirl number promote vortex breakdown according to Delery [85] and this mechanism therefore causes the vortex dilution and breakdown to move upstream.

The ride height for which the downforce enhancing mechanism through increased vortex strength is in equilibrium with the limiting mechanism of (downstream) vortex breakdown can be recognized in figure 3.11 as the local maximum in downforce at $h/c = 0.222$. For lower ride heights the limiting mechanism dominates, as the vortex dilution and breakdown moves continuously upstream. It is expected that the lower edge vortex effect loses all its influence on the wing downforce at the boundary between region $b$ and $c$. This can be concluded from the fact that the local decrease in downforce stops at this height with ride height reduction, which implies that the downstream vortex breakdown has destroyed all the downforce contribution of the lower edge vortex effect and that the channeling effect is the only remaining mechanism at work[7], leading to the growth in downforce after the local drop.

Experimental evidence for the existence of this downforce limiting mechanism can be found in figure 3.19. From this figure it can be concluded that the strong lower edge vortex still exists $10mm$ downstream of the endplate (at $x/c = 0.995$) for a ride height of $h/c = 0.317$, while it has been diluted severely for $h/c = 0.211$. The location of the breakdown can be approximated from figure 3.20, which shows the imprint of a strong lower edge vortex in the streaklines for $h/c = 0.317$, extending all the way till the trailing edge of the endplate. At the lower ride height of $h/c = 0.211$ in figure 3.20 (b) the first part looks comparable, however 2/3 from the leading edge of the endplate the inclination of the streaklines with the freestream direction decreases, indicating the dilution due to downstream breakdown of the vortex. Finally at $h/c = 0.099$, figure 3.20 (c), even the first part of the vortex imprint has changed and shows weakened strength, whereas the downstream part from $x/c = 0.74$ onwards shows complete flow reversal. Therefore vortex breakdown must have taken place upstream of this location. Similarly the effect of the lower edge vortex dilution on the flap surface can be seen in figure 3.18 (b), where the curvature of the streaklines close to the endplate has been reduced compared to in figure 3.18 (a).

Furthermore figure 3.21 (a) gives even more insight into the location of the vortex dilution and breakdown. This plane does not coincide with the vortex core, since it is at an arbitrary $25mm$ inside of the endplate and parallel to the symmetry plane, but still shows that considerable widening and slowing down of the vortex takes place from $x = 220mm$ onwards at the ride height of $h/c = 0.211$. Despite being obscured by reflections of the

---

[7] This conclusion is confirmed by the fact that the downforce increases almost linearly from this point onwards, instead of the previous exponential growth that was experienced when the lower edge vortex effect was still acting together with the channeling effect in region $a$.

endplate edges, it still looks like small scale flow reversal takes place from $x = 240mm$ to $260mm$. This implies that from the start of the vortex breakdown effect at $h/c = 0.236$ in region $b$ until the diminishing of the lower edge vortex effect influence at $h/c = 0.211$ (the boundary between region $b$ and $c$) the actual vortex breakdown does not occur directly close to the flap or main element suction surface. Therefore it is assumed that it is not the (downstream) vortex breakdown as such, but the upstream weakening and dilution of the vortex that forms the physical principle of this downforce limiting mechanism.

The dilution and eventual breakdown of the lower edge vortex counteract the increased suction on the second part of the main element and on the flap due to the second downforce enhancing mechanism. Figure 3.17 (b) shows how the suction on the second part of the main element, from $x/c = 0.25$ onwards, reduces after reaching a maximum level around the ride height of $h/c = 0.211$. The behaviour is similar for the first part of the flap, although the suction keeps increasing on the second part, from $x/c = 0.7$ onwards, until $h/c = 0.141$. This is most likely because this part of the flap is far enough away from the lower edge vortex to not be affected in a negative way. Contours of $x-$vorticity, presented by Mahon [12], showed that the upper edge vortex does not break down when the wing moves towards the ground. The main reason for this would be that there is no sufficiently large adverse pressure gradient imposed on the upper edge vortex, outside of the endplate.

**Flow separation effect** The downforce of the double element wing in ground effect is also limited by flow separation processes. Mahon distinguished two types of flow separation[8] that occur in different locations. These are normal trailing edge separation - both for the main element and for the flap - and detached separation in the main element wake. The first one is a mechanism that limits the maximum lift of a wing in freestream at a certain angle of attack and is also known as ‘stall’, while the second has been discovered by Petrov [72, 73] as a lift limiting mechanism for a multi-element wing of high camber. Under certain conditions the wake of an upstream element can burst due to an adverse pressure gradient and result in loss of aerodynamic loading on the following elements even though the flow directly at the surface of these elements is still attached. This detached separation will be discussed separately in the next paragraph.

---

[8] Additionally there is a bubble-type separation on the outside of the endplates over the full endplate height near the leading edge, which does hardly change over the ride height range and also separation along the connection between the endplate and the suction side of the flap, as can be seen by the recirculation foci on the endplate and flap in the oil flow pictures at $h/c = 0.211$ in Mahon’s thesis [12]. The latter form of separation can only be distinguished clearly in his results for $h/c = 0.247$ and 0.211.

Trailing edge separation is the cause of the reduction in downforce in the regions *e* and *f*. The continuous, but ever increasing, loss in downforce with decreasing ride heights is the result of separation from the main element trailing edge moving upstream. The sudden discontinuous difference in downforce between the force regions *f* and *d* on the other hand can be traced to a full flow separation from the flap surface at centre span. In a similar way to leading edge stall for a wing in freestream, this separation leads to an abrupt significant loss in downforce. The trailing edge separation of the main element can be noticed at centre span in figures 3.18 (c) and (d), whereas the flap separation for the increasing ride height branch is clearly visible in figure 3.18 (d). Both phenomena occur exclusively for the central section of the wing, showing that the flow at the outside two thirds of the span near the endplates of this low aspect ratio wing are dominated by tip end effects. Some asymmetry can be distinguished in the centre span separated area and this could be similar to the asymmetric separation experienced in diffuser flow at low ride heights [14]. The complete separation from the flap surface can also be observed in figure 3.15 (d), compared to figure 3.15 (c).

The effect that the centre span flow separation has on the pressure distribution can be examined in figure 3.17 (a). The pressure recovery on the main element does not continue towards the trailing edge for the $h/c = 0.039$ cases, but instead reaches a constant plateau at approximately $x/c = 0.33$. This is a typical sign of flow separation. Furthermore the suction on the first part of the flap is reduced due to separation as well, whereas the plateau for the second part shows slightly higher suction, which is possibly caused by the recirculation in the separated zone. The pressure sides of the wing elements are also influenced in the hysteresis flow regions, displaying lower pressures than for the other ride heights.

Finally, figure 3.16 also gives an indication of the extent of the flow separation phenomena. However the limitations of the experimental technique have to be kept in mind when analyzing this data[9]. Hereto, the data has been compared to newly acquired PIV

---

[9] Mahon obtained the wake data with a pitot tube wake rake, however this method should not be used in a reversed flow region. First of all because the total pressure measurement would take place in a wake instead of at a stagnation location when the flow is reversed and would therefore be underpredicted. Secondly, even if the total pressure is measured correctly at a different location with for example a tunnel wall mounted probe then still would the static pressure measurement be questionable, because the flow is disturbed, coming over the non-streamlined backside of the wake rake. Somehow the method was not capable of showing accelerated flow (with $u/U_\infty > 1$) either and the wall jet phenomenon has therefore not been captured.

data[10] for two ride heights, see figure 3.16 (a). This shows good agreement in the non-reversed and non-accelerated parts of the wake profile for $h/c = 0.141$. The new PIV data and Mahon's data for the reversed wake at lower ride height are not taken at exactly the same $h$, but do show that the size and velocity magnitude of the flow reversal region are overpredicted with the wake rake. Flow reversal takes place at $h/c = 0.035$, when the flow separates from the flap (see figure 3.16 (a)) and the flap and main element wake merge under these conditions. Despite the discrepancies, figure 3.16 (b) can still be interpreted to show that the flap wake is relatively unaffected by the ride height, while the main element wake grows via a downwards movement of the lower wake edge with ride height reduction.

**Detached separation** The decline in downforce growth with reducing ride height, which is experienced in force region $d$ (see figure 3.11), has been explained by Mahon as main element wake bursting. This form of off-surface separation, which is called detached separation by Petrov [72], is in principle a 2D full span phenomenon. The only experimental evidence that Mahon presents for this mechanism is a figure with wake profiles underneath the flap, which shows reversed flow of up to $u/U_\infty = -0.3$ over a small part of the wake profile at $x/c = 0.835$ for $h/c = 0.099$. However figure 3.16 (a) showed that the reversed flow regions and velocity magnitudes are considerably overpredicted in the pitot wake rake measurements. The rake was also not aligned with the flow direction and the tubes were kept horizontal even though the flow follows the flap contour in this region at 24° to the freestream direction. In fact the new PIV data in figure 3.15 (c) captures the same location and shows retarded flow in the wake but no flow reversal[11]. Furthermore the origin of the wake bursting should be close to the trailing edge of the main element, however figure 3.15 (b) shows no sign of this phenomenon either.

Instead figure 3.21 reveals what is actually happening in this force region. Namely, a detached separation area with reversed flow does exist close to the endplate for $h/c = 0.106$. Closer inspection shows that this separated region originates from the lower edge of the endplate. From this data at the wing tip and at centre span it can be concluded that the downforce limiting mechanism in region $d$ is not main element wake bursting, as postulated by Mahon, but actually lower edge vortex bursting. Up to force region $c$ the lower edge

---

[10] The PIV data has been averaged over 250 image sets, but does not provide smooth curves due to the discrete resolution of the method and due to the data extraction.

[11] This data is obtained at a slightly higher ride height of $h/c = 0.106$, but flow reversal does not occur in a non-presented data set at $h/c = 0.070$ either.

vortex has been diluted and has started to break down with decreasing ride height[12], but in region *d* the remains of this vortex burst and create a zone of reversed flow. The flow along the suction side of the flap remains attached, because it is fed by the jet through the flap gap, but is still affected by the neighbouring detached separation area in a similar way as discussed by Petrov [72].

Further proof of this novel finding can be gathered from figure 3.18. The divergence of the streaklines on the main element close to the endplate has increased, when comparing $h/c = 0.317$ to 0.099, and becomes even larger for $h/c = 0.063$. This flow deflection indicates that the flow is slowed down in the burst vortex area, creating a higher pressure zone, which subsequently expands into the neighbouring lower pressure accelerated flow regions. It can also be seen that the vortex induced curvature of the streaklines on the flap surface close to the endplate becomes less at $h/c = 0.099$, while the influence of the vortex completely disappears at $h/c = 0.063$. At this ride height the streaklines run parallel to the endplate again, driven by the jet flow through the flap gap. The effect of the burst vortex on the pressure distribution can be derived from figure 3.17 (b). The suction on the second half of the main element and on the complete flap decreases at the tip from $h/c = 0.141$ to lower ride heights. This results in the decline in downforce growth in force region *d*, because the channeling effect and vortex burst mechanisms balance each other out. The influence of the vortex burst zones increases with decreasing ride height, as they move upstream and affect a larger area of the main element in this way. This effect is even stronger, because the burst zones are also deflected upwards towards the wing surface for ride heights in close proximity to the ground, as can be seen from figure 3.21 (c). The experimental data seems to indicate that the vortex burst zones exist in force region *d* and survive for lower ride heights. This implies that force region *e* and *f* are also influenced by this downforce limiting mechanism.

**Summary** The combination of the downforce enhancing and limiting mechanisms can be used to explain the behaviour of the wing force coefficients in the following way. From the highest ride height down to $h/c = 0.236$ (region *a*) both the channeling effect and the lower edge vortex effect are acting, producing an exponential growth in downforce. The increase in drag is primarily lift induced and therefore follows a similar shaped curve. Initially the ratio of the downforce of the flap and main element remains constant, but

---

[12] Even though the vortex has weakened and is diluted in region *b*, which led to the ending of the lower edge vortex effect, the vortical flow still exists below this region, as can be seen from figure 3.19 (c).

close to the lower region boundary the main element starts producing relatively more downforce, leading to the centre of pressure moving forwards. In the next region ($b$), down to $h/c = 0.211$, the downstream vortex burst effect becomes effective as well and initially this only limits the contribution of the lower edge vortex effect, but towards the lower heights it completely overrides the lower vortex effect. This downforce limiting mechanism leads to bigger losses than the downforce gain due to the channeling effect and therefore the downforce locally drops. The drag reduces accordingly and the centre of pressure has a local maximum upstream position, because the losses in downforce occur at the second part of the main element and the first part of the flap, downstream of the location where the resulting force acts. The downforce enhancement by the lower edge vortices and the subsequent limiting via vortex dilution and downstream breakdown is reminiscent of the behaviour of the vortices for a diffuser [16].

Through the following region ($c$), down to $h/c = 0.123$, only the channeling effect is effective, producing an almost linear growth in downforce. The lower edge vortices do still exist in a diluted, weakened form, however they no longer affect the pressure distribution along the wing surfaces. The increase in drag is once more mainly lift induced, whereas the centre of pressure starts moving forwards faster, because the channeling effect primarily influences the suction peak on the main element. The downforce stays relatively constant down to the beginning of the hysteresis zone at $h/c = 0.081$ (region $d$), because the increases in downforce due to the channeling effect are counteracted by the losses due to the vortex burst effect. The destruction is however mainly at the tip, while the production takes place at centre span. The drag decreases in proportion with the lift induced contribution, because the vortices are breaking down completely and the induced upwash therefore reduces as well, leading to less downforce induced drag. The centre of pressure moves forwards at an even higher rate, since the downforce generation takes place upstream of the location of this point and the destruction downstream.

Finally, from $h/c = 0.081$ to $h/c = 0.042$, two branches exist depending on the direction of the variation in ride height. The continuous reduction of downforce in both regions is the result of main element trailing edge separation, which gradually moves upstream, destroying more and more of the downforce of the main element. The flap loses downforce as well because the suction reduces proportionally to the reduction in suction at the main element trailing edge. The discontinuous change in downforce at the region boundary for the increasing ride height branch (region $f$) is caused by centre span full chord separation from the flap suction surface, which originates from the start-up phase at the lowest ride height and persists until the hysteresis boundary. The downforce limiting mechanism of trailing edge separation is balanced with the downforce production due to the channeling effect at the upper boundary of these regions until the influence of the separation gets the upper hand. Interestingly, however, the pressure distributions on the flap are very similar for the increasing and decreasing ride height branch. This observation holds both at the centre, where they are virtual identical, and at the tip, where the increasing branch has slightly more suction at the trailing edge, but less in the middle part. The real loss in downforce for the increasing ride height branch is caused by a reduction in suction over the central part of the underside of the main element[13]. It is expected that the increasing branch has less suction over the centre of the main element, because of the adverse pressure gradient caused by the separated flow downstream[14] and possibly because the flow is less channeled by the burst lower edge vortices. These are located much closer to the endplate than for the decreasing branch (see the difference in $y^*$-location in table 3.5), effectively widening the channel and thereby reducing the downforce. At the location of the port tip pressure measurements the suction is however larger for the increasing branch, caused by the proximity of the burst recirculation zone, but this is only a localized effect.

The initial reduction in drag for the hysteresis zones results from the lower pressures on the pressure sides of the elements, whereas the following continuous decrease is related to the reduction in downforce induced drag. When the lowest ride heights are approached, the drag starts growing again for the decreasing branch (region *e*); in contrast to the increasing branch drag. The larger suction over the central part of the main element for the decreasing branch is the main reason for the higher drag. The downstream shift of the suction peak means that the induced thrust on the leading edge of the main element reduces. For the increasing branch this is counteracted by the separation on the flap, leading to an overall drag reduction with decreasing ride height. However for the decreasing branch the loss in thrust is relatively larger and combined with the lack of flap separation this result in an increase in drag. The centre of pressure shifts downstream at the boundary for region *f*, confirming that most of the loss in downforce occurs on the main element. For lower ride heights it moves upstream again, because the separation losses on the flap are larger than for the main element. The downstream movement of the centre of pressure for

---

[13] Suction loss most likely also occurs near the recirculation foci, but no experimental data is available for this location to show this.

[14] The beneficial dumping effect and off-the-surface pressure recovery, which are typical for multi-element wings [71], have been reduced as well.

the decreasing branch at the lowest ride heights is a direct consequence of the drag rise experienced under these conditions.

### 3.2.3 CFD correlation at representative ride height

The CFD simulations for the isolated wing have completely been updated compared to Mahon's work. Changes have been made to the CAD geometry, the grid technique and to the domain (see section 2.4). All simulations have been performed with a steady RANS solver, in accordance with industry standards. This saves a considerable amount of computational time compared to unsteady simulations and is an acceptable compromise considering that most of the flow is attached. The computational solutions have first been correlated to the experimental results at one typical ride height, which combines characteristics of the wing in free flow and in ground effect conditions. The results of these simulations at $h/c = 0.317$ are discussed in this section. Ideally a grid dependency study and comparison of the turbulence models would be performed at each ride height because of the changes in physics and flow features, but for time considerations both have only been conducted at this representative height. The grid sensitivity analysis has been modeled with the default settings, incorporating the SA turbulence model. The subsequent examination of the turbulence models gives an idea of the relative strengths and weaknesses of each of the models with respect to the current problem. Finally, based on this examination, one turbulence model has been selected for all the other isolated wing simulations.

**Grid sensitivity** Three different grid sizes have been constructed to examine the grid dependency of the solution. The baseline grid (see figures 2.16 to 2.18 for an indication of the grid), which has also been used in the rest of the simulations, consists of 3.8 million cells. The finer grid has 5.9 and the coarser 2.7 million cells. This corresponds to a refinement in cell dimension per direction of 15.5% from the baseline to the finer grid and 12.6% from the coarse to the baseline grid. Refinement (and coarsening) has been implemented systematically throughout the grid - including the boundary layer density - but due to the complex block topology and connectivity it was impossible to apply a completely uniform refinement.

The results for the three different grid size cases are presented in table 3.3. The differences in force coefficients due to the changes in grid density are small, less than 0.4% for all of them, considering the considerable changes in the number of grid cells.

Furthermore the values consistenly converge in the direction of the experimental values at a diminishing rate. The pitching moment is the only exception to this observation, since the coarse grid value is closer to the experimental data than the baseline grid. This irregularity is most likely caused by a disadvantageous alteration of the pressure distribution, caused by a different discretization of the contour, considering the small value differences. The pressure contours and wake profiles are almost coinciding for the three grid sizes and therefore it has been decided not to present these here. However it is interesting to notice that the global maximum suction value is found in the lower edge vortex core for the baseline and fine grid cases, whereas it is located on the main element suction surface for the coarse grid case instead.

Based on the results shown in table 3.3 it can be concluded that the simulations for this specific grid design approach the asymptotic limit of the force coefficients. It is however expected that bigger steps in correlation improvement can still be made by well considered local refinement instead of global refinement. By including more cells in the vortex regions and at the trailing edges of the elements it should be possible to capture the unsteady phenomena and blunt trailing edge vortex shedding better and this could even have an effect on the steady averaged results. The current grids, including the finest, show no signs of unsteady behaviour for the SA turbulence model and the force coefficients converge completely. The GCI values for the wing simulations have been calculated as well; based on the fine grid these are $\text{GCI}_{C_L} = 0.4\%$, $\text{GCI}_{C_D} = 0.6\%$ and $\text{GCI}_{C_{M53mm}} = 0.3\%$.

The relative large correlation difference in the pitching moment (-18.8% compared to -6.3% for the downforce and +2.1% for the drag) shows a clear disadvantage of having to mount the load cell outside the wing model. It is anticipated that a large part of this correlation difference is caused by uncertainty of the pitching moment calibration, because it is difficult to apply a pure load. Furthermore deformation of the (support) structure will have an influence as well via the required translation of the moment. The experimental downforce and drag values are much less sensitive to these. The experimental pitching moment should therefore be considered as a general indication, which still shows consistent behaviour with model and flow changes, but not as an absolute correct value. Overall, the correlation of the force coefficients is satisfactory and has improved compared to Mahon's results. It is expected that the main cause for the difference in $C_L$ and $C_D$ is related to deformation of the experimental wing and general limitations of the computational method. The influence of the support structure, which has been omitted from the CFD, plays a part as well, just like the resulting difference in blockage.

**Turbulence models** After having tested the grid sensitivity for a given turbulence model (SA), the next step in the correlation of the CFD results is to examine the influence of the turbulence model choice for a given grid (using the baseline grid of the previous section). The grid was completely identical for all of the following turbulence model simulations. Some of the results could possibly be improved by adapting the grid to the specific turbulence model application, but for time considerations this has not been implemented within the current research. The results of the turbulence model comparison have been summarized in table 3.4. Purely looking at the force coefficients, it can be concluded that the SA model correlates best with the experimental data; followed by the standard k-$\omega$ and the standard k-$\epsilon$ models. The best drag prediction of all by the realizable k-$\epsilon$ model is most likely only a result of the lower lift induced drag, since this case predicts a lower downforce value than the previous mentioned models.

For a full understanding of the relative performances of the turbulence models it does however not suffice to look at these integral parameters only. A further examination of the on- and off-surface correlation is necessary to reveal whether the correlation is the result of a correct prediction of the flow features or that it is a coincidental combination of several errors. Figure 3.22 shows the chordwise pressure distributions at the centre and at the wing tip for the baseline ride height of $h/c = 0.317$. This figure also includes the experimental data of Mahon, as well as his CFD result with the SA model. At centre span, figure 3.22 (a), the turbulence models perform very similarly from a qualitative perspective. They also all show improvement compared to Mahon's results in predicting the suction values, which is mainly a result of the improved CAD geometry and grid technique. The tip results, figure 3.22 (b), give a more diverse impression, due to differences in the prediction of the tip vortices. The SA and standard k-$\epsilon$ and k-$\omega$ models correlate best with the experimental data, but the RNG k-$\epsilon$, the k-$\omega$ SST and the RSM models predict considerably less suction on the second part of the main element and the first part of the flap. In contrast, the suction on the last part of the flap is widely overpredicted by the k-$\omega$ SST model - leading to the highest pitching moment coefficient of all - and to a lesser extent by the RNG k-$\epsilon$ model.

The behaviour of the k-$\omega$ SST model has been traced back to a large separated zone at the juncture of the suction side of the flap with the endplate (see figure 3.23 (a) and (b) for a presentation of this separation at the juncture for a different case). All turbulence models, except for the RNG k-$\epsilon$, predict a small elongated separated zone in this region, but the k-$\omega$ SST model result shows a much wider zone, which also covers a part of the endplate underneath the flap. The overprediction of the suction at the tip of the flap from $x/c = 0.6$ onwards features a plateau with relatively constant pressure, which is typical for separated flow. The discrepancies in the pressure distribution at the tip for the RNG k-$\epsilon$ and RSM models are the result of vortex breakdown in the simulation results. Both models predict a considerable region of reversed flow at the vortex core underneath the flap. This is reflected in the lower suction on the second part of the main element and the first part of the flap, which is similar to the physics seen in the experiments at lower ride heights in force region (b). The realizable k-$\epsilon$ model is the only other model that shows flow reversal in the vortex core, but at a much smaller scale, which can also be concluded from the limited influence on the pressure distribution. Only the SA model predicts a lower $C_P$ in the vortex core than in the suction peak on the main element, see the $C_P$ global values in table 3.4. This is typical for a strong vortex and the additional vortex strength might explain why the SA model gives the best force coefficient correlation, since the lower edge vortex effect is best predicted (see figure 3.22).

Correlation of the wake profiles, shown in figure 3.24, reveals that all models have improved on the results of Mahon by better prediction of the velocity deficit in the main element wake and by showing a more continuous curve in the wall jet area. The wake velocity deficits and the confluence point between the two wakes are best resolved by the standard k-$\omega$ model, which is in line with the expectations resulting from the turbulence models discussion in section 2.4.7. The SA model performs adequately but is definitely not among the best models when it comes to the wake prediction. The standard k-$\epsilon$ model shows a distinctive velocity deficit at the top of the wall jet region, but it is impossible to judge whether this is more or less realistic than the outcomes for the other models as a result of the previously discussed limitations of the experimental data.

A final aspect that needs to be discussed for the various turbulence models is the convergence behaviour. The SA model is extremely robust and converges completely without any signs of potential problems. The RNG and realizable k-$\epsilon$ models as well as the RSM model were however much more critical and required more effort to converge. For example these cases had to be started from a SA solution and with first order turbulence discretization during the beginning of the simulation. The turbulent viscosity ratio was automatically limited by the solver in a few cells (in the order of a 100) for each of these cases, but without any destabilizing effects. Flow reversal in the vortex core on the pressure outlet was experienced in the RSM solution, indicating that this unphysical boundary condition was not ideal for this turbulence model. Therefore it is anticipated that some of the applied models may perform better after some turbulence model specific grid and solver setting modifications. A few models did also pick up a degree of flow unsteadiness once converged, see the $C_L$ variations in table 3.4 for an indication.

Based on these results it has been decided to continue the isolated wing simulations using the SA turbulence model. The standard k-$\epsilon$ and k-$\omega$ models would be good alternatives, but the robustness and relative low computational cost of the SA makes it preferable. The flow reversal in the vortex core underneath the flap for the RNG, realizable k-$\epsilon$ and for the RSM model is in disagreement with the experimental results for this height and the large separated zone on the flap tip predicted by the k-$\omega$ SST model has not been found in experiments either, making the results of these models questionable for the current grid and solver settings.

### 3.2.4 CFD validation over ride height range

The correlation study at the baseline ride height of $h/c = 0.317$ revealed that the SA turbulence model gives a satisfactory accurate prediction of the force coefficients and flow field. It has been explained that the discrepancy in pitching moment coefficient is a direct consequence of locating the load cell outside the wing model and of the delicate calibration process of the pitching moment component. The next step in analyzing the applicability of CFD to an inverted wing in ground effect problem is to validate the method over the range of ride heights. This would give insight into whether CFD resolves the correct physical phenomena and flow features and additionally into whether these are captured at a similar ride height range as in the experiments. Previously comprehensive studies in 2D have been performed for this problem [8, 11, 12], but to the author's knowledge no other examples of this application to a 3D geometry are available in the literature.

**Grid creation** The grids used for these simulations were based on the baseline grid of the grid sensitivity study. A complete extended grid module was created around the wing, which stretched from the velocity inlet to the pressure outlet and from the symmetry plane to the port side wall. In the vertical direction the block stopped just below the wing geometry and close to the upper boundary. The right height could now relatively simply be varied by extruding a block with grid refinement from the underside of the module towards the ground and a coarse block from the top of the module to the upper domain boundary. The total number of grid cells decreased continuously from 4.0 to 3.3 million, when the wing was lowered from respectively $h/c = 0.634$ to $h/c = 0.042$. The reason for this reduction in grid size is that cells from the fine cell distribution below the wing were replaced by coarse cells at the top of the domain.

Additionally the length of the laminar zones was varied according to the experimental oil flow results of Mahon [12]. His results showed that the transition position on the suction side of the main element remained at $x/c = 0.07$ from the highest ride height until $h/c = 0.099$. From this ride height and downwards transition would take place at $x/c = 0.12$. This relocation of the transition position is a direct consequence of the increasingly preferable pressure gradient upstream of the lowest point, which postpones transition. In a similar way the transition position on the flap stayed at $x/c = 0.54$ for the higher ride heights, whereas it moved downstream to $x/c = 0.56$ for the $h/c = 0.063$ case and lower ride heights. The transition on the pressure side of the main element and flap is kept constant throughout the ride height domain at $x/c = 0.03$ and $x/c = 0.53$ respectively, as discussed by Mahon.

**Force coefficients** The variation of the computational force coefficients with ride height is presented in figures 3.25, 3.26 and 3.27. The experimental curves are included in these figures for reference, as well as a new division in force regions from $A$ to $E$. These new regions are more illustrative to discuss the differences in results between experiments and CFD. Region $A$ runs from the highest ride height of $h/c = 0.634$ until $h/c = 0.317$. The force coefficients do no longer converge asymptotically from this height downwards till $h/c = 0.158$ and vary erratically within a certain range (see figure 3.28 (b)). In this region $B$ the average values are presented as the main curve, whereas the upper and lower boundary of the variation in force coefficients are visualized with error bars and with respectively a green and a red curve. The next region, $C$, reaches till the global maximum in downforce at $h/c = 0.106$. Region $D$ continues till the kink in the downforce and moment curve, which coincides with the change in direction of the drag curve, at $h/c = 0.070$. Finally region $E$ covers the lowest ride heights until $h/c = 0.042$.

The simulations for varying ride height showed three different types of convergence behaviour. In region $A$ the residuals drop continuously for about four orders of magnitude and then level off within a range as can be seen in figure 3.28 (a); the force coefficients grow asymptotically towards a completely converged value. Region $B$ shows the previously discussed alternative convergence behaviour with varying force coefficients. Interestingly, figure 3.28 (b) reveals that the residuals first seem to converge before they suddenly start growing again. This is almost as if the flow approaches a solution, which is no longer sustainable from a certain condition onwards. The remaining regions for the lower ride heights converged completely once more, although a kink in the convergence rate can be distinguished in figure 3.28 (c) at a similar number of iterations as where the residuals started growing again in region $B$. The force coefficients reach their final value in an asymptotic way, like in region $A$, but this time the drag and pitching moment coefficients first overshoot the value and then decrease towards the final value. No unstable divergence problems of the residuals were observed with these SA simulations, but the flow field had to be initialized with a higher turbulent viscosity ratio for the lowest three regions - after the strange convergence in region $B$ - to achieve this.

The relative differences between the CFD and experimental force coefficients are presented in figure 3.29 for further analysis. These relative differences are defined as the difference between the computational value and the experimental value, normalized by the experimental value. Both the experimental and the computational force region boundaries are visualized in this figure as well. This figure is very useful in analyzing how well the downforce enhancing and limiting mechanisms are resolved in the CFD solutions and whether they appear at the correct ride height. The downforce curve shows, remarkably, that the relative difference remains constantly around 6% through region $A$ and the beginning of region $B$, if the upper boundary curve is followed, until the experimental downforce reaches a local maximum in region $b$. This indicates that the governing mechanisms are similar in the experiments and in the computations, whereas the offset difference under these circumstances can be explained with a constant discrepancy between the experimental or computational approach, such as a different geometry, blockage[15], calibration, or test conditions. From $h/c = 0.236$ down to $h/c = 0.070$ the relative difference disappears almost completely, however it reappears for the lowest ride heights at the constant level of 6%. This is a revealing sign showing that the governing mechanisms are not captured in the same way in the intermediate period.

The relative difference in drag actually decreases with ride height reduction in region $A$. It is anticipated that this is caused by deformation of the model, as it is expected that unwinding of the experimental wing[16] will have a larger influence on the drag then on the downforce. The shape of the pitching moment curve is almost an exact copy of that of

---

[15] The wheel CFD results also showed an underprediction of the general flow velocities and this could indicate an effect due to the blockage difference between the experiments with support structures and the CFD without them.

[16] Unwinding in the form of a tail downwards rotation of the flap and endplates; because the main element is stiffly supported by the pillars its orientation will change less.

the drag curve, which clearly shows that the translated drag component is dominant in the pitching moment representation. This implies that the pitching moment curve can in general be explained with the use of the same arguments as the drag curve. As a side remark, it is interesting to see that the global minimum $C_P$-value occurs in the vortex core for the cases from $h/c = 0.387$ till 0.095, whereas above and below this region it appears on the main element surface.

**Flow phenomena and mechanisms** Analysis of the flow features per force region, as captured by the CFD simulations, revealed the following:

- The channeling effect is captured accurately as can be concluded from the constant relative difference in downforce coefficient in region $A$. The computational centre span pressure distributions for various ride heights in figure 3.31 (a) provide proof of this by showing that the suction peak becomes larger and thus that the flow velocity in the channel increases for ride height reduction. Furthermore the differences between the experimental and computational pressure distributions remain relatively constant as well, except for at the lowest presented ride height, which indicates an accurate simulation of the channeling effect.

- The lower edge vortex effect seems to be resolved equally well considering the same data for region $A$. Of course it is possible that one of these two mechanisms is underpredicted while the other is overpredicted in this force region, however the constant level of the relative difference between the computational and experimental data shows that the rate of change of both mechanisms with ride height variation is still captured accurately. Therefore it is expected that the effect of both mechanisms themselves is predicted accordingly.

- Dilution of the lower edge vortex starts in region $B$. The dilution seems stronger for solutions close to the red boundary curve than for those close to the green boundary curve (see the following discussion on page 112). Nevertheless the magnitude of the dilution and its influence on the on-surface pressure distribution is in general underpredicted, despite having given the best correlation of this aspect for the various turbulence models. This can be concluded from the fact that this mechanism starts in region $b$, which is exactly where the constant relative difference in the downforce changes and diminishes. This shows that there is more downforce reduction in the experimental than in the computational results. A reason for this could be that the CFD does not predict flow reversal in the vortex core until $h/c = 0.158$ - at the end of region $B$ - so the predicted dilution is not coupled to downstream vortex breakdown, as in the experiments. It is expected that the underprediction of this mechanism is the main cause of the change in relative difference over the following regions.

- Separation on the inside of the endplate is captured by the CFD in region $B$. This feature also affects the tips of the flap because the recirculation zone from the endplate touches on the suction surface of the flap, see figure 3.23 (a) and (b). A similar separated zone can be distinguished as a topological focus point in the experimental oil flow picture of figure 3.20 (b). Overprediction of this separation by the CFD, especially for the solutions on the upper (green) boundary in region $B$, is the reason for the increase in relative drag difference in figure 3.29. The sudden decrease in relative difference at the end of region $B$ results from the disappearance of this separation.

- Separation at the trailing edge of the main element, gradually moving upstream along the suction side with decreasing ride height, can be found in region $E$, see figure 3.32 (a). However the flap element does not experience the large scale flow separation that was discovered for the increasing ride height experiments in region $f$. Since the relative difference in downforce returns to the level of region $A$ and stays on this level in region $E$, it is likely that the extent of the trailing edge separation on the main element is accurately captured.

- Lower edge vortex burst with reversed flow zones, see figure 3.32 (a), exists in regions $C$, $D$ and $E$. The recirculation zone grows in size with decreasing ride height and connects to the inside of the endplate for the two ride heights below $h/c = 0.060$. This is at a lower ride height than in the experiments, because figure 3.20 (b) shows the imprint of the reversed flow in the oil flow on the endplate at $h/c = 0.099$. The CFD results give the impression that the behaviour in region $C$ can still be classified as downstream vortex breakdown, whereas in region $D$ the vortex burst phenomenon takes place, which directly influences and limits the downforce production as in experimental force region $d$. The reversed flow zone in the CFD starts at $x = 210mm$ for the $h/c = 0.158$ case and at $x = 148mm$ for $h/c = 0.106$, while the trailing edge of the main element is located at $x = 140mm$. This indicates that the vortex burst has to be close to the main element before it starts affecting the downforce.

> Since the linear growth in downforce in region $C$ is smaller for the CFD than in the experiments (see figure 3.25) and since the decay in region $D$ is more severe than in the experiments, it is expected that the influence of this downforce limiting mechanism is overpredicted in CFD. This can also be concluded from the general growth in relative downforce difference in region $C$ and $D$. The relative constant level of downforce in region $d$ shows that the channeling effect and vortex burst effect are balanced in the experiments over this region, however in the computations the vortex burst effect dominates.

Two more issues need to be addressed in order to conclude the validation of the CFD simulations for the wing in ground effect. These are the convergence behaviour in region $B$ and the hysteresis effects in the experiments, which are not reproduced in the computations.

**Convergence behaviour** It is revealing to compare two solutions at different stages of the convergence process for a height of $h/c = 0.211$ in region $B$. One solution is obtained after 1500 iterations, around the time when the rise in residuals starts, while the other is selected at 12500 iterations after the residuals have settled at the higher level, see figure 3.28 (b). The downforce has been reduced by 0.7%, the drag increased by 1.9% and the pitching moment has grown by 1.8% for the second case, compared to the first. The force coefficients increase and decrease synchronously in the second convergence region, as can be concluded from the detail insert in the right figure of 3.28 (b). This implies that a rise in downforce is always accompanied by a rise in drag and pitching moment and thus that a solution close to the green downforce boundary in figure 3.25 will also be relatively close to the green boundaries of the drag and pitching moment figures.

Strictly speaking the low iteration result can not be labeled as a physical solution, because the continuation of the simulation showed that it was unsustainable. However comparing the flow features of the 1500 and 12500 iterations cases could reveal more about the physics of the flow problem. It is fascinating to see that the red boundary curves seem to be smooth continuations of the drag and pitching moment curves, whereas the downforce curve seems to fit better with the green boundary curve. Furthermore it can be observed that if the CFD force coefficients would follow the green curve up to the local maximum in region $b$ at $h/c = 0.222$ and subsequently would drop to the level of the red curve, then this would mean that the qualitative behaviour of the computational force coefficients is similar to that of the experimental results.

Figure 3.23 presents various aspects of the flow fields to get a better insight into the differences between the solutions at the two convergence stages. A comparison of the two top figures shows that the separated zone on the endplate and the tip of the flap suction side has increased considerably from the 1500 to the 12500 iterations case, now reaching all the way to the bottom of the endplate. Furthermore the difference in $C_P$ between the two cases has been visualized in figure 3.23 (c) , which reveals that the pressures in the imprint area of the vortex on the endplate are higher for the 12500 iterations case. This indicates that the vortex velocities are lower during the second stage of the convergence and indicate that dilution of the lower edge vortex takes place in a similar way as in the experiments. The chordwise pressure distributions along the elements are also included in figure 3.31. At centre span there is hardly any difference between the two cases, but the effects of the weaker vortex and larger separation zone are clearly visible at the tip. The pressure distribution on the tip of the flap is actually quite similar to that for the k-$\omega$ SST turbulence model. With this information available it can now be concluded that this turbulence model did thus not simulate an incorrect flow field, but captured flow phenomena that should only have been present at lower ride heights.

In summary it is therefore assumed that in force region $B$ two flow solutions can occur depending on the magnitude of the adverse pressure gradient. The convergence process could then be described as follows: the flow field converges towards a solution on the green boundary curves, but the adverse pressure gradient grows along as well and at some point becomes too adverse for the flow field. The separation from the endplate takes on a larger scale and the vortex dilutes more as well. However the effect of this on the pressure distribution is that the pressure gradient reduces and thus that the separation and vortex dilution decrease again. This interaction causes the convergence instability that is experienced in force region $B$. The solutions within the converged zone of region $B$ do not necessarily combine the largest dilution of the lower edge vortex with the biggest separation from the endplate; some trade-off seems to take place depending on which mechanism is stronger at the beginning of the next convergence cycle.

The decrease in downforce for the 12500 iterations case can be explained by the reduction in suction on the second part of the main element and on the first part of the flap at the tip, which overrules the increase in suction due to the recirculation in the separated zone. The extra drag is caused by the additional suction in the separated recirculation zone on the flap, whereas the pitching moment increase is mainly affected by the large moment arm of the increased suction on the flap in the separated zone. Since the drag is more influenced by these force limiting mechanisms than the downforce is, it is expected that the vortex dilution is underpredicted but that the extent of the endplate separation is overpredicted. The loss of a unique converged solution in region $B$ is most likely caused by the steady solver having to cope with intrinsic unsteady physics related to the vortex dilution and downstream breakdown.

**Hysteresis effects** Finally, the experiments show hysteresis effects for the lowest ride heights, where the force coefficients depend on the direction in which the ride height changes. The difference between the increasing branch (region $f$) and the decreasing branch (region $e$) is caused by centre span separation on the flap element, which seems only to occur for the first case. Mahon [12] did not perform oil flow visualization for the $h/c = 0.039$ decreasing ride height case. However the downforce curve (see figure 3.25) does not indicate that the flap experiences separation, because the drop in $C_L$ of nearly 0.3, which is typical for the beginning of the hysteresis zone, is not noticeable in the decreasing ride height branch.

The computational cases are initialized with the velocity from the inlet[17], which is the freestream velocity. Flow separation on the flap is not detected for any of the ride heights in the simulations. This implies that the simulations resolve the flow field for the decreasing ride height branch and consequently it is thought unlikely that the currently used computational method (SRANS) and settings could reproduce the increasing ride height branch. Guilmineau et al. [79] have nevertheless showed that it is possible to capture dynamic stall and hysteresis phenomena with the help of unsteady 2D simulations and by imposing an oscillating pitch angle.

Within the hysteresis zone the correlation is not as good as at other ride heights outside the hysteresis zone, as revealed by the pressure distributions in figure 3.31. The centre span suction peak on the main element is underpredicted by 23%, although the experiments have been performed at a marginally lower ride height of $h/c = 0.039$ instead of 0.042. The pressure side and the flap are resolved relatively well at centre span. The pressures at the tip are in better agreement for the suction peak of the main element, but overpredict the suction on the second part of the main element and on the first part of the flap. This shows that the current approach is less accurate in the hysteresis region.

Looking back to the relative differences in force coefficients, it is remarkable that the downforce difference returns to the level of 6%. This indicates that the downforce enhanc-

---

[17] However a test simulation with the flow field initialized at zero velocity converged to exactly the same solution - albeit in a larger number of iterations - as would be expected for a steady simulation.

ing and limiting mechanisms are at least of the same order as in the experiments. The reduction in relative difference of the drag and pitching moment in region $E$ is promising and it can be seen from the force coefficients themselves that the CFD picks up the sudden increase of drag for the lowest ride heights, which is also experienced for the decreasing ride height branch in the experiments. The use of a different turbulence model or solver method, such as DES, could result in a different, better correlation between CFD and experiments, but considering the limitations of the method the SA model has produced satisfactory results over the ride height range.

**Summary** The validation of the CFD method over the ride height range has led to the following conclusions about the prediction of the downforce mechanisms. In general, at a high ride height with little ground effect, the downforce is slightly underpredicted due to underprediction of the suction on the underside of the wing, while the drag is marginally overpredicted. The magnitude of the combination of the channeling effect and the lower edge vortex effect is predicted well within the first computational region. This is until convergence behaviour instability occurs at $h/c = 0.317$. From this ride height downwards to $h/c = 0.158$ vortex dilution (without downstream vortex breakdown) and endplate separation take place. The first effect is underpredicted, while the latter is overpredicted. Nevertheless, if the CFD would converge towards an upper boundary solution for the higher ride heights and would drop to a lower one when the wing height is further reduced, then this would result in a prediction that looks qualitatively similar to the experimental results. The underprediction of the lower edge vortex dilution is the main cause of the discrepancies between the computational and experimental results.

Downstream vortex breakdown starts too late (at $h/c = 0.158$ instead of 0.236), at a lower ride height than in the experiments. However once it occurs, it limits the downforce more severely than in the experiments. Proper vortex burst effects start at a lower ride height as well ($h/c = 0.106$ instead of $h/c = 0.123$) and once again reduce the downforce at a larger rate than in the experiments. Therefore the vortex burst effect is overpredicted in CFD and this is the main reason for the relative difference to return to the same level as for the highest ride heights. Trailing edge separation from the main element starts at a similar height in the CFD compared to in the experiments. The influence of this mechanism is captured accurately, if it is assumed that the CFD predicts the decreasing ride height branch. With the current computational methodology it is not possible to simulate the increasing ride height branch and no centre flap separation is captured for any ride height in accordance with this. The influence of separated regions on the drag is in general overpredicted, leading to a higher relative drag difference at lower ride heights.

### 3.2.5 Discussion of downstream flow field

The reference results analysis will be concluded with a discussion of the wing flow field, focusing on the downstream aspects that will have most influence on the wheel aerodynamics for the combined wing - wheel cases. The main characteristics of the downstream flow field are the trailing vortices and the wake structure, which will be summarized separately in the following paragraphs. The effect of Reynolds number changes on the wing aerodynamics have not been presented in Mahon's thesis [12], therefore appendix C shows new force data over a range of test velocities. The ride height at which hysteresis occurs is dependent on the Reynolds number and moves to higher ride heights for lower test velocities. The effect of downstream vortex breakdown on the wing aerodynamics in force region $b$ is however remarkable constant for a case at approximately 2/3 of the original Reynolds number. The levels of the curves change with Reynolds number, but the variations are less than 3% for the downforce and pitching moment and less than 5% for the drag within a test velocity range from $20 m/s$ to $35 m/s$.

**Vortices** It has been discussed previously that the wing generates two trailing vortices per endplate of which the lower edge vortex is the most prominent. These vortices are visualized in figure 3.32 (b) for the SA CFD solution at $h/c = 0.317$, using iso-surfaces of $Q$. Both vortices rotate in anti-clockwise direction, if observed from a downstream position. Therefore the vortices twist around each other with the upper edge vortex initially moving outwards and downwards and the upper edge vortex moving inwards and upwards in downstream direction. From a certain position onwards the vortices merge (not visualized in the figure) and continue to induce a swirling motion on the wake, which is directed towards the symmetry plane along the ground, then upwards, outwards above the wing and back downwards in the area outside of the port endplate. Another related phenomenon that can be distinguished in figure 3.32 (b) is the creation of a secondary counter-rotating vortex from the ground boundary layer. This is in line with the research by Harvey et al. [87], which was discussed in the literature review, and causes the rebounce of the merged vortex pair away from the ground.

The characteristics and the existence of the trailing wing vortices depend on the wing ride height. For the higher ride heights until force region $b$, the appearance is very similar to the previous description. The main change is that the creation of the secondary vortex obviously moves upstream with reducing wing ride height, while the lower edge vortex is displaced towards the symmetry plane as can be deduced from table 3.5. The size of the lower edge vortex increases in region *b* due to the downstream vortex breakdown and the velocity deficits grow as well. The vortex breakdown moves upstream for continuing ride height reductions and leads to complete vortex bursting from region *c* onwards. From then on the wake no longer consists of the two vortex pairs, as the lower edge vortices are replaced by small scale vorticity separated recirculation zones. The upper edge vortex is swallowed by these zones at some downstream location and the secondary vortices cease to exist as well at such a height, because the burst lower edge vortices no longer induce the large peak adverse pressure gradients.

**Wake** The boundary layers on the endplate are entrained into the wing vortices, however those from the wing elements separate from the trailing edges into free shear layers with reduced total pressure and velocity compared to the undisturbed flow. The extent of these zones at centre span can be derived from the figures 3.16 and 3.30, which show respectively the experimental and computational results. The size of the flap wake stays relatively constant with ride height, just like the velocity deficit in this zone. It is only at lower ride heights - just before the flap and main element wakes merge - that the deficit decreases slightly and that the velocity in the confluence point between the wakes reduces as well. This is all part of the transformation process into a single wake. The merging of the wakes for the increasing ride height branch is the result of the flow separation from the centre of the flap. However the CFD, see figure 3.30, indicates that merging also takes place without flap separation, if the wing is low enough. It can be imagined that this happens when the main element wake comes too close to the ground and expands upwards.

The main element wake on the other hand grows in size with wing ride height reduction, whereas the velocity deficit in the main element wake increases as well. The difference in influence of the ride height on the flap and on the main element wake can be explained from the fact that the main element downforce increases significantly with ride height reductions, whereas the flap loading increases only slightly. The growth of the main element wake is restricted at the upper boundary due to the higher energy flow through the flap gap above it. Therefore the main element wake expands towards the ground by lowering the lower boundary, as can be seen in figure 3.16. The flow between the main element wake and the ground increases in velocity with reducing wing ride height. This is a direct consequence of the wall jet flow underneath the wing and of the increased blockage due to the expanding wake. The CFD simulations in figure 3.30 show a similar flow acceleration in the zone above the wake for the lowest ride heights, due to the increased blockage.

The flow field around the wing is characterized by several areas with reversed flow, but most of them[18] will not directly influence a downstream positioned wheel. At centre span hardly any flow reversal is expected to take place in the wing wake downstream of the wing, as can be derived from the experimental results in figure 3.16 (a). Even when the flow separates completely from the flap, in region $f$ for the increasing ride height branch, then still does the part of the wake with flow reversal end within $35mm$ from the trailing edge of the endplate, see figure 3.15 (d). Whenever the wheel is placed downstream of the wing, it will therefore not be subjected to reversed flow regions resulting from the element wakes. However the reversed flow zones at the wing tips due to the burst lower edge vortices at lower ride heights, see figure 3.21, would be immediately upstream of the wheel and it could be that these zones do have an effect on the wheel aerodynamics.

---

[18] For example an area of reversed flow exists at the outside of the endplate, where flow separation takes place from the leading edge, but this flow reattaches to the outside of the endplate fairly quickly for all of the ride heights, see figure 3.32 (a).

| Case | $C_D$ | $C_L$ | Stagnation | Separation | $C_{Pmax}$ | $C_{Pmin}$ |
|---|---|---|---|---|---|---|
| Experimental (Exp) | 0.623 | - | 5.6° ±0.5° | 275° | 2.10 | -1.25 |
| Exp, stationary | 0.711 | - | - | - | - | - |
| Coarse | 0.579 | -0.0906 | 5.6° ±1.4° | 277.5° | 3.596 | -2.136 |
| BaseLine (BL) | 0.582 | -0.0910 | 4.7° ±1.2° | 278.0° | 3.602 | -2.215 |
| Fine | 0.576 | -0.0925 | 6.0° ±1.0° | 278.5° | 3.655 | -2.330 |
| ACFD | 0.575 | -0.096 | 5.3° ±2.9° | 275° | 1.03 | -0.77 |
| Realizable k-$\epsilon$ | 0.499 | -0.128 | 4.7° ±1.2° | 265° | 3.59 | -2.42 |
| k-$\omega$ SST | 0.528 | -0.126 | 4.7° ±1.2° | 275° | 3.63 | -2.10 |
| DES | 0.572 | -0.064 | 4.7° ±1.2° | 275° | 3.30 | -2.08 |
| Stationary | 0.634 | -0.579 | 4.7° ±1.2° | 235° | 0.95 | -0.48 |
| Road only, no wind | - | - | - | - | 2.97 | -1.78 |

Table 3.1: Results for the isolated wheel; experimentally and from CFD (all others). The grid sensitivity results are all obtained with SA turbulence model. The $C_{Pmax}$ and $C_{Pmin}$ values are extracted from the centreline pressure distributions and are not necessarily the global extremes, the stagnation and separation locations are for the centreline as well. In the stationary case both the road and the wheel were kept stationary, whereas in the road only case the road was moving and the wheel rotating but the wind was off. These last two cases use the same SA SRANS solver settings and grid as the BL case.

| | $C_D^s$ | | | | | $C_L^s$ | | | | |
|---|---|---|---|---|---|---|---|---|---|---|
| Case | P1 | P2 | P3 | P4 | P5 | P1 | P2 | P3 | P4 | P5 |
| Exp | 1.04 | 0.45 | -0.07 | 0.77 | -0.11 | -0.70 | -0.04 | 0.05 | -0.18 | 0.00 |
| Coarse | 1.01 | 0.55 | -0.10 | 0.72 | -0.04 | -0.51 | 0.24 | 0.05 | -0.01 | 0.02 |
| BL | 1.02 | 0.55 | -0.11 | 0.72 | -0.04 | -0.51 | 0.24 | 0.04 | -0.01 | 0.02 |
| Fine | 1.02 | 0.54 | -0.10 | 0.72 | -0.04 | -0.49 | 0.24 | 0.04 | -0.02 | 0.02 |
| DES | 1.04 | 0.57 | -0.12 | 0.70 | -0.04 | -0.56 | 0.25 | 0.06 | 0.04 | 0.03 |
| ACFD | 1.00 | 0.51 | -0.12 | 0.73 | -0.06 | -0.46 | 0.21 | 0.06 | -0.04 | 0.03 |

Table 3.2: Sectional wheel force coefficients for the isolated wheel for each of the pressure sensor locations via integration of the pressure distributions.

| Isolated wing at $h/c = 0.317$ | | | | | | |
|---|---|---|---|---|---|---|
| Grid | Cells | $C_L$ | $C_D$ | $C_{M53mm}$ | $C_P$ ME | $C_P$ global |
| Coarse | 2692719 | 1.8615 | 0.26030 | -0.29566 | -4.98 | -4.98 |
| Baseline (BL) | 3843790 | 1.8661 | 0.25925 | -0.29554 | -4.98 | -5.24 |
| Fine | 5918712 | 1.8699 | 0.25859 | -0.29587 | -5.02 | -5.41 |
| Experimental (Exp) | - | 1.991 | 0.2539 | -0.3639 | -5.35 | - |

Table 3.3: CFD results for the isolated wing at $h/c = 0.317$ with three different grid sizes, using baseline settings and conditions and SA turbulence model; $C_P$ ME is the maximum suction on the main element, $C_P$ global is in the whole flow domain.

| Isolated wing at $h/c = 0.317$ | | | | | | |
|---|---|---|---|---|---|---|
| Turbulence model | $C_L$ | $C_D$ | $C_{M53mm}$ | $C_P$ ME | $C_P$ global | $C_L$ variation |
| Spalart Allmaras | 1.866 | 0.2593 | -0.2955 | -4.98 | -5.24 | 0 |
| Standard $k-\epsilon$ | 1.816 | 0.2605 | -0.2886 | -4.79 | -4.79 | 0 |
| RNG $k-\epsilon$ | 1.737 | 0.2636 | -0.2856 | -4.57 | -4.57 | ±0.003 |
| Realizable $k-\epsilon$ | 1.798 | 0.2585 | -0.2848 | -4.78 | -4.78 | 0 |
| Standard $k-\omega$ | 1.846 | 0.2622 | -0.2942 | -4.91 | -4.91 | ±0.008 |
| $k-\omega$ SST | 1.837 | 0.2610 | -0.2982 | -4.88 | -4.88 | ±0.025 |
| RSM | 1.786 | 0.2624 | -0.2876 | -4.71 | -4.71 | ±0.001 |
| Experimental (Exp) | 1.991 | 0.2539 | -0.3639 | -5.35 | - | - |

Table 3.4: CFD results for the isolated wing at $h/c = 0.317$ with different turbulence models; $C_P$ ME is the maximum suction on the main element, $C_P$ global is in the whole flow domain, $C_L$ variation shows how much the downforce coefficient still varies for the converged solution.

| | Lower Edge Vortex | | | | Upper Edge Vortex | | | |
|---|---|---|---|---|---|---|---|---|
| $h/c$ | $A_v$ $(mm^2)$ | $\Gamma$ $(m^2/s)$ | $y^*$ $(mm)$ | $z^*$ $(mm)$ | $A_v$ $(mm^2)$ | $\Gamma$ $(m^2/s)$ | $y^*$ $(mm)$ | $z^*$ $(mm)$ |
| 0.317 | 316 (201) | 2.22 (1.81) | 24 (24) | 6 (3) | (188) | (0.96) | (-20) | (99) |
| 0.247 | 1341 | 3.36 | 28 | 8 | NA | NA | NA | NA |
| 0.211 | 2137 (2527) | 3.08 (3.71) | 34 (36) | 12 (9) | (172) | (0.91) | (-20) | (99) |
| 0.176 | (3344) | (3.73) | (43) | (9) | (175) | (0.90) | (-19) | (99) |
| 0.141 | 1678 | 1.73 | 43 | 2 | 159 | 0.83 | -19 | 108 |
| 0.099 | 1156 | 0.91 | 50 | 5 | 156 | 0.75 | -17 | 109 |
| 0.063↓ | 970 | 0.53 | 74 | 8 | 181 | 0.74 | -18 | 112 |
| 0.063↑ | 874 | 0.70 | 13 | 5 | 182 | 0.73 | -17 | 112 |
| 0.039↓ | 1090 | 0.59 | 61 | 11 | 206 | 0.74 | -18 | 115 |

Table 3.5: Experimental vortex characteristics in the plane $x/c = 0.995$ for a range of ride heights; area of the vortex core ($A_v$) as a measure of the size, determined as the maximally connected area with the $\lambda_2$-criterion [82], and circulation in this area $\Gamma$ as a measure of the strength; the location is expressed in $y^*$, which is the distance from the inside of the endplate towards the symmetry plane, and $z^*$, which is the distance from the lowest point of the main element upwards; data in brackets is new PIV data, all other data from Mahon [12]; presented lower and upper vortex are on the port side of the wing.

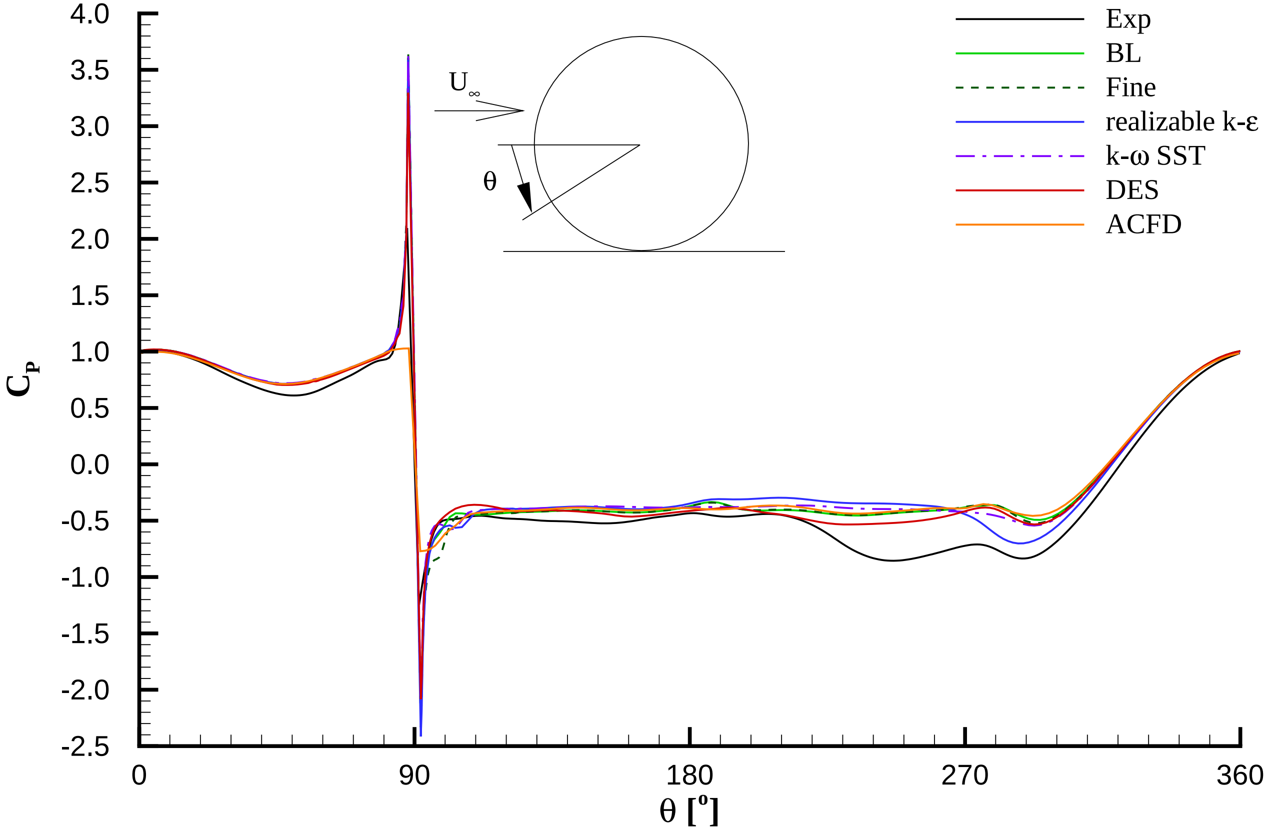

Figure 3.1: Pressure distribution around the centre of the isolated wheel, location P1, from experiments and various CFD cases.

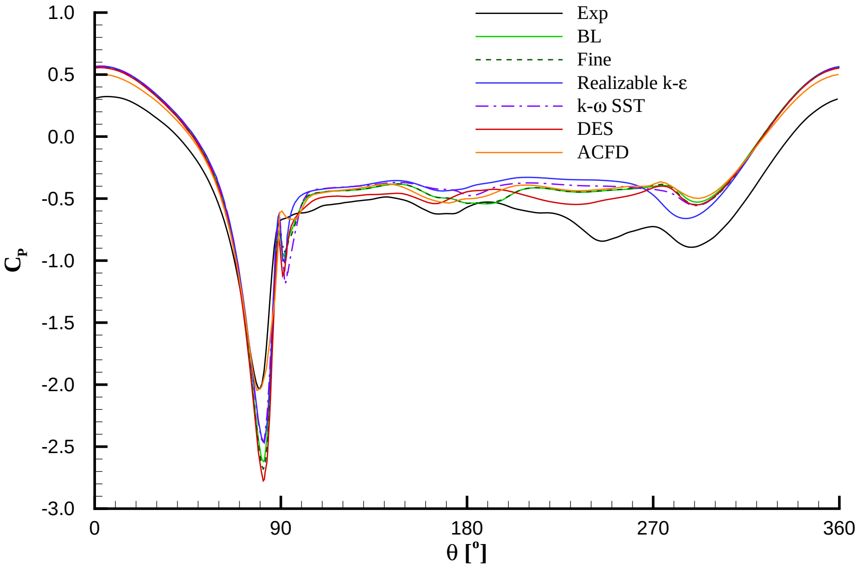

Figure 3.2: Pressure distribution around the outside contact patch of the isolated wheel, location P2, from experiments and various CFD cases.

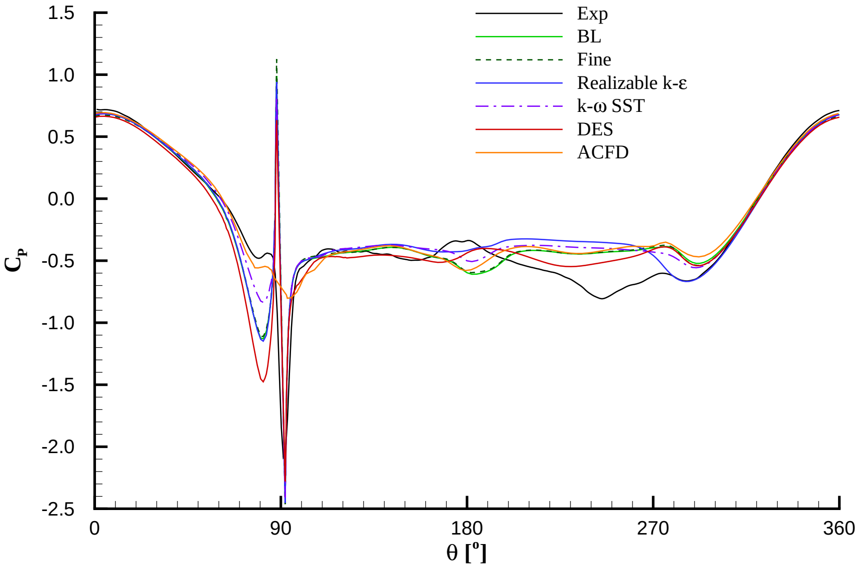

Figure 3.3: Pressure distribution around the inside contact patch of the isolated wheel, location P4, from experiments and various CFD cases.

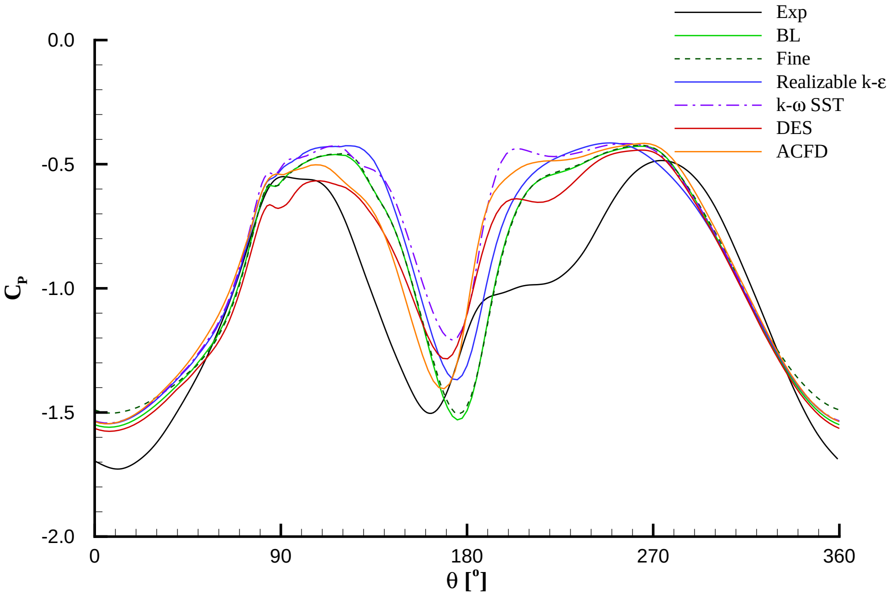

Figure 3.4: Pressure distribution around the outside side wall of the isolated wheel, location P3, from experiments and various CFD cases.

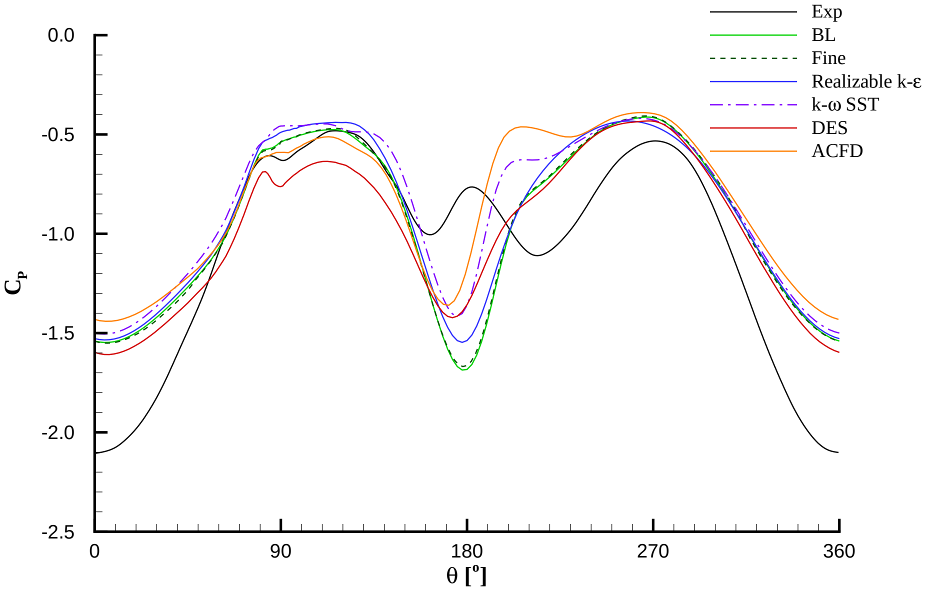

Figure 3.5: Pressure distribution around the inside side wall of the isolated wheel, location P5, from experiments and various CFD cases.

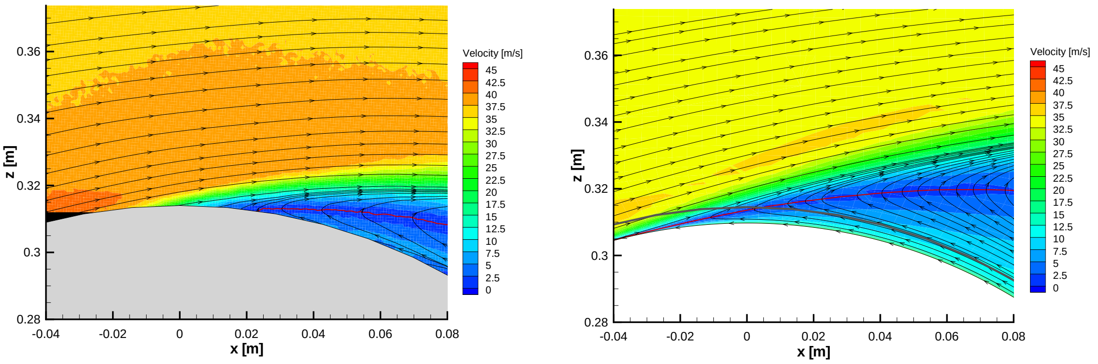

(a) Top of the wheel, vertical streamwise plane, $y = -0.353m$.

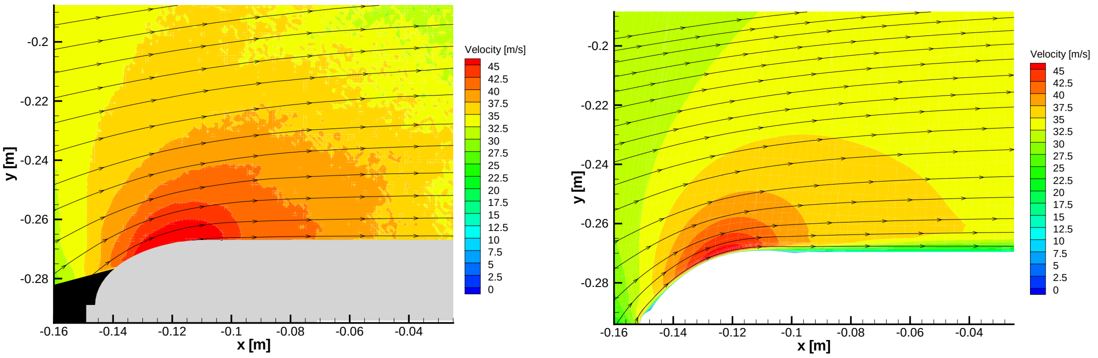

(b) Upstream corner of the wheel, horizontal streamwise plane, $z = 0.165m$.

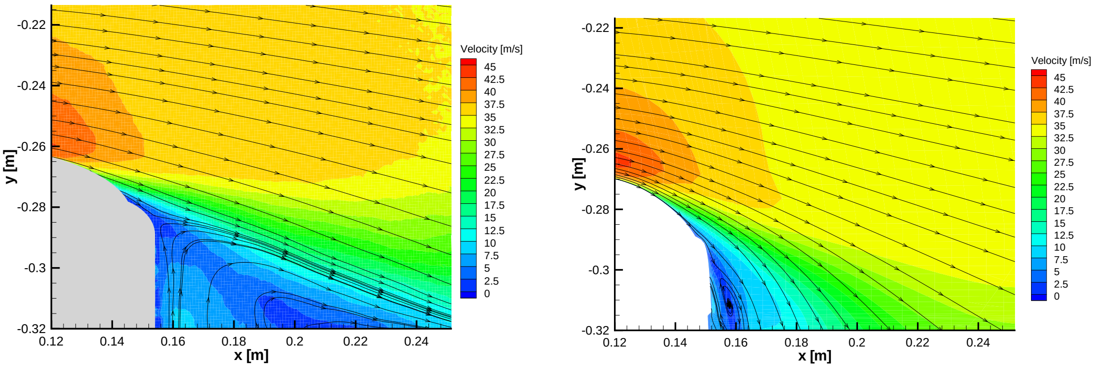

(c) Downstream corner of the wheel, horizontal streamwise plane, $z = 0.174m$.

Figure 3.6: Comparison of PIV (left) and CFD flow field (right) for the port side isolated wheel; CFD results from the BL SA RANS simulation; $x$-position of origin at wheel axis; red lines in figure (a) represent $U = 0$-curves.

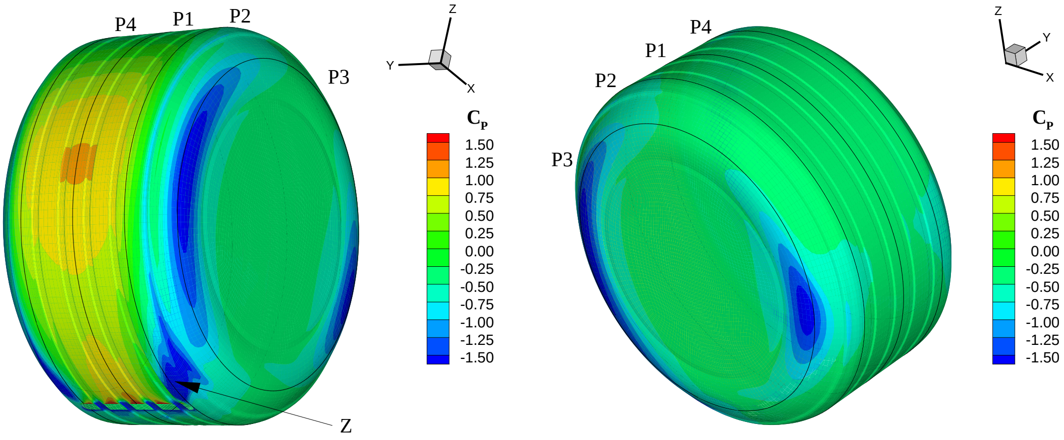

Figure 3.7: Pressure contours on the isolated wheel surface from the BL SA RANS simulation; the extracted pressure sensor location distributions are denoted P$i$ and visualized as black curves.

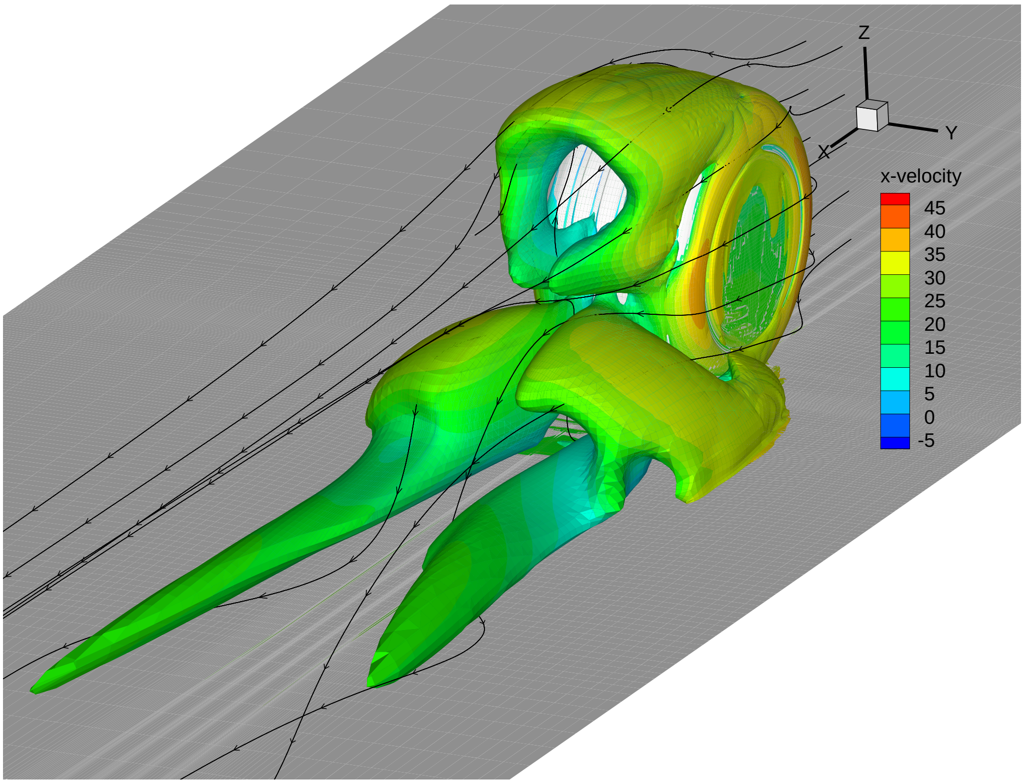

Figure 3.8: Spatial representation of the isolated wheel flow based on an iso-surface of non-dimensionalized $Q$ (value $\bar{Q} = 1$) coloured by the velocity in $x$-direction and streamtraces as vectors; results from the BL SA RANS simulation.

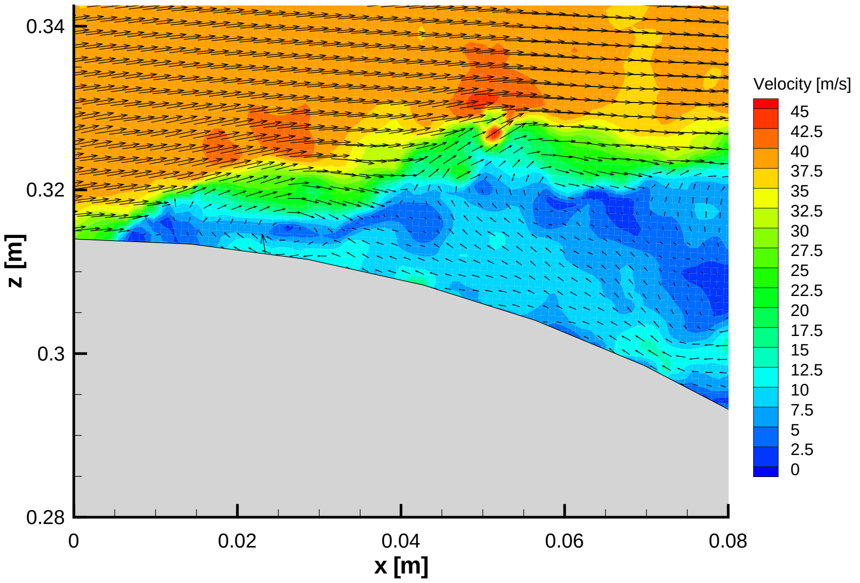

Figure 3.9: Instantaneous velocity contours and vectors over the top of the isolated wheel, vertical streamwise plane, $y = -0.353m$; $x$-position of origin at wheel axis location.

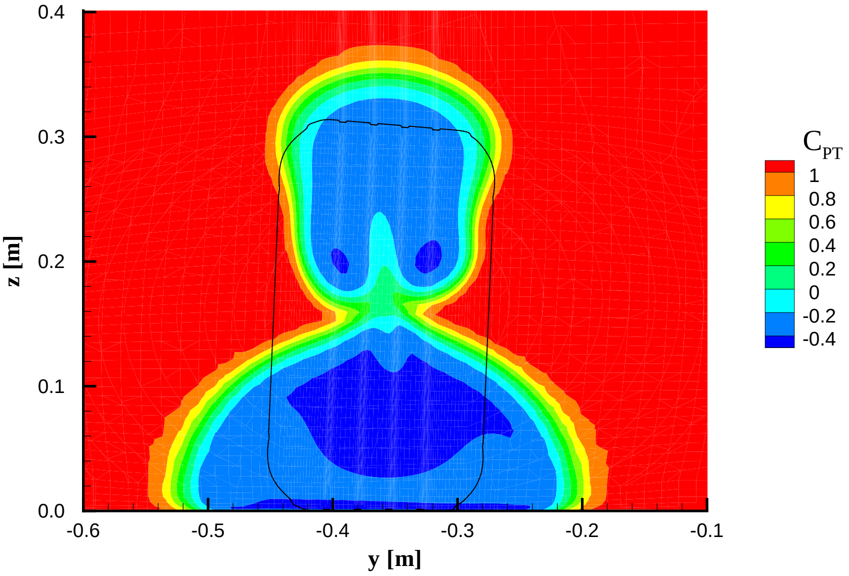

Figure 3.10: Contours of total pressure coefficient in the isolated wheel wake at $x = 0.2m$ from the BL SA RANS simulation, the black curve represents a projection of the wheel contour.

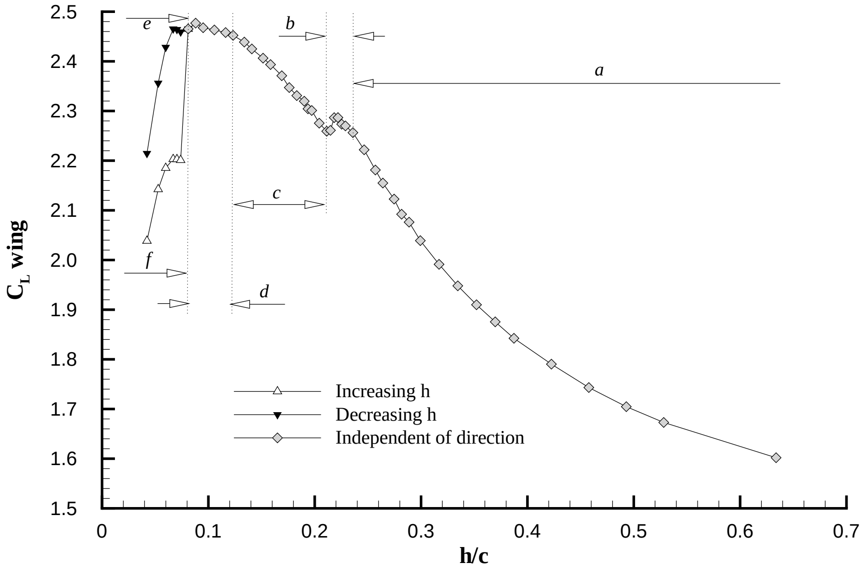

Figure 3.11: Variation of experimental downforce coefficient with ride height and definition of the experimental force regions for the isolated wing.

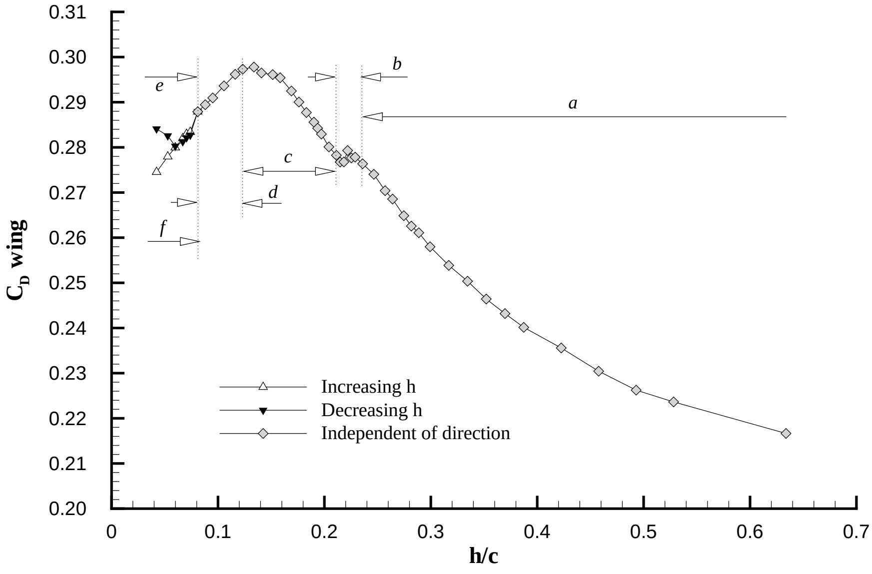

Figure 3.12: Variation of experimental drag coefficient with ride height for the isolated wing.

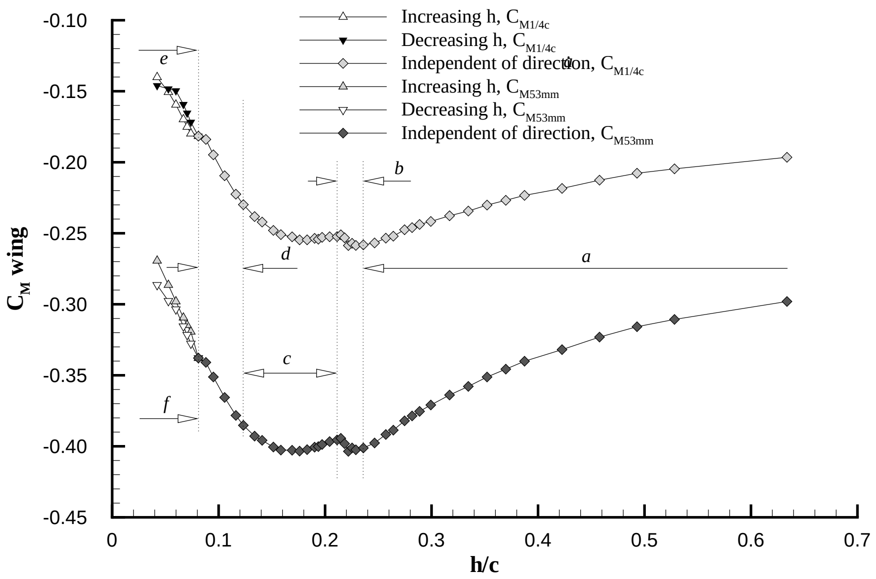

Figure 3.13: Variation of experimental pitching moment coefficient with ride height for the isolated wing; resolved around $1/4c$-point at $x = 71mm$ and around $x = 53mm$.

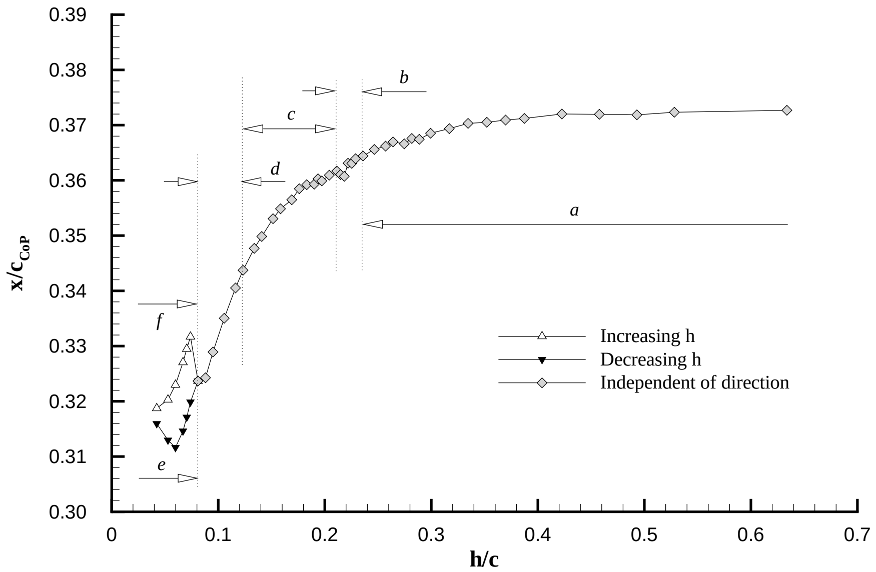

Figure 3.14: Variation of the experimental centre of pressure location with ride height for the isolated wing.

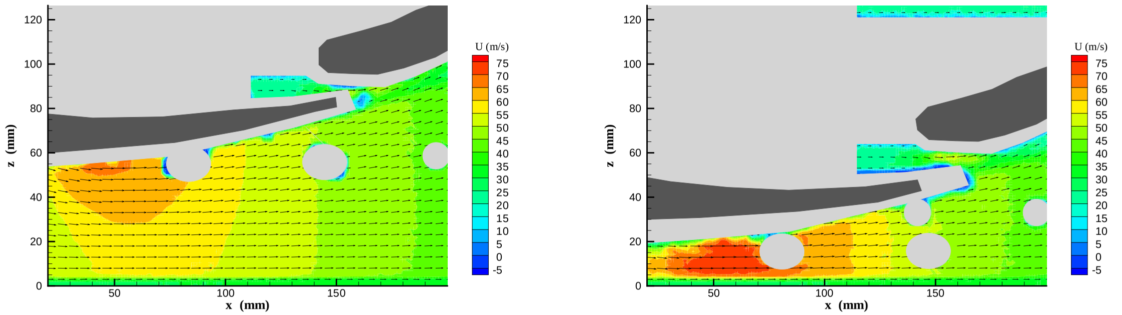

(a) $h/c = 0.211$, boundary of $b$ and $c$.

(b) $h/c = 0.106$, region $d$.

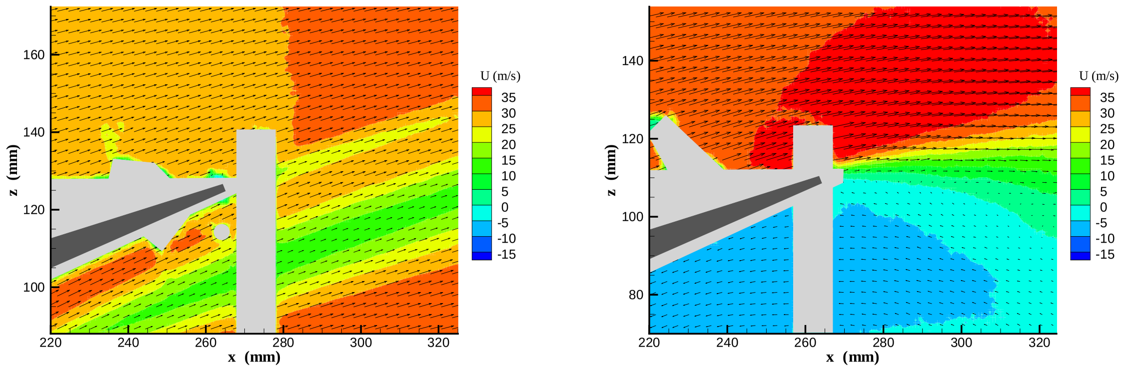

(c) $h/c = 0.106$, region $d$.

(d) $h/c = 0.035$, region $f$.

Figure 3.15: Centre span $x$-velocity contours and vectors downstream of the main element underneath the flap (a and b) and at the flap trailing edge (c and d); flow from left to right, showing the elements (dark grey; no exact representation) and blanked out areas because of reflections, shadows and parallax effects (light grey), the light grey circles in (a) and (b) are fitting holes for the endplate feet.

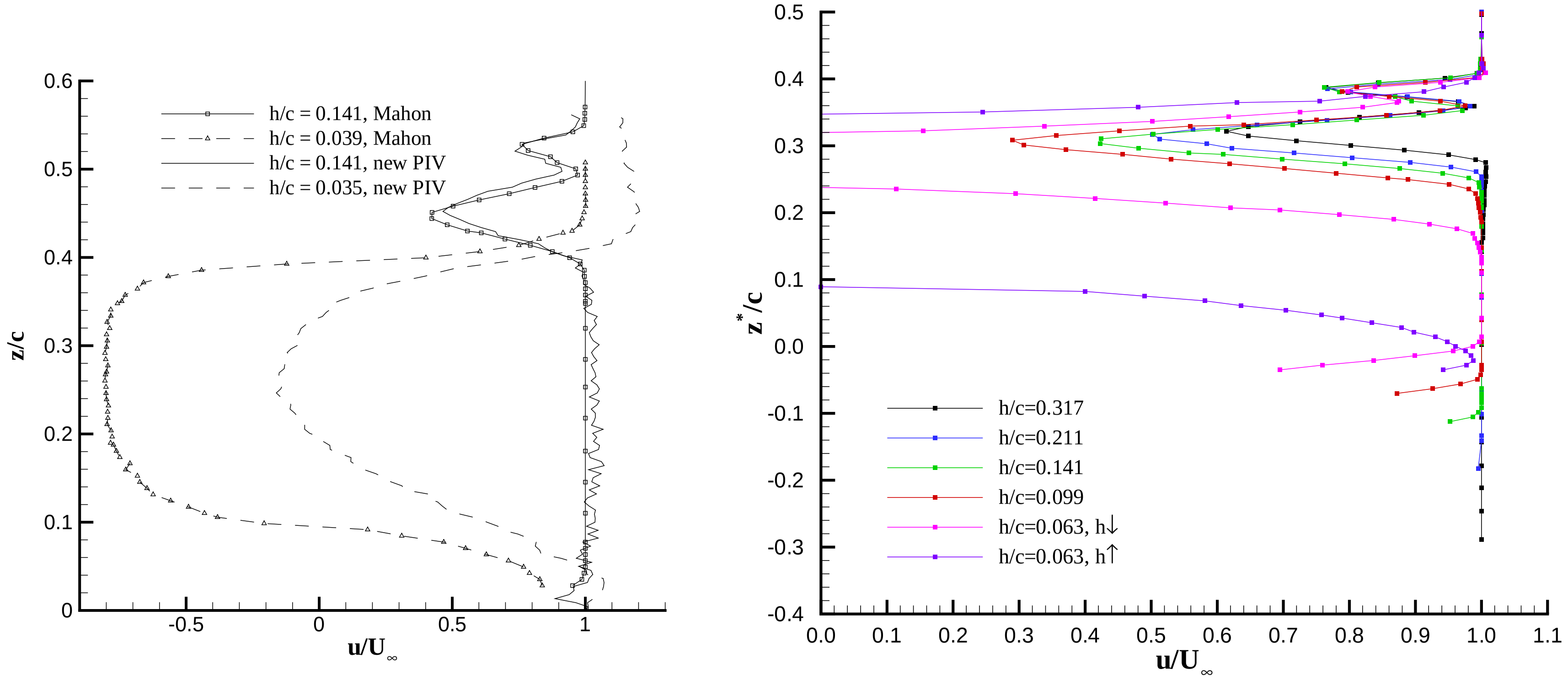

(a) Comparison of new PIV data with Mahon wake rake data.

(b) Wake profiles for various ride heights, data from Mahon [12].

Figure 3.16: Centre span non-dimensional wake profiles of $x$-velocity at $x/c = 1.127$, $47.5mm$ downstream of the trailing edge of the endplate; $z^*$ in (b) is an alternative representation of the vertical coordinate with the origin fixed at the lowest point of the main element - thus being equal to and varying with the ride height.

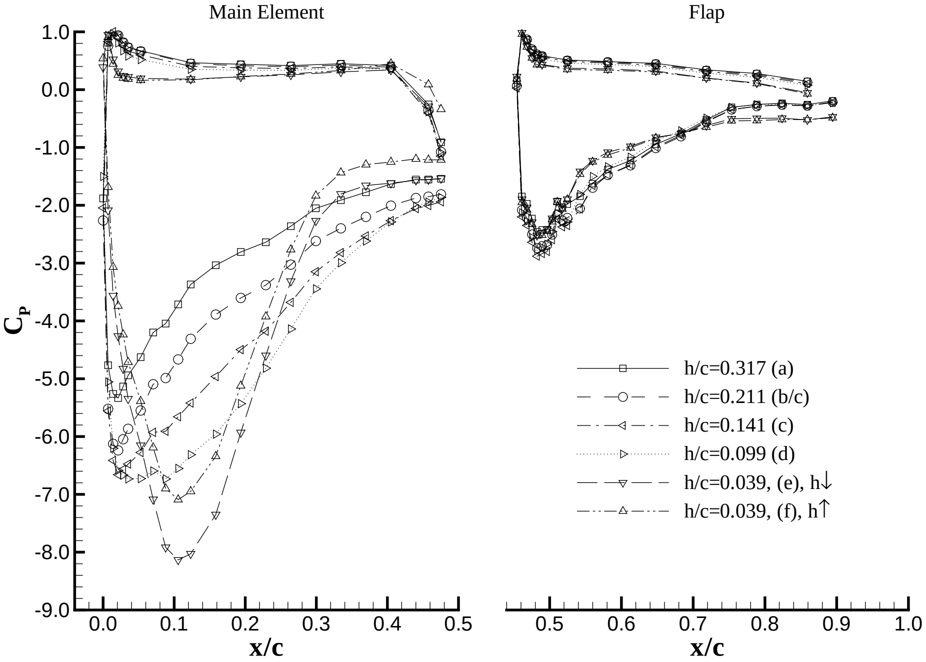

(a) Centre span, $y/c = 0$.

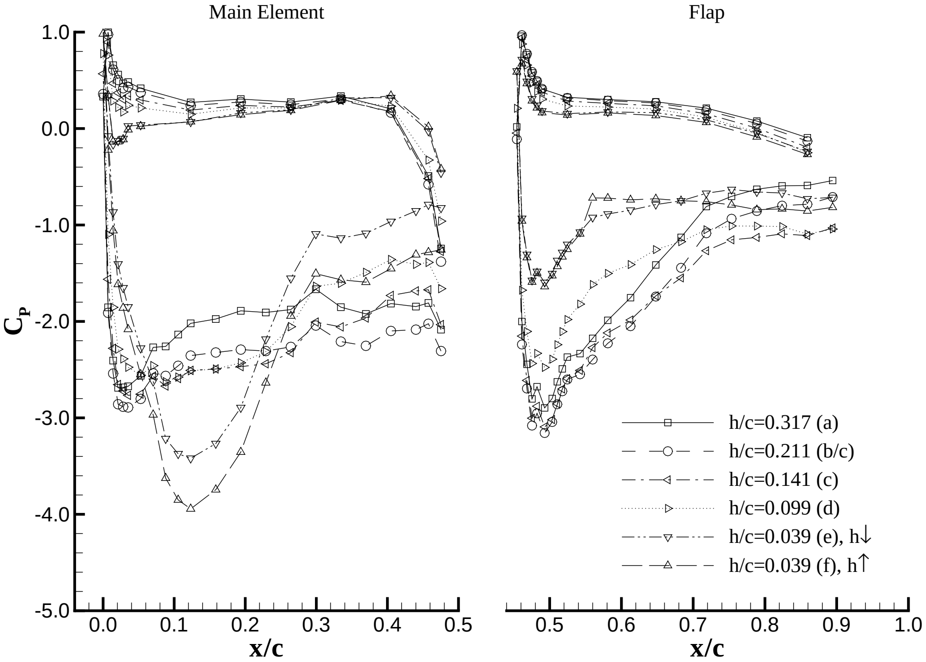

(b) Port tip, $y/c = -0.933$, $25mm$ inboard of the endplate.

Figure 3.17: Chordwise pressure distributions of the isolated wing for a selection of ride heights, main element and flap at centre span (a) and at the port tip (b); data from Mahon [12].

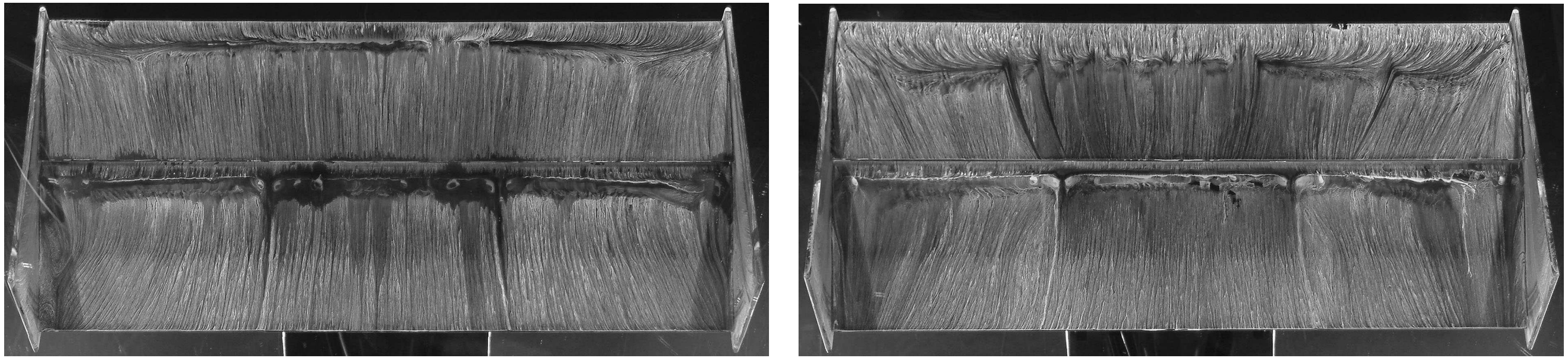

(a) In region $a$ at $h/c = 0.317$.

(b) In region $d$ at $h/c = 0.099$.

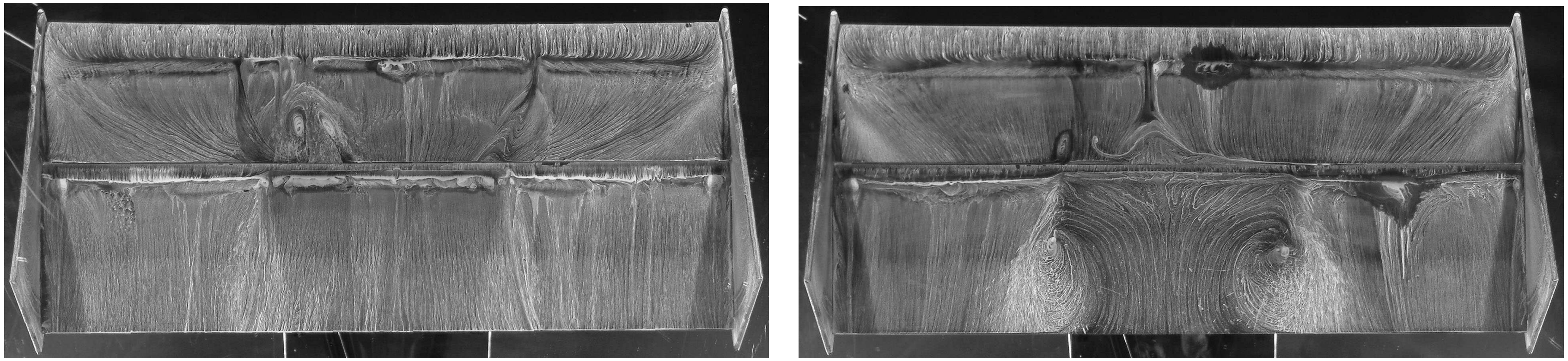

(c) In region $e$ at $h/c = 0.063$, decreasing $h$.

(d) In region $f$ at $h/c = 0.063$, increasing $h$.

Figure 3.18: Surface streaklines on the suction side of the isolated wing, visualized with oil flow (flow direction from top to bottom); pictures from Mahon [12].

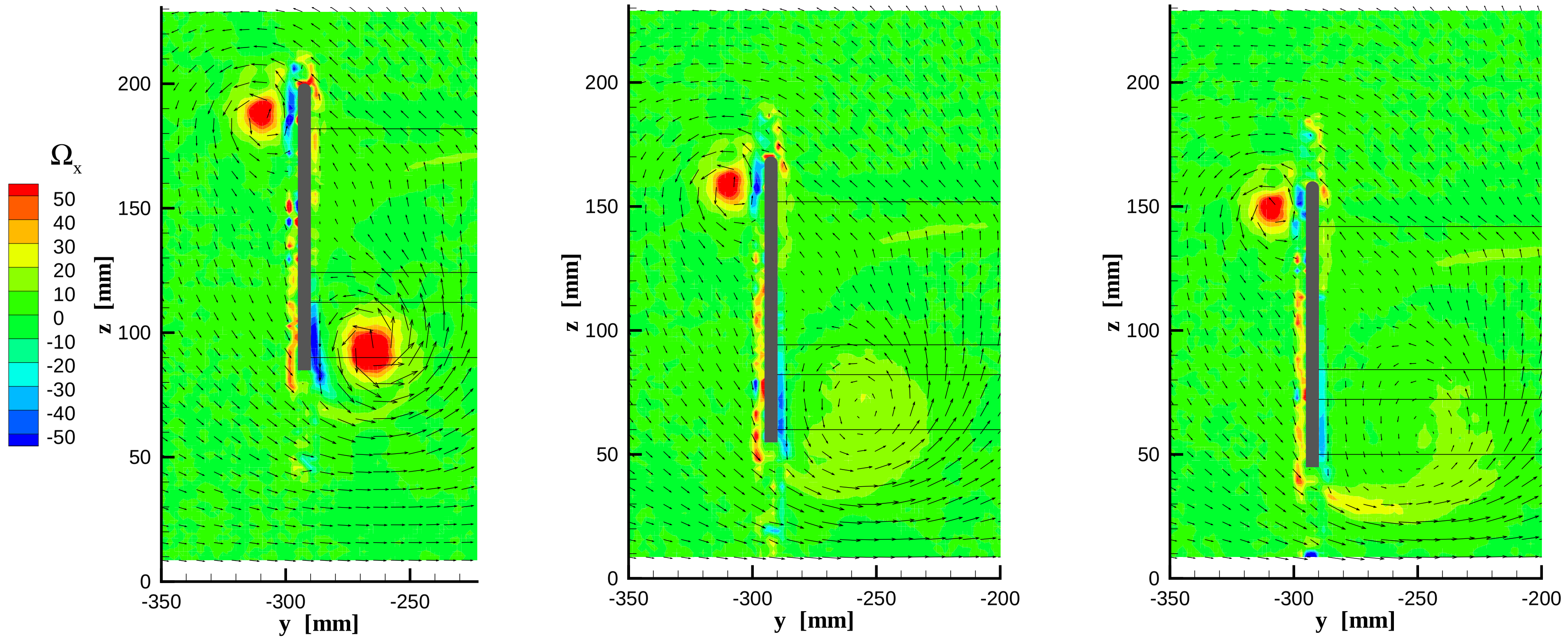

(a) $h/c = 0.317$, region *a*.

(b) $h/c = 0.211$, boundary of *b* and *c*.

(c) $h/c = 0.176$, region *c*.

Figure 3.19: Time-averaged non-dimensionalized $x$-vorticity contours and velocity vectors from PIV data behind the port side wing endplate at $x/c = 0.995$ ($10mm$ downstream of the endplate trailing edge) for various ride heights; looking upstream, showing the endplate (grey) and wing element contours (black lines); a positive $\Omega_x$ indicates an anti-clockwise rotation in this view direction.

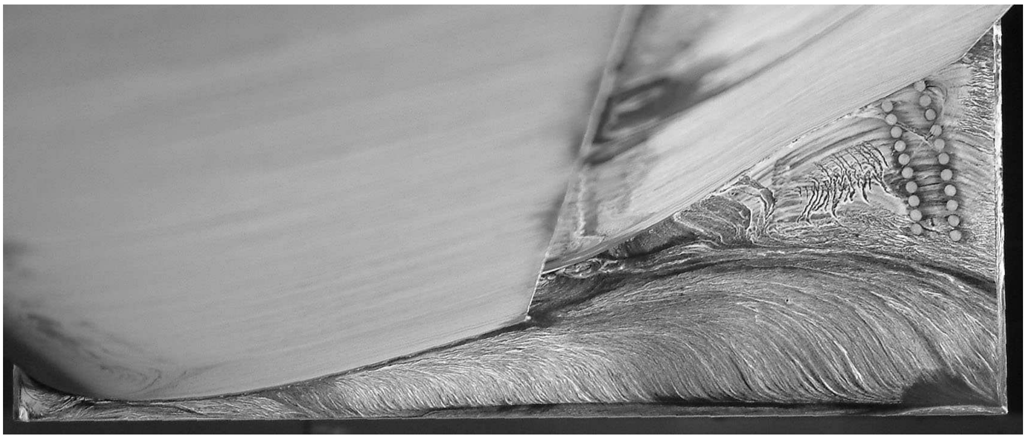

(a) In region $a$ at $h/c = 0.317$.

(b) On the boundary of region $b$ and $c$ at $h/c = 0.211$.

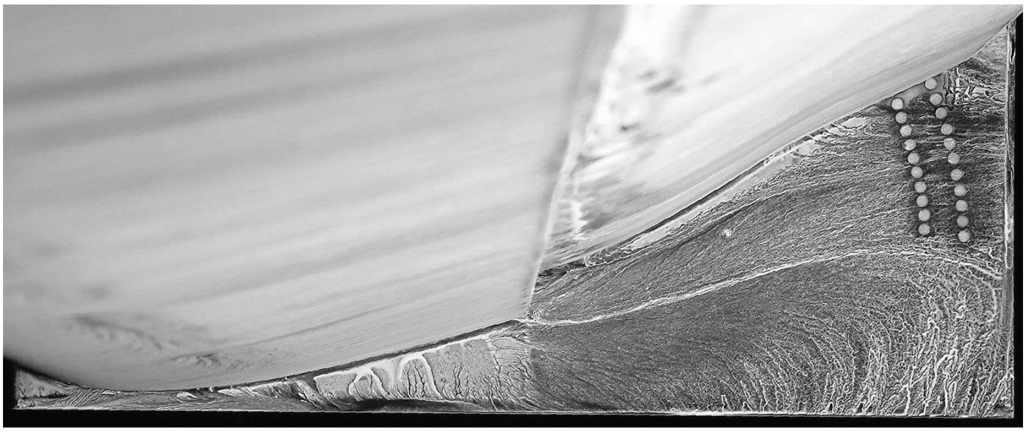

(c) In region $d$ at $h/c = 0.099$.

Figure 3.20: Surface streaklines on the inside of the starboard endplate for the isolated wing, visualized with oil flow (flow direction from left to right); pictures from Mahon [12].

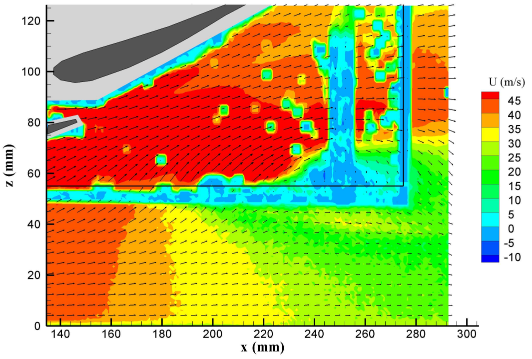

(a) $h/c = 0.211$, boundary of $b$ and $c$.

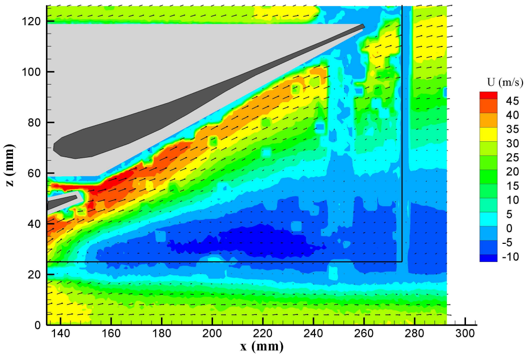

(b) $h/c = 0.106$, region $d$.

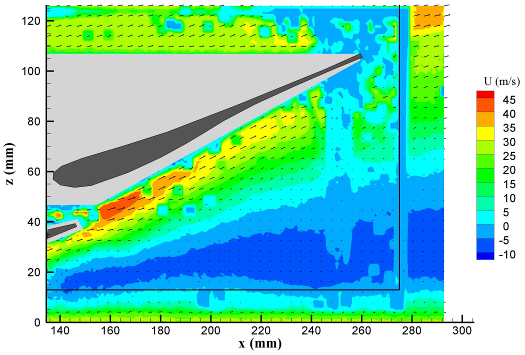

(c) $h/c = 0.063$, increasing $h$, region $f$.

Figure 3.21: Time-averaged $x$-velocity contours and velocity vectors from PIV data in a streamwise plane underneath the flap at $y/c = -0.933$, $25mm$ inside of the port side endplate; flow from left to right, showing the outline of the endplate (black lines), the elements (dark grey; no exact representation) and blanked out areas because of reflections, shadows and parallax effects (light grey).

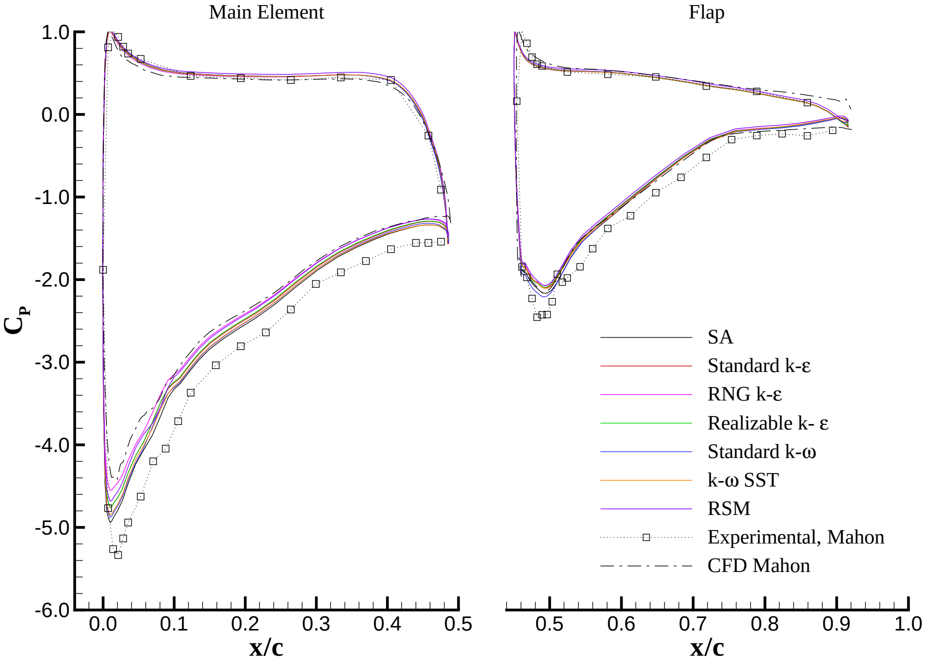

(a) Centre span, $y/c = 0$.

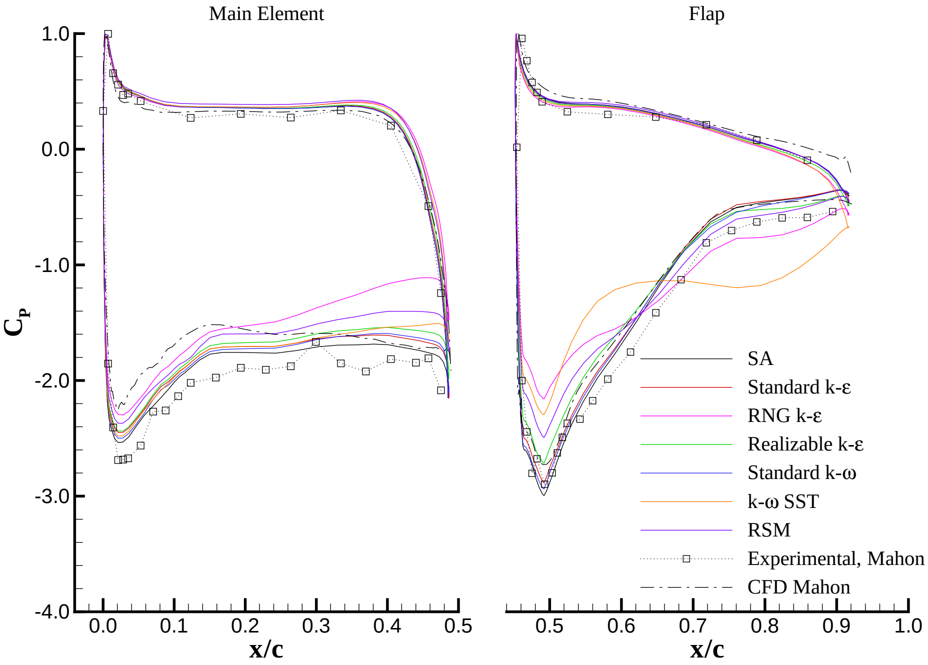

(b) Port tip, $y/c = -0.933$, $25mm$ inboard of the endplate.

Figure 3.22: Chordwise CFD pressure distributions of the isolated wing for a variety of turbulence models at $h/c = 0.317$, main element and flap at centre span (a) and at the port tip (b); experimental data from Mahon [12].

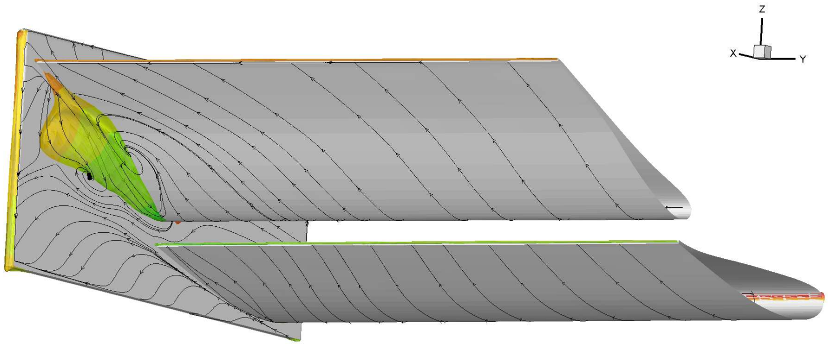

(a) 1500 iterations.

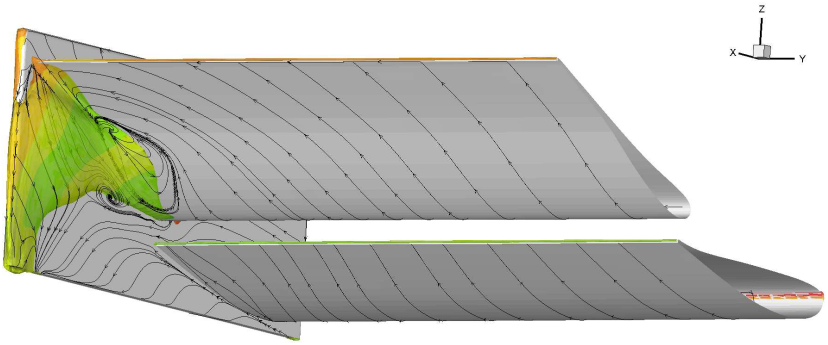

(b) 12500 iterations.

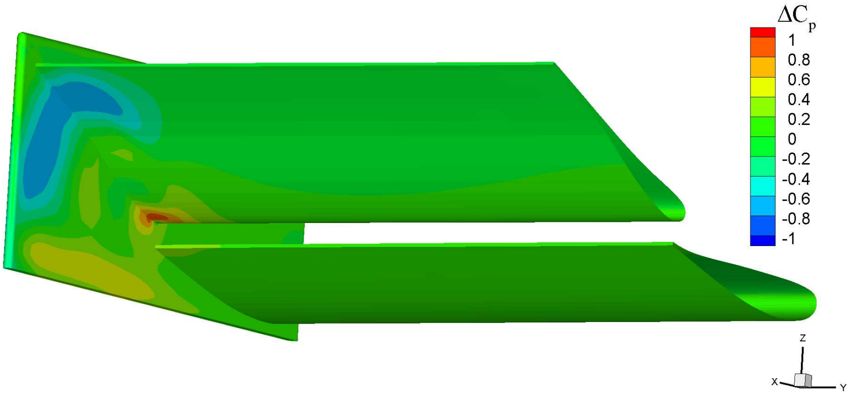

(c) $\Delta C_P$-values; the results for the 1500 iterations case is subtracted from the 12500.

Figure 3.23: Comparison of CFD results for $h/c = 0.211$ at two stages in the convergence process; surface streaklines based on wall shear stress and reversed flow zones with $U < 0$ coloured by $C_P$ in (a) and (b); $\Delta C_P$-values in (c).

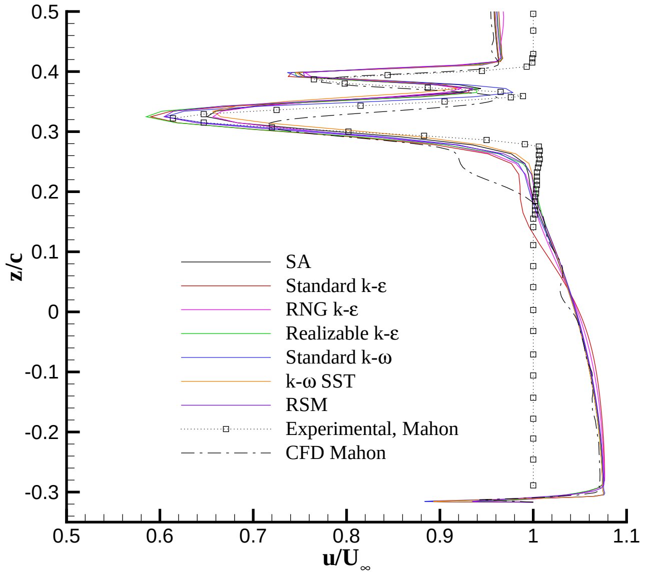

Figure 3.24: Centre span CFD wake profiles at $x/c = 1.127$ for various turbulence models at $h/c = 0.317$.

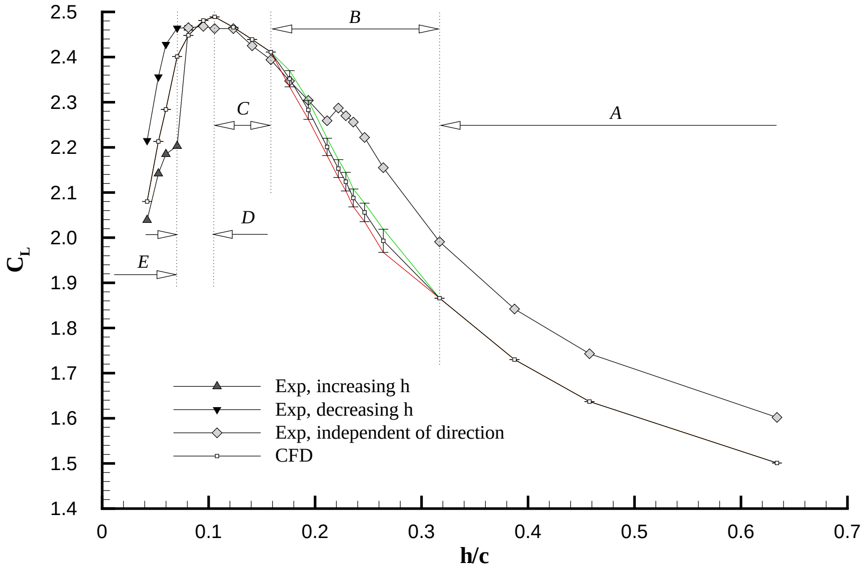

Figure 3.25: Changes in CFD downforce coefficient with ride height and definition of the CFD force regions for the isolated wing; red and green curves are boundaries of the $C_L$ variation.

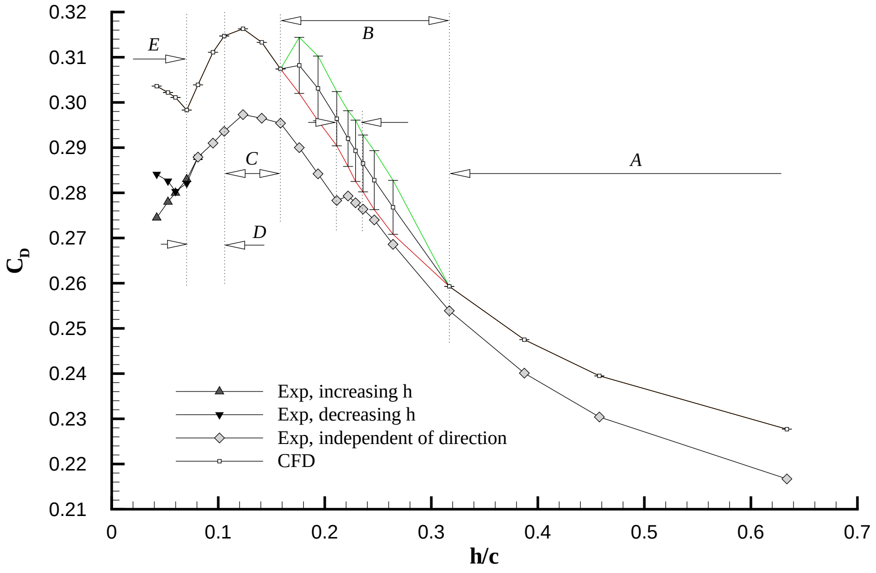

Figure 3.26: Changes in CFD drag coefficient with ride height for the isolated wing; red and green curves are boundaries of the $C_D$ variation.

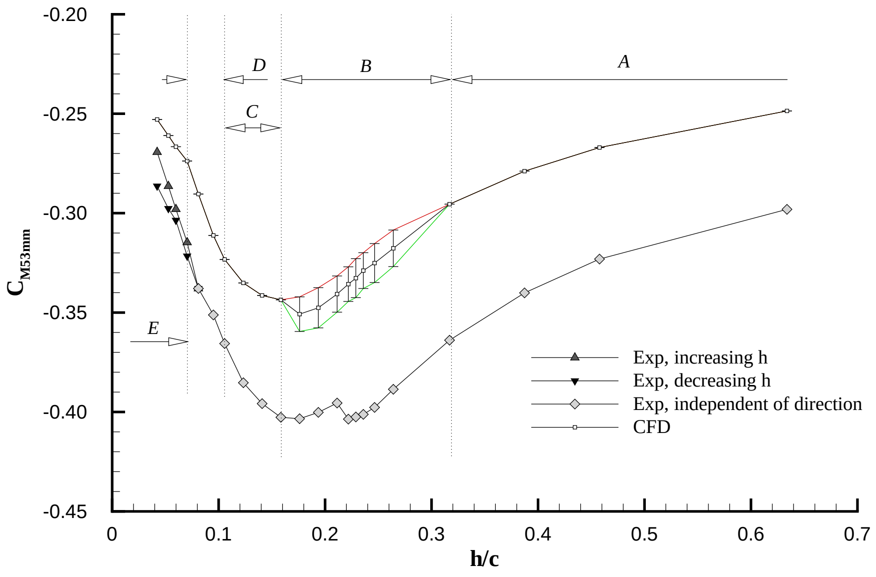

Figure 3.27: Changes in CFD pitching moment coefficient with ride height for the isolated wing; resolved around $x = 53mm$; red and green curves are boundaries of the $C_M$ variation.

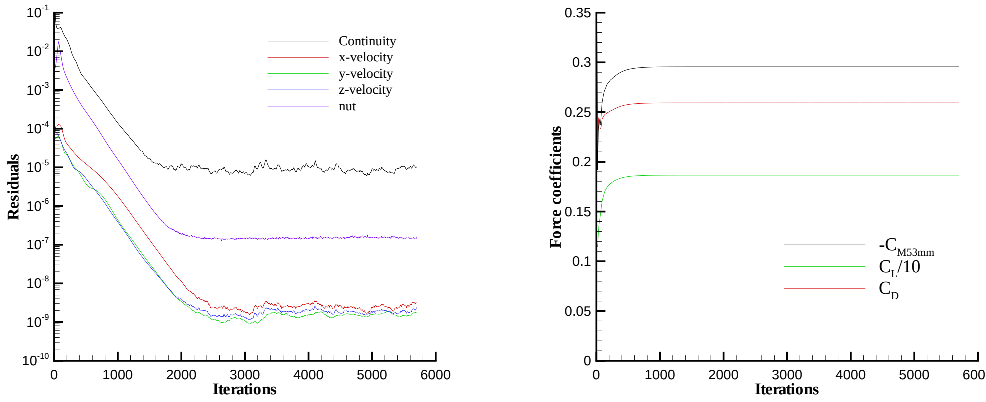

(a) $h/c = 0.317$; boundary of region $A$ and $B$.

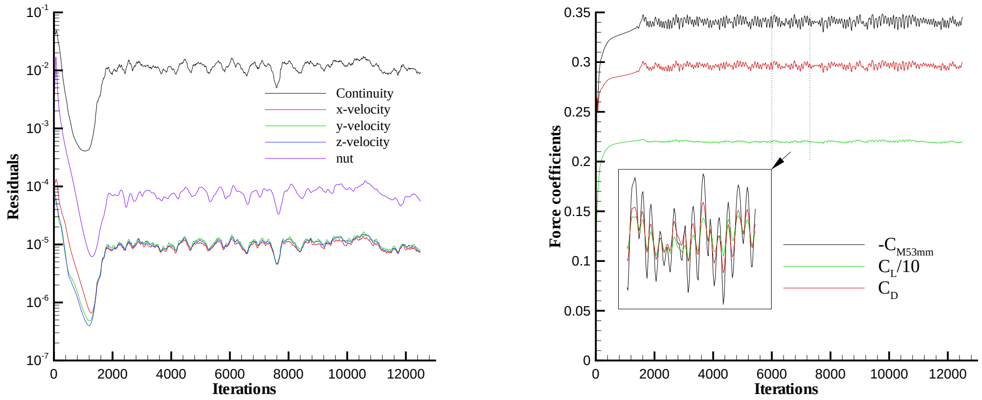

(b) $h/c = 0.211$; region $B$.

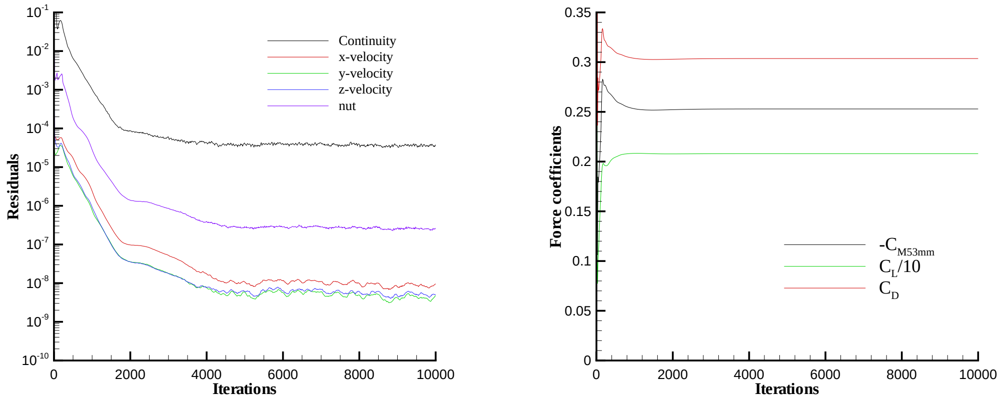

(c) $h/c = 0.042$; region $E$.

Figure 3.28: Normalized residuals and force coefficients from CFD versus number of iterations for the isolated wing for various ride heights; the sign of $C_{M53mm}$ has been reversed and the $C_L$ has been divided by 10 to fit in the same figures.

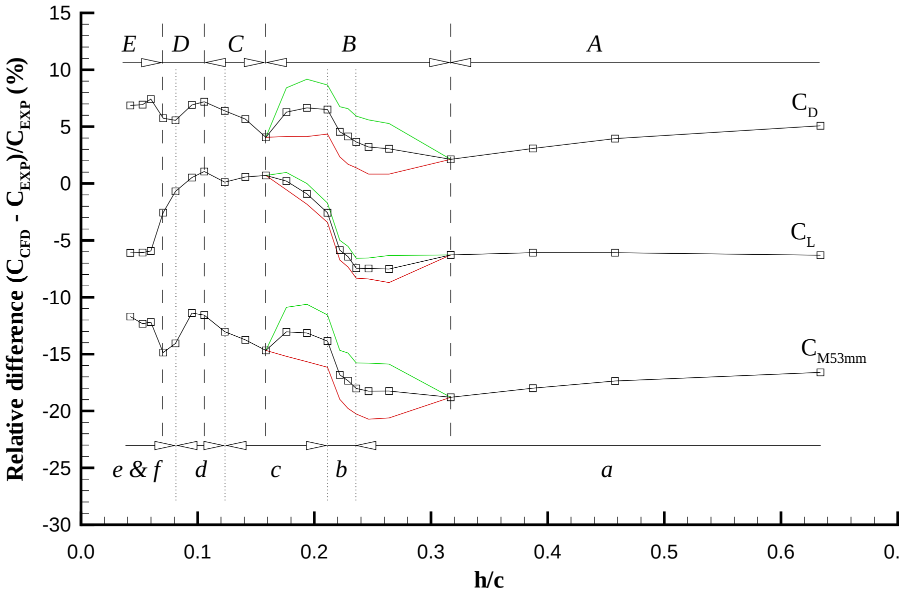

Figure 3.29: Relative differences between CFD and experimental force coefficient results over the ride height range; red and green curves are boundaries of the computational load coefficient variations.

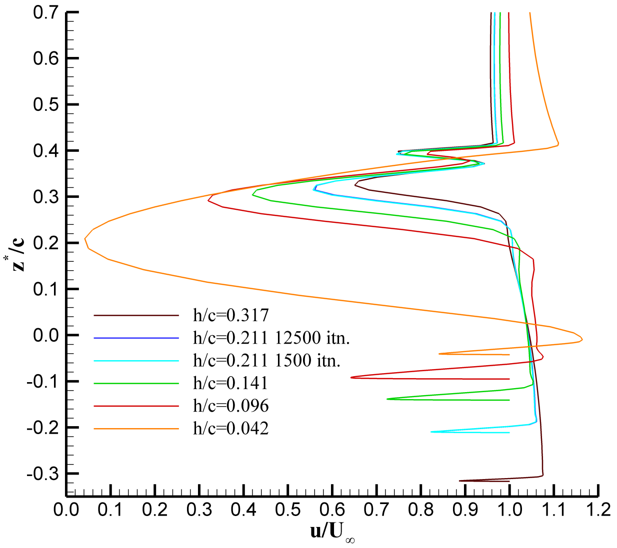

Figure 3.30: Centre span CFD wake profiles at $x/c = 1.127$ for various ride heights; with $z^*$ measured from the lowest point on the main element, as in figure 3.16.

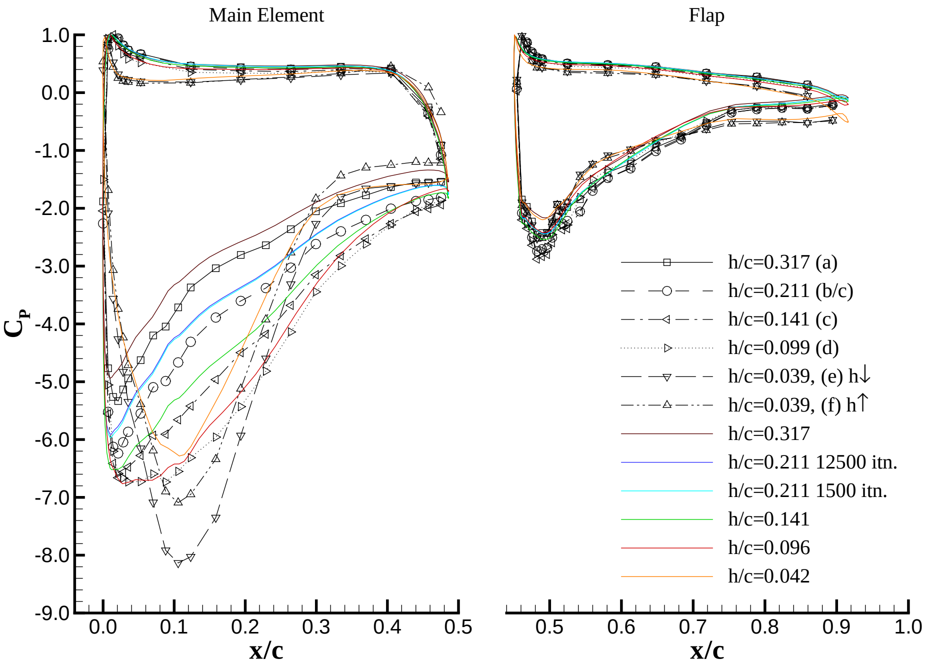

(a) Centre span, $y/c = 0$.

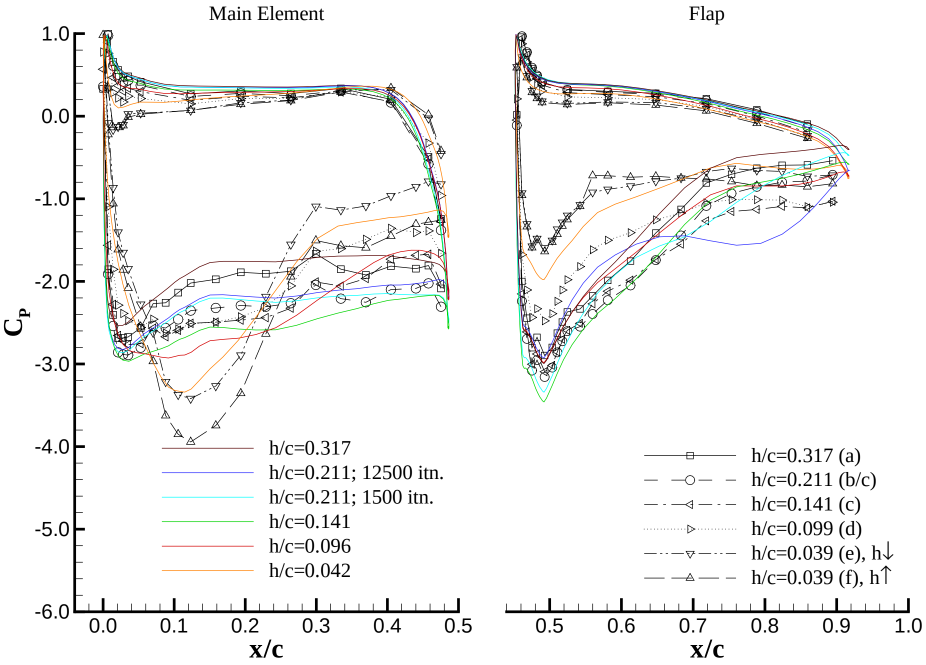

(b) Port tip, $y/c = -0.933$, $25mm$ inboard of the endplate.

Figure 3.31: Chordwise CFD (colour) and experimental (black) pressure distributions of the isolated wing for a variety of ride heights, main element and flap at centre span (a) and at the port tip (b); experimental data from Mahon [12].

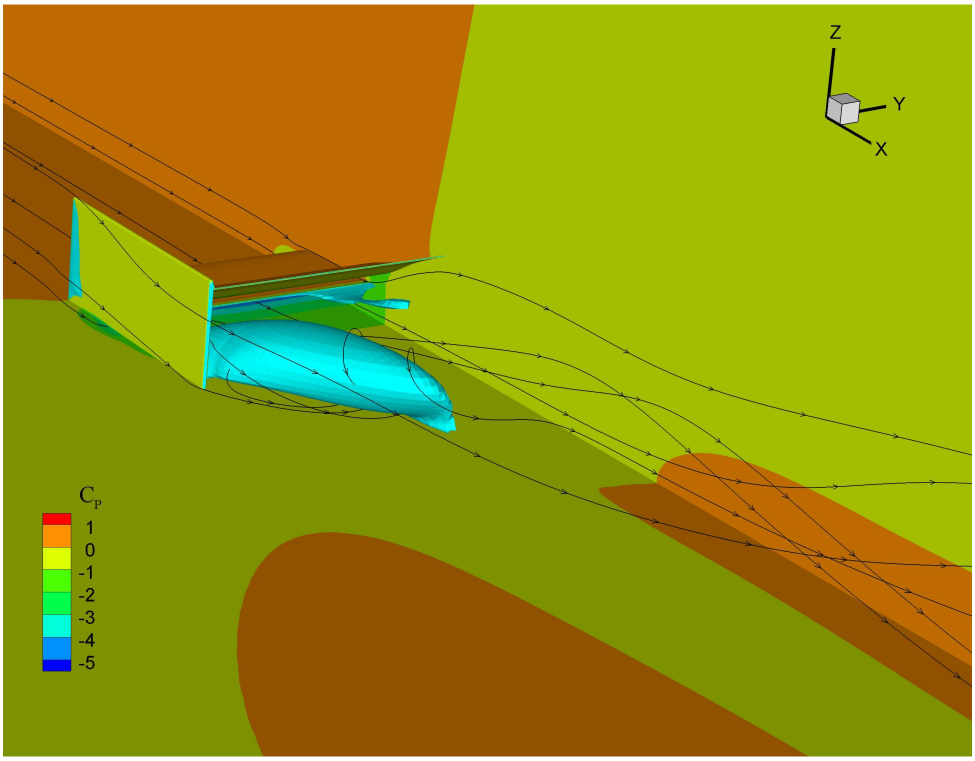

(a) Iso-surface of $U = 0$ (light blue), pressure contours and streamtraces at $h/c = 0.053$.

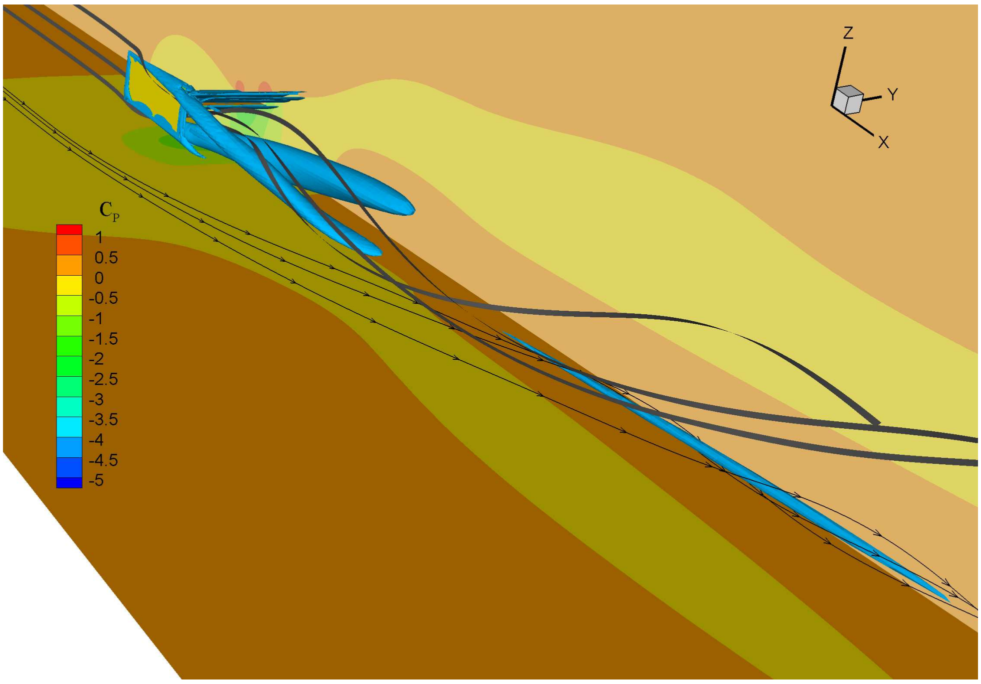

(b) Iso-surface of $\bar{Q} = 5$ (blue), pressure contours and streamtraces at $h/c = 0.317$.

Figure 3.32: Visualization of CFD flow field for two ride heights, each with an iso-surface of a different quantity; iso-surfaces are not coloured by $C_P$.

# Chapter 4

# Effect of Wing Presence on Wheel Aerodynamics

The following three chapters will answer the first three research questions by looking at how the aerodynamic behaviour of the isolated components changes when their flow fields are interacting. These chapters are based on experimental results, whereas a selection of the CFD outcomes will be presented in the following chapter 7. The current chapter deals with the influence of an upstream positioned wing on the wheel aerodynamics. The wing - wheel overlap and gap have both been set to the baseline configuration value of $20mm$ for this purpose, while the influence of the wing ride height is included as a parameter of variation in this examination. The effect of overlap and gap variations will later on be analyzed in chapter 6.

The first section of this chapter discusses the force behaviour as a result of wing ride height variation. Several force regions will be defined based on this and the dominant flow mechanisms that cause the differences between these regions will be introduced in section 4.2. After this several additional flow features will be analyzed, which have no global quantitative effect on the force coefficients, and finally the different force regions will be summarized.

## 4.1 Force behaviour

Aerodynamic interaction between the upstream positioned wing and the wheel flow field result in changes to the wheel aerodynamics. This can immediately be noticed from figure 4.1, which shows the global behaviour by visualizing the experimental wheel drag as function of the wing ride height. For the baseline configuration settings the wheel drag varies between a 14.6% lower value at $h/c = 0.074$ and a 22.8% higher value at $h/c = 0.458$, compared to the isolated wheel. This large variation in wheel drag can have a considerable effect on the overall performance of the racecar, since it has been mentioned in the introduction that the wheels can produce up to 40% of the total drag of the vehicle. Associated alterations of the wheel lift and side force can influence the performance even further and can also change the stability of the car. The wheel drag is the only force that has been measured directly during this research and the force regions will therefore be defined based on the behaviour of this quantity. Table 4.1 does however also present the sectional downforce values, which result from integrating the experimental 2D pressure distributions, in order to give an indication of the variation of this force.

The wing ride height range in figure 4.1 has been divided into six force regions, of which the two hysteresis zones are coinciding but dependent on the direction of ride height variation. The boundaries between the various regions are in decreasing ride height order defined as the global maximum wheel drag at $h/c = 0.458$, the local minimum at $h/c = 0.306$, the local maximum at $h/c = 0.158$ and the start of the hysteresis zone at $h/c = 0.067$. This division results in the following force regions:

- Region *I*, from the highest ride height, at which the wheel drag is larger than for the isolated wheel case, downwards the wheel drag increases gradually until it levels off at the lower boundary.
- Region *II*, the wheel drag decreases continuously with ride height reduction, but this region is primarily characterized by a disproportional large wheel drag reduction around $h/c = 0.35$, or $h_{EPt}/D = 0.67$, where $h_{EPt}$ is the height from the ground to the top of the endplate ($h_{EPt} = h + 110mm$) and $D$ is the wheel diameter.
- Region *III*, the wheel drag rises again, but remains lower than for the isolated wheel case over the complete region. The second half of this region presents a plateau of almost constant wheel drag.
- Region $IV$, the wheel drag drops off at fairly constant rate to a level that is comparable to that at the beginning of region *III*.
- Region *V*, the decreasing ride height branch of the hysteresis zone displays an almost constant wheel drag.

- Region *VI*, the wheel drag for the increasing ride height branch remains quite constant as well, but is higher than that for the decreasing branch and changes discontinuously at the upper boundary of the region.

The influence of the $Re$-number on these results is presented in appendix C. The wheel drag values are very similar for the cases obtained at $20m/s$ and $30m/s$. The main differences are the displacement of the upper boundary of the hysteresis zone to a higher ride height and of the local maximum at the boundary between regions *III* and $IV$, which moves to a higher ride height as well. Due to the plateau around the latter boundary it is very well possible that this second translation is more the result of measurement accuracy than of a change in flow physics for the lower $Re$-number.

## 4.2 Governing mechanisms

The previously discussed variations in wheel drag are the result of a combination of several individual influences. The balance between these effects defines the wheel drag and in this way presents an integral parameter for the flow aerodynamics at those specific settings. Most of the time it can however be quite complicated to derive the changes in this balance, which cause the resulting wheel drag behaviour. This section focuses on three effects that have the largest influence on the wheel drag and discusses the flow mechanisms that govern these effects. A variety of experimental data has been obtained and is presented to support the proposed explanations. The on-surface pressure measurements in figures 4.3 to 4.7 and the off-surface PIV results in figures 4.8, 4.9 and 4.10 prove particularly useful in this process.

### 4.2.1 Delayed separation effect

The separation from the top of the wheel is one specific area that is influenced considerably by the wing presence and relative location. Fackrell [34] proposes that separation takes place just downstream of the location of the largest suction at the top of the wheel, where the following small adverse pressure gradient changes into a favourable pressure gradient again. From figure 4.3 it can be derived that separation defined in this way occurs around $\theta = 274°$ for the isolated wheel at the centreline. Furthermore it can be seen that the separation for the combined case moves downstream with increasing wing ride height, over the crown of the wheel, to $\theta = 250°$ for $h/c = 0.458$. The other two pressure distributions for sensor locations on the tyre tread, figures 4.4 and 4.5, show that this trend can be observed over the complete width of the wheel. The downstream movement of the separation position at higher ride heights is however even more pronounced for these locations near the side of the wheel than for the centreline.

An alternative way of looking at this effect is by studying the PIV data over the top of the wheel. Figure 4.8 (b) reveals that the separation lines, defined by $U = 0m/s$, at the centre of the wheel move downstream as well with increasing ride height. This trend is consistent with the one derived from the pressure distributions[1], even though the actual separation location is not visible in this figure, because it is blocked by the cambered wheel surface. The value of the downstream local pressure minimum after separation, between $\theta = 240°$ and $250°$ in figure 4.3, could be related to the vertical distance between the separation line and the wheel surface. For the isolated wheel it has been proposed that this feature is the time-averaged contribution of unsteady pressure fluctuations as a result of large scale eddies in the recirculation region. The maximum possible size of the eddies determines the suction increment due to this feature in this explanation. It is expected that the eddies will be smaller when the separation line lies closer to the wheel surface for higher ride heights, see figure 4.8 (b), and therefore that the local suction maximum after separation will be less for these cases. Figure 4.3 reveals that the suction maximum downstream of separation becomes smaller compared to the maximum suction upstream of separation for increasing ride heights, which is in agreement with this explanation.

Two different flow mechanisms seem responsible for the delay in separation with increasing wing ride height. The primary mechanism is most likely related to the circulation that the upstream-located downforce-producing wing induces on the wheel. In order to generate downforce the wing introduces an anti-clockwise circulation around the $y$-axis. This is in the same direction as the wheel rotation. The wing circulation induces an opposite circulation on the annulus of flow around the wheel. Just like wheel rotation promotes separation from the top of the wheel, this opposite wing-induced circulation postpones the separation. Figure 4.2 gives a schematic impression of this effect. This wing induced circulation mechanism is most effective when the wing and wheel are closest to each other at $h_{Fte}/D \approx 0.5$ and increasingly loses significance for higher and lower ride

---

[1] One difference between the two methods is that the PIV separation lines seem to indicate that separation for $h/c = 0.063$ and for $0.106$ takes place upstream of the location for the isolated wheel, while the pressure distributions suggest that separation for the combined wing - wheel case always occurs downstream of that for the isolated wheel. It needs to be kept in mind though that this is a comparison of two totally different definitions of the separation location and furthermore that the PIV plane was set up vertically instead of perpendicular to the cambered wheel surface.

heights. Alternatively the increase in flow directed over the top of the wheel for higher ride heights could provide an explanation for the delayed separation as well.

The second mechanism that delays the separation over the top of the wheel results from the trajectory of the upper edge vortex of the wing. CFD simulations have revealed that the trajectory of this upper edge vortex changes from passing on the inside of the wheel for low ride heights to over the wheel for the higher ride heights as shown in figure 4.11. The switch between these two options occurs at the sharp change in wheel drag, which is at $h_{EPt}/D = 0.67$ for these configuration settings. The upper edge vortex re-energizes the flow layer around the wheel, when it passes over the top, while the anti-clockwise flow rotation - when looked from behind - of the vortex pushes the flow towards the wheel surface, postponing the separation in this way.

The delayed separation leads to a larger suction over the top of the wheel from $\theta = 300°$ to close to 200°, as can be concluded from figure 4.3. The resulting influence on the wheel drag is relatively small and most prominent near the boundaries of this region, as can be concluded from the fact that the pressure distribution has to be multiplied by $cos(\theta)$ to determine the drag contribution. However, interestingly, this reveals that separation delay is accompanied by an increase in wheel drag. This observation is counter-intuitive to the classical results for infinite circular cylinders [18]. The last paragraph of section 8.1 pays more attention to this paradox. The contribution of the delayed separation to the wheel lift is however considerably larger, making the additional suction over the top of the wheel one of the main factors of influence for the wheel lift. It can be assumed that the side force on the wheel is not very dependent on the location of separation over the top of the wheel. Nevertheless the side force towards the symmetry plane will be larger when the upper edge vortex passes on the inside of the wheel, inducing lower pressures on this wheel surface, than when it passes over the top.

### 4.2.2 Channel inflow effect

The lower frontal area of the wheel is much affected by the wing flow as well. Figure 4.3 and especially figure 4.5 show that the pressures are noticeably lower in the wheel segment from $\theta = 0°$ to 90° when the wing is present. The amount of additional suction is ride height dependent and alters significantly for ride heights above the sudden wheel drag change at $h_{EPt}/D = 0.67$. The outside of the wheel tyre tread, see figure 4.4, is less influenced and shows a rise in pressures in contrast.

The flow mechanism behind this additional suction on the frontal lower inside of the wheel is the constraining of the wing flow by the wheels. The partly accelerated flow downstream of the wing is guided into a new channel formed by the inside surfaces of the wheel and the ground, instead of being allowed to freely recover to freestream conditions. Due to the positive overlap between the wing and wheel for this baseline configuration, the flow near the wing endplates has to be turned into the wheel channel. Hereto the flow is accelerated around the corner of the wheel, resulting in the suction on the wheel surface. Similarly the lower edge vortex has to be diverted into the channel as well, which can lead to additional suction on the wheel in this area.

The influence of the channel inflow effect on the wheel pressures seems largest when an accelerated part of the wing wake is in close proximity to the wheel surface. For example, higher velocities and thus larger suction occur when the trailing edge of the flap is slightly below the most forward point of the wheel ($h_{EPt}/D \approx 0.4$), or when the lower edge vortex passes this most forward point ($h/D \approx 0.5$), as can be derived from figures 4.9 (b) and 4.9 (e) respectively. Whereas the velocities are much lower, even below the level for the isolated wheel case, at an intermediate ride height of $h/c = 0.211$, see figure 4.9 (c). The channel inflow effect reduces the drag on the wheel as a result of the lower pressures on the front. The wheel lift is reduced as well, whereas the asymmetric suction on the inside of the wheel generates a larger side force towards the symmetry plane.

### 4.2.3 Wake effect

A final area of the wheel on which the wing flow has a dominant effect is the wheel wake. To improve the understanding of the wake physics it is elucidating to divide the wake into two zones: the upper and the lower wake. The upper wake reaches from the top of the wheel down to $\theta \approx 190°$, depending on the spanwise position. The upper wake primarily consists of the arch shaped vortex at the top of the wheel, which has also been found for the isolated wheel. CFD simulations have revealed that this feature exists for lower ride heights[2]. The lower wake covers the lower region of the wake and extends downwards to the downstream side of the contact patch. CFD showed again that the lower wake is similar to that for the isolated wheel case at the highest ride heights[3], consisting of the two counterrotating longitudinal vortices near to the ground (see feature 'H' in figure 4.11). At

---

[2] The arch shaped vortex, see feature 'E' in figure 4.11 (b), remains relatively unchanged up to $h_{EPt}/D \approx 0.5$ and still characterizes the upper wake up till the sudden change in wheel drag at $h_{EPt}/D = 0.67$.

[3] At the highest ride height of $h/c = 0.634$, when the lower edge vortex is well above the axis of the wheel, the two longitudinal vortices are as distinct as for the isolated case, however towards the sudden change in wheel drag the vortex at the inside of the wheel starts weakening.

the lower ride heights the inside longitudinal vortex disappears, resulting in an asymmetric wake, while its void is filled by the lower edge wing vortex. The high-vorticity ‘bow-wave’ zone (feature ‘D’ in figure 4.11) originating from the upstream side of the contact patch disappears as well for the inside of the wheel at lower ride heights.

**Upper wake** The features of the upper wake partly overlap with those described for the top of the wheel in the section on delayed separation. Figure 4.3 shows that the upper wake pressures at the centreline are characterized by the recovery from the second local minimum that is caused by the unsteady pressure fluctuations. At the lower boundary the pressures are very similar for each of the ride heights and reach the base pressure experienced in the lower wake. However at the upper boundary the pressures very much depend on the suction over the top of the wheel and therefore ride heights above $h_{EPt}/D = 0.67$ imply more suction over the upper wake wheel surface. The pressure distributions on the sides of the tyre tread, P2 and P4, show a comparable decay in suction with reducing $\theta$, although the pressures do not reach the same value at the lower boundary. Especially for the inside of the wheel it can be concluded that the higher ride heights, above the sudden wheel drag change, lead to more suction at the lower boundary of the upper wake as well.

The flow mechanism that causes this difference in behaviour between the lower and higher ride heights is again primarily the change in trajectory of the upper edge wing vortex. From CFD simulations for various ride heights it could be concluded that the arch shaped vortex in the upper wake (feature ‘E’ in figure 4.11) is replaced by attached flow near the centreline of the wheel at higher ride heights, while the legs (feature ‘F’ in figure 4.11) of this vortex change into two regions with strong vorticity, where the flow along the side spills over the edge of the wheel into the wake. These regions of high vorticity are the reason for the higher suction at the sides of the tyre tread near the lower boundary of the upper wake for higher ride heights. The region on the inside of the wheel (location P4) displays more suction than on the outside, because it is energized by the upper edge wing vortex (feature ‘A’), which passes over the wheel for the higher ride heights. A complex interaction between this region of high vorticity (F), the upper edge wing vortex (A) and the lower edge wing vortex (C), which passes on the inside of the wheel, can occur for certain settings. It is expected that this interaction and the resulting higher suction on the wheel surface in the upper wake is partly responsible for generating the highest wheel drag at $h/c = 0.458$.

For the lower ride heights, when the upper edge wing vortex passes on the inside of the wheel as well, the upper wheel wake is similar to that for the isolated wheel. The arch shaped vortex is the most dominant feature of the upper wake under these conditions. Only small increases in suction on the wheel surface are noticeable for increasing ride height and these are directly related to the suction over the top of the wheel. The upper wake effect causes more wheel drag and lift for the higher ride heights, while the side force is again mostly influenced by the location of the upper edge wing vortex.

**Lower wake** The pressure distributions for the lower wake do not present a very clear consistent trend with ride height change. For the 45°-segment closest to the ground it seems that the suction, in general, reduces with increasing ride height. In the remaining part of the lower wake this trend can be noticed up till around the ride height of the sudden change in wheel drag, after which the suction grows again with increasing ride height in order to match the value at the upper boundary. This variation is roughly similar for each of the three pressure distribution locations on the tyre tread.

The flow mechanism responsible for the behaviour in the lower wake is difficult to point out. It could be that the suction reduction with increasing ride height in the lower segment is induced by the replacement of the inside longitudinal vortex and 'bow wave' zone with the remains of the lower edge wing vortex. At the lowest ride heights this lower edge vortex has burst upstream of the wheel, but it still leaves its marks on the flow field and seems to produce higher velocity flow around the corner of the wheel than when the longitudinal vortex is present. At the lowest ride height the outside longitudinal vortex seems to be missing as well in the CFD results. This influence of the replacement of the longitudinal vortices reduces when the wing moves away from the ground, leading to less suction in this area of the wheel surface.

The increase in suction closer to the middle of the wake for higher ride heights seems to be related to the flow field presented in figure 4.10. The equivalent position of this horizontal plane in the pressure distributions is at $\theta = 187°$ and 189° for respectively the P4 and P5 location. This is in the region where the higher ride heights show considerably more suction, as can be seen in figures 4.5 and 4.7. The strong recirculation in the PIV data, which can be noticed in the figures 4.10 (d), (e) and (f), only occurs for ride heights above the sudden increase in wheel drag[4]. The highest wheel drag is experienced when the recirculation zone lies closest to the back of the wheel at $h/c = 0.458$, inducing the

---

[4] The case for $h/c = 0.317$ has not been included in this figure, but the flow field looks very similar to the $h/c = 0.211$ case showing slightly more deflection into the wake, while still no signs of recirculation are visible.

highest velocities on the surface. It is therefore expected that the flow mechanism causing this recirculation is fundamental to the value of the wheel drag. It is proposed here that a complex interaction of the vortices originating from the wing and wheel is responsible for the recirculation in the wheel wake. This mechanism seems to be confirmed by CFD results for the 3D flow domain, but is difficult to prove with the experimental data.

Following the previous discussion, it is to be expected that the influence of the lower wake effect on the wheel force coefficients is complicated. The suction near to the contact patch has little influence on the drag, but has more relevance to the lift. The drag contribution most likely reduces slightly with increasing ride heights when the wing is close to the ground and then grows suddenly when the recirculation occurs. After reaching a maximum it most likely reduces again due to the recirculation moving away from the wheel surface. The wheel lift contribution initially increases due to the reduced suction over the lowest segment, while for higher ride heights it may reduce, but this depends on the location where the recirculation effect is most prominent. The side force increases when the outside longitudinal vortex appears as the wing starts to move away from the ground. The symmetry of the lower wake is restored for the higher ride heights, when both longitudinal vortices are present, and this should lead to a reduction of the side force. No experimental data is available for the outerside of the wheel and therefore it is unknown whether the recirculation zone exists on that side as well.

## 4.3 Additional flow features

Apart from the previously discussed effects, which have a large influence on the wheel force coefficients, the results also show several minor influences of the wing presence on the wheel flow. This section summarizes these features by looking at subsequently the stagnation point, at the pressure distributions over the sides of the wheel and at the off-surface flow field.

**Stagnation point** From figure 4.3 it can be concluded that the wheel flow does not reach stagnation conditions at the centreline when the wing is present. The location of the highest experienced pressure moves upwards with increasing ride height compared to the isolated wheel case, but the $C_P$-value is below 1 for each of the ride heights. The resolution of the experimental measurements in $y$-direction along the tyre tread is in no way sufficient to determine the spanwise movement of the stagnation point. The CFD grids on the other hand offer better resolution with an averaged spacing of just over $2mm$

in spanwise direction over the parts of the tyre tread between the grooves and of $1.3mm$ in the grooves. The resolution in $\theta$-direction is 2.4°. Although the CFD results have not been validated extensively for the location of the stagnation point, it needs to be remembered that the position for the isolated wheel matched the experimental data at the centreline within the accuracy of the resolution (see page 87). Therefore, if used carefully, the CFD could give an indication of the stagnation point movement due to the wing presence and ride height. The values that are presented in the following discussion are based on the various CFD simulation cases and are obtained by inspection of the results.

The general trend is that the presence of the wing moves the stagnation point on the wheel upwards. At $h/c = 0.063$ it lies approximately 2.4° upwards from the isolated wheel position. Then it moves upwards with increasing ride height, to the upper side of the wheel until it is roughly 10° above the isolated wheel location for $h/c = 0.211$. Subsequently it stays at this $z$-position for increasing wing ride height and only moves slightly down for the highest ride height. For the lowest ride height the spanwise position has moved $3mm$ in a direction away from the symmetry plane compared to the isolated wheel. It reaches the same spanwise position as the isolated wheel case for $h/c = 0.211$ and moves continuously inwards till it is displaced $22mm$ towards the symmetry plane at the highest ride height. The stagnation position is located both upwards and inwards - even passing one groove to the next tyre tread patch - for this ride height compared to the isolated wheel.

At low ride heights the wing flow will primarily try to pass the wheel along the sides. It is this mechanism that causes the stagnation point to move outwards compared to the isolated wheel case, while the circulation induced by the wing leads to an upwards movement as well. When the wing is moving away from the ground a larger part of the flow can be deflected upwards and downwards. The stagnation point thus starts moving inwards, because less flow has to pass along the outside of the wheel. The reason for the stable height of the stagnation point over much of the higher ride height range is probably that the influence of the wing induced circulation is in balance with the displacement due to the flow over the top of the wheel. Despite the fact that the stagnation point on the wheel is influenced by the wing flow, it can however be concluded that the relative movements have little influence on the force coefficients.

**Wheel sides** The pressures, resulting from the flow over the sides of the wheel, have limited influence on the wheel drag and lift due to the orientation of the surfaces. Further analysis of the pressure distributions for the sensor locations P3 and, especially, P5 can however help to improve the understanding of the flow interactions. A very characteristic feature in figure 4.7 is the distinct local pressure minimum for the middle three ride heights between $\theta = 310°$ and $350°$. This pressure minimum is the imprint of the upper edge wing vortex on the wheel surface. It can be seen that this feature moves up, to smaller $\theta$-values, for increasing ride height. For the lowest ride height of $h/c = 0.106$ it can be recognized as the small minimum at $\theta = 3°$, below the centre of the wheel. More revealing is however that no imprint can be found for the highest presented ride height of $h/c = 0.458$, hereby confirming that the upper edge vortex passes over the wheel for the higher ride heights without causing an imprint at this sensor position.

The global minimum just below the wheel centre, from $\theta = 0°$ to $30°$, is caused by either the lower edge wing vortex, or possibly by a new wing vortex, depending on the ride height. The CFD shows that the lower edge wing vortex is responsible for this imprint at the highest presented ride height of $h/c = 0.458$ and it is expected that a similar feature will be visible for all ride heights above the sudden change in wheel drag. For the lower ride heights though this global minimum could result from a new additional vortex (feature 'B' in figure 4.11), which originates from the separated zone at the intersection of the wing endplate and the flap, according to CFD. At these ride heights this vortex and the upper edge vortex are located between the wheel and the lower edge wing vortex and the latter therefore leaves no imprint on the wheel surface under these conditions. Finally, the pressure distribution between $\theta = 90°$ to $225°$ on the inside of the wheel mainly shows the complexity of the flow field in this area. However it can be seen from figure 4.7 that this part of the pressure distribution for the highest ride height is qualitatively more similar to that of the isolated wheel case than any of the others. This confirms that the lower wake is less affected by the wing for the higher ride heights.

**Off-surface flow field** Some characteristics of the 3D flow field, such as the vortex trajectories, have already been touched upon in the previous discussion. Additionally, the PIV figures 4.9 and 4.10 contain more information on the flow field, which will be discussed here to conclude the current analysis. From the flow paths[5] in figure 4.9 (e) and (f) it can be deduced that the lower edge wing vortex passes through this vertical plane at a ride height between $h/c = 0.528$ and $0.634$. The velocities in the cross section through

---

[5] These flow paths in the PIV figures are based on the two velocity components in the plane and do not represent physical streamlines or particle paths for which the third velocity component would be required as well. The flow paths are visualized here nevertheless to increase the insight into the flow field.

the vortex region at $h/c = 0.528$ reach more than twice the freestream velocity, showing that the vortex is not breaking down.

Regarding the PIV at the downstream corner of the wheel it is noteworthy to mention that the flow turns sharper into the wake with increasing ride height for this plane. After the highest wheel drag this seems to change and it is only at the highest ride height that the wake regains a similar width as the wheel itself. Comparing the flow paths with those for the upstream corner seems to indicate that the inflow at this location is primarily related to whether the lower edge wing vortex is located below or above this plane. A consequence of the extreme deflection into the wake at $h/c = 0.458$ is that the flow is retarded in the top right corner of the picture, creating a zone with low horizontal flow velocity behind the wing. For the $h/c = 0.528$ case, which is not presented here, the inflow angle into the wake is less than that for the $h/c = 0.458$ case, but the velocities in the plane drop even further to below a third of the freestream velocity. Finally, figure 4.11 (b) shows the existence of the secondary rebound vortex (feature 'J'), originating from the ground.

## 4.4 Discussion of force regions

As a conclusion to this chapter it will now be summarized how the balance between the various governing mechanisms and flow features changes over the ride height range in order to produce the drag behaviour presented in figure 4.1. The new insight into the physics will also be used to make an educated guess about the wheel lift / downforce and side force variations over the force regions. The force regions can broadly be divided into two groups: those with a higher drag than for the isolated wheel case (regions *I* and *II*) and those with a lower drag (the other four regions) - on the other side of the sudden change in wheel drag. Figure 4.11 shows the characteristic flow topology for both of these groups. The more subtle differences in force behaviour between the regions originate from:

- In region *I* the wheel drag is higher than for the isolated wheel due to the recirculation in the wake and the delayed separation over the top of the wheel. The suction as a result of the wake effect increases, when the wing is moved downwards from the highest ride height, resulting in a gradual drag increase. It is also anticipated that the separation from the top of the wheel moves slightly downstream with decreasing ride height, which contributes to the drag increase. The CFD result (see figure 7.8) indicated such a movement, but no experimental data is available to confirm this for these ride heights. The influence of the channel inflow effect reduces from $h/D \approx 0.5$ downwards, which is another reason for the rise in wheel drag. The initial wheel lift at the highest ride height is larger than that for the isolated wheel, mainly due to the suction over the top resulting from the delayed separation. The side force towards the symmetry plane is larger than for the isolated case as well, due to the suction on the wheel inside created by the passing wing flow. Furthermore the recirculation on the inside of the wheel will be stronger than that on the outside due to the interaction with the upper edge vortex, which leads to an increase in side force with ride height reduction in this region.

- The wheel drag in region *II* reduces with reducing ride height. Initially primarily due to a reduction in suction caused by the wake effect, since the recirculation zone moves away from the wheel surface, as well as by the separation position moving upstream, but then suddenly at a much larger rate when the upper edge wing vortex starts moving to the inside of the wheel instead of passing over the top. The channel inflow effect keeps reducing, but this drag enhancing effect is overshadowed by the changes to the recirculation and separation. The wheel lift could change into downforce in this region, because of the loss of suction over the top and back of the wheel and the additional suction over the lower front end resulting from the channel inflow effect. The side force increases due to the extra suction from the upper edge vortex on the inside of the wheel.

- In force region *III* the wheel drag is always below the level of the isolated wheel, but it increases slightly with decreasing ride height. The causes of this behaviour are less clear and the delicate balance between the various governing mechanisms in this region and region *IV* result in either a plateau, a rise or a decrease in drag. The upstream moving separation will decrease the wheel drag slightly, but this can not be a driving mechanism considering the location at which these pressures act. It is expected that the reduction of the channel inflow effect in region *III* with decreasing ride height (see figure 4.5) is the main contributor to the wheel drag increase. A helping factor is the increasing base suction in the lower wake near to the ground. Since the extra base suction acts at a far more effective location than the channel inflow suction, it is expected that the downforce increases. The side force reduces proportional to the channel inflow effect.

- Force region *IV* is characterized by a decline in wheel drag for which the increase in channel inflow effect as a result of the accelerated flow on the suction side of the flap is mainly responsible. Furthermore the wake widens as well, which results in a reduction in suction on the base (compare the velocities in the base region in figures 4.10 (c) and (b) with each other). The wing flow field undergoes a major change between $h/c = 0.211$ and $h/c = 0.106$ as the lower edge vortex bursts, probably at $h/c = 0.113$. However no exact experimental data is available to confirm the exact ride height. Therefore it is uncertain whether the vortex breakdown is related to the local maximum in wheel drag, but it could be that the vortex breakdown is one of the reasons for the wake widening. It is difficult to say how the wheel downforce is influenced by the suction reduction over the top of the wheel, due to upstream moving separation, as well as in the upper wake and by an opposite increase in suction in the lower wake near to the ground. Based on the pressure distributions and table 4.1 it is suggested that the downforce will stay constant or increase slightly. The side force may reduce a little bit further due to the reduction of inflow into the wake, which implies less suction on the downstream inside edge.

- Region *V* represents the decreasing ride height branch of the hysteresis zone. The wheel drag hardly changes during this final reduction in wing ride height. It is expected that neither the flow physics nor the force coefficients differ qualitatively from those in the previous region.

- For the increasing ride height branch of region *VI* the wheel drag is constantly approximately 3% higher. At the upper boundary of the region the wheel drag reduces discontinuously to match the value in region *IV*. It is anticipated that the difference is caused by the changes in the upstream flow field, causing an instantaneous change in pressures on the wheel. The additional flow separation from the wing leads most likely to less interaction with the lower wheel wake and thus via less suction in this area to more wheel drag. This sudden change would result in more lift (or less downforce) from the wheel and a reduction in the side force as well.

From the above discussion it can be concluded that the flow mechanisms that cause the large difference between the two groups of force regions are easier to deduce from the results than the subtleties that cause the behaviour differences within the two groups. The next chapter will look at the influence of the wheel presence on the wing flow.

| | $C_D^s$ | | | | | $C_L^s$ | | | | |
|---|---|---|---|---|---|---|---|---|---|---|
| $h/c$ | P1 | P2 | P3 | P4 | P5 | P1 | P2 | P3 | P4 | P5 |
| | IWh | | | | | | | | | |
| - | 1.04 | 0.45 | -0.07 | 0.77 | -0.11 | -0.70 | -0.04 | 0.05 | -0.18 | 0.00 |
| | CWW2020 | | | | | | | | | |
| 0.106 | 0.97 | 0.51 | -0.08 | 0.54 | -0.10 | -0.58 | 0.03 | 0.04 | 0.19 | 0.05 |
| 0.211 | 0.96 | 0.54 | -0.05 | 0.51 | -0.09 | -0.61 | -0.08 | 0.03 | 0.22 | 0.06 |
| 0.264 | 0.95 | - | - | 0.44 | -0.10 | -0.61 | - | - | 0.30 | 0.07 |
| 0.317 | 1.01 | 0.64 | -0.13 | 0.48 | -0.11 | -0.73 | -0.23 | -0.01 | 0.12 | 0.04 |
| 0.458 | 1.14 | 0.72 | 0.00 | 0.74 | -0.10 | -0.77 | -0.16 | 0.00 | -0.11 | 0.00 |

Table 4.1: Sectional wheel force coefficients per pressure sensor location for the CWW2020 configuration via integration of the experimental 2D pressure distributions; see figure 2.2 for definitions of the pressure sensor locations.

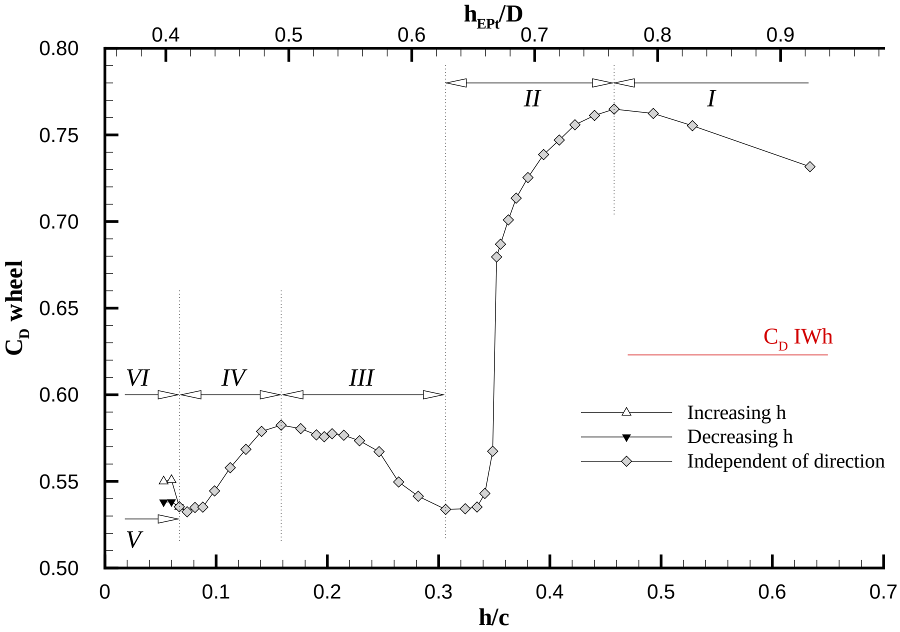

Figure 4.1: Variation of the experimental wheel drag coefficient with ride height for the CWW2020 configuration and definition of the experimental force regions; level for isolated wheel drag shown in red.

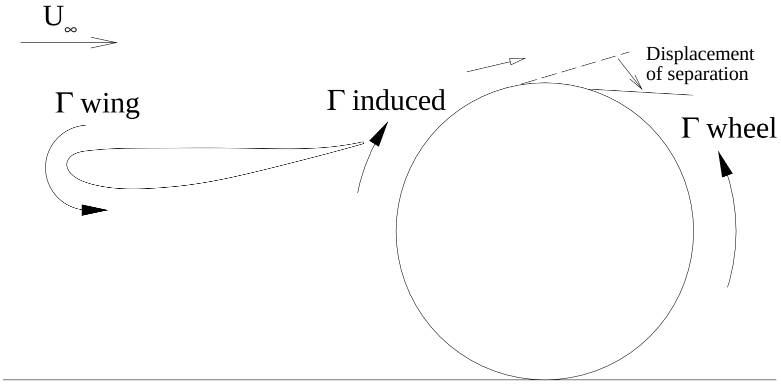

Figure 4.2: Schematic presentation of the wing induced circulation effect on flow separation from the top of the wheel; circulation indicated with black arrows, wing circulation induced velocity with white arrow and separation position movement with open arrow.

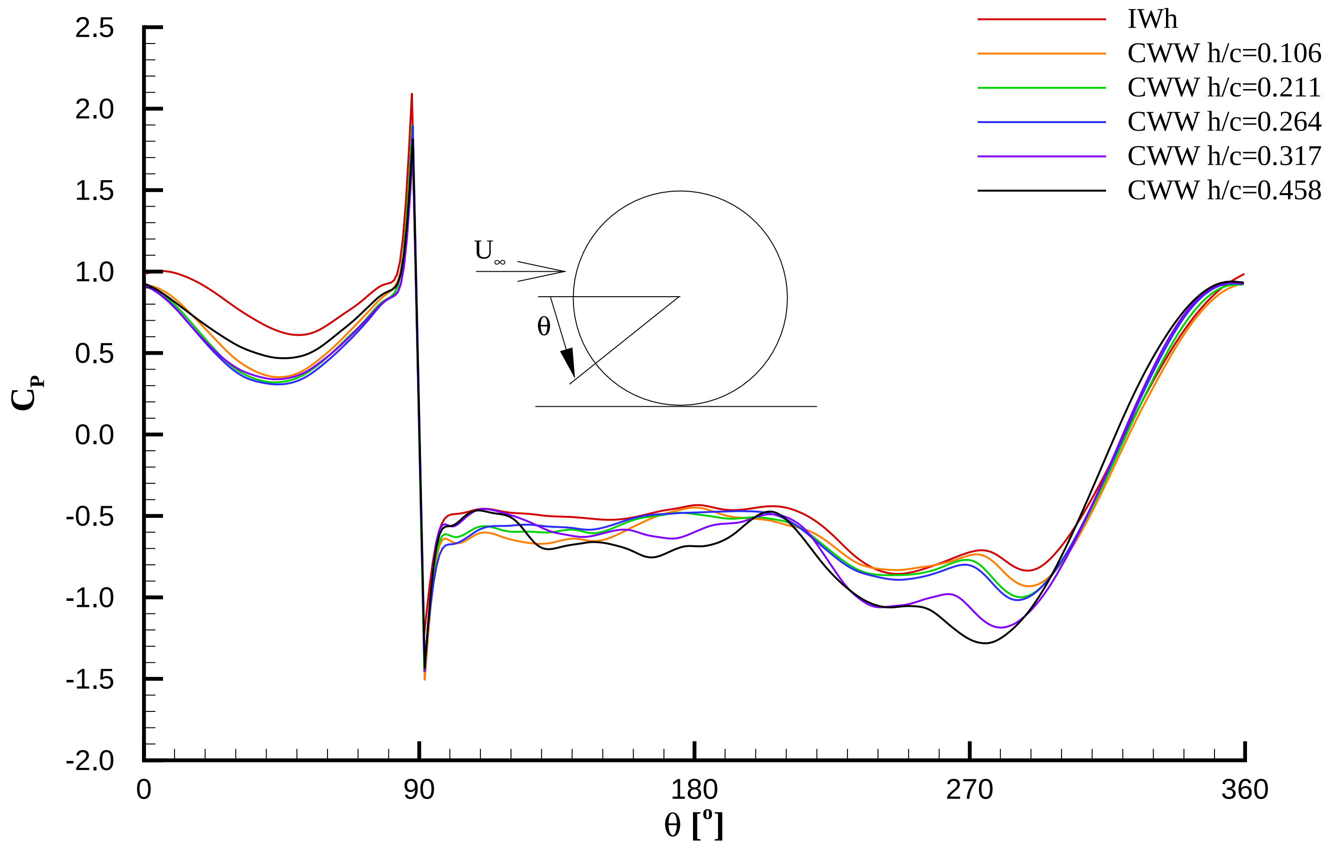

Figure 4.3: Pressure distribution around the centre of the wheel, location P1, for CWW2020 at various ride heights.

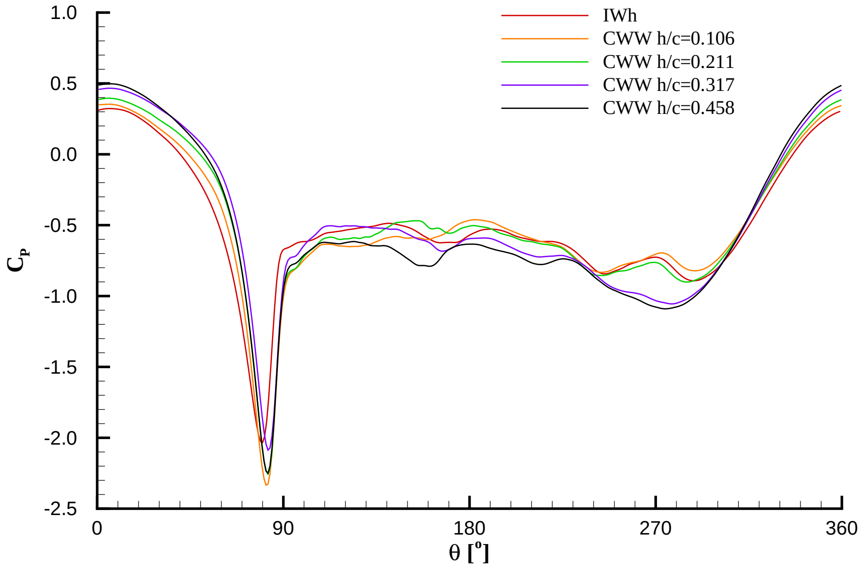

Figure 4.4: Pressure distribution around the outside contact patch of the wheel, location P2, for CWW2020 at various ride heights.

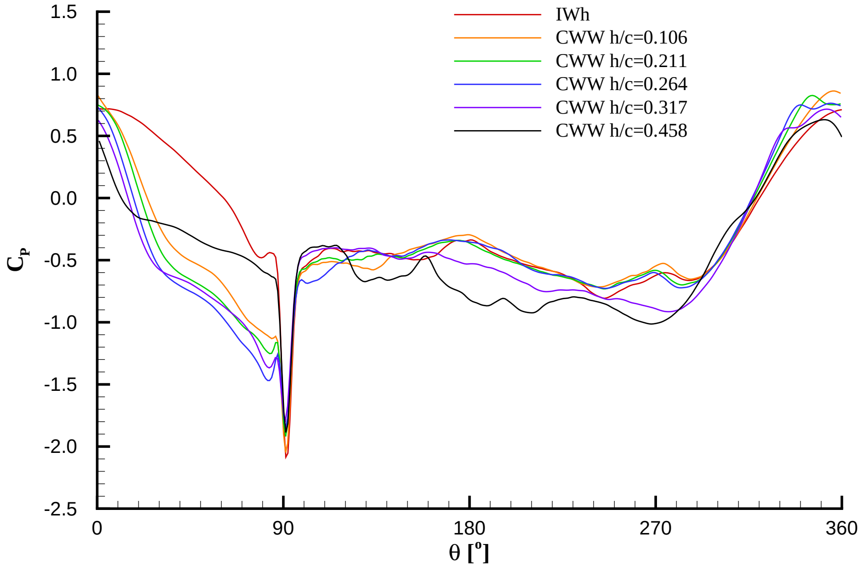

Figure 4.5: Pressure distribution around the inside contact patch of the wheel, location P4, for CWW2020 at various ride heights.

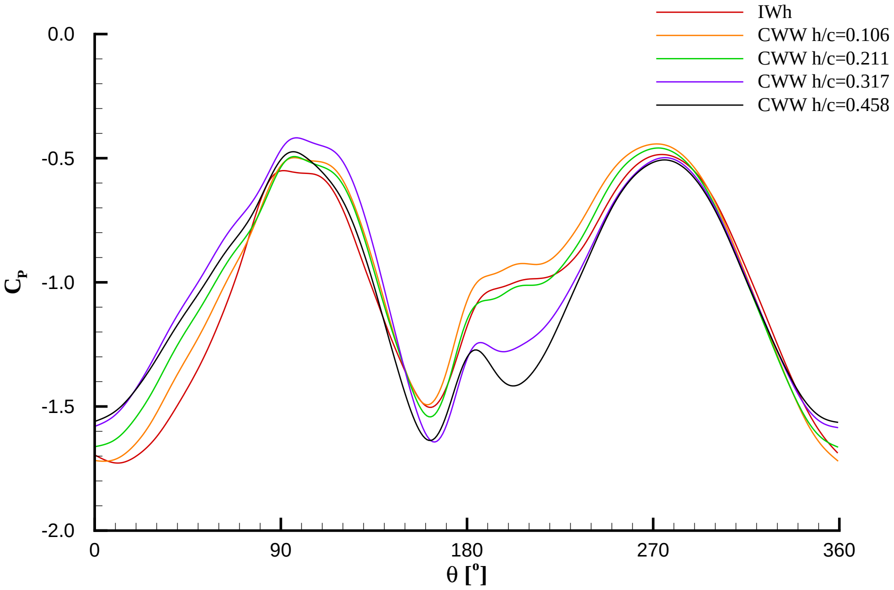

Figure 4.6: Pressure distribution around the outside side wall of the wheel, location P3, for CWW2020 at various ride heights.

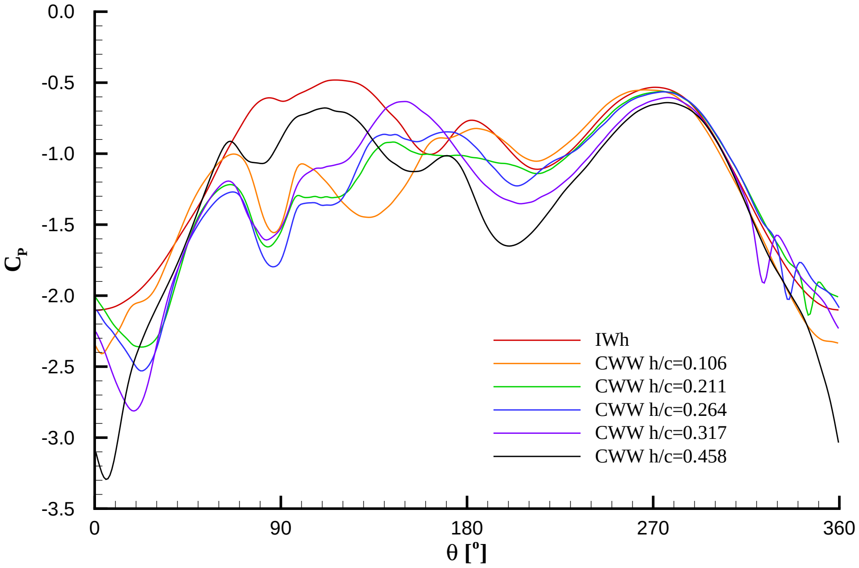

Figure 4.7: Pressure distribution around the inside side wall of the wheel, location P5, for CWW2020 at various ride heights.

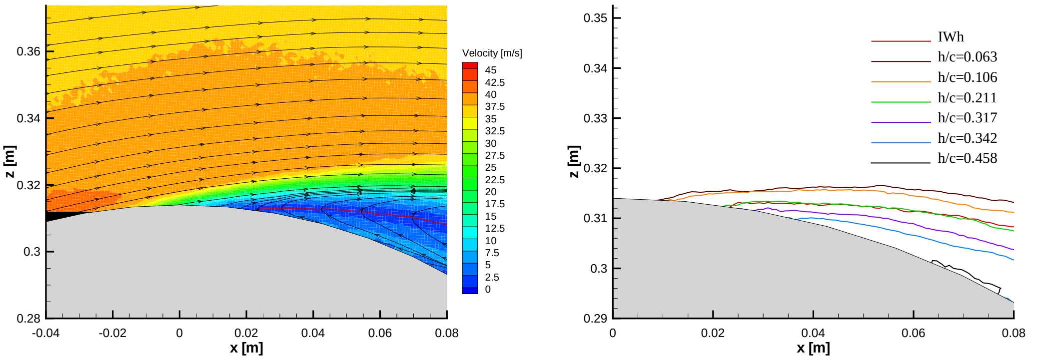

(a) Isolated wheel.

(b) Separation lines $U = 0m/s$.

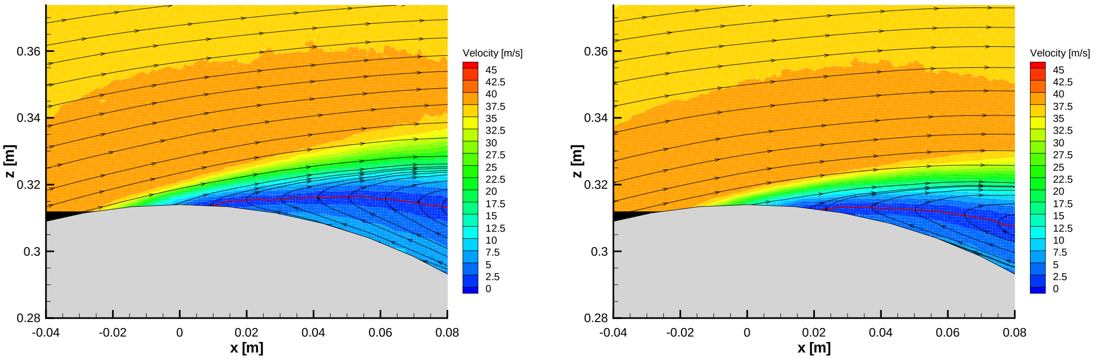

(c) $h/c = 0.063$.

(d) $h/c = 0.211$.

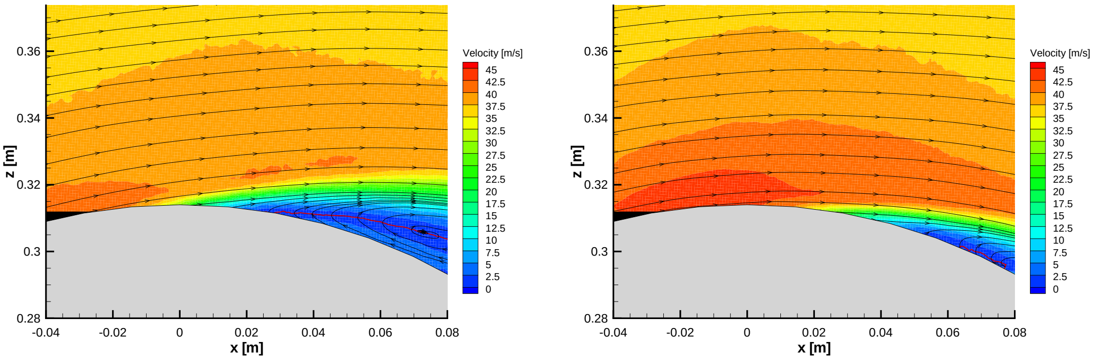

(e) $h/c = 0.317$.

(f) $h/c = 0.458$.

Figure 4.8: PIV results for the top of the port side wheel in CWW2020 configuration for various ride heights; vertical streamwise plane, $y = -0.353m$; $x$-position of origin at wheel axis; red lines in figures represent $U = 0$-curves.

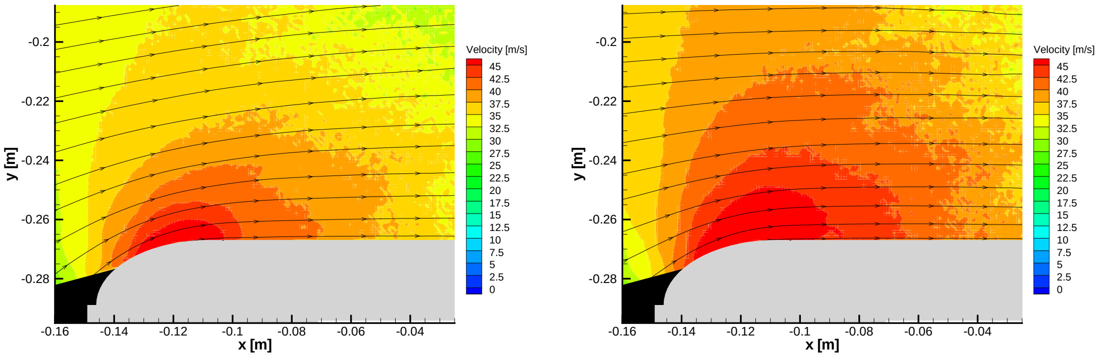

(a) Isolated wheel.

(b) $h/c = 0.063$.

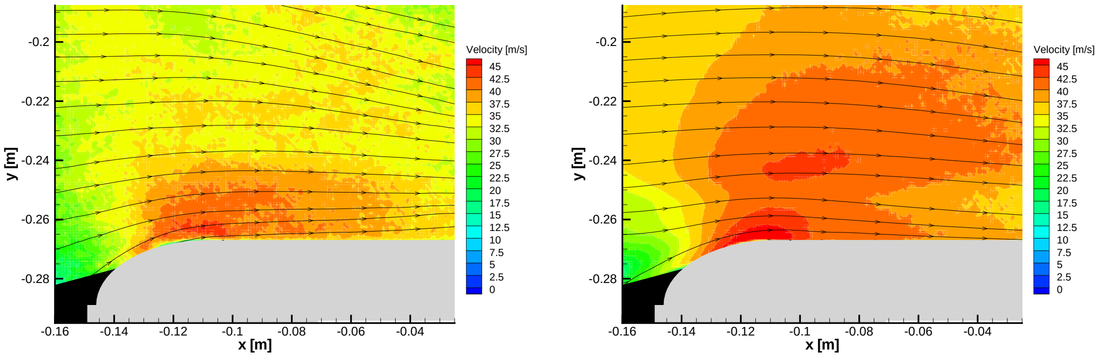

(c) $h/c = 0.211$.

(d) $h/c = 0.342$.

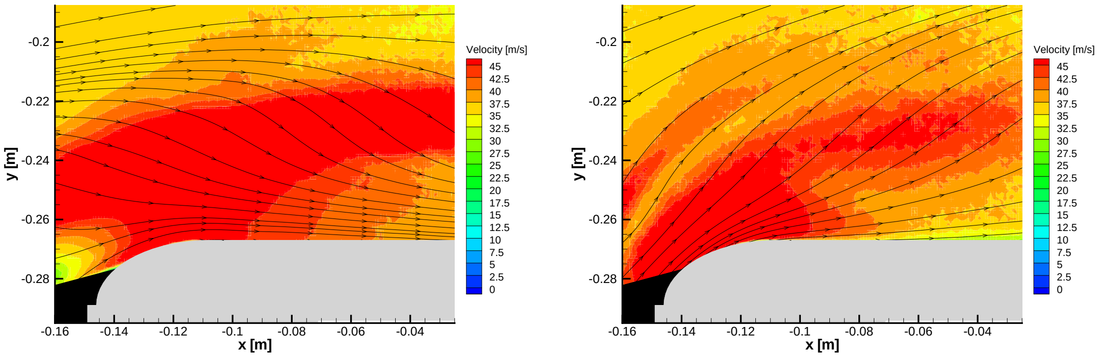

(e) $h/c = 0.528$.

(f) $h/c = 0.634$.

Figure 4.9: PIV results for the port side wheel upstream corner in CWW2020 configuration for various ride heights; horizontal streamwise plane, $z = 0.165m$; $x$-position of origin at wheel axis location.

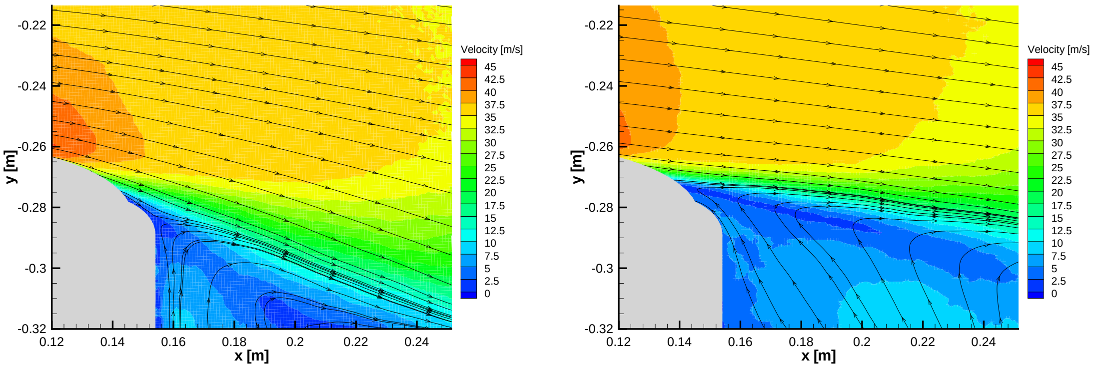

(a) Isolated wheel. (b) $h/c = 0.063$.

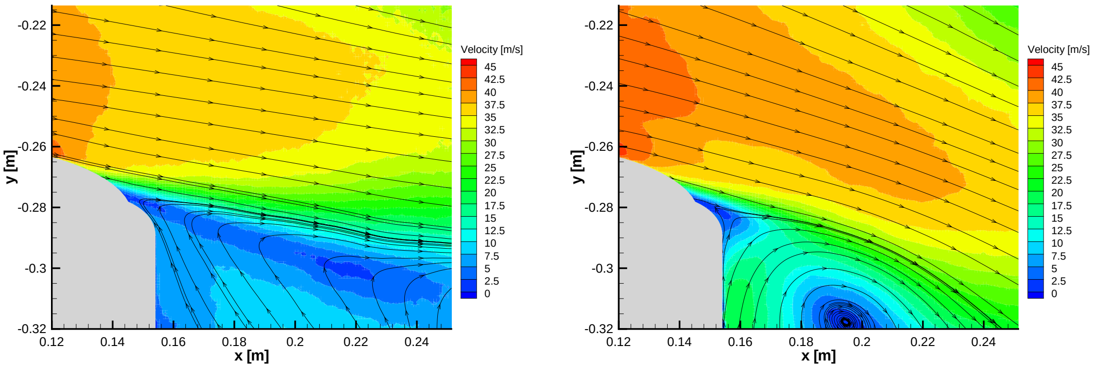

(c) $h/c = 0.211$. (d) $h/c = 0.342$.

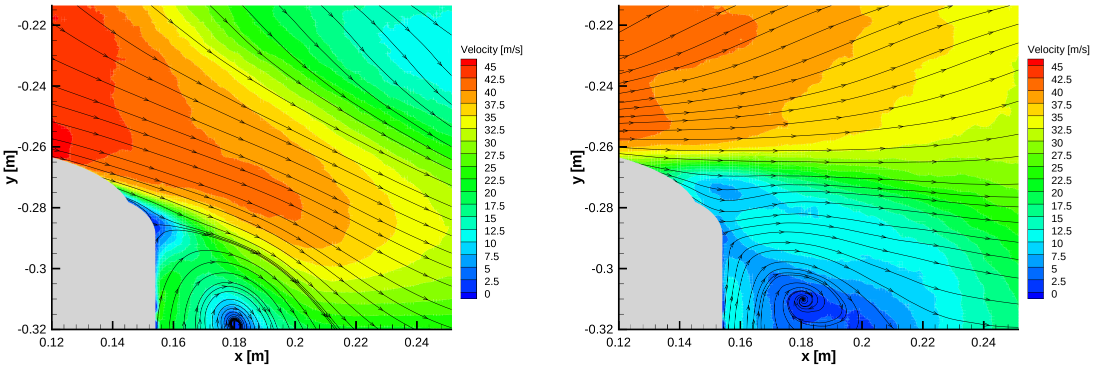

(e) $h/c = 0.458$. (f) $h/c = 0.634$.

Figure 4.10: PIV results for the port side wheel downstream corner in CWW2020 configuration for various ride heights; horizontal streamwise plane, $z = 0.174m$; $x$-position of origin at wheel axis location.

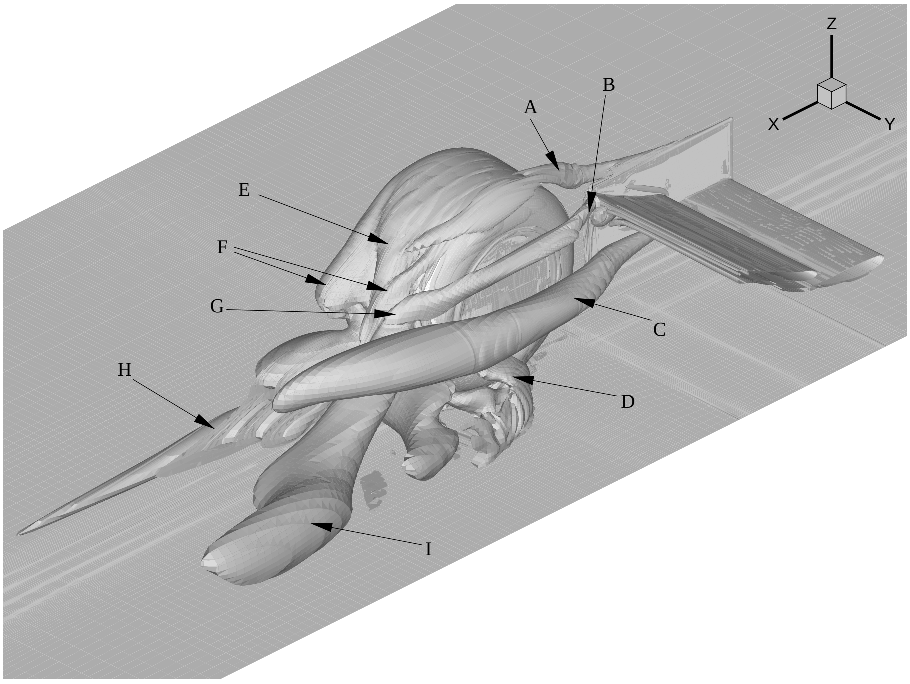

(a) Ride height in high wheel drag region.

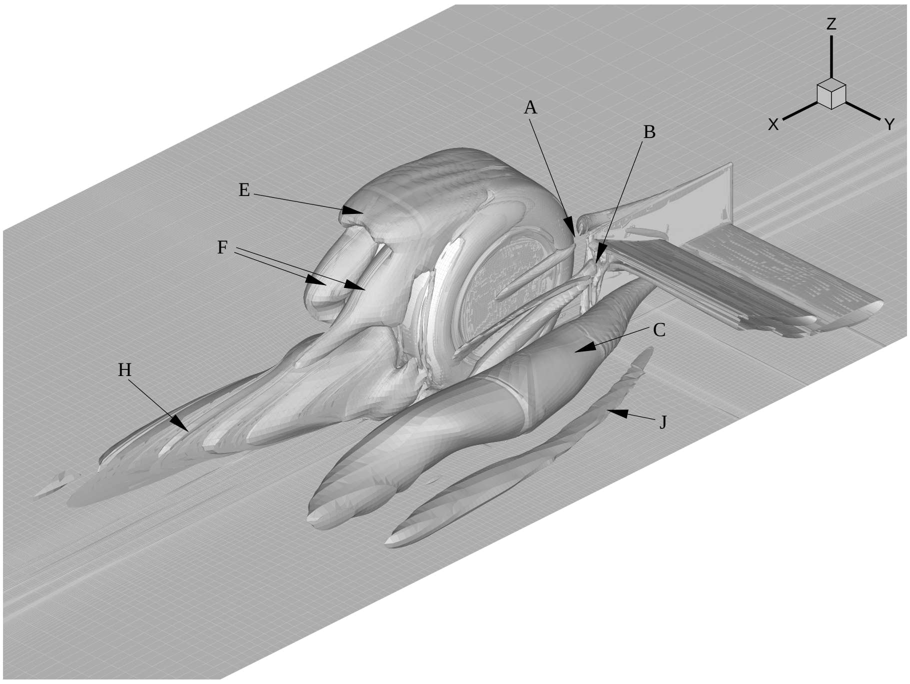

(b) Ride height in low wheel drag region.

Figure 4.11: Flow field topology for the CWW2020 configuration at high ($h/c = 0.458$) and low ($h/c = 0.211$) ride height; visualization based on iso-surfaces of $Q$ that were obtained from SRANS CFD simulations.

# Chapter 5

# Effect of Wheel Presence on Wing Aerodynamics

The wing obviously influences the aerodynamic behaviour of the downstream positioned wheel, as studied in the previous chapter. However, for subsonic flow conditions, the opposite happens as well and the presence of the wheel will therefore change the flow characteristics of the upstream located wing. This chapter analyzes the effect that the wing - wheel interaction has on the wing aerodynamics. The first section compares the force variation over the ride height range for the combined wing - wheel case with that for the isolated wing case. The next section looks at how the governing flow mechanisms, which have previously been derived for the isolated wing, are influenced by the wheel flow. Then, section 5.3 presents additional flow physics and features for the wing that occur due to the wheel presence. Finally, the last section discusses the wing aerodynamics for each of the different force regions that have been defined in the previous chapter for the wheel force behaviour.

## 5.1 Modified force behaviour

The downforce produced by the wing is affected by the wheel presence and the extent of the influence is ride height dependent. Figure 5.1 shows the downforce curves for both the CWW2020 configuration and for the isolated wing. The equivalent graphs for wing drag, pitching moment and centre of pressure location are presented in figures 5.2, 5.3 and 5.4 respectively.

The wing downforce is generally lower than for the isolated wing case, however from approximately $h/c = 0.15$ downwards the wing produces more downforce in the combined configuration. The maximum downforce value is 16.2% higher when the wheels are present and occurs at $h/c = 0.067$, on the boundary of the hysteresis zone. The hysteresis zone starts at a lower ride height for the combined case and the plateau in downforce for the isolated wing prior to this region is replaced by a section of continuous growth. Finally, the temporary local decline in downforce in region *b* for the isolated wing is not present in the combined case curve, whereas furthermore a new sudden rise in downforce can be noticed at the lower boundary of region *II*.

The drag follows a similar trend as the downforce for the combined case. At the highest ride height the value is equal to that for the isolated wing and then remains lower up till the end of region *II*. From then on it keeps growing, even when the isolated wing drag reduces again, and reaches a 30.8% higher maximum value than that for the isolated wing. The pitching moment around the $x = 53mm$-point shows lower absolute values up till region *III*, or the local maximum at the end of wing region *b*, from whereon it surpasses the isolated wing moment. The maximum pitching moment has a 14.1% higher absolute value and is reached at a $0.08c$ lower ride height. The centre of pressure location, at last, has moved downstream compared to that for the isolated wing, by approximately 2% of the combined chord. The variation in location with ride height is similar to that for the isolated wing, however the centre of pressure moves upstream at a faster rate compared to when the wheels are not present.

## 5.2 Influence on governing flow mechanisms

The downforce enhancing and limiting mechanisms that have previously been discussed for the isolated wing are also governing the behaviour of the combined configuration. However each of these mechanisms is influenced by the wheel presence and therefore the balance between them has changed as well, resulting in the modified force behaviour. In the following sections it will be analyzed what influence the wheels have on each of these mechanisms. Pressure data (figures 5.5 and 5.6), oil flow figures (5.7 and 5.8) and PIV figures (5.9) will once more be used to illustrate the changes.

### 5.2.1 Channeling effect

The channel, which causes diffuser-like flow acceleration for the isolated wing, consists of the ground and the wing elements in vertical direction and the endplates in spanwise direction. When the wheels are added to the configuration, the flow is further constrained downstream of the trailing edge by the wheel flow field, inducing a second acceleration of the flow into the extra channel between the wheels. The deflection of the lower edge wing vortices by the wheels - in case of a positive overlap between wing and wheels - gives rise to an additional reduction in channel cross section. Figure 5.10 shows that the centre span velocity under the wing is up to 7% higher due to the wheel presence at $h/c = 0.106$. However on the other hand, the same figure also reveals that for the higher ride height of $h/c = 0.317$ this velocity is lower for the combined configuration, especially near the wing surface.

Since the results in figure 5.10 are obtained at a centre span location it is expected that the influence of 3D effects is negligible and that the differences in velocity are caused primarily by the channeling effect. It can therefore be concluded that the channeling effect gets enhanced at lower wing ride heights, but that it is reduced at higher ride heights. It is suggested that the main reason for this is the additional influence of the wheel rotation. The wheel surface has an effective velocity component in downstream direction for any point beneath the wheel axis location, whereas this velocity is directed upstream for points above the wheel axis (see figure 5.11). The latter condition slows the wing flow down, leading to a reduction in the channeling effect. This could also explain why the reduction in channeling effect is larger close to the wing surface than near to the ground, because the limiting influence is dependent on the distance to the wheel surface. Figure 5.6 (a) gives an impression of the influence that the modified channeling effect has on the centre span pressure distribution for the wing. For $h/c = 0.141$ both cases produce a similar downforce level and the main element pressure distributions almost fall on top of each other. Above this ride height the combined configuration generates less suction than the isolated wing, whereas below this ride height it reaches larger suction values.

### 5.2.2 Separation effects

The downforce of the isolated wing is limited by separation from the suction surface of the main element for both of the hysteresis regions and also by flap separation for the increasing ride height branch. Furthermore small scale separation at the endplate / flap intersection occurs for the middle and higher ride heights, but this phenomenon has less influence on the wing forces. The downforce limiting mechanism at low ride heights that was attributed to detached separation by Mahon [12] has not been found experimentally and vortex burst is considered to be the limiting mechanism instead. All vortex effects, including bursting, will be discussed in the next section.

The oil flow picture in figure 5.7 (d) clearly shows that the wing still experiences trailing edge separation from both the main element and from the flap for the increasing ride height branch. The effect of the separation on the pressure distribution can be derived from figures 5.5 and 5.6, showing a more distinct plateau from $x/c \approx 0.3$ on the main element at the low ride height of $h/c = 0.063$ than for the isolated wing. The flap pressures indicate that the flow separates at centre span for the increasing ride height branch in a similar way as for the isolated wing. The main influence of the flap separation can however once more be recognized in the loss in peak suction for the main element (see figure 5.5), just like for the isolated wing.

The flap tip separation at the intersection with the endplate increases in significance and reaches to the trailing edge, when the wheels are present. These areas were already inclined to separation for the isolated wing and the additional adverse pressure gradient resulting from the downstream wheels causes separation to take place over the whole ride height range. A recirculation zone located at about half the flap chord can be recognized in the oil flow results of figure 5.7, followed by an expanding wedge that reaches its largest width at the flap trailing edge. The width of this zone at the trailing edge is ride height dependent and varies from $15mm$ at $h/c = 0.458$, via $50mm$ at $h/c = 0.317$ and $45mm$ at $h/c = 0.211$ to $22mm$ at $h/c = 0.063$. The separation zone is thus widest when the trailing edge of the flap is in close proximity to the wheel surface, just above the wheel centreline.

From the oil flow data on the endplates, see figure 5.8, it can furthermore be concluded that the separated zones reach all the way to the lower edge of the endplate for the higher ride heights. The imprint of the lower edge vortex never reaches the trailing edge of the endplate as a result, in contrast to for the isolated wing (see figure 3.20 (a) for example) at higher ride heights. The influence of the separated zones on the pressure distributions can only be examined for ride heights where the zones overlap the port tip pressure measurement location. The plateau-like suction on the flap from $x/c \approx 0.6$ onwards for $h/c = 0.211$ in figure 5.6 (b) gives the best example, while the $h/c = 0.141$ case still shows some effect, even though the separated zone hardly stretches this far in spanwsie direction.

### 5.2.3 Vortex effects

The lower edge vortex has either a downforce enhancing or a limiting influence for the isolated wing, depending on the ride height. For high ride heights till just above $h/c = 0.211$ the lower edge vortex enhances the downforce by generating additional suction on the downstream part of the main element and on the flap close to the endplate. This effect diminishes due to vortex dilution, resulting from downstream vortex breakdown, at which stage the lower edge vortex temporarily has no influence on the wing downforce. Eventually, however, the vortex bursts underneath the flap resulting in a loss of downforce at the tips. The same mechanisms are active for the combined configuration as well, but the extent of their influence changes due to the wheel flow field.

It is difficult to derive from the experimental data at which ride height the lower edge vortex exactly bursts for the combined configuration. Non-presented PIV data in a spanwise vertical plane $10mm$ downstream of the endplate shows that the vortex is still strongly present and coherent at $h/c = 0.211$, but that it is starting to break up at $h/c = 0.106$. This view is supported by the streamwise PIV data in figure 5.9. The oil flow pictures in figure 5.8 give the same impression, because flow reversal can only be distinguished close to the endplate trailing edge for the $h/c = 0.106$ case. For the isolated wing the influence of the vortex burst can be noticed as a reduction in suction at the tip from $x/c \approx 0.25$ onwards for the $h/c = 0.141$ and lower ride height cases in figure 3.17. However for the combined configuration this feature is only visible very close to the trailing edge from $x/c \approx 0.4$ and this could actually still be the same local dip in suction that is also present for the $h/c = 0.317$ combined case. Thus the pressures seem to indicate that vortex burst has not occurred above this ride height.

Finally the wing downforce in figure 5.1 shows a kink at $h/c = 0.141$ and one at $h/c = 0.113$. It is expected that the first one represents a data discrepancy of the following point[1], because the subsequent downforce growth is higher again, which would be hard to explain if the vortex has burst. From this it can then be derived that the vortex bursts just above $h/c = 0.113$, resulting in a consistent reduction in downforce growth. Although still growing at a considerable rate, the downforce no longer increases exponentially, but nearly linearly instead from $h/c = 0.113$ downwards. This is the clearest indication that the vortex has burst prior to this ride height. The downforce grows only slowly after

---

[1] The repeatability and uncertainty in region *IV*, where vortex burst appears, is worse than for the higher ride height regions and it is expected that this is related to the inherent instabilities involved in vortex breakdown and in the interaction phenomena with the wheel flow.

vortex burst for the isolated wing, however the growth is much larger for the combined case. This is partly caused by the channeling effect enhancement and partly by the fact that the influence of the vortex burst on the wing pressures is limited. Figure 5.9 explains this second reason, since it can be concluded that the reversed flow region is smaller due to the wheel presence and also deflected downwards by the wheel rotation. The velocity along the wing surfaces reaches higher values as a result, leading to less influence of the vortex bursting compared to for the isolated wing.

Additional PIV data (not shown) in a vertical spanwise plane $50mm$ downstream of the wheel revealed that the lower edge wing vortex is still coherent and distinguishable behind the wheel for higher ride heights down to $h/c = 0.317$. For the next lower ride height of $h/c = 0.211$ the vortex had broken up and lost its strength. The dilution in the plane downstream of the wheel compared to that upstream of the wheel is larger for the lower ride heights. At $h/c = 0.458$ the diameter has increased by approximately 70% while the circulation is 30% lower, whereas at $h/c = 0.317$ the diameter increased nearly 200% but with only 4% loss in circulation.

The wing downforce for the combined configuration shows no local drop, as seen for the isolated wing, when the lower edge vortex effect is no longer active due to vortex dilution from $h/c = 0.211$ downwards. Since it is difficult to distinguish between the influences of the channeling effect and of the lower edge vortex effect, it is hard to say how the wheels affect the latter. It could be suggested that the kink in downforce at $h/c = 0.141$ signals the end of the lower edge vortex effect, but no experimental proof for this statement is available. It is likely that the lower edge vortex effect has less influence on the wing downforce in general for the combined configuration, because the previously discussed separated zones at the flap endplate junctures limit the area on which the lower edge vortex suction operates. The nearly linear growth in the first part of region *III* can then be explained by the fact that the separation in this region is the largest, blocking out any influence of the lower edge vortex effect, which implies that the downforce increase results completely from the channeling effect. The following exponential growth in downforce for lower ride heights then indicates that the lower edge vortex effect is active as well, due to the reduction in size of the separated areas.

## 5.3 Additional physics

The wheel flow not only modifies the governing flow mechanisms in the previously discussed way, but also introduces a new mechanism and flow feature to the wing aerodynamics. First the additional flow mechanism, that results from the wheel rotation will be discussed, and then the new flow feature in the form of an extra wing vortex, which originates from the flap tip separation area, will be analyzed.

### 5.3.1 Wheel circulation effect

The additional circulation generated by the wheel rotation is responsible for a new flow mechanism. This circulation could affect the wing (tip) in a similar way as the circulation of a downstream located flap element would [71], because it has the same circulation direction. However, the influence of the circulation effect is dependent on the relative position of the wing and wheel, just like in the case of a flap which only delivers a positive contribution when it is positioned on the suction side of the main element. The conditions are comparable to that for a multi-element wing configuration when the trailing edge of the flap is positioned below the wheel axis, whereas, in order to mimic the influence of the gap between the elements of a wing, the flap trailing edge should be some distance below the wheel axis. When the flap trailing edge is at a similar or higher vertical position than the wheel axis, the effect will be reversed and the induced velocities will no longer be beneficial but have a negative influence instead. Figure 5.11 gives a visual explanation of this wheel circulation effect in the form of a schematic overview for high and low wing ride height.

This trend in the influence on the downforce can be recognized in the curve of figure 5.1, which shows that the downforce is larger than for the isolated wing case when the trailing edge of the flap is below 43% of the wheel diameter and vice versa. The positive influence of the circulation effect is best reflected in the pressure distribution for the suction side at the tip in figure 5.6 (b) for the lowest two ride heights, while the highest ride height shows the negative influence[2]. The increase in pressure on the pressure side of the flap also results from the wheel circulation effect.

---

[2] The extra suction for the $h/c = 0.317$ case compared to the isolated wing has previously been explained to result from recirculation in the endplate tip separation zone instead of from the wheel circulation induced velocities. This result, despite being for a ride height for which the influence should be negative, is therefore not contradicting the trend shown here.

### 5.3.2 New flow feature

The results of the CFD simulations show that the wheel presence results in the generation of an additional vortex from the wing flow field. This has been visualized as feature ‘B’ in figure 4.11. Despite being orientated in streamwise direction, like a longitudinal vortex, this additional vortex does not originate from a geometrical edge aligned in streamwise direction. Instead it is expected that, if this vortex exists, it starts from the almost stagnated flow field around the flap tip trailing edge separation on which a swirl velocity is imposed by the strong downwash from the wheel on the outside and the upwash resulting from the lower edge vortex on the inside. The resulting vortex has the same direction of rotation as the upper and lower edge wing vortex. CFD simulations show that the vortex extends past the wheel and that it interacts with the vortical structure over the side of the wheel for the higher ride heights (see feature ’G’ in figure 4.11).

Despite the clear presence of this vortex in the CFD predicted flow field, not much experimental evidence exists for the occurrence of such a phenomenon. The imprint of a vortex can be recognized in the pressure distribution on the side of the wheel in figure 4.7 in the first 45°-segment, but it is not possible to distinguish whether this results from the lower edge vortex or from the new additional vortex. Furthermore available PIV data in vertical spanwise planes do not give conclusive evidence either, because of the locations of the planes and the PIV resolution, especially close to the wheel. The existence of this additional vortex could be an interesting subject for future study. Nevertheless, due to the predicted trajectory in the CFD simulations, it is expected that the influence of such a vortex on the primary force coefficients of the wheel and wing will be limited. The main influence would probably be of an indirect nature via the interaction with the other vortices.

## 5.4 Discussion of force regions

The force regions, which have been defined in chapter 4 for the combined wing - wheel case, are based on the variations in wheel drag. The same force regions have been used here to discuss the wing force behaviour, in order to emphasize the relations between the changes in flow field and force behaviour. This implies that the force regions could be subdivided further, based on the wing physics, and this will be done if necessary. The following discussion explains the changes in the wing flow field from one force region to another and how these affect the force behaviour. The results will also be compared to the force variations for the isolated wing to derive the interaction effects resulting from the wheel presence.

Starting from a high ride height the force behaviour varies as follows for the regions:

- Region *I*, the wing downforce in this region is approximately 20% lower than that for the isolated wing, yet it grows at an almost similar rate. Reasons for the lower downforce are the negative influence resulting from the wheel circulation effect at these ride heights and the additional reduction in channeling effect due to the relative wheel wall movement. The increase in downforce with ride height reduction is caused by the increase in channeling effect and lower edge vortex effect, just like for the isolated wing. The growth in downforce increases, because the previously mentioned downforce limiting mechanisms reduce with decreasing ride height.

  The drag is initially on the same level as for the isolated wing case, because the largest downforce losses are concentrated around the leading edges, whereas some additional downforce is created by higher pressures on the pressure sides near the trailing edges, see figure 5.6. Both changes have a relatively large influence on the drag, as the first leads to a reduction in forward suction and the latter to additional pressure drag at the most upright location of the flap profile. The slower growth in wing drag for the combined case is a direct consequence of the lower downforce level and therefore lower induced drag. The centre of pressure has moved more than 2% of the total wing chord downstream with the wheels present, which reflects the changes in the wing pressure distributions. However, whereas the centre of pressure location is fixed for the isolated wing at these ride heights, the centre of pressure actually moves forward for the combined case. This reveals that the increase in downforce over this region is mainly caused by the increase in channeling effect.

- The higher ride height part of region *II*, is governed by the same flow mechanisms as the previous region. The distinction between both regions is made because of the maximum wheel drag occurring at the boundary between these regions, however the changes in flow physics in the wheel wake do not seem to cause qualitative alterations to the wing flow field. It is only just above $h/c = 0.35$ that fundamental changes start to take place. For the wheel it was discovered that the lower edge wing vortex starts passing on the inside of the wheel rather than over the top, which leads to a forward movement of the top separation position and widening of the wheel wake. The resulting sharp reduction in wheel drag is accompanied by a sudden increase in wing downforce near the lower boundary of this region. The wing pressure distributions reveal no qualitative changes during this downforce rise and it has to be concluded therefore that the downforce rise is caused by a global rise in suction over the wing. However the centre of pressure location moves a little bit downstream at the same time, implying that the downforce gains on the flap are relatively larger than those on the main element.

It is expected that the mechanism behind this rise in downforce is related to the wheel circulation effect changing from a negative to a positive influence for the wing flow. The flap will be most influenced by this since it is closest to the wheel. The coupling between the wing and wheel flow field alterations can possibly be attributed to the fact that the increased circulation for the wing and acceleration on the wing suction surfaces lead to lower pressures on the inside of the wheel, which sucks the upper edge vortex away from the top of the wheel. The increased circulation also delays the separation over the wheel top further, while the longer attached flow in turn generates a stronger recirculation in the wheel wake. The wing drag follows the same trend as the downforce and the increase is thus mainly due to the downforce induced contribution.

- Region *III* sees a nearly linear growth in downforce down to $h/c \approx 0.23$, followed by an exponential growth for the lower ride heights. The main contributor to the linear growth is the continuously increasing channeling effect, which is enhanced compared to the isolated wing case by the wheel circulation effect. The sum of the flap tip separation effect and the lower edge vortex effect seem to average each other out. The exponential growth for lower ride heights signals the end of this fine balance, since the influence of the separation effect reaches its maximum around $h/c = 0.317$ and then diminishes with ride height reduction. The influence of the vortex dilution, resulting in a local minimum in downforce as noticed for the isolated wing, is not present for the combined case. This is partly because the lower edge vortex survives longer due to the enhanced channeling effect and partly because the channeling effect overshadows the lower edge vortex effect for the combined case. The quicker growth for the lower ride heights compared to that for the isolated wing reflects both the enhanced channeling effect and the shifting balance of the lower edge vortex effect and the flap tip separation effect. The drag behaviour is still mainly influenced by the downforce induced component, although the flap tip separation causes an additional increase over the first part of the region. The upstream movement of the centre of pressure shows that the main element profits most from the (enhanced) channeling effect.

- Region $IV$ is governed by the same mechanisms as the previous region and the boundary between them once more results from a (local) maximum in wheel drag. Within region $IV$ the wing flow physics do however change as the lower edge vortex bursts, most likely around $h/c = 0.113$. It is possible to divide this region into a part before the vortex burst (region *IVa*) and one after (region *IVb*). The first part forms a direct continuation of region *III*, whereas region *IVb* is characterized by a slower, almost linear, increase in downforce. The downforce reaches much higher levels in this region than for the isolated wing. The enhancement of the channeling effect and the limited influence of the vortex bursting are responsible for the continuous growth, whereas in contrast these mechanisms are balanced for the isolated wing. The centre of pressure moves even faster upstream after the vortex burst, because the flap tips are mostly affected. The drag rise is again primarily downforce induced. The suction peak moves towards the lowest point of the element and the transition shifts downstream in this region as well, just like for the isolated wing.

- Region $V$ starts at the beginning of the hysteresis behaviour. Both this decreasing branch and the increasing branch are governed by the same mechanisms as for the isolated wing case. The reduction in downforce results from centre span trailing edge separation from the main element. The extra increase in drag rise is because the loss of channeling suction on the first part of the main element is not compensated by extra suction near the trailing edge of the flap due to recirculation, as is the case for the increasing branch. It is interesting to see that the downforce drops off at a similar ride height as for the isolated wing, whereas the hysteresis is postponed to a $0.02c$ lower ride height. The first observation leads to the conclusion that the adverse pressure gradient at which the main element trailing edge separation becomes dominant must be reached at a similar ride height. Figure 5.6 (a) shows indeed that the pressure difference between the suction peak and the trailing edge is roughly similar for both cases at $h/c = 0.063$. The reason that the combined case can reach larger suction peak values on the main element without detrimental separation is that the wheel circulation effect and enhanced channeling effect allow the suction side of the flap to recover to a more negative pressure value on the trailing edge. This in turn allows a higher suction peak on the main element and a higher suction on the trailing edge of the main element, as can be derived from figure 5.6 (a). The later start of the hysteresis zone is also a direct consequence of these larger suction values on the flap trailing edge, which postpone flap separation caused by adverse pressure gradient growth.

- Region *VI*, the increasing branch, shows the same behaviour as the equivalent region for the isolated wing. The sudden change in downforce over the boundary is caused by full chord flap separation at centre span, see figure 5.7 (d). The resulting reduction in circulation leads to a loss in suction on the main element, which explains the local downstream movement of the centre of pressure at the boundary.

The major influence of the wheel on the wing flow is thus related to the wheel circulation. Additional influence can be noticed from the adverse pressure gradient resulting from the wheel presence, which results in flap tip separation near the endplates. The following chapter will look at the influence of overlap and gap variations on the combined wing - wheel results.

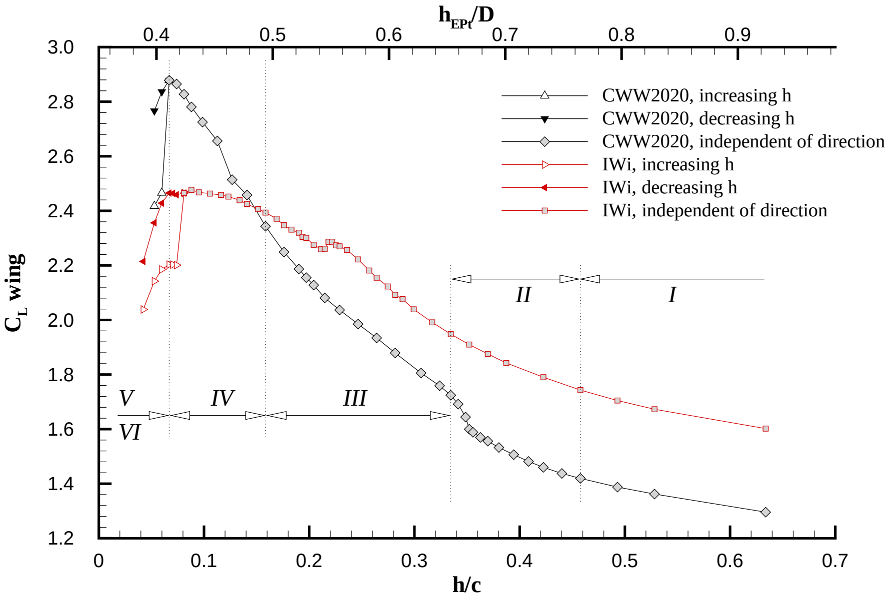

Figure 5.1: Variation of the experimental wing downforce coefficient with ride height for the CWW2020 configuration and visualization of the experimental force regions.

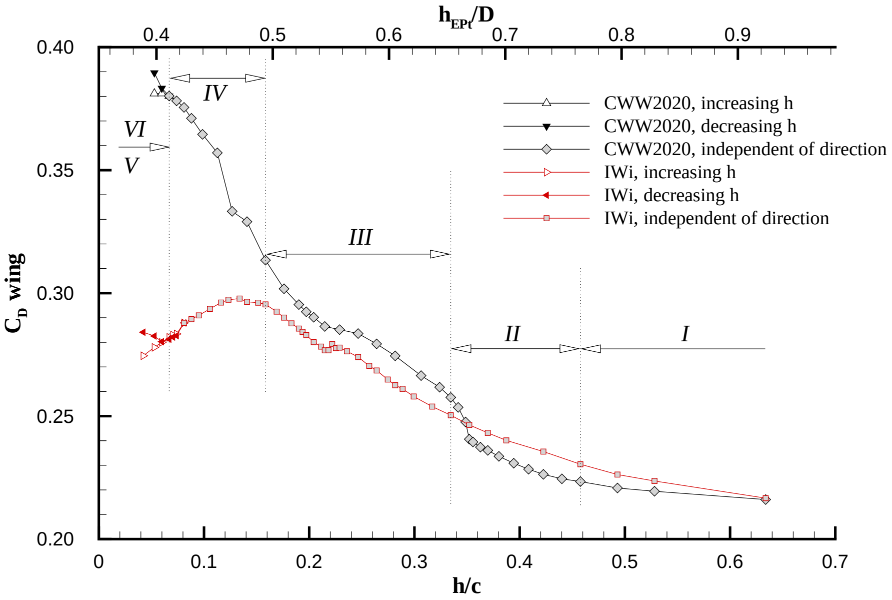

Figure 5.2: Variation of the experimental wing drag coefficient with ride height for the CWW2020 configuration.

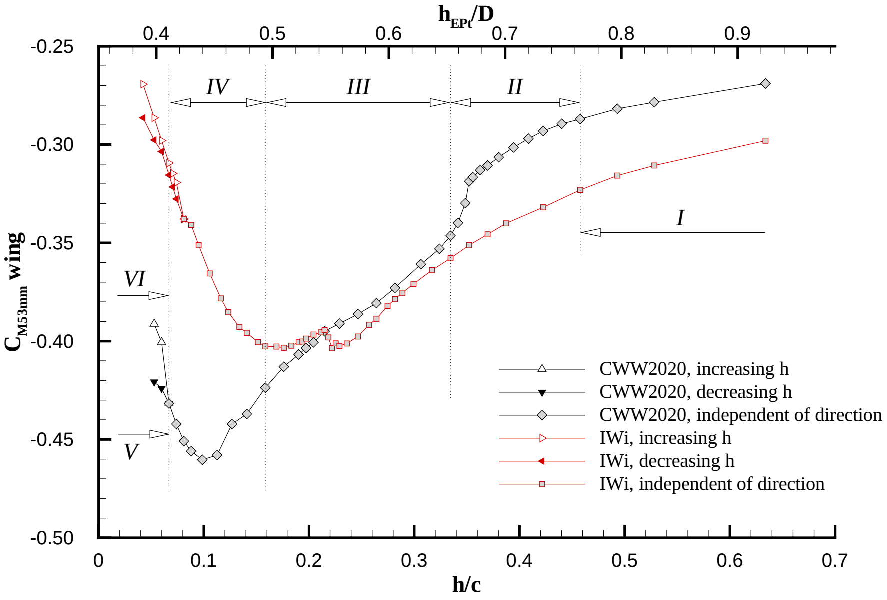

Figure 5.3: Variation of the experimental wing pitching moment coefficient around $x = 53mm$ with ride height for the CWW2020 configuration.

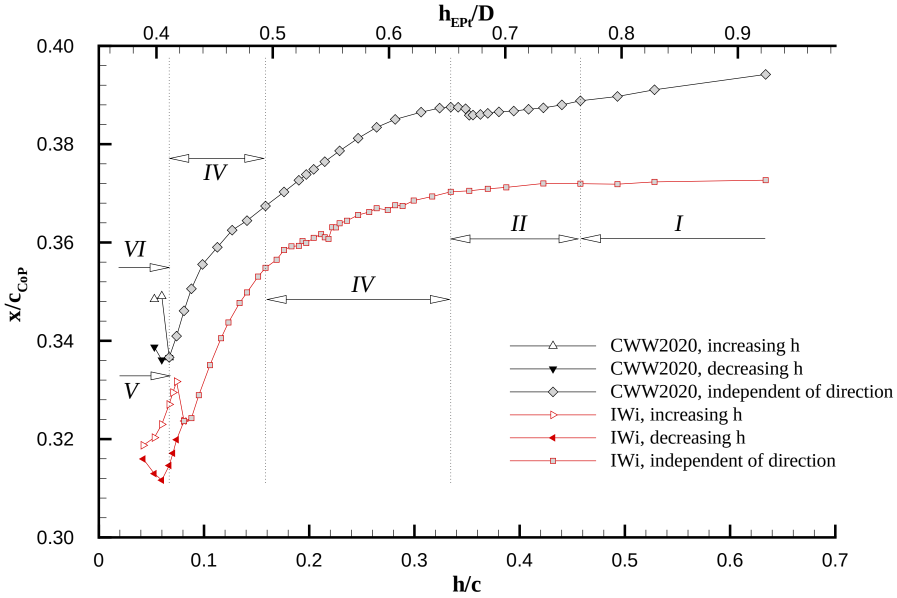

Figure 5.4: Variation of the experimental wing centre of pressure location with ride height for the CWW2020 configuration.

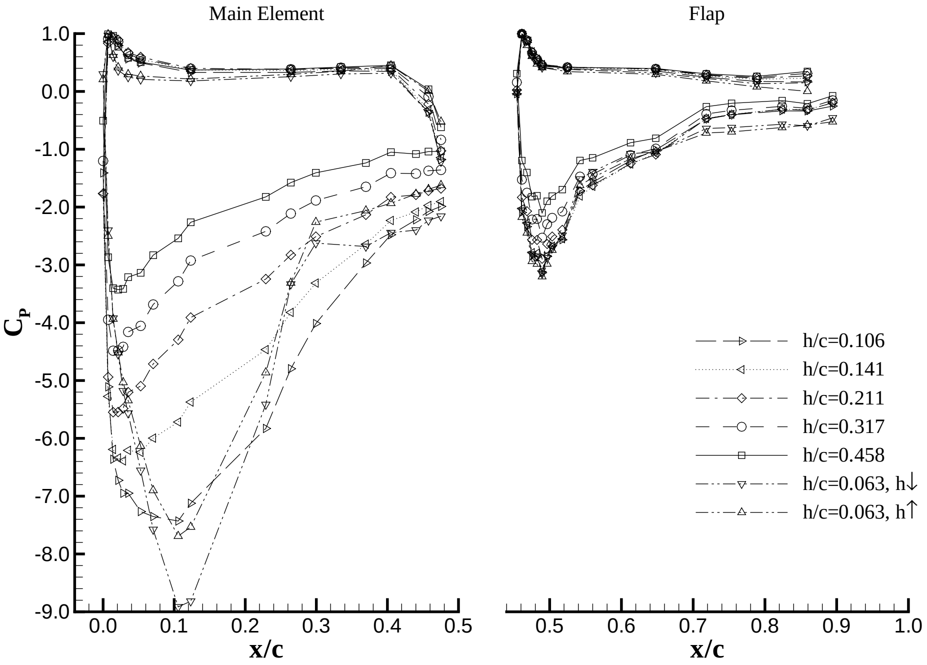

(a) Centre span, $y/c = 0$.

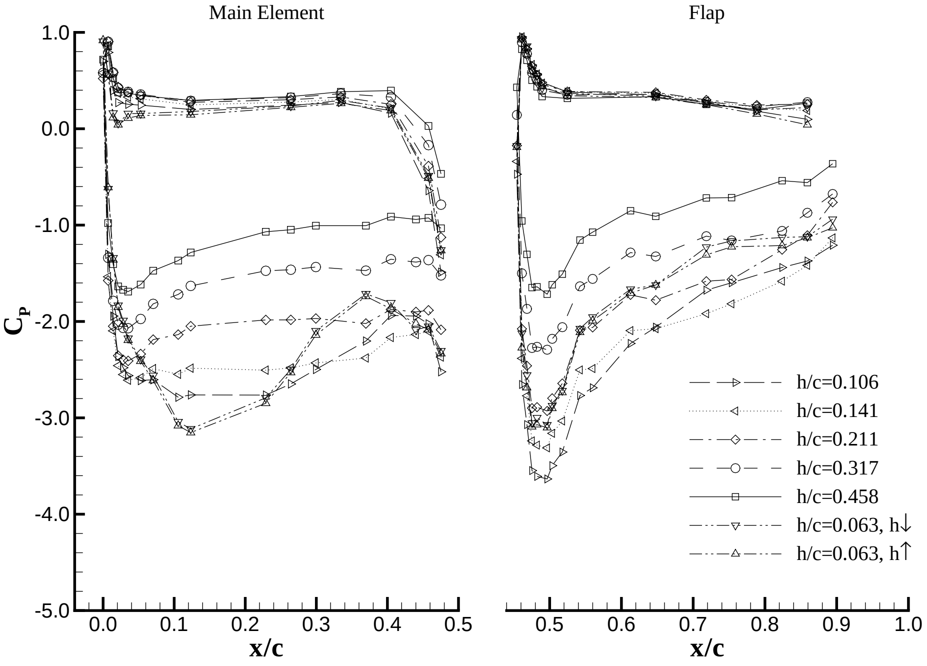

(b) Port tip, $y/c = -0.933$, $25mm$ inboard of the endplate.

Figure 5.5: Chordwise pressure distributions for the wing in CWW2020 configuration for a selection of ride heights, main element and flap at centre span (a) and at the port tip (b).

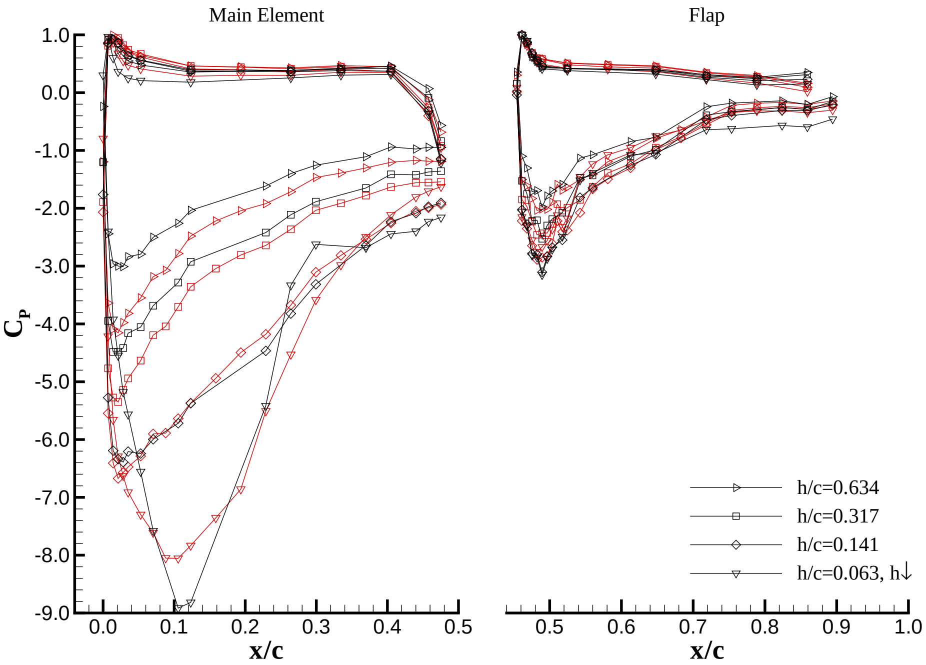

(a) Centre span, $y/c = 0$.

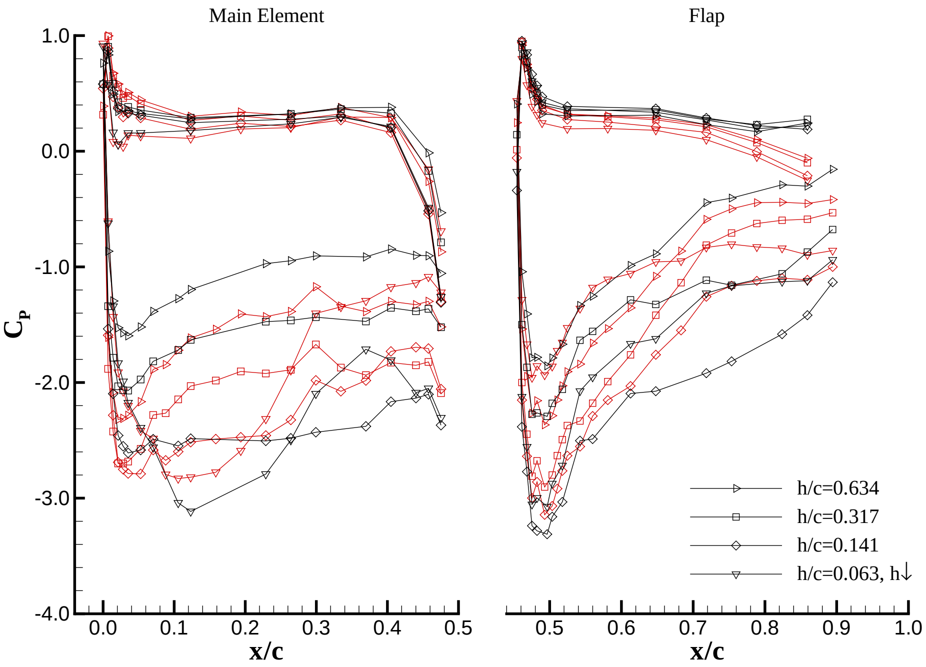

(b) Port tip, $y/c = -0.933$, $25mm$ inboard of the endplate.

Figure 5.6: Comparison of chordwise pressure distributions for the isolated wing (red) and CWW2020 configuration (black) for a selection of ride heights, main element and flap at centre span (a) and at the port tip (b).

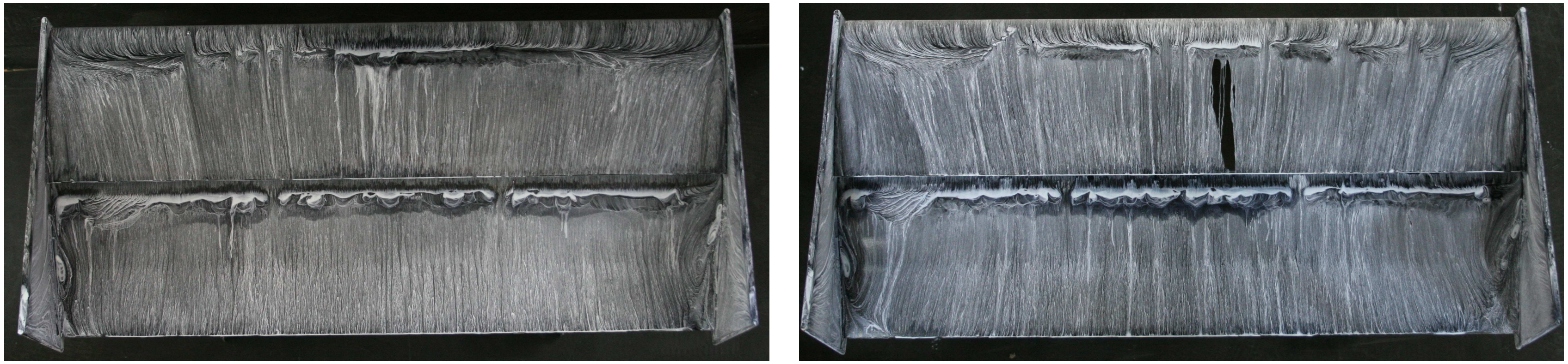

(a) Boundary of $I$ and $II$ at $h/c = 0.458$.

(b) In region $III$ at $h/c = 0.317$.

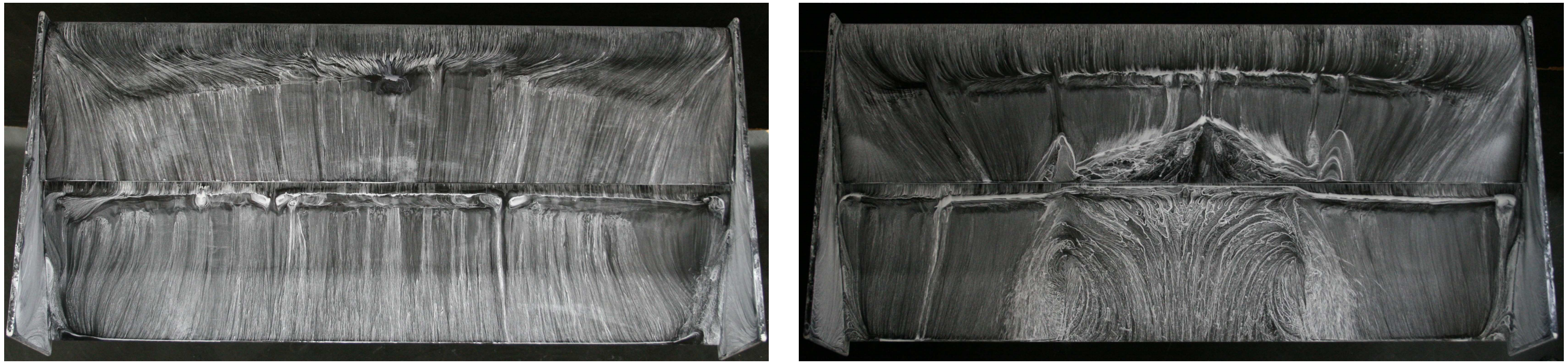

(c) In region $IV$ at $h/c = 0.106$.

(d) In region $VI$ at $h/c = 0.063$, increasing $h$.

Figure 5.7: Surface streaklines on the suction side of the isolated wing for the CWW2020 configuration, visualized with oil flow (flow direction from top to bottom).

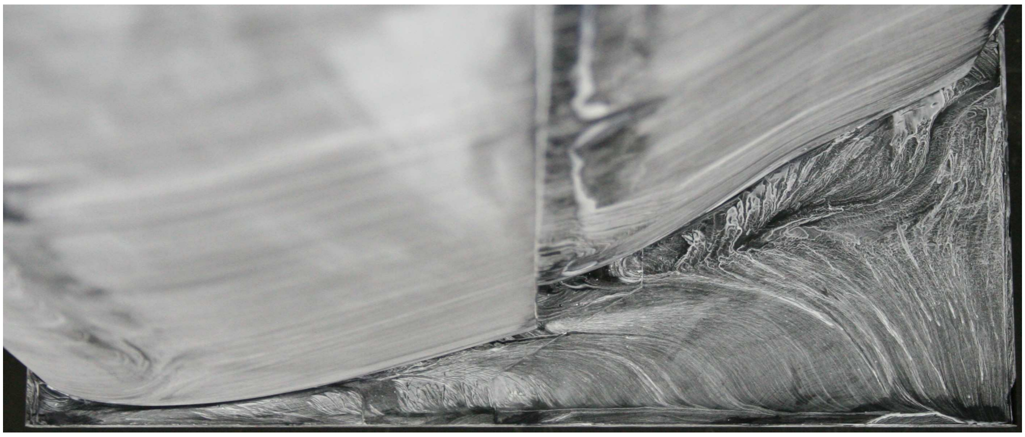

(a) In region $II$ at $h/c = 0.342$.

(b) In region $III$ at $h/c = 0.211$.

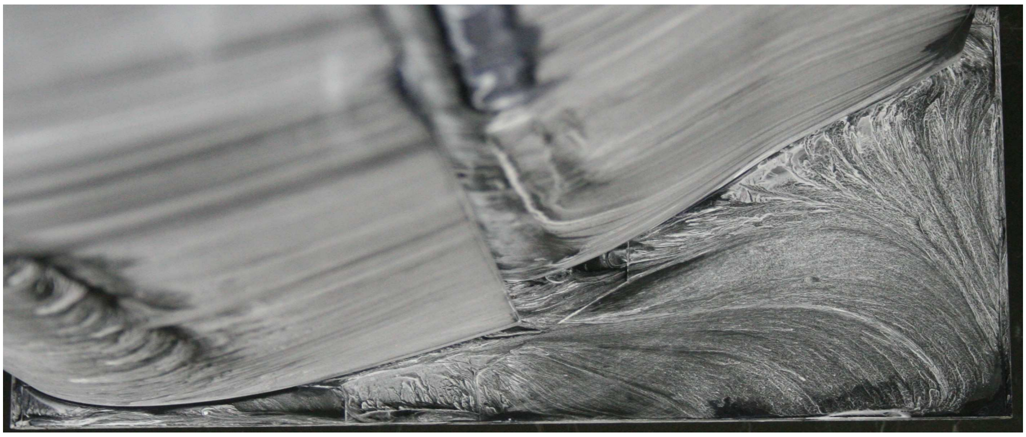

(c) In region $IV$ at $h/c = 0.106$.

Figure 5.8: Surface streaklines on the inside of the starboard endplate for the CWW2020 configuration, visualized with oil flow (flow direction from left to right).

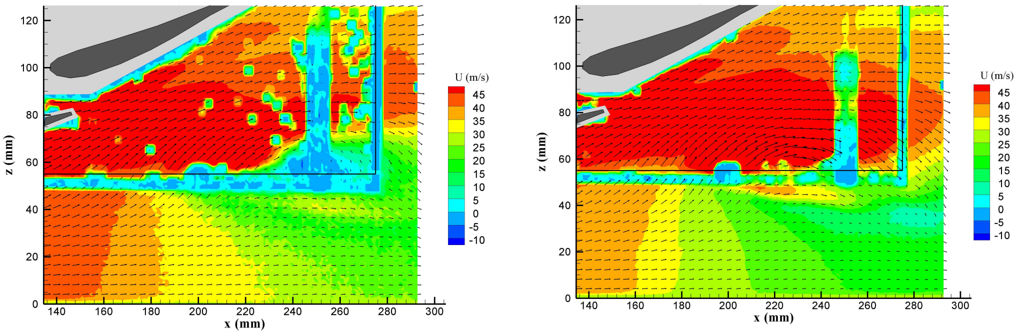

(a) $h/c = 0.211$, boundary of $b$ and $c$.
(b) $h/c = 0.211$, region *III*.

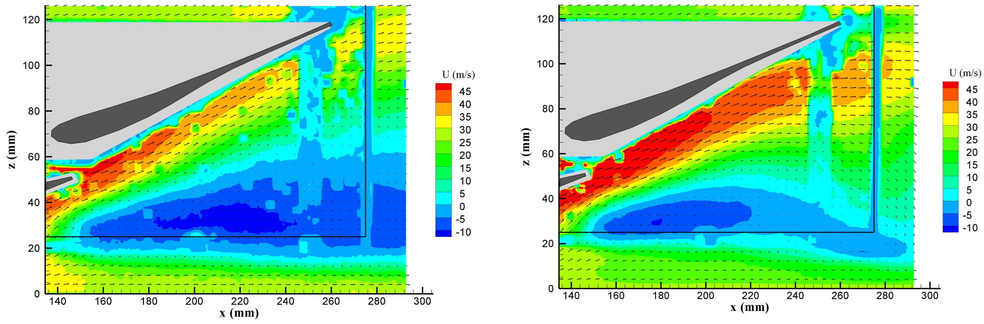

(c) $h/c = 0.106$, region $d$.
(d) $h/c = 0.106$, region *IV*.

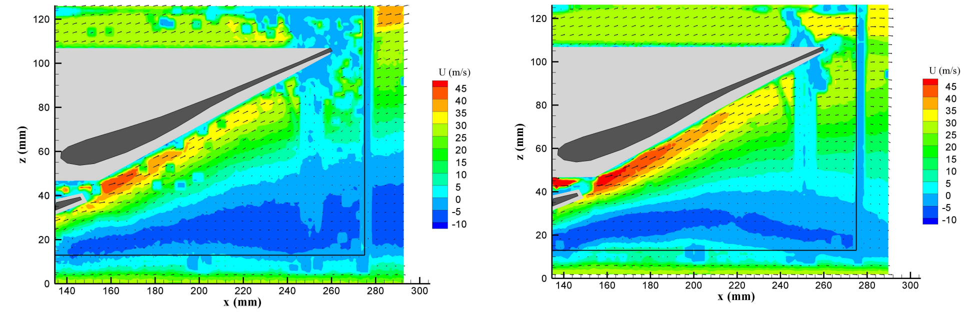

(e) $h/c = 0.063$, increasing $h$, region $f$.
(f) $h/c = 0.063$, increasing $h$, region *VI*.

Figure 5.9: Time-averaged $x$-velocity contours and velocity vectors from PIV data in a streamwise plane at $y/c = -0.933$, $25mm$ inside of the port side endplate, for the isolated wing (left) and CWW2020 configuration (right); flow from left to right, showing the endplate outline (black lines), the elements (dark grey; no exact representation) and blanked out areas due to reflections, shadows and parallax effects (light grey).

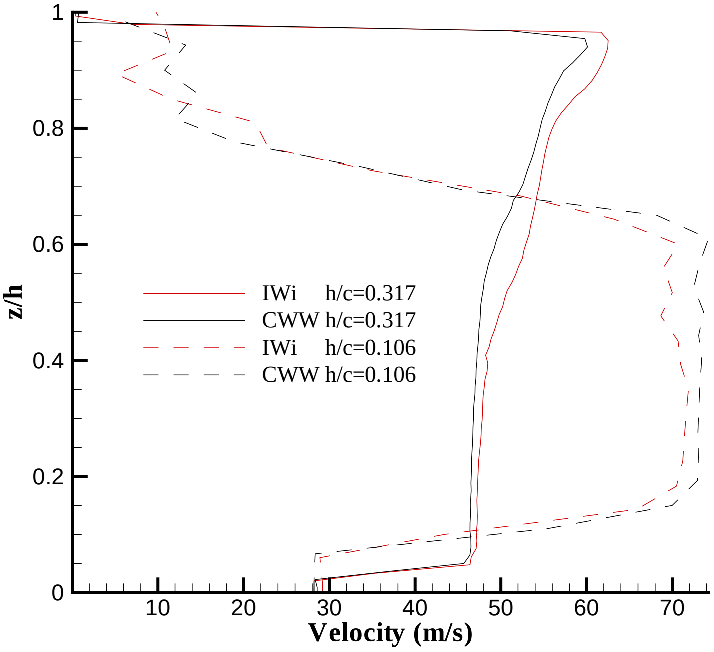

Figure 5.10: Influence of wheels on channeling effect under wing for IWi and CWW2020 configuration; centre span at lowest point main element, $x/c = 0.112$; presented Velocity is the combination of $U$- and $V$-component; data extracted from PIV, parallax effects block data close to wing and ground, especially for $h/c = 0.106$.

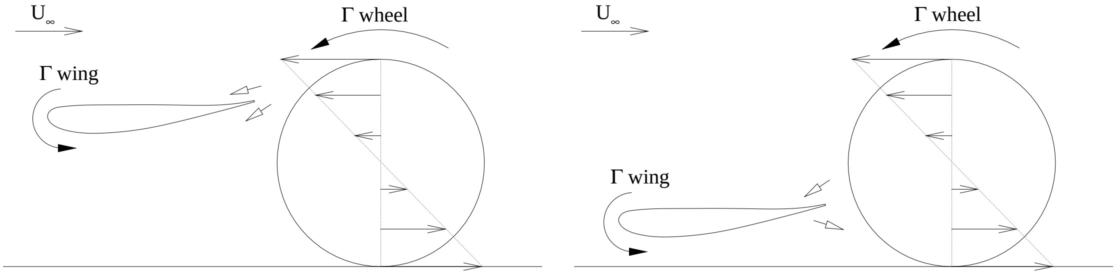

Figure 5.11: Schematic presentation of the wheel circulation effect; negative influence for high ride heights (left) and positive influence for low ride heights (right); circulation indicated with black arrows, freestream and wheel velocity with open arrows and wheel circulation induced velocity on trailing edge of wing with white arrows.

# Chapter 6

# Influence of overlap and gap settings

The previous two chapters examined the influence of the wing on the wheel and vice versa for fixed baseline overlap and gap settings. Additional experimental results have been obtained for different overlap and gap setting combinations. Force data has been acquired for an arbitrary selection of settings with the overlap ranging from $-15mm$ to $50mm$ in combination with a gap variation from $10mm$ to $55mm$. The results that will be presented here are primarily restricted to those with only one parameter variation at a time; so with either a $20mm$ overlap and varying gap, or with a $20mm$ gap and varying overlap. However it needs to be kept in mind that the trends with overlap or gap variation are dependent on the value of the other fixed parameter as well. The ride height resolution has been reduced compared to the baseline settings and this can have an effect on the accuracy of the region boundaries. Pressure (only at the wing tip, figure 6.1, and on the wheel for the P1 and P5 locations, figures 6.2 and 6.3), oil flow and / or PIV data have been used to confirm the proposed ideas, whenever available, but this set of data for overlap and gap variations is very limited compared to that for the baseline settings.

The following sections discuss the broad influence of overlap and gap variations on the governing mechanisms, force behaviour and regions. The resolution of the force data set and of the additional on-surface and off-surface results is insufficient to define force regions in the overlap - gap parameter space. However with four or five data samples it is possible to give an indication of the trends that occur for overlap and gap variations. Unlike the baseline ride height variation, which spans quite an extreme range with non-practical upper and lower limits in order to improve the understanding of the flow physics, the overlap and gap variations have been kept within realistic boundaries that are representative for real racecar settings. This chapter is subdivided in four sections that investigate in subsequent order the influence of overlap and gap variations on the wheel aerodynamics followed by the effects of the same parameter changes on the wing aerodynamics, concluding with a summary.

## 6.1 Effect of overlap on wheel aerodynamics

The discussion of the influence of overlap on the wheel aerodynamics centers around figure 6.4, which shows the wheel drag curves for five different overlap values at the constant baseline gap setting. The overlap settings can be divided into two different categories: those with an effective positive overlap (50, 35 and $20mm$) and those with no or with negative overlap (0 and $-15mm$). For the last configuration the wheel is no longer located behind the wing in streamwise direction, but slightly offset away from the symmetry plane, leaving a $15mm$ opening in spanwise direction between wing and wheel, measured at a height of $150mm$ above the ground.

**High ride heights** At high ride heights before the sudden wheel drag change, in the first two force regions, the force behaviour primarily results from the delayed separation effect over the top of the wheel and from the wake effect. The actual value of the global maximum of the wheel drag is also heavily dependent on the channel inflow effect, because the deflection of the lower edge wing vortex around the most upstream part of the wheel takes place at a similar ride height as that for which the maximum wheel drag occurs. The resulting suction of the vortex imprint has the largest effect on the wheel drag when the location of the imprint is closest to $\theta = 0°$, which is - if upwards or downwards deflection of the lower edge wing vortex in streamwise direction are neglected - around $h/c = 0.5$.

An increase in overlap would then require more inflow around the wheel front corner, which leads to a larger suction imprint of the lower edge vortex on the wheel and thus to a reduction in wheel drag. It is however expected that more overlap also results in a larger horizontal cross flow away form the wheel, which limits the inward deflection of the wheel wake and therefore changes the location of the recirculation centre. Zero or negative overlap would in contrast induce less vortex suction on the front of the wheel, because the wing vortex requires no deflection around the wheel and thus leaves hardly any imprint on the wheel surface. Under these conditions the flow can turn more easily into the wheel wake as well, leading to a higher suction level in the recirculation region on the back of the wheel and thus to an even higher wheel drag.

This general trend can be recognized in figure 6.4, which shows an overall reduction in wheel drag with increasing wing - wheel overlap. Furthermore it can be seen that the decline in drag for the ride heights above the global drag maximum is slower when the overlap is larger. This is most likely caused by the separation delaying effect that the upper wing vortex has when it passes over the top of the wheel. This mechanism is most effective when the overlap is positive and the vortex passes over a larger part of the wheel. The influence reduces when the overlap disappears or becomes even negative, leading to earlier top separation, less suction in the upper wake region and thus to a faster drag reduction.

**Low ride heights** For the lower ride heights, when the upper edge wing vortex passes on the inside of the wheel, the drag value is mainly dependent on the channel inflow effect and on the lower wake effect. The general trend for the channel inflow effect is similar to that for the higher ride heights: more overlap leads to more suction on the front of the wheel and thus to a lower drag. However, as mentioned for the baseline settings, the largest suction on the wheel results when either the accelerated flow of the lower edge vortex or near the flap trailing edge is closest to the wheel. In between these ride heights the channel inflow effect has less influence, which is one of the reasons for the drag rise with decreasing ride height in region *III*. The offset between the minimum wheel drag on the upper boundary of this region and the local maximum on the lower boundary becomes larger as well with increasing overlap, because the difference between minimal and maximum channel inflow effect increases.

Figure 6.4 shows the general reduction in wheel drag with increasing overlap, but it can also be seen that the variation in wheel drag over the lower ride height regions is larger for increasing overlap, as expected. Another interesting influence of the overlap variation on the force behaviour is that hysteresis effects are noticeable in the wheel drag for the positive overlap cases, whereas these disappear for the zero and negative overlap. For the latter two cases the wheel drag of the increasing branch is now nearly identical to that of the decreasing branch, without any instant discontinuity over the region boundary. This is a further indication that the hysteresis effects in the wheel drag are directly resulting from differences in the wing flow field, since they are only experienced when the wheel is effectively exposed to the wing wake due to a positive overlap.

**Concluding remarks** From the previous analysis it can be concluded that the channel inflow effect is the mechanism that is most affected by overlap variations. It is this mechanism that causes the change in wheel drag behaviour and the primary trend is that a larger positive overlap leads to a stronger channel inflow effect and to a general lower drag. A secondary effect is that the variation in wheel drag with ride height for the lower ride height regimes becomes less extreme with reducing overlap. The decline in drag for the ride heights above the global maximum drag is larger for cases with less overlap, because the upper edge wing vortex delays the separation over a smaller part of the wheel for these cases. All these trends are visible for the cases with a baseline gap setting of $20mm$ in figure 6.4, however they are partly obscured by variations in region boundary locations. It is worth mentioning that the three available cases with a $35mm$ gap setting show these trends more clearly and for almost constant region boundary locations[1], proving the point that the trends are gap setting dependent as well. The local maximum at $h/c = 0.211$ for the CWW3520 case seems to be a setting dependent feature, which could not be studied in more detail due to the lack of additional relevant experimental data..

The available pressure distributions for the wheel, see figures 6.2 and 6.3, enhance the above argument on the influence of overlap variations on the flow mechanisms. It can be concluded that the suction around and above $\theta = 180°$ on the centreline reduces from the $20mm$ case to the $35mm$ overlap case at $h/c = 0.458$ due to the wider wake. Furthermore it is interesting to see that the suction just after the contact patch has increased at $h/c = 0.106$ due to the larger overlap. However to confirm the proposed physics it would be necessary to have pressure data for different locations, for example P4, which has unfortunately not been obtained.

The lack of experimental pressure data for the wheel for different overlap settings also makes it difficult to study the influence of overlap variations on the wheel lift and sideforce. Therefore only a global indication can be given here. It is assumed that the wheel lift mainly varies due to the top separation. Since this separation is delayed over a larger part of the wheel when the overlap increases, it is expected that the wheel lift generally becomes larger with increasing overlap. The side force on the other hand is

---

[1] The $20mm$ gap cases have been selected for presentation nevertheless, because for $35mm$ gap only three (0, 20 and $35mm$) overlap settings were available instead of the five for $20mm$, which includes one with a negative overlap. The reasons that the $35mm$ cases show a more regular trend are probably that the channel inflow effect becomes more gradual with the larger gap and that the analyzed overlap variations are smaller, which ensures that the balance of the flow mechanisms does not change fundamentally within this range.

mainly determined by the suction due to the channel inflow effect on the side of the wheel. The suction on the upstream part of the wheel will increase for larger overlap, but it could be that the downstream part experiences less suction due to the wider wake. It is impossible to say, without additional data, what the overall effect of this would be on the sideforce.

## 6.2 Effect of gap on wheel aerodynamics

The influence of gap variations on the wheel drag can be derived from figure 6.5. In contrast to the influence of overlap, it seems that the gap variations have little effect on the general drag level. The two characteristics of the drag curves that are visibly influenced instead are the location of the local wheel drag minimum on the lower boundary of force region *II* and that of the global maximum on the upper boundary. The key change seems to be that the sudden change in wheel drag moves to a lower ride height when the gap increases. Changing the gap setting does not lead to such a fundamental alteration of the balance between the mechanisms, as experienced when the overlap was varied and thereby the channel inflow effect enhanced or reduced, but to a shift of the ride heights at which the mechanisms operate.

Based on these observations it is expected that the governing influence of the gap variations is related to how easily the upper edge vortex can change its trajectory. For ride heights below the sudden change in wheel drag this vortex passes on the inside of the wheel, but for higher ride heights the vortex goes over the top of the wheel. The vortex requires a certain distance in streamwise direction in order to be able to manoeuvre from one trajectory to the other and it is expected that a small gap restricts this transformation. The wheel drag still rises with increasing ride height for small gap values, but only at a higher ride height and at a slower rate (see the $10mm$ gap case in figure 6.5). The reason for this is that the drag rise is caused by a reduced vortex interaction and recirculation in the wake since the upper edge wing vortex is not involved in these processes. Furthermore the separation over the top of the wheel only results from the wing circulation effect, without enhancement by the upper edge vortex, which will lead to less separation delay and therefore to a lower drag. For a large gap on the other hand, the upper edge vortex is more easily sucked to the top of the wheel by the low pressures in this area. This leads to a drag rise at lower ride height and to a larger drag increase, as can be seen for the $50mm$ gap case in figure 6.5.

Not only does the sudden change in wheel drag move to a lower ride height with increasing gap, but the global maximum moves in the same direction. The drag at the highest ride height of $h/c = 0.634$ is lowest for the case with the largest gap, since the drag reduces at a comparable rate after the maximum in wheel drag for each of the gap settings. At low ride heights however the drag curves nearly fall on top of each other, showing that the wheel drag is relatively independent of the gap setting under these conditions. The hysteresis effects for each of the gap settings are also comparable to that for the baseline case. The location of the local maximum in wheel drag at the lower boundary of region *III* seems unaffected by gap variations as well, however the value of this local maximum decreases with increasing gap. This could possibly be related to a reduction in suction in the lower wake, because the flow turns in slower for a larger gap setting.

The information that can be extracted from the pressure distributions for the wheel reveal a few new details, but are once more not detailed enough to explain all the changes. For the $h/c = 0.106$ height the centre pressures show generally less suction when the gap is increased form $20mm$ to $50mm$, but for $h/c = 0.458$ the loss in suction seems to be concentrated over the top of the wheel. Interestingly, figure 6.3 shows some kind of imprint just below the top of the wheel for the $50mm$ gap case at $h/c = 0.458$. It could be that the upper edge wing vortex starts slipping back to the side of the wheel for these settings and ride height, since it can be concluded from figure 6.5 that the wheel drag has been reducing over a longer ride height interval since the maximum value compared to the baseline case.

The wheel lift and sideforce most likely show a similar behaviour as for the baseline case, but with modified force region boundaries. The sudden change in wheel drag at a lower ride height for a larger gap, for example, will also result in a change from wheel downforce into wheel lift at this lower ride height due to the delayed separation. The sideforce will also reduce at this height, because the upper edge vortex no longer passes on the inside of the wheel, creating suction on the wheel side.

## 6.3 Effect of overlap on wing aerodynamics

The influence of overlap variations on the wing downforce is portrayed in figure 6.6. The same five cases are presented as for the study of the influence of overlap on the wheel drag. The cases with positive overlap will be discussed separately from those with zero or negative overlap, because of the differences in displayed behaviour.

**Positive overlap** The wing downforce for a combined wing - wheel configuration is dependent on a combination of mechanisms; both the channeling effect, which is either enhanced or reduced by the wheel circulation effect, and the lower edge vortex effect enhance the downforce, while the separation effects and vortex burst have a limiting influence. The reduced channeling effect and the flap tip separation near the endplate are responsible for a reduction in downforce at high ride heights, compared to the isolated wing case. The negative influence of both of these mechanisms increases for larger overlap settings and it can therefore be seen in figure 6.6 that the wing downforce level is lower in the highest three force regions for larger overlap settings. For low ride heights however the channeling effect is enhanced by the wheel presence and the vortex burst influence reduced compared to for the isolated wing case. These positive effects enhance the downforce at low ride heights in comparison to the isolated wing case. Both effects also become more dominant with increasing overlap, leading to a potentially higher downforce level for larger overlap settings. This trend is visible for force region $IV$ in figure 6.6. The highest downforce level is however obtained for the $35mm$ overlap case instead of for the larger $50mm$ overlap. This is probably caused by the extent of the flap tip separation, which covers a larger area for the latter case and thus having a more limiting influence on the downforce.

The hysteresis effects are influenced by the overlap settings as well, as can be concluded from figure 6.6. The start of the hysteresis zone moves to a higher ride height for larger overlap values. The width of the channel between the wheels reduces with increasing overlap, since the wing span is kept constant, which means that the secondary channel acceleration increases proportional to the overlap. It is expected that the rise in adverse pressure gradient, that this causes, can only be overcome at a higher ride height for larger overlap cases. This would then result in a longer lasting hysteresis zone for cases with larger overlap. A final point about the wing downforce is that the overlap also affects the characteristics of the sudden downforce change at the lower boundary of region $II$. Due to the resolution of the curves it is difficult to derive the effect from the $20mm$ gap cases, but the $35mm$ gap cases (not shown) once more show a clearer trend. From this data set it can be concluded that the downforce increase at this boundary becomes larger with increasing overlap. It has previously been discussed for the baseline settings that the mechanism behind this rise in downforce is the change from a negative to a positive influence of the wheel circulation effect. The reason that this rise is bigger for larger overlap settings can then easily be related to the larger area of the wing that is exposed to this mechanism when the overlap increases.

The influence on the wing drag is presented in figure 6.7, which includes the baseline case and the $50mm$ and $-15mm$ overlap cases. The wing drag for the largest positive overlap setting is everywhere lower than for the baseline settings. The general difference in level can be explained to result from the lower contribution of the downforce induced drag component for the $50mm$ overlap case and from the difference due to the larger flap tip separation zones. The drag level in the hysteresis zone is still lower for the larger overlap case, even though the downforce is at a comparable level here, which implies that the stronger flap tip separation zones yield less drag. The additional drag resulting from the flap tip separation is largest in region *III* and seems enhanced compared to the baseline setting, as would be expected since the flap tip separation area has increased for the larger overlap. The contrast between maximum separation influence in region *III* and minimal influence at low and high ride heights has increased, but the actual drag value stays below that for the baseline setting, despite the extra separation drag in region *III*.

The curve of the centre of pressure location for the $50mm$ overlap case is included in figure 6.8. It can be noticed that the centre of pressure lies, in general, more upstream for the larger overlap. It is interesting to see that it moves faster upstream at the higher ride heights than for the baseline case. This is caused by the larger flap tip separation areas, which lead to downforce losses on the flap. The downstream movement at the lower boundary of region *II* is larger as well, which is in line with the explanation that the increase in downforce at these heights is related to the wheel circulation effect. This effect primarily influences the tip of the flap element and a positive influence of this effect thus leads to a downstream movement of the centre of pressure.

Finally, the port tip wing pressure distributions for the CWW5020 case are presented in figure 6.1. This figure shows that the pressures on the suction side for the $50mm$ overlap case are nearly always below those for the $20mm$ case. The larger influence of the flap tip separation zone due to the bigger overlap can be recognized as a more prominent plateau from $x/c = 0.6$ onwards. Furthermore it can be seen that the pressures on the upper surfaces near the trailing edges have increased for both elements as a result of the larger influence of the wheel circulation effect. The pressure distributions for the baseline and $50mm$ overlap setting are very similar at this port tip location for $h/c = 0.063$ , which is in agreement with the comparable downforce levels.

**Zero and negative overlap** The global trends that were derived for the cases with positive overlap also hold for those with zero or negative overlap. Thus figure 6.6 shows that the general downforce level increases from the baseline setting to the $0mm$ overlap case, whereas the $-15mm$ overlap setting features the highest downforce at high ride heights of all the combined configurations. However the downforce is still considerably below that for the isolated wing, even for this $-15mm$ overlap case. The wheel presence therefore has a detrimental effect on the wing downforce, except for at the lowest ride heights. The sudden downforce increase at the lower boundary of region $II$ seems to reduce still with reducing overlap, even when the overlap becomes negative, although this is more difficult to see due to the resolution of the data around this height.

The main difference for the cases without physical overlap is however that the downforce growth in region $IV$ is reduced from a certain ride height downwards. For both the $0mm$ and $-15mm$ overlap case this happens between $h/c = 0.123$ and $0.095$. A similar but less severe reduction in downforce growth from $h/c = 0.113$ has been discovered for the baseline case with $20mm$ overlap, whereas the $35mm$ and $50mm$ overlap cases did not show such a feature. For the baseline case this reduction in downforce growth results from the influence of the vortex burst zones underneath the flap, which destroy the suction on the flap. For the other positive overlap cases these burst vortex zones have less downforce limiting effect, because they are deflected more downwards and inwards. Also the channel effect is more enhanced with larger overlap, which means that the downforce growth for these ride heights does not reduce as much. Based on this explanation it can now be understood that the burst vortex zones have more influence on the flap pressures for negative overlap, because they are less deflected by the wheels. Nevertheless, compared to the isolated wing case the downforce still grows faster, even with negative overlap. This indicates that the channeling effect is even enhanced for negative overlap and that its positive influence is stronger than the negative effect of the vortex burst.

The maximum downforce reduces with increasing negative overlap as a result of the decline in downforce growth. This means that the decreasing branch ride heights also produce less downforce than the baseline case. Yet the hysteresis effects start at a similar ride height as for the baseline case and the increasing branch shows a comparable downforce level to this case as well. The differences in drag, see figure 6.7, can once more be primarily explained by the downforce induced drag contribution. It is also interesting to see that the local additional drag due to the flap tip separation in region $III$ has disappeared for the negative overlap case. It is therefore expected that the flap tip separation is considerably less or even non-existent when the overlap becomes negative. Finally, the centre of pressure in figure 6.8 is located more downstream for the $-15mm$ case compared to the baseline settings. It is also located downstream with respect to the isolated wing case. From this and from the upstream movement in the first two regions it can be concluded that the wheels still affect the flap pressures, even for negative overlap. The centre of pressure moves less downstream at the lower boundary of region *II*, because the wheel circulation effect has less influence when the wing and wheels do not overlap.

## 6.4 Effect of gap on wing aerodynamics

The influence of the gap variations on the wing downforce curves is presented in figure 6.9. It can immediately be noticed that the level of the curves is less affected than by the overlap variations, similarly to the trends for the wheel drag. The maximum downforce values, for example, change by only 3.5% from the highest for the $10mm$ gap to the lowest for the $50mm$ gap, whereas the difference due to the overlap variation from $35mm$ to $-15mm$ is 7.9%. Most of the curves converge to a similar downforce value at the highest ride height, except for the $10mm$ gap case, which shows a slightly higher downforce than the others. It is also this gap setting that produces, in general, the highest downforce over the complete ride height range. The reason for this is that the additional channeling effect by the wheels is most effective when the wheels are closest to the wing. It has previously been discussed that the wheel wall movement reduces the channeling effect for the higher ride heights compared to for the isolated wing, but figure 6.9 indirectly reveals that the resulting channeling effect for a given ride height is always larger for a smaller gap value. However the negative influence of the downstream adverse pressure gradient resulting from the wheel presence needs to be taken into account as well.

The main qualitative influence of the gap setting on the downforce behaviour is that the sudden rise in downforce at the lower boundary of region *II* shifts to a lower ride height for increasing gap values. It also seems that this rise increases in magnitude for the larger gap cases. This implies that the ride height for which the wheel circulation effect starts having a positive influence moves to a lower value with increasing gap. The reason for this could be that the flow leaves the trailing edge of the wing under an upwards directed angle, similar to the flap angle, which enlarges the zone in which the suction side is negatively influenced with increasing gap dimensions. It is only when the upwards directed flow has reached the same critical height close to the wheel that the losses on the suction side start reducing, leading to the downforce rise. Since the wheel circulation induced velocity component that is aligned with the trailing edge of the flap grows with the distance from the wheel centre, it is expected that the downforce rise is larger for bigger gap values. Unfortunately, however, no experimental pressure data for different gap settings has been acquired to confirm these hypotheses.

The difference in wing drag seems once more primarily related to the downforce induced component, but the $50mm$ gap case shows a relatively larger drag reduction due to the reduced influence of the separated flap tip zones. The centre of pressure is located further downstream with decreasing gap. This implies that the flap is most effective for the smallest gap setting and shows that the additional channeling by the wheels acts primarily on the nearby flap surface. The local downstream shift of the centre of pressure at the lower boundary of region *II* is limited as a result of the relatively small overlap setting, which means that the wheel circulation effect only acts on a small part of the wing.

## 6.5 Summary

To complete this chapter the influence of overlap and gap settings will be briefly summarized. From the previous discussion it can be concluded that an increase in overlap leads to a vertical translation of the wheel drag and wing downforce curves with the largest setting resulting in the lowest force coefficients. A change in gap in contrast leads to a partial horizontal shift of the curves and in particular of the sudden force coefficient changes at the lower boundary of force region *II*. A positive overlap leads to a higher maximum wing downforce than a negative overlap as a result of the stronger channeling effect. The main physical principle behind the influence of overlap on the wheel flow field is the channel inflow effect, whereas the wing aerodynamics are most affected by the influence on the channeling effect and the vortex breakdown. The effect of gap variations on the wheel flow characteristics are mainly related to the ease with which the upper edge wing vortices can change their trajectories for increasing gap values, while modification of the channeling effect and a shift in the height, from which the wheel circulation effect becomes positive, determine the changes to the wing flow field.

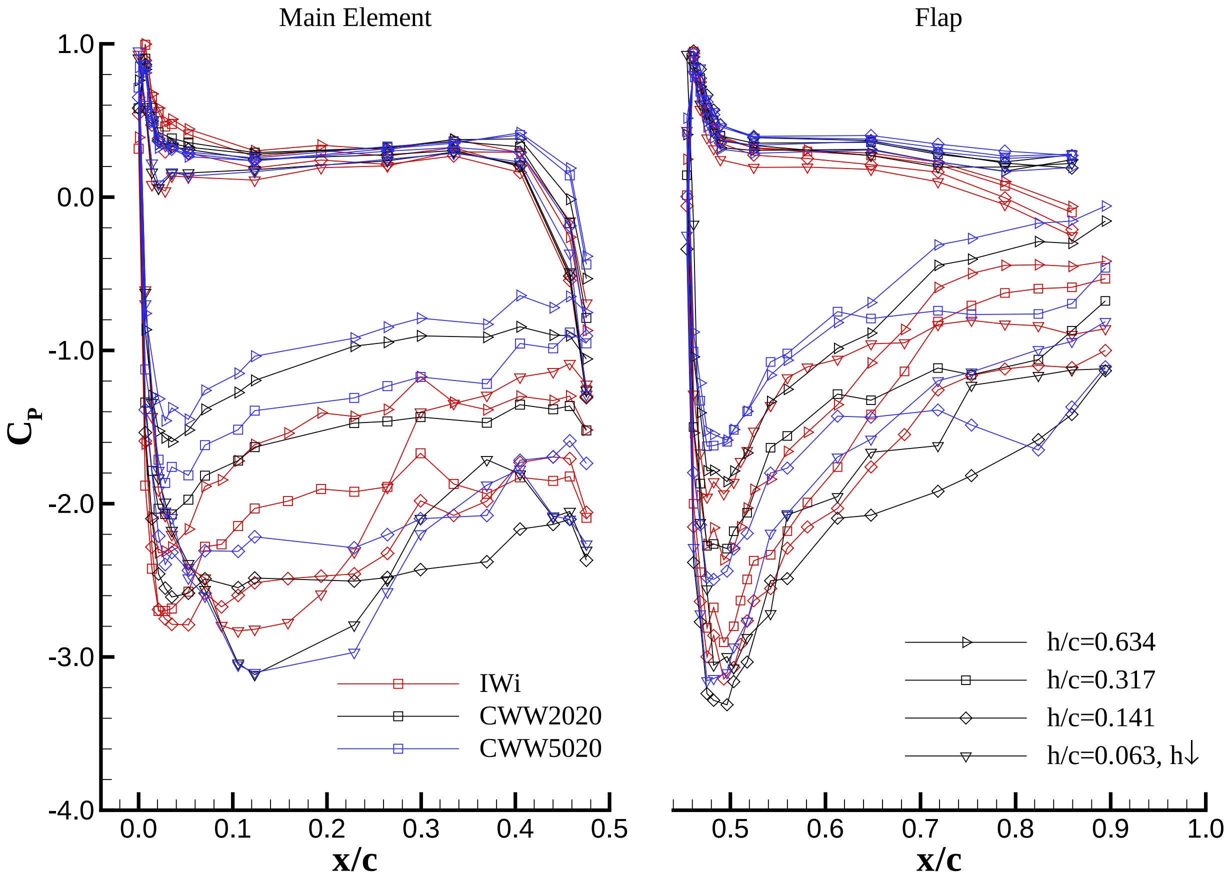

Figure 6.1: Chordwise pressure distributions for the wing in IWi, CWW2020 and CWW5020 configuration for a selection of ride heights, main element and flap at the port tip, $y/c = -0.933$, $25mm$ inboard of the endplate.

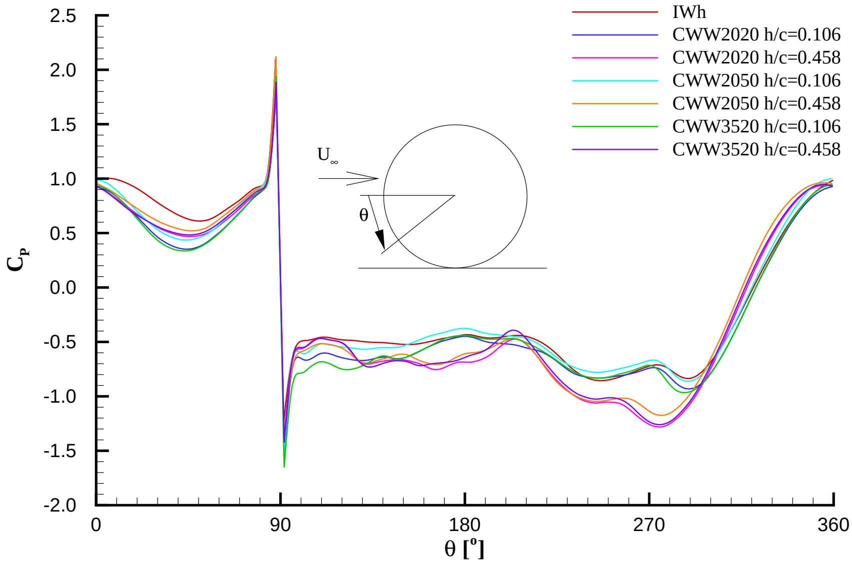

Figure 6.2: Pressure distribution around the centre of the wheel, location P1, for overlap and gap variation at $h/c = 0.106$ and $h/c = 0.458$.

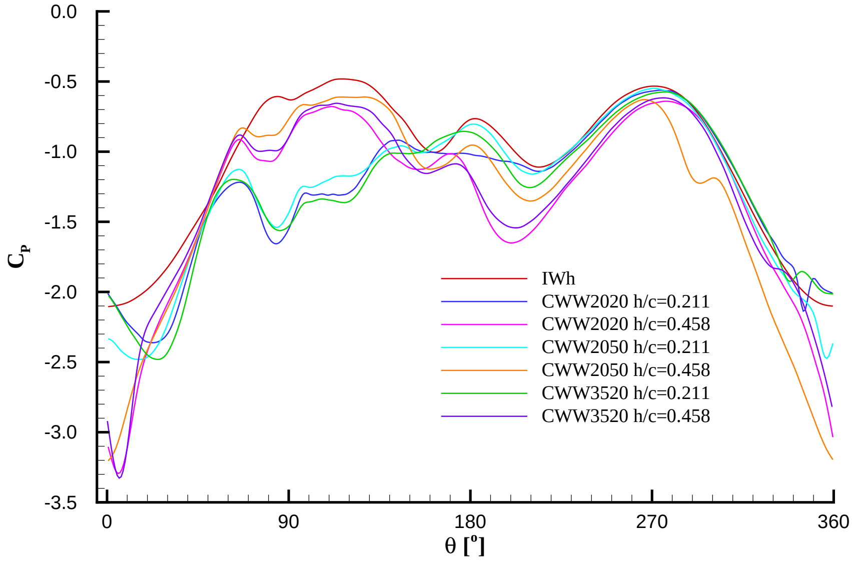

Figure 6.3: Pressure distribution around the inside side wall of the wheel, location P5, for overlap and gap variation at at $h/c = 0.211$ and $h/c = 0.458$.

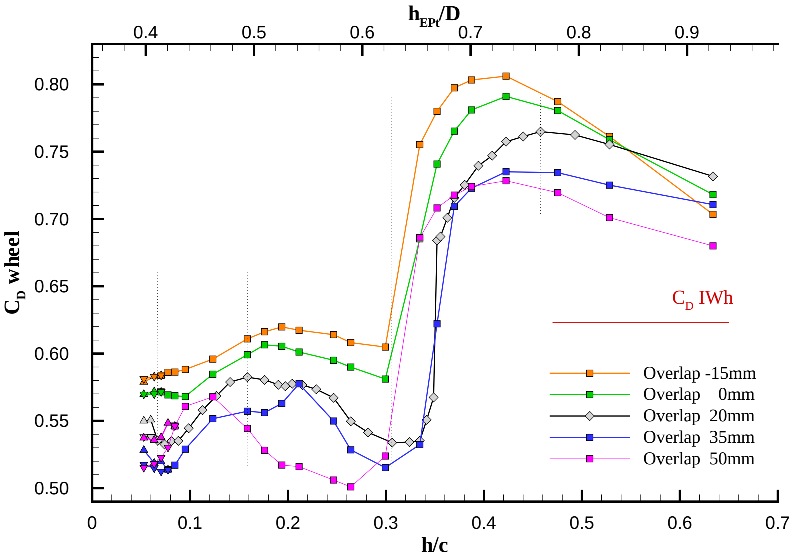

Figure 6.4: Variation of the experimental wheel drag coefficient with ride height for wing - wheel overlap variations at the baseline gap setting of $20mm$; isolated wheel drag level included in red.

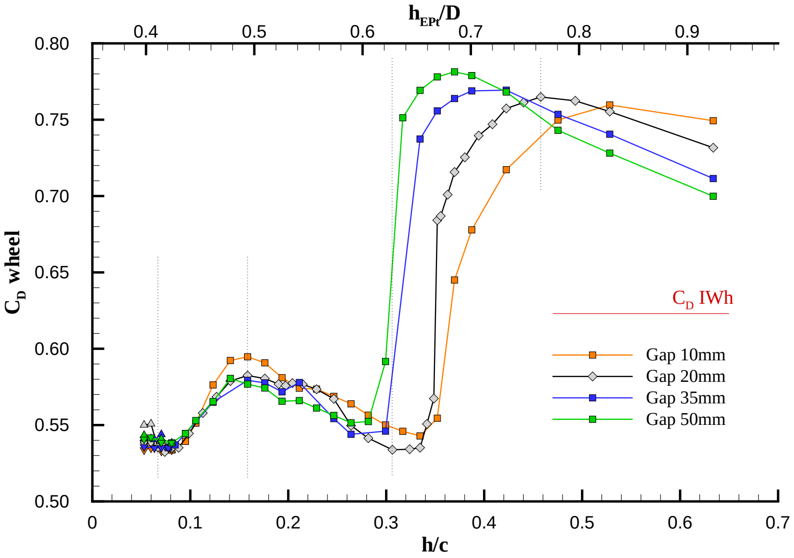

Figure 6.5: Variation of the experimental wheel drag coefficient with ride height for wing - wheel gap variations at the baseline overlap setting of $20mm$; isolated wheel drag level included in red.

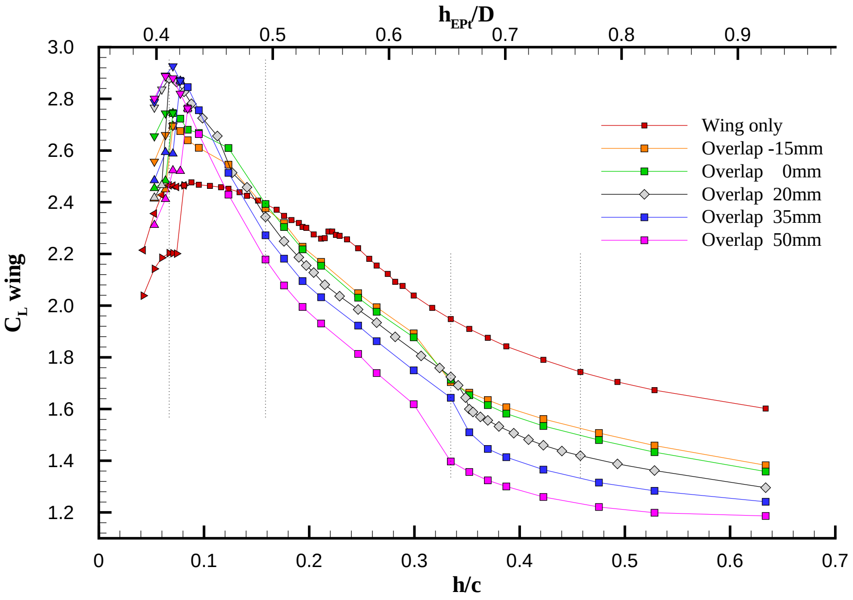

Figure 6.6: Variation of the experimental wing downforce coefficient with ride height for wing - wheel overlap variations at the baseline gap setting of $20mm$.

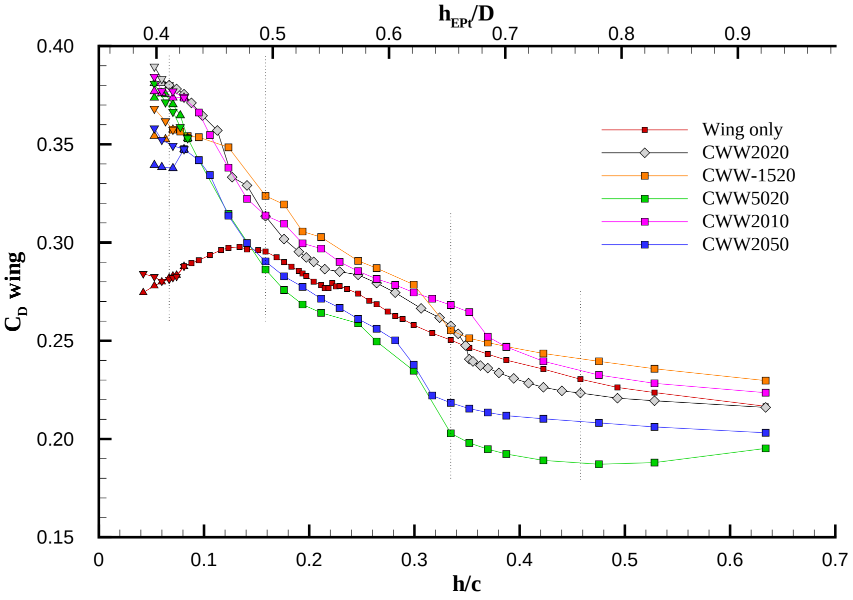

Figure 6.7: Variation of the experimental wing drag coefficient with ride height for wing - wheel overlap and gap variations.

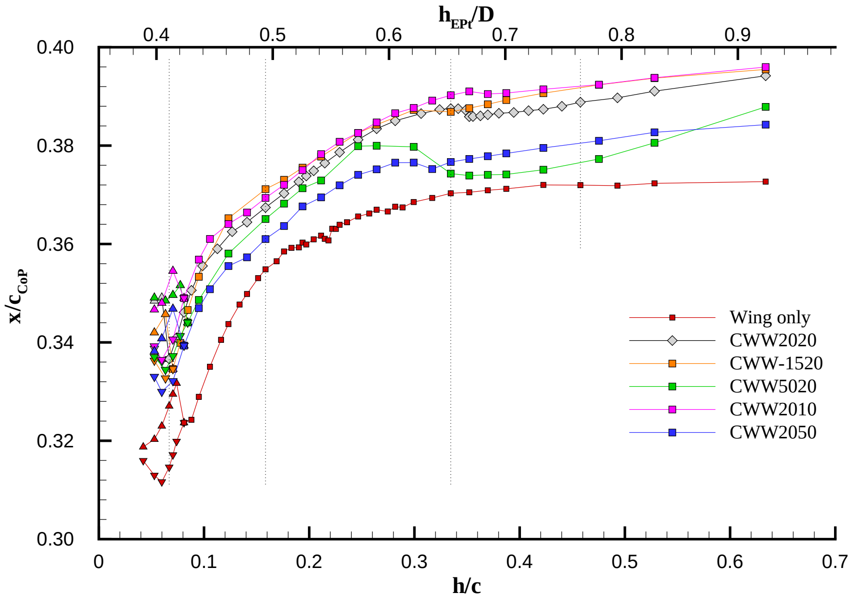

Figure 6.8: Variation of the experimental wing centre of pressure location with ride height for wing - wheel overlap and gap variations.

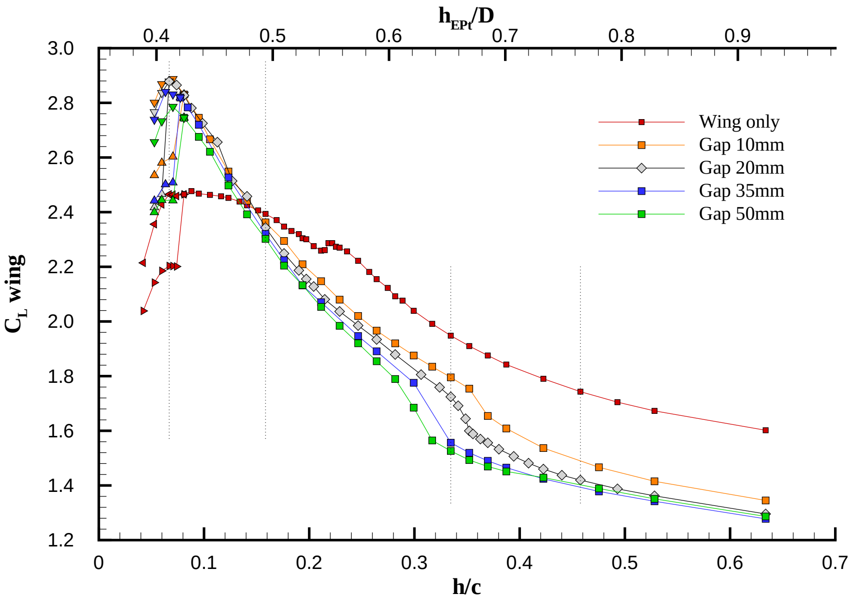

Figure 6.9: Variation of the experimental wing downforce coefficient with ride height for wing - wheel gap variations at the baseline overlap setting of 20$mm$.

# Chapter 7

# CFD Simulation of Wing - Wheel Interaction

The combined wing - wheel configuration has also been modeled computationally in order to answer the fourth research question. Some results and findings have already been presented briefly in the preceding three chapters, but this chapter gives a more complete overview. The results and discussion will be focused on the main question whether a CFD method can produce data similar to the experimental findings. However only one specific approach has been selected, based on the SA SRANS simulations that were applied to the isolated components, instead of performing an evaluation of different methods. Alternatively, unsteady RANS or DES simulations could be used, but due to time constraints and industrial relevance it has been decided to use the SRANS approach only. Since a grid sensitivity study has already been performed for each of the isolated components this step has been omitted to save time. Nevertheless in future research it might be worth checking whether the combined solutions, which include complicated interaction physics, are similarly grid independent as well.

The results presented here are all obtained for the baseline configuration with $20mm$ overlap and gap settings; no overlap or gap variations have been simulated. The influence of ride height has nevertheless been included in the CFD analysis and the results are thus comparable to the experimental data of the chapters 4 and 5. CFD is a powerful tool that can be used to produce data that can not be acquired experimentally. The $Q$-iso-surfaces in figure 4.11 are a good example of this. The downforce / lift and the sideforce on the wheel can also be derived from the simulations and have been included in this chapter to provide additional insight and to complement the experimental data.

The first section of this chapter discusses the computational modeling approach, focusing on the aspects that are new for the combined configuration. Next, section 7.2, presents the force correlation with the experimental data for the combined configuration. The final two sections look at how well the CFD approach captures the governing flow mechanisms for respectively the wheel and the wing and at how this can be used to explain the differences in force behaviour compared to the experiments.

## 7.1 Computational modeling

The general computational approach has been discussed in section 2.4. The wheel and wing mesh modules that are used for the combined configuration simulations have been introduced in that section as well. The complete grid has been constructed from these modules by merging the wing module into the total wheel grid. However a non-conformal box around the wing had to be used, because the number of grid cells on the wing and wheel module differed, making it impossible to use one-to-one connections. This non-conformal box was placed around the wing, consisting of an upstream, downstream, upper and side non-conformal boundary. The ground and symmetry plane boundaries were not connected to any other zones and did not have to be modeled as non-conformal boundaries as a result.

Figure 2.19 shows the total grid for the combined configuration in which the edges of the non-conformal box are visualized with blue lines. The number of cells in $x$-direction is 76 for the wing module and 26 for the outer wheel grid. The main reason behind this large difference is that the non-conformal boundary has also been used to save on cells in this direction, since it is unnecessary to have the wing grid density this far upstream of the wheel where the flow changes relatively little. In $y$-direction the number of cells for the wing module is 70, whereas the outer wheel grid contains 63 cells. It would be possible to connect these zones without non-conformal boundaries, but this would require rebuilding a part of either the wing or wheel module. Finally, the wing-side of the non-conformal box has 108 cells in $z$-direction and 48 for the outer wheel grid. The grid density inside the box has been increased in this direction to benefit from the additional offered freedom, especially in order to capture the velocity gradient underneath the wing better. Non-conformal zones are not the only possibility - and not necessarily the preferred choice in industry - to connect zones with different grid density. However better grid quality could be obtained with this option than with, for example, an unstructured ‘glue’ zone due to characteristics of the utilized grid generation program.

Another advantage of using a non-conformal block around the wing is that the wing ride height can be adjusted relatively easily. The wing grid within the non-conformal block can be considered to be an independent module and changing the wing ride height has therefore no consequences for the outer total grid. The number of cells in the complete grid varied from 4.4 to 4.5 million, depending on the wing ride height. Additionally the extent of the laminar zones had to be adjusted for some of the ride height variations. For the $h/c = 0.106$ and lower ride height cases the laminar zone on the suction side of the main element has been extended from $x/c = 0.07$ to $x/c = 0.15$, according to the experimental oil flow results presented in figure 5.7. In total 11 different ride heights, which span the complete range, have been simulated within this research. The complete grid also featured a wake block, similar to that for the isolated wheel, downstream of the wing and wheel. This wake block has been included for improved control of the cell quality and volume changes.

The computational model for the combined configuration comprises the same solver settings, turbulence model, boundary conditions and initialization procedure as for the isolated components. This means that a steady RANS solver has been used in combination with the one-equation SA turbulence model. No alternative turbulence models have been tested for this configuration. The solutions have not converged absolutely for the wing - wheel configuration, as used to be the case for the isolated wheel and for some of the isolated wing ride height cases. The variation in the wheel force coefficients seems to be an order of magnitude larger than that for the wing coefficients. Nevertheless both the residuals and force coefficients have converged to within a certain band, similar to in figure 3.28. For a SRANS simulation of a bluff body configuration this is deemed to be as close to a converged state as possible.

## 7.2 Force behaviour correlation

The evaluation, whether CFD can be used to predict the aerodynamics for a combined wing - wheel configuration, is split into two parts again. This section looks at the global force correlation, whereas the remaining part of this chapter studies the capturing of the flow physics in order to explain differences between the computational and experimental results. The following is divided in a part concerning the wheel force coefficients and a subsequent part dealing with the wing correlation.

**Wheel force coefficients** The computational wheel drag as function of the wing ride height is presented in figure 7.1. The equivalent experimental data is also included in this figure, but for a reduced resolution in comparison to figure 4.1. The wheel downforce and sideforce have only been acquired computationally and are shown in figure 7.2. Regarding the wheel drag, it can be derived from figure 7.1 that the CFD underpredicts this force coefficient over the complete ride height range. This is in agreement with the isolated wheel simulation, for which the CFD predicted a 6.6% lower drag value. However for the combined configuration the underprediction is even larger, ranging from 7.8% at the lowest ride height to 27.6% at $h/c = 0.458$.

The general trend in wheel drag variation is simulated correctly; the CFD only shows an opposite decline with increasing ride height for the lowest two ride heights. However, the sudden rise in wheel drag above $h/c \approx 0.35$ is much less extreme in the CFD and it is above this ride height in particular that the simulations seem less accurate. In the experiments the wheel drag for the combined configuration reaches a higher level than for the isolated wheel at the high ride heights, but in the CFD it always stays below the computational level of the isolated wheel[1]. Confirmation that the extent of this feature in the experimental results is genuine and not the result of, for example, instrumental flaws can be found in the fact that it is both repeatable (see figure B.2) and independent of the *Re*-number (see figure C.5).

The wheel creates an aerodynamic downforce between $h/c \approx 0.15$ and 0.35 according to the CFD. This is in stark contrast to the results for the isolated wheel, which showed an upwards directed force coefficient of 0.09. Below $h/c \approx 0.15$ the vertical force for the combined configuration is similar to that for the isolated wheel, but above $h/c \approx 0.35$, after the sudden drag increase, the lift on the wheel has more than doubled compared to for the isolated wheel case. The sideforce on the wheel is always directed towards the symmetry plane according to the CFD, as would be expected because of the lower pressures due to the accelerated flow on the inside of the wheel. The sideforce varies in a similar way as the wheel downforce, although the rate of change is different. The large increase in wheel lift above $h/c \approx 0.35$ is for example accompanied by only a small decline in sideforce, whereas at low ride heights the variations have a similar magnitude.

---

[1] Some of the underprediction of the wheel drag at high ride heights can be explained with the difference in blockage between the CFD and experiments. Both use the same channel, based on the wind tunnel cross section, but the support structures have not been modeled in the CFD. This means that the computational blockage is almost half that of the experiments, however the difference in blockage correction - 0.963 for the CFD versus 0.927 for the experiments at $h/c = 0.458$ - is not enough to explain the discrepancy.

**Wing force coefficients** The computational wing downforce correlates quite well with the experimental results, as can be seen in figure 7.3. From a quantitative point of view the relative difference remains within a range of -1.0% to 4.8%. Qualitatively the trend in downforce behaviour with ride height variation is predicted accurately as well, with only the $h/c = 0.528$ data point and those for low ride heights showing a slightly different trend. It is remarkable to see that the downforce underprediction of approximately 6% that was present for the isolated wing, especially at higher ride heights, has disappeared for the combined configuration. However the correlation difference in pitching moment, see figure 7.4, reveals that it is merely a coincidence that the downforce correlates so well, because the pitching moment is underpredicted even more than for the isolated wing. This implies that the pressure distribution on the wing differs from CFD to experiments and therefore that the accurate wing downforce correlation does not present the complete picture.

Figure 7.5 shows that the wing drag is in general overpredicted by 5 to 10% in the CFD compared to in the experiments. This is in agreement with the isolated wing simulations, which yielded a higher drag as well. The correlation has however slightly deteriorated after the wheels have been added to the configuration. The local deterioration of the correlation at $h/c = 0.528$ can be distinguished for the wing drag and pitching moment as well, while the improvement in correlation for the lowest ride height actually seems to indicate a change in predicted flow physics. In the experiments the drag locally increased disproportionally in force region *III*, the CFD results show this less, although the drag curve gives the impression that the influence zone of this additional drag is extended to lower ride heights. The centre of pressure location, which has been derived from the other force coefficients using equation A.4, is presented in figure 7.6. The computational centre of pressure is located approximately 4% of the wing chord more upstream than the one that follows from the experiments. This is a large difference since the total variation over the complete ride height range is of a similar order. The general qualitative trend in variation is again predicted more accurately, despite some local differences in the rate of change.

## 7.3 Wheel flow

The computational wheel drag coefficient behaviour showed reasonable qualitative correlation with the experiments, but a global underprediction in quantitative sense. This section looks at the on-surface and off-surface wheel flow characteristics as predicted by CFD in order to analyze what causes the differences. In this way it can be explained how well suited a SRANS simulation is to solving this complicated flow problem. Figure 7.7 provides helpful insight into the correlation by showing the relative difference in the wheel drag coefficient. It can be seen that this relative difference grows towards an absolute maximum on the boundary between force region *I* and *II*. This implies that some of the drag inducing physics are considerably underpredicted in the CFD at $h/c = 0.458$.

Figure 7.8 reveals that the CFD predicts less suction in the wake; a trend that is repeated for location P2 and to a lesser extent for P4. On the other hand the pressure on the front of the wheel is higher in the CFD, which should in contrast increase the drag. However a comparison with the isolated wheel shows that the loss in suction in the wake is relatively larger than the extra pressure on the front. A reason for the lower suction in the wake can be found in figure 7.11 (c), where it can be seen that the inflow into the wake is less for the CFD. The recirculation zone is located further away from the wheel surface as a result, leading to lower velocities along the surface and thus higher pressures. Another reason for the generally lower wheel drag in the computations can be derived from figure 7.9, as the suction between $\theta \approx 45^\circ$ and $90^\circ$ is much larger, which hints at a stronger acceleration around the wheel corner in the CFD. The trend in separation position from the top of the wheel seems to be predicted similarly to in the experiments. Furthermore the translation of the upper edge wing vortex from over the top of the wheel to the inside is distinguishable in the CFD as well.

The reduction in wheel drag in force region *II* is captured in the simulations as well, but the sudden fall in wheel drag is less severe. It is anticipated that the vortex interaction in the wheel wake, which is partly responsible for the higher wheel drag at high ride heights, is underpredicted in the CFD. Nevertheless even at the lower ride heights the drag is more underpredicted compared to for the isolated wheel case due to the difference in channel inflow effect. The imprints of the upper edge wing vortex on the side of the wheel are weaker in the CFD than for the experiments, see the $h/c = 0.211$ and $0.317$ case in figure 7.10. This also indicates that the vortices and vortex interaction are not captured accurately in the SRANS simulations. The use of non-conformal zones between the wing and the wheel could be partly responsible for this, since these would lead to an averaging and thus smearing of the vortices at the connection between the different grid blocks.

The relative difference in wheel drag stays fairly constant from $h/c = 0.342$ to $0.158$, in force region *III*. The relative difference for the ride heights below this interval decreases, but this does not necessarily mean that the flow physics are captured better, because the direction of the drag curve is opposite to that in the experiments. The decline in drag in the experiments has been explained to result from an increase in channel inflow effect and from a stronger flow interaction in the lower wake, leading to more suction in this area. The figures 7.8 and 7.9 show that it is the latter phenomenon in particular that is underpredicted in the simulations at $h/c = 0.106$ (also for the not presented P2 location on the outside of the wheel), since the suction between $\theta = 105°$ and approximately 145° is considerably less in the CFD. However the off-surface flow features for $h/c = 0.106$ in figure 7.12 do look quite similar from CFD to experiments.

To summarize the previous, it can be concluded that the effect of the wing flow field and vortices on the wheel aerodynamics is captured in a weakened form in the CFD. This could partly be caused by the use of the non-conformal zones between the wing and the wheels. The result of this is that the effect of the wing interaction on the wheel drag is displayed in a reduced, less extreme, form compared to in the experiments. Especially the results at high and low ride heights are compromised, because these are most dependent on the interaction of the flow fields.

## 7.4 Wing flow

Although the wing downforce is predicted quite accurately by the CFD, the discrepancies in drag and especially pitching moment showed that this does not translate to an accurate correlation of all the flow quantities. Figure 7.13 confirms this notion by giving further insight into the on-surface flow features. The pressure distributions on the wing differ noticeably for the lowest ride height and at the (flap) tip, whereas the rise in pressures near the trailing edge of the flap on the pressure side is not captured very well either. In the following paragraphs it will be discussed how these differences contribute to the correlation of the force coefficients.

The relative differences between the computational and experimental wing downforce and drag have been included in figure 7.7. The downforce graph can be subdivided into four zones, if the local discrepancy at $h/c = 0.528$ is disregarded[2]. From the highest downforce to $h/c = 0.380$ the relative difference is fairly constant, then it decreases temporarily when the wheel drag suddenly decreases. Over the following segment until $h/c = 0.158$

---

[2] This difference in correlation at $h/c = 0.528$ can not be explained with any obvious change in flow features and is not considered to represent a fundamental difference in flow physics.

the relative difference grows continuously, as the rate of change of the computational downforce is overpredicted compared to that of the experiments. Finally the relative difference for the lowest two ride heights reduces again until it almost disappears for $h/c = 0.063$. It is anticipated that each of these four zones indicate a change in the capturing of the governing flow physics by the CFD.

The fairly constant relative difference in downforce over the first zone is reminiscent of the outcomes for the isolated wing, albeit at a better correlation level. The relative wing drag difference slowly decreases - just as for the isolated wing - from 7.5% to 6.0%. Compared to the isolated wing simulations, the CFD predicts a relatively higher downforce and drag, whereas the centre of pressure lies relatively further forward. The explanation for this can be found when the next segment is analyzed as well. From $h/c = 0.380$ to 0.317 the relative difference in downforce decreases and becomes even negative. The sudden rise in experimental downforce in this region was contributed to the change in influence of the wheel circulation effect. Above these ride heights the influence on the downforce is negative due to the induced upstream velocity on the suction side of the flap (see figure 5.11), whereas the influence has a positive effect below this interval. From figure 7.3 it can be concluded that both the limiting influence on the downforce above $h/c = 0.38$ as well as the enhancing influence below 0.35 are underpredicted and thus that the wheel circulation effect is underpredicted in the CFD.

It is interesting to see in figure 7.6 that the experimental centre of pressure location moves approximately $0.02c$ downstream when the wheels are added, but that the computational location is hardly influenced by this change from an isolated wing to a combined wing - wheel configuration. It is expected that the higher pressures near the trailing edge on the pressure side of the flap are primarily responsible for this movement in the experiments, whereas the lack of these higher pressures in the CFD explains why the centre of pressure hardly moves in the simulations. However these results also shows that the experimental pitching moment results have to be used carefully, because they are receptive to errors due to deformation as a result of the external position of the wing load cell and suffer from calibration uncertainties.

At the end of the second zone the relative difference in downforce has reached a negative value, because the experimental value has outgrown the computational due to the larger influence of the wheel circulation effect. Nevertheless, in the next zone, the relative difference increases again and, just like for the isolated wing, it is expected that this is primarily caused by the reduced influence of vortex dilution in the simulations.

The larger suction in the computations on the second half of the main element and on the first part of the flap are proof of this (see figure 7.13). The difference in prediction of the downforce enhancing lower edge vortex effect in CFD compared to in the experiments has however also increased relative to for the isolated wing configuration. The relative difference in wing drag rises proportional to the downforce, except for the $h/c = 0.211$ data point, which shows a large discrepancy. The reason for this is that the additional drag contribution due to the flap tip endplate juncture separation extends to a lower ride height in the computations, which leads to a local increase in relative difference between CFD and experiments. Figure 7.13 (b) still shows the resulting characteristic plateau in the computational flap pressure distribution for $h/c = 0.211$, whereas this effect is hardly visible in the experiments for the same ride height. Therefore the additional drag influence ends at $h/c \approx 0.211$ for the experiments and only at 0.158 for the CFD.

Finally, the relative difference in downforce decreases again for the last two ride heights. This is the region in which the limiting mechanisms such as vortex breakdown and flow separation become active. The downforce has already started to decrease for the lowest data point, despite the appearance in figure 7.3, since the maximum experimental value occurs at $h/c = 0.067$ (see figure 5.1). In the CFD results vortex burst is not apparent until $h/c = 0.106$, which is the highest ride height for which flow reversal takes place in the vortex core. This in in agreement with the experiments, where it was deduced that vortex breakdown would occur at $h/c \approx 0.113$. However, just as for the isolated wing, the influence of vortex burst is overpredicted in the CFD and this is the reason for the earlier and stronger decline in downforce according to the CFD. The main element trailing edge separation that was responsible for the downforce decay in the experiments (see figure 5.7 (d)) is captured accurately in the computations. In accordance with the experiments this feature only appears for the lowest ride height of $h/c = 0.063$.

In summary it can therefore be concluded that the upstream influence of the wheel on the wing is predicted more accurately than the influence of the wing on the wheel. The latter is for an important part dependent on vortex interaction, which is hampered by the computational method (SA SRANS) and the use of non-conformal zones. The influence due to the induced flow velocity field is captured better in both directions, although the wheel circulation effect on the wing is underpredicted. Apart from that the wing results still suffer from the same problems that were discovered for the isolated wing, such as general overprediction of the drag, less effect of vortex dilution on the downforce and larger influence of vortex breakdown, once it occurs.

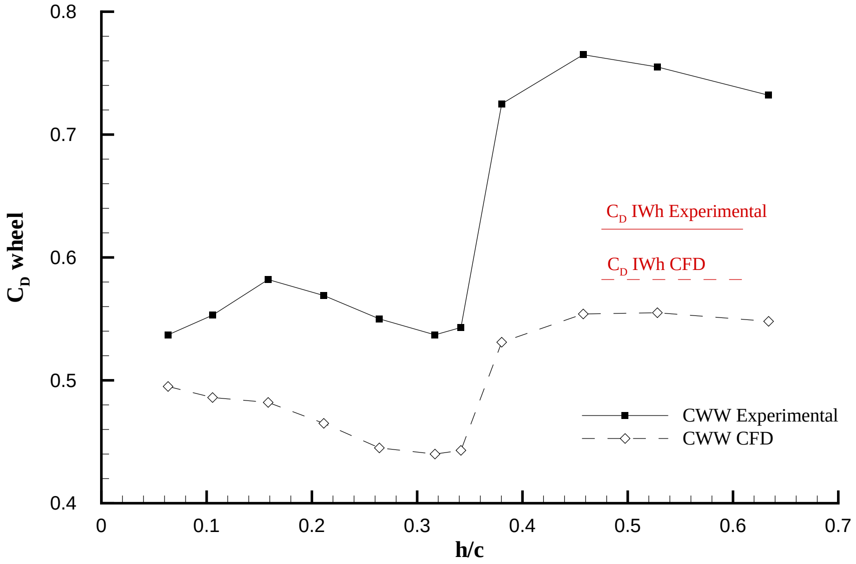

Figure 7.1: Comparison of computational and experimental wheel drag for the baseline wing - wheel configuration; isolated wheel drag level included in red.

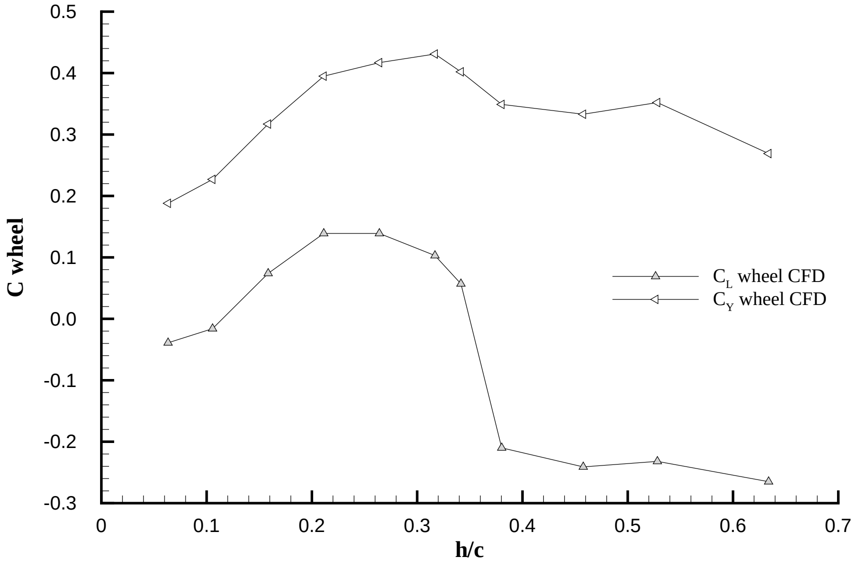

Figure 7.2: Computational wheel downforce and sideforce for the baseline wing - wheel configuration.

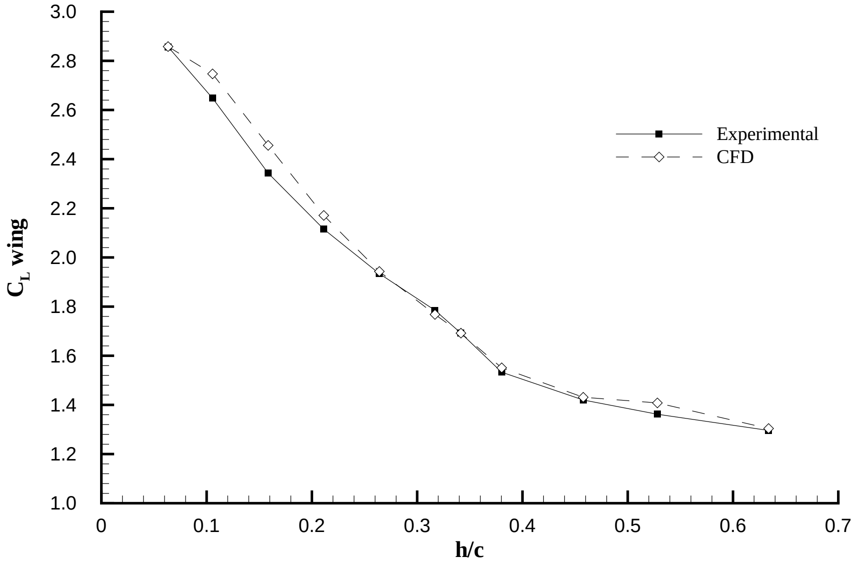

Figure 7.3: Comparison of computational and experimental wing downforce for the baseline wing - wheel configuration.

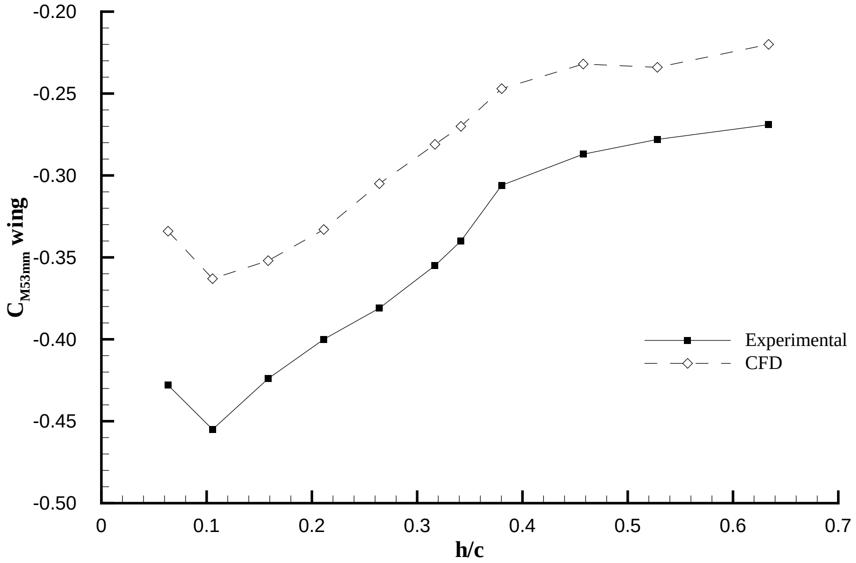

Figure 7.4: Comparison of computational and experimental wing pitching moment for the baseline wing - wheel configuration.

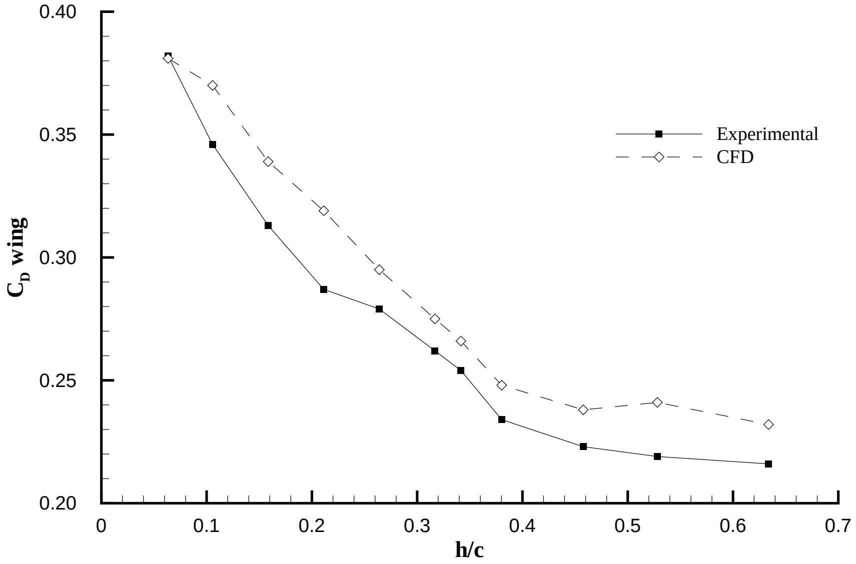

Figure 7.5: Comparison of computational and experimental wing drag for the baseline wing - wheel configuration.

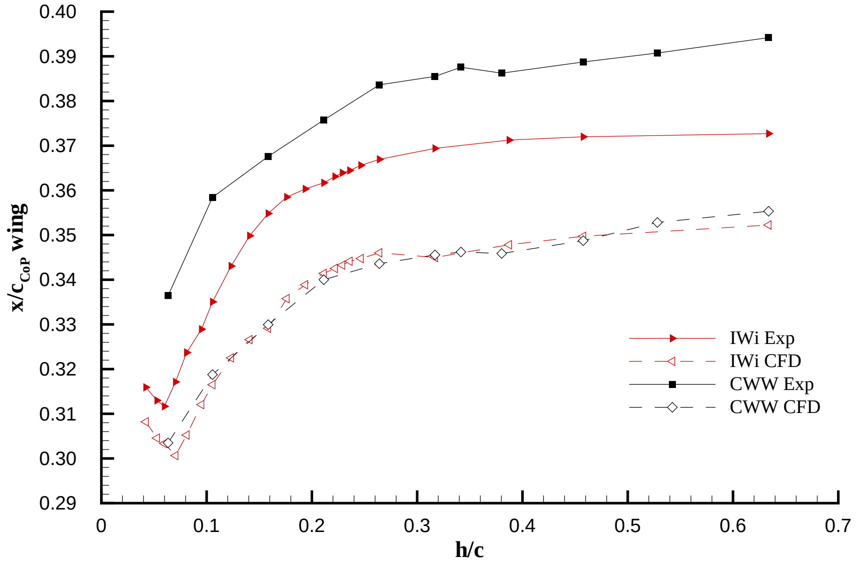

Figure 7.6: Comparison of computational and experimental wing centre of pressure location for the isolated wing and the baseline wing - wheel configuration.

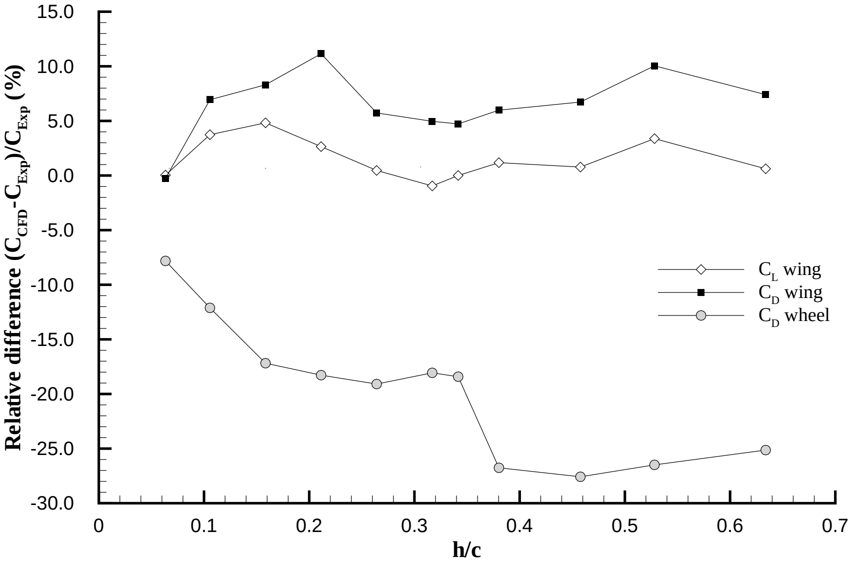

Figure 7.7: Comparison of relative differences between computational and experimental force coefficients for the baseline wing - wheel configuration.

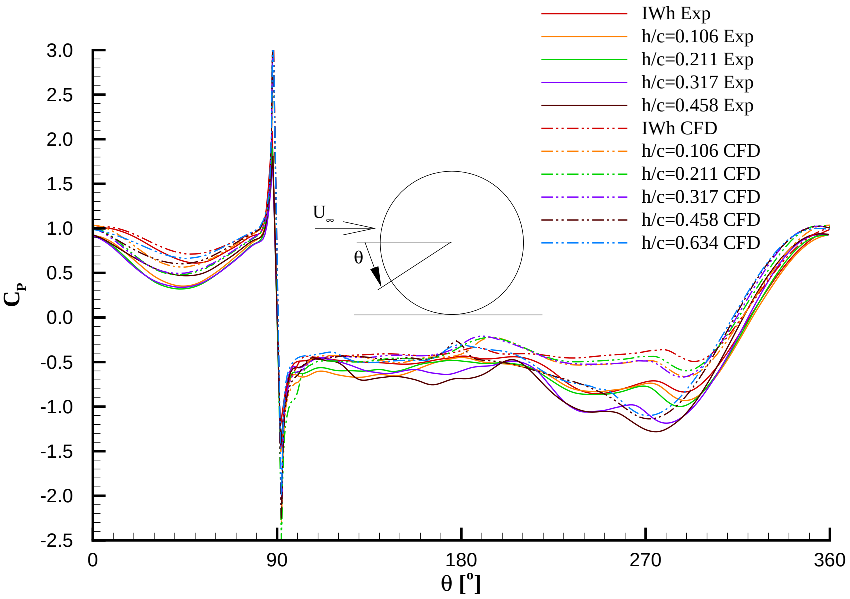

Figure 7.8: Comparison of computational and experimental pressure distribution around the centre of the wheel, location P1, for various ride heights.

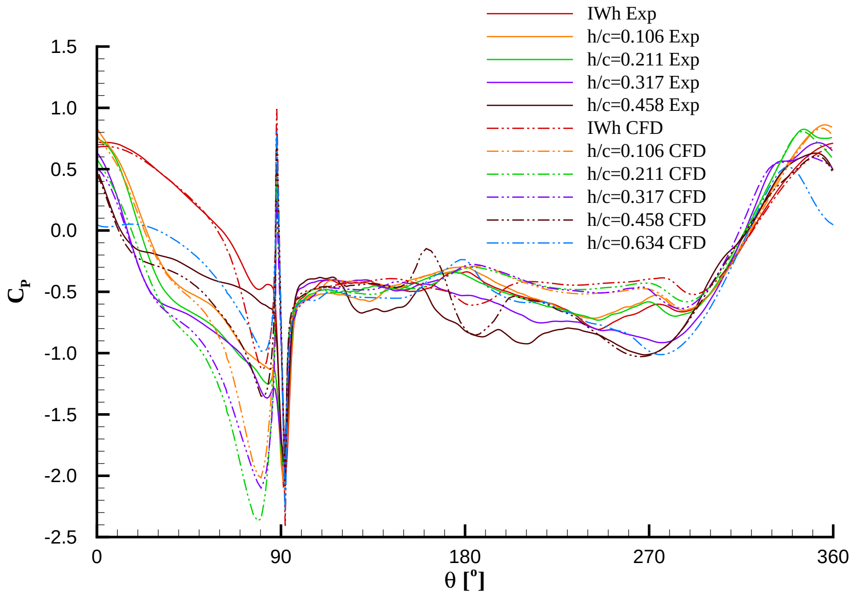

Figure 7.9: Comparison of computational and experimental pressure distribution around the inside contact patch of the wheel, location P4, for various ride heights.

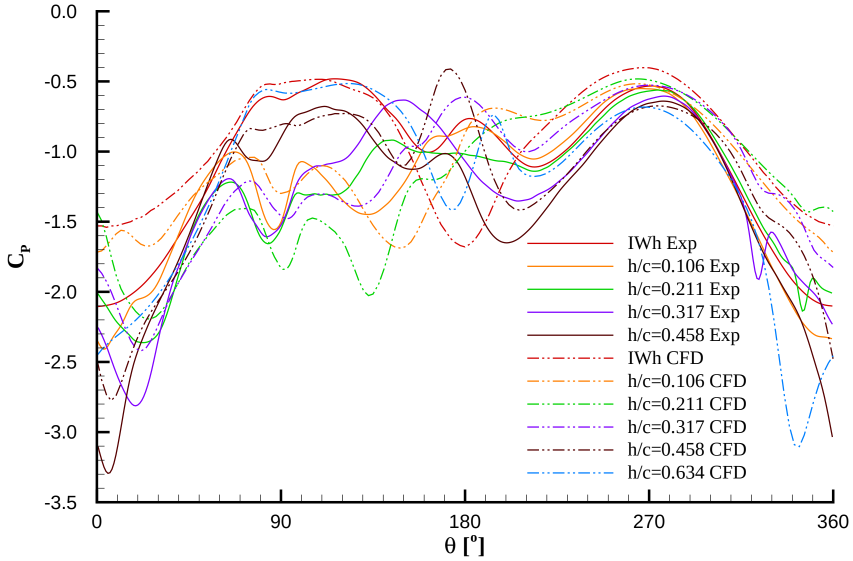

Figure 7.10: Comparison of computational and experimental pressure distribution around the inside side wall of the wheel, location P5, for various ride heights.

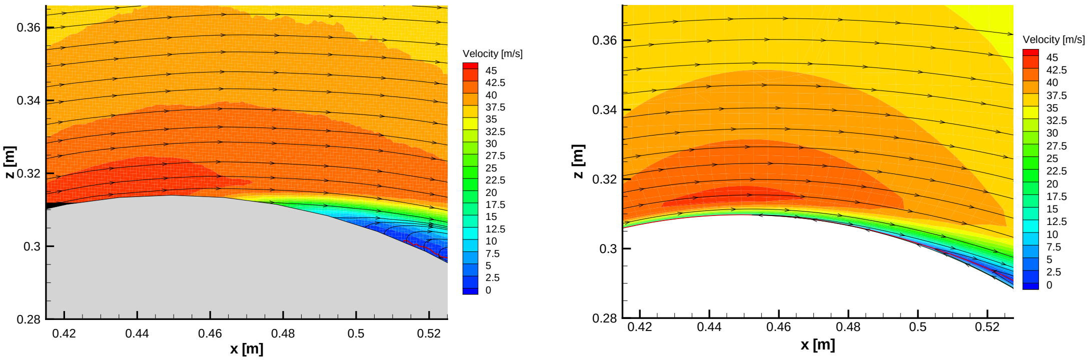

(a) Top of port side wheel, vertical streamwise plane at $y = -0.353m$ .

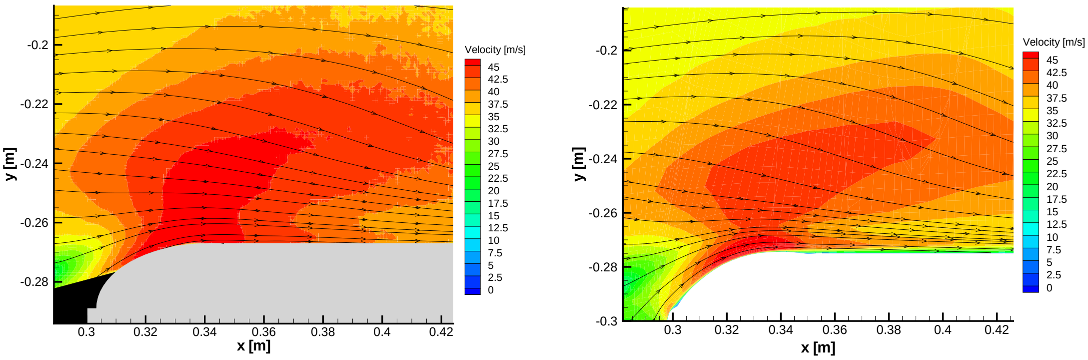

(b) Upstream inside corner of port side wheel, horizontal plane at $z = 0.165m$ .

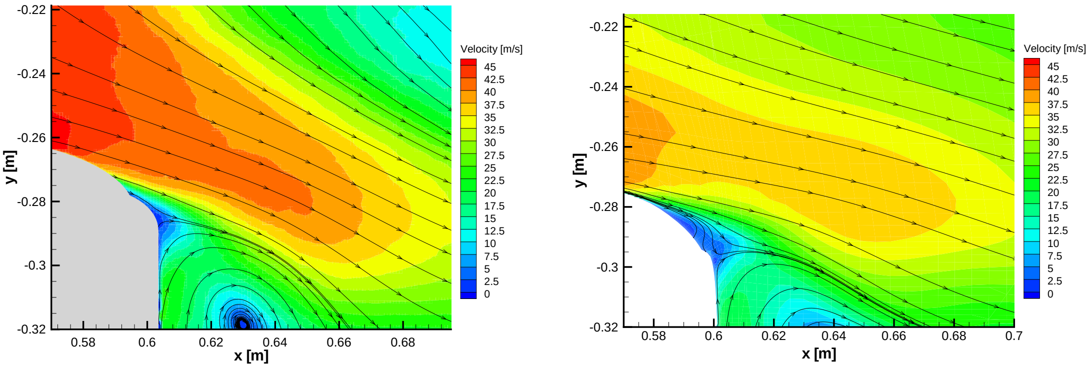

(c) Downstream inside corner of port side wheel, horizontal plane at $z = 0.174m$ .

Figure 7.11: PIV and CFD comparison of off-surface flow features around the wheel for the CWW2020 configuration at $h/c = 0.458$; left figures from PIV, right from CFD; red lines in figure (a) represent $U = 0$-curves.

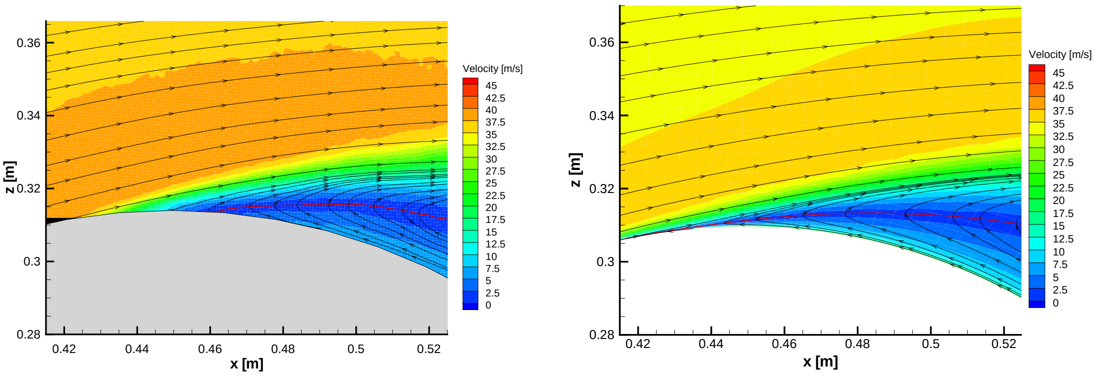

(a) Top of port side wheel, vertical streamwise plane at $y = -0.353m$ .

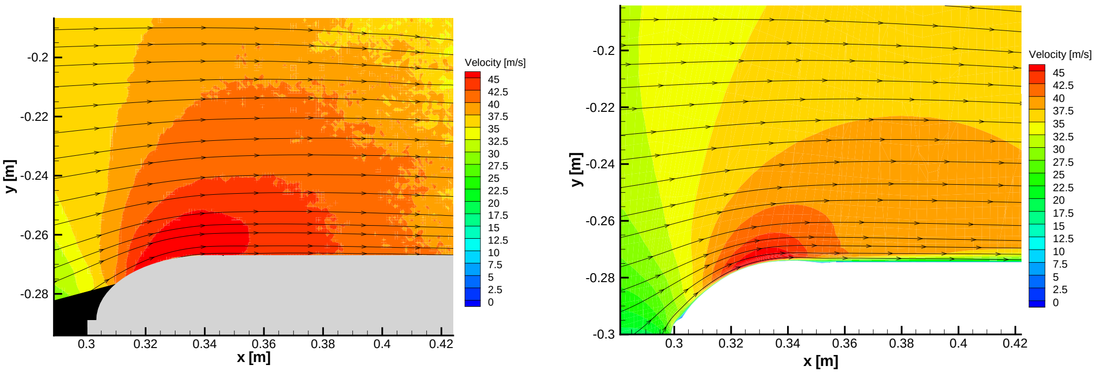

(b) Upstream inside corner of port side wheel, horizontal plane at $z = 0.165m$ .

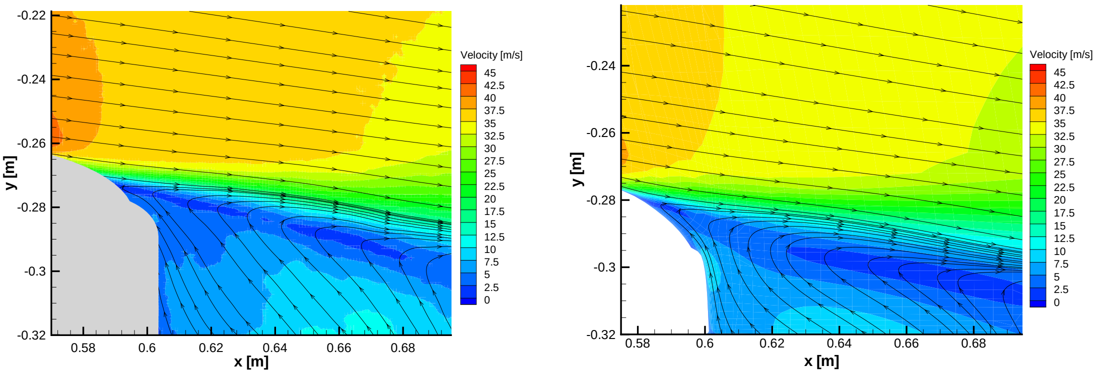

(c) Downstream inside corner of port side wheel, horizontal plane at $z = 0.174m$ .

Figure 7.12: PIV and CFD comparison of off-surface flow features around the wheel for the CWW2020 configuration at $h/c = 0.106$; left figures from PIV, right from CFD; red lines in figure (a) represent $U = 0$-curves.

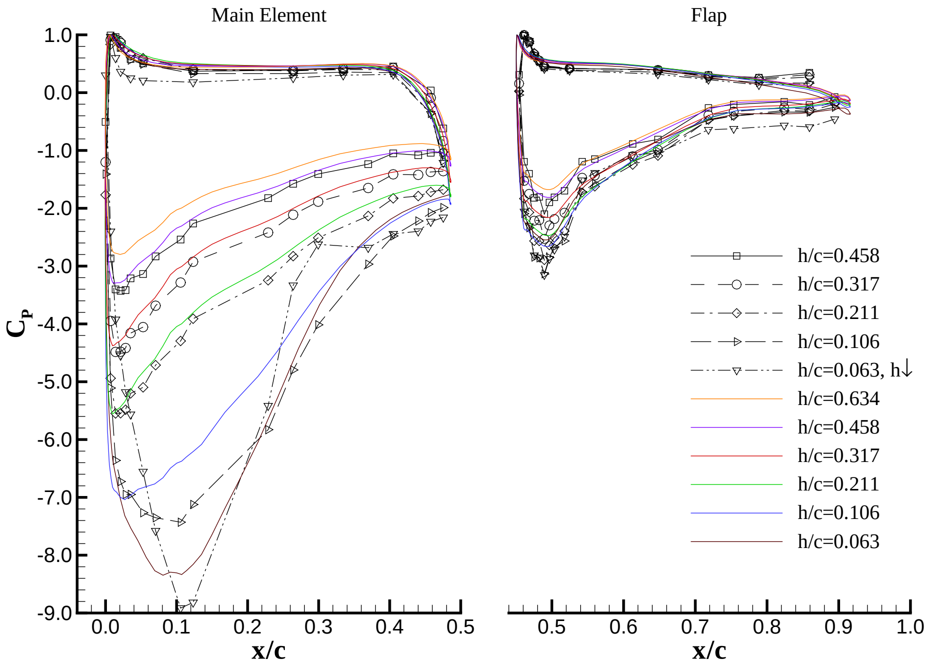

(a) Centre span, $y/c = 0$.

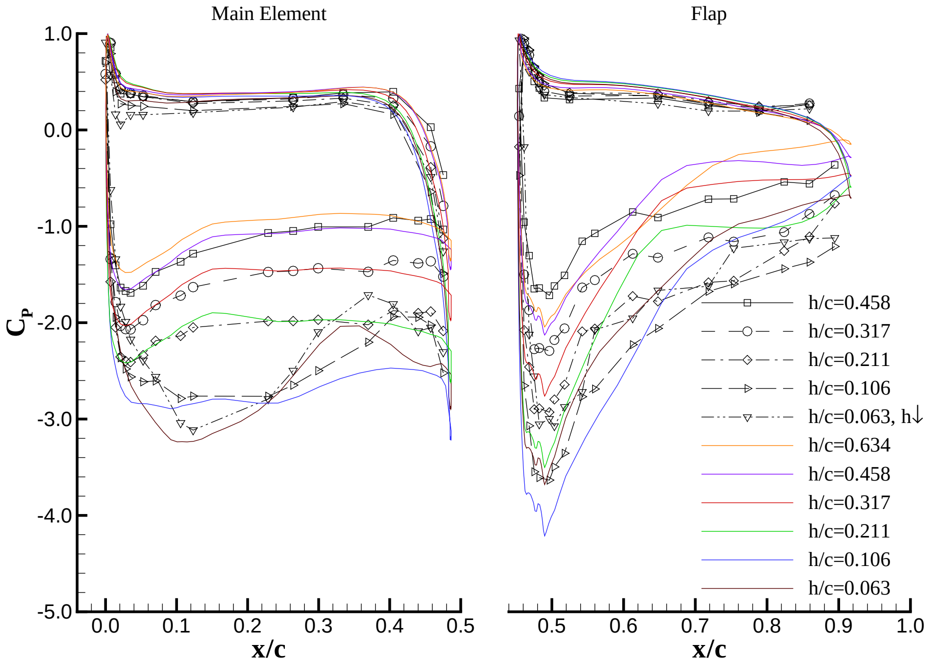

(b) Port tip, $y/c = -0.933$, $25mm$ inboard of the endplate.

Figure 7.13: Comparison of experimental (black) and computational (colour) chordwise wing pressure distributions for the CWW2020 configuration, main element and flap at centre span (a) and at the port tip (b).

# Chapter 8

# Interpretation and Applications

The research questions from section 1.5 have been answered in the previous chapters, which were primarily aimed at presentation and analysis of the data. The current chapter is more application orientated and comprises of further discussion and practical applications to complete this thesis. The first section focuses in more detail on the wing - wheel interaction phenomena and compares some of the physics with those for a multi-element airfoil. Next, section 8.2 presents a closer look at the parameters that govern the phenomena and associates the trends to physical interpretations. Finally, the last section places the results into a practical context by analyzing how the outcomes can be used for realistic racecar purposes.

## 8.1 Further discussion

The wheel aerodynamics for the combined configuration are governed by the phenomena that occur for the isolated wheel and by additional interaction effects resulting from the wing flow, such as the delayed separation, the channel inflow and the interaction of the wing vortices with the wheel wake. In return the phenomena that govern the wing flow field, which are based on channeling effect, vortex effects and separation effects, are modified as well. Whereas the wheel circulation provides an additional mechanism of wing downforce enhancement and limitation, depending on the ride height. It is this phenomenon in particular that will be examined in more detail.

**Circulation effects** Smith [71] has presented an overview of the physics for 2D multi-element high lift aerodynamics in which he defines the five fundamental mechanisms for this subject area. These are the slat effect, the circulation effect, the dumping effect, off-surface pressure recovery and the fresh boundary layer effect. With respect to the current research the circulation effect and the dumping effect are especially interesting, because these physical principles can be recognized for the combined wing - wheel configuration. Smith analyzed a single element airfoil with either a point vortex or a circular cylinder positioned downstream of it to model the influence of a flap element. The study revealed that both the induced velocities of the vortex as well as the flow field around the obstruction effectively places the trailing edge of the wing at a high angle of attack. Due to the Kutta condition this causes the circulation around the airfoil to increase and thus leads to a higher lift of the airfoil. In addition to this circulation effect the airfoil also discharges its boundary layer at the trailing edge into a region with locally higher velocity. This is the dumping effect, which again allows the airfoil to produce higher lift because of the reduced pressure recovery demands.

The circulation effect therefore results from the induced velocity across the trailing edge of the airfoil, which increases the circulation, whereas the dumping effect is related to the higher tangential velocity along the wing surface at the trailing edge. Generating high lift is best achieved by inducing a higher circulation around the airfoil by other means than by pitching the airfoil, according to Smith [71]. Large angles of attack for the airfoil lead to a suction peak at the nose, which requires more pressure recovery and thus promotes separation. This is the dominant lift limiting mechanism for such a case. The circulation effect however provides a means to induce a higher circulation without increasing the nose suction peak. A wheel positioned downstream of a wing can - dependent on the ride height - have a similar effect on a wing in two different ways: the wheel rotation induces a flow field with beneficial higher velocity across the trailing edge of the wing, whereas the obstruction by the wheel also leads to an advantageous cross flow.

This knowledge can also be applied to get a better understanding of the wheel circulation effect on the wing downforce. What was previously named the ‘wheel circulation effect’ is actually a combination of three potentially beneficial mechanisms. Firstly, the wheel rotation aspect always has a positive influence on the wing downforce, because it induces a velocity along the trailing edge of the wing that enhances the circulation. Secondly, the obstruction by the wheel also induces a velocity along the trailing edge, however this effect is ride height dependent. It is expected that this mechanism has a positive effect on the wing downforce when the trailing edge of the flap is roughly below the wheel axis and a negative effect when it is at a higher ride height. Finally, the dumping effect has a positive influence when the trailing edge is located in a region of locally higher velocity.

From figure 5.6 (b) it can be concluded that the suction on the underside of the flap at the trailing edge is larger with the wheels added for all ride heights, except for the $h/c = 0.634$ case. This implies that the discharge velocities are higher for these cases and thus that the dumping effect positively contributes to the downforce. It is difficult to define when the sum of these three effects together starts having an enhancing influence on the downforce, but the results indicate that this is most likely when the sudden change in wing downforce and wheel drag takes place. This is at a ride height for which the trailing edge of the flap is located above the wheel axis, which implies that below this height the positive influence of the wheel rotation will overshadow the influence of the obstruction induced velocities, which are still negative at that height.

The (positive) influence of the wheel circulation effect is primarily noticeable at the part of the wing where there is a physical overlap with the wheel. This explains why the wing in the combined configuration does not perform better than the isolated wing for all of the ride heights with the flap trailing edge located below the wheel axis. However the separation at the junction of the flap and endplate and the reduction in channeling effect due to the wheel wall movement play a role in this as well. In chapter 7 it was found that the wheel circulation effect was underpredicted in the computations. Based on the above it can now be confirmed how the non-conformal zones are partly responsible for this, because the velocity along the trailing edge, which is induced by the wheel circulation effect, will be dampened at the non-conformal boundary.

An interesting observation is that the separation from the suction side of the main element at low ride heights starts occurring between $h/c = 0.106$ and 0.063 (see the oil flow figures 3.18 and 5.7) for both the isolated wing and for the combined configuration. The previous discussion suggested that enhanced circulation due to the wheel presence would reduce the required pressure recovery and thus delay separation. There are however two reasons why the ride height at which separation starts occurring has not changed noticeably. First of all the influence of the wheel circulation effect at centre span, where the separation takes place, is very limited and secondly the suction peak at the nose is overshadowed by the suction resulting from the diffuser-like channeling effect at the lowest point of the profile for this height. Since the location and strength of the latter is not driven by the circulation of the wing section, the pressure recovery for the combined case has to be similar, or even larger due to the enhanced channeling effect, and the flow thus separates at a similar ride height as for the isolated wing case.

**Wheel aerodynamics** Smith [71] indirectly also presents confirmation of the wing circulation effect on the separation over the top of the wheel. In the discussion of the circulation effect he states that the upstream element has a feedback on the downstream element as well. Circulation on the forward element effectively reduces the angle of attack of the rear element, as well as the velocities on its surface and hence reduces its lift. If the analogy of the previous discussion is continued with the wheel being the downstream element, then it can be concluded that this feedback is one of the reasons for the delayed separation over the top of the wheel.

Chapter 4 showed that the delayed separation over the top of the wheel is accompanied by an increase in wheel drag. This trend is opposite to that for a circular cylinder or sphere, where prevention of laminar flow separation by tripping of the flow is used as a principal method for drag reduction. This reveals that the wheel drag is more dominated by the secondary flow around the sides as a result of the low aspect ratio and by the interaction of wing vortices with the wheel wake. The lesson to be learned from this is that the classical approach for drag reduction by separation delay and wake size limitation is not necessarily applicable to wheel flows. In contrast the results indicate that it is much more important for drag minimization to ensure that the upper edge wing vortex passes on the inside of the wheel instead of over the top. Finally, it needs to be mentioned that the wing presence seems to have hardly any influence on the pressure peaks at the contact patch of the wheel. The results in figure 4.3 appear to be unaffected within the resolution of the data. This once more shows that this area of the wheel is governed by unique physics, which have limited overall influence on the flow and resulting force coefficients.

## 8.2 Parametrical study

The aerodynamic loads on the wing and wheels for a combined configuration depend on a large number of parameters. In this research the influence of ride height, overlap and gap have been studied, but the outcomes also depend on, among others, the wing and wheel geometries. The models used for the current research have been kept as simple as possible, but nevertheless geometrical details are still influential. The kink in the profile of the wheel, where the side wall meets the tyre tread (visualized in figure 2.2 with the $21mm$ dimension), is one feature in particular that could have introduced geometry dependent solutions. Although it is expected that this feature has not caused any fundamental changes in governing physical principles, it is possible that boundaries of the force regions and variations in wheel drag have locally been affected. Therefore it has to be kept in mind in the following parametrical study that relations between the variables can be obscured by these details.

It would be quite a challenge to derive one parametrical model that takes all variables and their complex interactions into account in order to produce an empirical estimate of the aerodynamic loads for the combined configuration. Instead, without trying to be complete, the aim of this section is to provide evidence in the form of parametrical relationships for the existence of the mechanisms that have been discussed previously.

**Channel inflow effect** The general level of wheel drag for a constant gap setting is primarily dependent on the channel inflow effect, as has been discussed in chapter 6. The channel area varies with overlap and figure 6.4 showed that the wheel drag curve translates in vertical direction as a result of overlap changes. To illustrate this point, figure 8.1 presents the wheel drag at $h/c = 0.158$ as function of the channel width, $a$, which is equivalent to representing this data against the channel area, since the height is fixed. The figure features curves for two different gap settings, which show a similar trend. The change in wheel drag with channel width can under these conditions be summarized as:

$$\frac{d(C_{Dwheel})}{d(a/b)} \approx 0.32, \tag{8.1}$$

which clearly confirms the drag increase with channel area increase that was predicted. The same figure also includes curves of the wing downforce coefficient at $h/c = 0.246$ for similar settings and conditions. This data shows that overlap is detrimental for the wing downforce and that the losses grow more than linearly with overlap increase.

**Wheel circulation effect** The wheel circulation effect, which has been discussed in more detail in the previous section, can be quantified with figure 8.2. Smith's exercise to examine the circulation effect with an airfoil and downstream cylinder [71] revealed that the lift of the wing reaches a maximum due to the obstruction influence, when the characteristic angle $\delta$ is near to 60°. This angle is defined as the angle between the horizontal and the line connecting the centre of the wheel and the trailing edge of the flap when the obstruction is positioned on the suction side of the airfoil. The airfoil lift increased continuously in Smith's experiment, when $\delta$ was varied from 0° (directly downstream of the airfoil) to 60°. Figure 8.2 shows how the maximum wing downforce (all occurring close to $h/c = 0.07$) decreases with increasing gap. Additionally the $\delta$-values for each of the cases are included as well and it can indeed be seen that the wing downforce increases with $\delta$-value.

**Wheel drag** The ride height at which the sudden change in wheel drag occurs varies with overlap and gap settings. If this characteristic ride height could be related to a physical quantity for given overlap and gap settings, then this would be very helpful in understanding what exactly happens. Several criteria have been tested, such as a minimum required distance between the top of the endplate from which the upper edge vortex starts and the wheel surface, or a threshold angle for the line from the flap trailing edge to the tangent point on the wheel, but without success. Nevertheless figure 8.3 might give an indication, as it seems that the tangential flow direction along the flap coincides for each of the three gap settings. This could imply that if the flow from the flap hits the wheel above a critical point, $\phi$, then the wheel drag will be of the higher level. For this overlap setting this value would be $\phi = 27.7°$. This physical explanation would then hint at a relation between the (rate of) flow over the wheel and the wheel drag, but more research is required to confirm this hypothesis. It would also provide an explanation for the coupling between the sudden changes in wheel drag and wing downforce; the latter has been discussed in section 6.4.

Finally, figure 6.5 shows that the maximum wheel drag increases with the gap value and that this maximum drag occurs at a lower ride height for larger gap values. This has been related to how easily the upper edge wing vortex can change location from the inside of the wheel to the top, which is easier achieved for a larger gap setting. Figure 8.4 confirms these trends, both with respect to the maximum wheel drag and the corresponding ride height. It can be noticed that the variation is fairly linear with gap changes, which suggests that the gap setting is the primary parameter in this process.

## 8.3 Practical applications of results

The results, which have been presented in this thesis, have been obtained for a specific wing - wheel configuration. This does however not imply that the findings are only applicable to this simplified geometry. Other car components, such as the nose cone, undertray and wheel suspension system, influence the quantitative values of the results, but the general trends and especially the governing flow physics do still hold. Therefore this section looks at the application of the findings to practical racecar situations. Hereto first new parameters including total drag and efficiency will be derived. Next, the results will be examined to find the optimal parameter settings for a number of aerodynamic design characteristics, based on the current simplified model. Finally, data will be presented for the front wheel drag of a complete F1 car model.

**Additional flow parameter derivations** Up till now the results have mainly been analyzed as they were measured, without further derivations. The translation of the pitching moment and the determination of the centre of pressure location form the only exceptions to this. However the experimental data contains more useful information, for example about the synergy effects of the combined configuration relative to the isolated components, that is worth examining. A new coefficient for the total drag, $C_{Dtotal}$ can be introduced to assess how the drag of the combined configuration compares to that of the isolated components. This quantity is defined as:

$$C_{Dtotal} = \frac{C_{Dwing} \cdot 0.16472 + 2 \cdot C_{Dwheel} \cdot 0.05201}{0.16472 + 2 \cdot 0.05201}, \tag{8.2}$$

where the coefficient is referenced to the total planform area[1] of the wing and wheels. For racecar purposes the drag coefficient is usually based on the frontal area, but this quantity changes with ride height and overlap. Nevertheless, if the total drag coefficient based on the frontal area is preferred, formula (B.1) can be used for a first estimate of the frontal wing area.

The total drag coefficient variation with ride height has been visualized in figure 8.5. The curve referring to the 'Separate components' has also been determined with the use of formula (8.2). The wing and wheel drag coefficients for this case are obtained from the isolated wing and wheel experiments, where the latter is independent of the ride height at $C_{Dwheel} = 0.623$. From this figure it can be seen that the total drag for the combined configuration is sometimes larger than that of the separate components. This happens at the lowest ride heights due to the higher downforce induced drag, at ride heights above the sudden wheel drag change and for the case with negative overlap. This latter case is interesting because the total drag is higher than that of the separate components over the complete ride height range as a result of the globally higher wheel drag. Fortunately the total drag is lower for all cases with positive overlap between approximately $h/c = 0.15$ and 0.3, which corresponds to the ride heights at which most open-wheel racecar front wings are operating. It is in this region that the synergy of the wing and wheel components have an advantageous effect on the total drag due to the interaction of the flow fields.

---

[1] This is the area of the wing and wheels projected in vertical direction onto the ground plane; the frontal area of the wheel is equivalent to the planform area due to its axi-symmetric nature.

Furthermore the aerodynamic efficiency is also important in racecar applications, because the usefulness of a certain configuration solution is often evaluated and limited by the amount of drag that is produced for a given amount of downforce. Figure 8.6 shows the wing efficiency, $L/D = C_{Lwing}/C_{Dwing}$, for the combined configuration and for the isolated wing. It is immediately obvious that the wing never reaches a similar efficiency as for the isolated wing, when the wheels are added. The fact that the case with the largest gap setting, CWW2050, produces the highest efficiency for the combined configurations is another sign that the overall influence of the wheels on the wing is detrimental for the wing efficiency. From figures 6.6 and 6.9 it can be concluded that the lower wing drag of CWW2050 is primarily responsible for this highest wing efficiency among the combined configurations.

Finally, the total efficiency of the configuration can be derived as well. However, due to the lack of experimental downforce data for the wheel, this has to be a hybrid parameter, $L_{wing}/D_{total}$, based on the wing downforce and the total drag of equation (8.2). The curves for this parameter are presented in figure 8.7, also including the data for the 'Separate components' once more. Logically the efficiency levels in figure 8.6 are higher than those in figure 8.7. The combined configuration has become even less efficient at high ride heights due to the large contribution of the wheel drag, however at medium ride heights the efficiency is almost as good as for the separate components. At the lowest ride heights the efficiency of the combined configuration is actually even better than that of the separate components as a result of the higher wing downforce and lower wheel drag. Fascinatingly, the efficiency in the highly relevant interval $h/c = 0.211$ to 0.264 is almost identical for the CWW2010, CWW2050 and CWW5020 configurations. This implies that the designer has a large degree of freedom in choosing an appropriate wing - wheel setting, when the influence of wheel downforce is neglected. If the contribution of wheel downforce / lift[2] could be included in figure 8.7 it is expected that the efficiency of the combined configuration will be higher than that of the separate components due to the predicted lift of the wheel for the isolated case. Most likely the advantageous synergy would especially be noticeable in the region $h/c = 0.15$ to 0.35, where the CFD predicts a downforce on the wheel for the combined configuration.

---

[2] For example by using the computational wheel downforce / lift behaviour of figure 7.2; however this is only available for the baseline CWW2020 configuration.

**Parameter design choice for optimal aerodynamic performance** In engineering it is very common to optimize a design for a specific quantity; in aerodynamics 'design for minimum drag' and 'design for maximum efficiency' are two well known criteria. The current configuration features three design parameters, the ride height, the overlap and the gap, which can all be varied independently. Within the next paragraphs the attention will however be fixed on reduced parameter space cases. The current FIA technical regulations state that the front wing can not go below $150mm$ and above $350mm$ from the reference plane[3]. If the skid block underneath the reference plane is for simplicity considered to coincide with the ground then the minimum wing ride height would be $h/c = 0.282$ for the 50% scale configuration. Because of the ground effect, designers always opt for the lowest ride height possible and the following analysis is therefore based on a fixed ride height of $h/c = 0.282$.

In case minimum drag is the outright design criterion, then the CWW5020 configuration performs best of all those tested. This holds with respect to the minimum wheel drag (for which the CWW3535 case comes a close second best) and the minimum total drag. The minimum wing drag is obtained with CWW5510, although the CWW5020 shows only a slightly higher wing drag at this ride height. A large overlap, which leads to an increased channel inflow effect, is thus both beneficial for the wheel drag and for the wing drag. A small gap is advantageous for the wheel drag, but usually leads to an increase in wing drag.

However if the configuration is optimized for maximum wing downforce, the least amount of overlap is preferable, as the CWW-1520 case delivers the highest value, followed by the CWW0020 case. Less overlap leads to less separation losses at the wing tips and thus to a higher downforce; the lower drag benefit of large overlap settings actually mainly results from the reduction in downforce induced drag. The gap should be kept as small as possible for maximum wing downforce, because at this ride height the wheel circulation effect is beneficial. This trade-off between overlap and gap can be recognized from the fact that the CWW2010 case performs better than CWW0035 and almost as good as CWW0020.

Design for optimum wing efficiency, as presented in figure 8.6, would lead to choosing the CWW2050 configuration. This clearly shows that efficiency is a compromise between downforce and drag, because these settings perform average for both quantities. The sec-

---

[3] See FIA Technical Regulation 3.7.1: this applies to the outsides of the wing near the tips, the part underneath the nose cone can be lower to the ground and is usually curved downwards.

ond best case is CWW0035, which still indicates that little interaction with the wheel (no overlap, larger gap) is advantageous for the wing efficiency. The fact that the separate components case has the highest overall wing efficiency is another clear sign of the detrimental effect of the wheels on this quantity. Nevertheless if the wheel drag is taken into account as well, like in figure 8.7, the picture changes again. Design for maximum total efficiency, based on the wing downforce and total drag, favours the CWW3535 configuration. This is a clear middle of the road solution between minimum drag and maximum downforce.

It is now worth returning to the comments by Katz [5] mentioned in section 1.4.3 of the literature review. He stated that the interaction phenomena between the wing tip vortices and the wheels favoured a narrow wing span design with as little overlap as possible. This is in agreement with the current results, when the wing downforce or efficiency is the main design criterion and the wheels are not part of the analysis. However, if the wheels are taken into account as well, then a little bit of overlap is quite beneficial. Some of the current F1 endplate designs seem to cater for both requirements by tilting the endplates inward at the top and by reducing the wing span towards the downstream end of the endplate. This combines the benefits of using the lower edge wing vortex and channel inflow effect to reduce the wheel drag, while the harmful influence of the wheels on the flap tips is reduced at the same time. Local changes in the wing twist and chord could be used to optimize the wing design to the combined wing - wheel flow field in a similar way as has been explained by Katz and Dykstra [90] for the adaptation of a rear wing to a car body.

Finally, design criteria in F1 are often based on stability requirements as well. Stability of the results for changes in car attitude are tested by varying the front and rear ride height independently to mimic conditions like braking and acceleration. Next to the changes in ride height this exercise also induces changes in angle of attack. Because the latter parameter has not been varied during this research it is not possible to assess for this design criterion. With the information presented in figure 6.8 it is however possible to state that the centre of pressure for the CWW5020 case is the most stable and thus that a change in ride height leads to little movement of the resulting aerodynamic force on the front wing. The results can not be examined for stability with respect to unsteady flow features either, nor for stability under yaw conditions and / or wheel steer angles. All three of these conditions could be interesting subjects for future research.

**Comparison for complete car** Actual racecars feature much more complicated wing and endplate designs compared to the simplified geometry used for this research. The wing surfaces show steps, twist and chord variation, whereas the endplate can have cuts, feet, flick-ups and be curved and angled in all directions. These additional geometrical aspects also introduce new flow features to the interaction. Mahon [12] showed for example that endplate feet generate additional vortices underneath these feet, originating from the outside edge. Furthermore the original lower edge wing vortices reduce in strength due to the addition of the endplate feet. Therefore it is expected that the interaction between the wing and wheel flow will be modified as well.

For reference a single test has been performed in the $11 \times 8$ wind tunnel of the University of Southampton with a 50% scale complete racecar. The wind tunnel model represented a F1 car from several years ago. The 050 wheel that was used for the current research was fitted in a 'wheels-off' set-up either with or without a brakedisc to block some of the flow through the wheel hub. No cover discs for the wheel were used in contrast to during the wing - wheel tests. The detailed car model featured a non-constant chord double element wing with flat endplates. The endplates were equipped with feet, which curved at the inside trailing edge, flick-ups around halfway the endplate height and v-shaped cuts at the top. The Aerotech 0551 load cell was used to measure the wheel drag. The model was moved around $h/c = 0.275$ over a $12.5mm$ ride height range at model scale in steps of $2.5mm$, where the front and rear ride height were changed equi-distant in order to keep the angle of attack constant. The overlap was approximately $20mm$ and the gap $11mm$.

The measured wheel drag varied from $C_D = 0.44$ to $0.46$ with the brakedisc in place and was around 0.47 without the brakedisc. This reveals that the wheel drag is lower for the complete car than for the simplified wing - wheel configuration; the respective wheel drag value for the CWW2010 case is between $C_D = 0.55$ and $0.57$. As expected, this shows that the designers have used the more complicated geometrical features to reduce the wheel drag. The variation in wheel drag over the $12.5mm$ ride height change is less than 4% for both the complete car case and for the combined wing - wheel case. The small ride height interval and different geometries make it impossible to compare the trends in wheel drag between the complete car and the combined wing - wheel configuration and it is therefore unknown in which force region the complete car model operates at these heights. Further analysis of the flow field and in particular the vortex trajectories could give more insight into this.

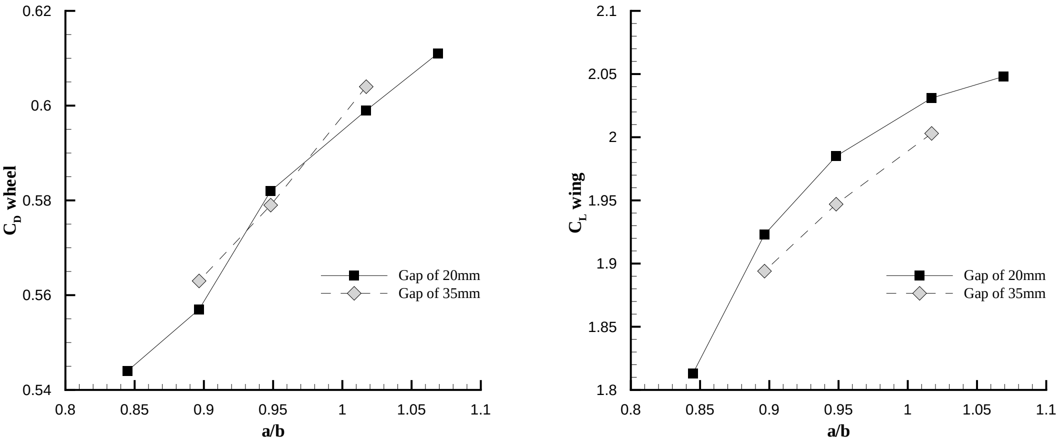

Figure 8.1: Wheel drag at $h/c = 0.158$ (left) and wing downforce at $h/c = 0.246$ (right) as function of the non-dimensional channel width a/b for two gap settings, with 'a' the spanwise distance between the wheels at $150mm$ from the ground plane and 'b' the wing spanwidth.

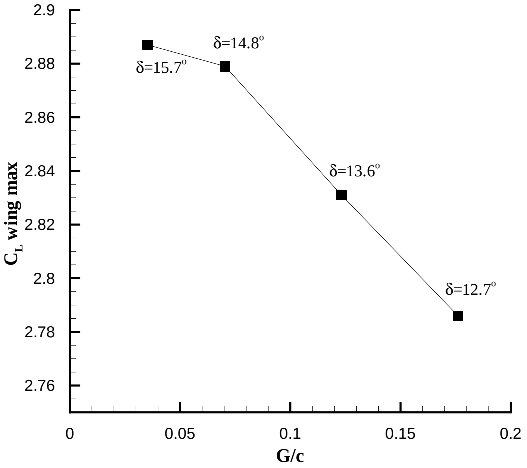

Figure 8.2: Maximum wing downforce as function of the non-dimensional gap for $20mm$ overlap with $\delta$ value presented per point, $\delta$ is the angle between the horizontal and the line through the centre of the wheel and the trailing edge of the flap.

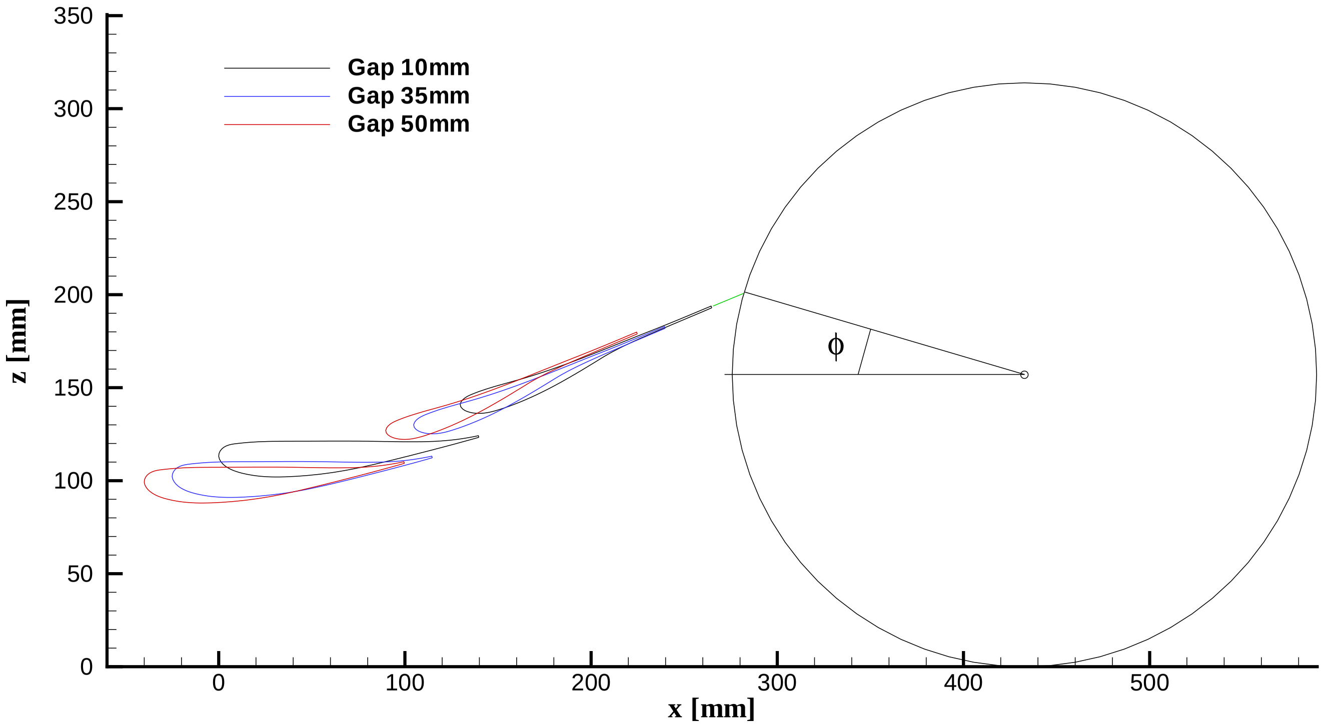

Figure 8.3: Sketch of the relative wing - wheel settings at the sudden change in wheel drag for different gap values at a fixed overlap of $20mm$; origin of $10mm$ gap case.

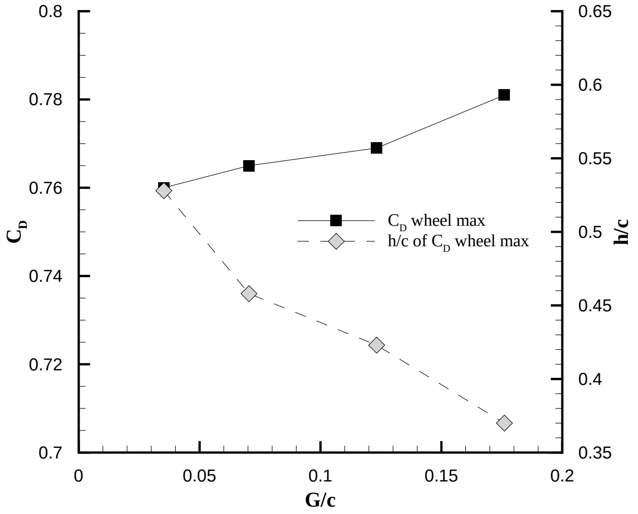

Figure 8.4: Maximum wheel drag and ride height of maximum wheel drag as function of the non-dimensional gap for $20mm$ overlap.

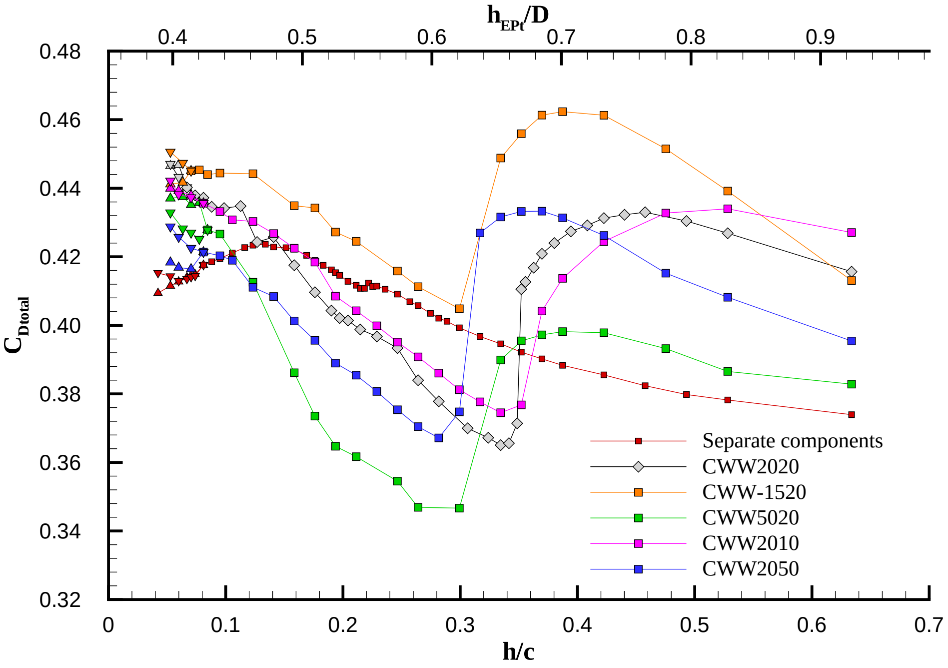

Figure 8.5: Variation of the experimental total drag, based on the wing and two wheels, for the combined configuration with ride height for wing - wheel overlap and gap variations.

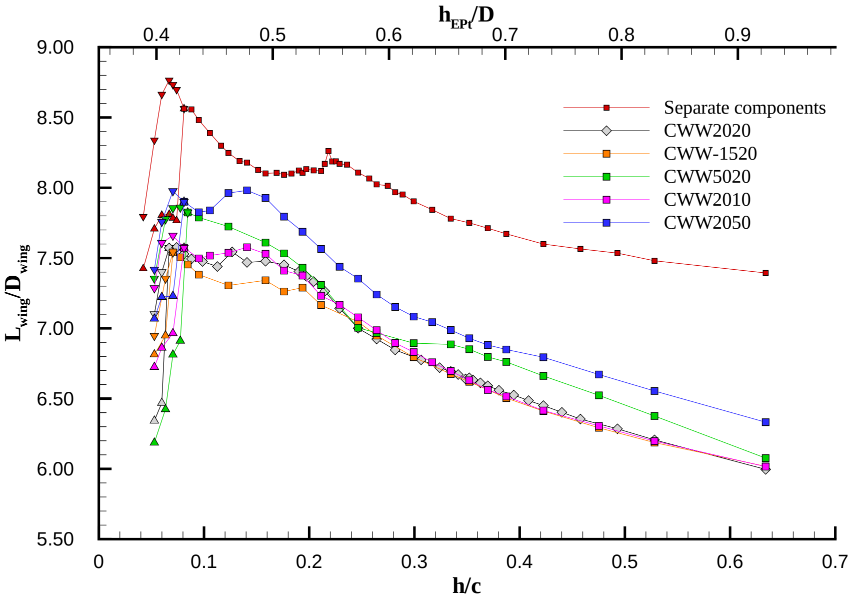

Figure 8.6: Variation of the experimental wing efficiency, based on only the wing downforce and drag, for CWW with ride height for wing - wheel overlap and gap variations.

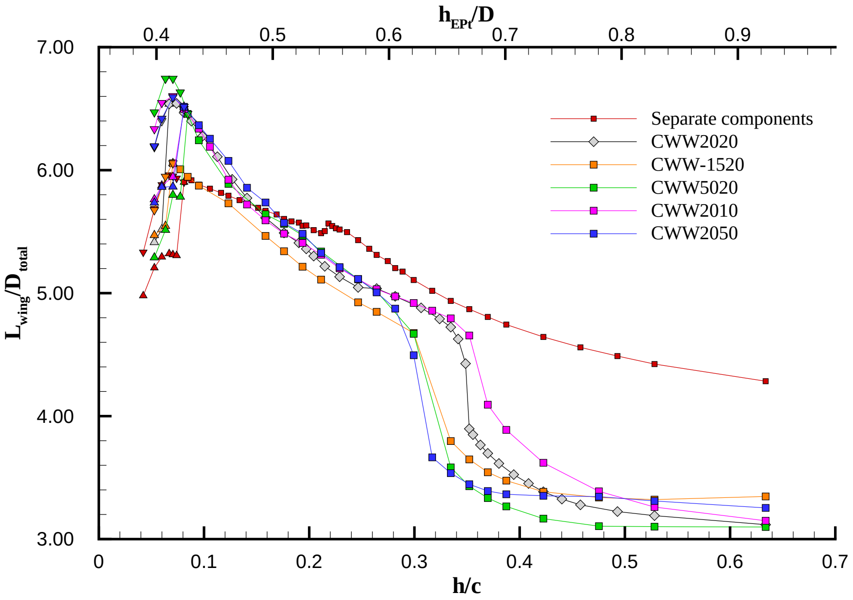

Figure 8.7: Variation of the experimental efficiency, based on the wing downforce and total drag, for CWW with ride height for wing - wheel overlap and gap variations.

# Chapter 9

# Conclusions and Recommendations

The goal of this study has been to answer the research questions posed in section 1.5. The first section of this chapter will summarize the outcomes of the study with respect to these objectives. The next section, 9.2, presents an overview of additional conclusions, followed by a summary of the novel contributions of this research in section 9.3. Finally, the last section gives recommendations for future work based on the findings of this research.

## 9.1 Research objective conclusions

The first research objective was to assess the influence of the wing on the aerodynamic wheel characteristics and vice versa. Experimental answers to this question can be found in chapter 4 and 5 for respectively the wheel and the wing, whereas chapter 7 presented the computational results. In summary it can be concluded that the wheel drag is dependent on the wing ride height for the combined configuration. Lower wheel drag than for the isolated wheel is experienced below approximately $h/c = 0.3$ and higher above this height. Both wheel downforce and side force also vary with wing ride height but no experimental data has been obtained for this. The wing on the other hand produces more downforce at low ride heights compared to the isolated wing and less at higher. A disproportional change in wing downforce is experienced at the same height as where the wheel drag suddenly changes. The wing and wheel circulation effects are the main contributors to this coupling. The wing drag is generally higher for low ride heights, when the wheels are added, while the centre of pressure moves downstream.

The influence of the positional parameters ride height, overlap and gap on the wing - wheel interaction was the subject of the second research objective. Chapter 6 provides answers regarding the latter two parameters, whereas the influence of ride height was integrated in the analysis throughout the study. In general, overlap variation leads to a vertical translation of the wheel drag curve due to the change in channel inflow effect, with the highest drag occurring for negative overlap values. Increase of the gap leaves the lower ride height results largely unaffected, but leads to a translation of the sudden wheel drag change and of the maximum wheel drag to a lower ride height, because the upper edge wing vortex trajectory can change position more easily with larger gap settings. Overlap variations similarly affect the wing downforce level, where negative overlap cases show higher downforce. However at low ride heights these cases experience more downforce limitation due to the vortex breakdown effects and therefore the cases with positive overlap reach a higher global maximum downforce. The sudden wing downforce change shifts to lower ride heights with increasing gap, in line with the sudden change in wheel drag, and larger gap settings lead to generally slightly lower downforce levels.

Research objective three was to define the mechanisms and physics responsible for the wing - wheel interaction. This question has been answered parallel to the previous two and studied in more detail in chapter 8. The effect of the wing on the wheel can be explained by the (delayed) separation over the top of the wheel, which primarily results from the wing circulation effect, by the extra suction on the inside of the wheel due to the channel inflow effect and by the wake interaction effects. The trajectory location of the upper edge wing vortex is dominant in the latter mechanism. The high wheel drag at larger ride heights always goes hand in hand with a strong circulation in the wake of the wheel and a vortex trajectory over the top - rather than at the inboard side - of the wheel. The wing is still governed by the same channeling, separation and vortex effects as the isolated wing, but their influence has been modified. Vortex breakdown and separation from the suction side are still the primary downforce limiting mechanisms, whereas channeling effect (enhanced by the wheel wall rotation for low ride heights) is the primary downforce enhancing mechanism. Additionally the wheel circulation effect enhances or reduces the wing downforce due to the wheel wall rotation, the downstream obstruction by the wheel and the dumping effects.

Finally the fourth research objective was to examine whether CFD could reproduce the wing - wheel interaction results. Hereto a steady RANS simulation with SA turbulence model has been applied, in line with current industry standards. The results showed that compared to the correlation for the isolated components the combined configuration aerodynamics are predicted less accurately. Qualitatively the force behaviour is captured, but the wheel drag can be underpredicted by more than 25% at higher ride heights. The correlation for the wing results is much better and reveals that the upstream interaction phenomena are better simulated than the downstream effects on the wheel. The latter rely among others on vortex interaction, which is a weakness of SRANS simulations. The use of non-conformal zones around the wing module has had a negative effect on the outcomes as well. All in all it can be concluded that the current simulation approach leads to acceptable predictions of the flow field and features, but that the exact flow quantities and integrated parameters, such as force coefficients, are not always accurate enough for practical applications.

## 9.2 Further conclusions

In addition to the four research objectives, three extra goals were included in section 1.5 as well. These are discussed next. Firstly, the influence of wheel camber on the results is very limited, as was concluded in section 3.1.5. The 2.4° camber of the current model leads to asymmetry in the pressure distribution and wake, but no fundamental modifications of the flow physics are apparent.

Secondly, considerable improvements have been made with respect to the correlation between the computational and the experimental results for the isolated wing. The finding that the CAD model that was used for the computational grid differed from the actual experimental geometry contributed most to this improvement and scanned wing data was thus used to correct for large scale discrepancies such as the difference in trailing edge thickness. The downforce was underpredicted by approximately 6% by the SA SRANS approach, although underprediction of vortex dilution and delayed, yet stronger, vortex breakdown led to local variations. The wing drag was overpredicted by roughly 5%, whereas the pitching moment showed larger differences, probably due to the experimental measurement method, because the measured moment had to be translated over a considerable distance.

Finally, new experimental data for the isolated wing also revealed that the downforce limiting mechanism at low ride heights did not originate from (2D) wake bursting as Mahon [12] suggested, but actually resulted from lower edge wing vortex bursting with flow reversal at the vortex core. PIV data and CFD results clearly showed that the flow reversal is restricted to the tip of the wings, whereas on-surface pressure and oil flow data confirmed that the influence was limited to a local area near the wing tips.

## 9.3 Novel contributions

During the research programme several novel contributions have been made to the research field. These can be summarized as:

- This study is the first of its kind in examining the aerodynamic interaction effects between a racecar front wing and the front wheels.
- The influences of the three geometrical parameters ride height, overlap and gap on this interaction have been analyzed and quantified.
- Physical principles and flow mechanisms have been presented to explain the interaction results.
- The application of a steady RANS simulation to this problem has been studied over a range of ride heights, revealing the strengths and weaknesses of this method for such a purpose.
- It has been rectified that off-surface detached separation, or wake bursting, is not one of the downforce limiting mechanisms acting on an isolated wing in ground effect, but that instead this decline in downforce at low ride heights can be contributed to lower edge wing vortex bursting.
- The 3D wing in ground effect problem has, to the author's knowledge, for the first time been studied with the use of SRANS simulations over a large ride height range. The detailed analysis showed which mechanisms and flow features are not captured accurately in CFD, providing a comprehensive case to assess the applicability of this method to such a flow problem.

## 9.4 Recommendations

The current research presents a comprehensive initial study of wing - wheel interaction. Nevertheless the process of research usually creates new questions to succeed those that have been answered. Due to time constraints the current work had to be restricted to the previously discussed objectives. Therefore the following section presents the newly posed questions in the form of recommendation for future work. The recommendations have been divided into three categories: continuation of the research, expansion of the research and changes to the research approach.

**Continuation of research** At several stages during the analysis of the data in the previous chapters it has been mentioned that the experimental data required to prove a proposed idea had not been acquired, because of time considerations. Thus it would be interesting to perform more experimental tests with the current configuration in order to confirm the mechanisms and flow physics that have been discussed here. The amount of pressure data for the wing and wheel was sufficient to derive the fundamentals of the flow field from, but it would be beneficial to acquire centre span wing pressure data for CWW5020 in addition to the results in figure 6.1. Furthermore wing pressure data for different settings, such as CWW2050, CWW2010 and CWW-1520, could be illustrating. The same applies to the wheel pressure data, whereas on top of this it would be helpful to acquire data for different pressure sensor locations as well. The currently used locations are shown in figure 2.2, but the model has already been prepared for the use of an extra six tap locations, distributed over the tyre tread and side wall. It is also relatively straightforward to expand this number even further to sensor locations in the grooves. A better resolution of the pressure curves along the wheel cross section would provide more information to examine the flow features and also creates the opportunity to derive an estimate of the experimental wheel downforce and side force via the indirect method.

The newly gained knowledge on flow physics and features could also be used to apply PIV measurements in a structured way in order to test more of the proposed ideas. For example, a finer ride height variation around the setting at which the lower edge wing vortex breaks down could confirm whether this happens at $h/c = 0.113$ for the CWW2020 configuration, as derived from the other experimental data. Hereto more PIV tests in the A1 and A2 plane of figure 2.11 would be helpful. Furthermore the existence of the additional vortex, which according to CFD originates from the wing when the wheels are present (feature ‘B’ in figure 4.11), could be checked experimentally with PIV. A further investigation of the streamwise vortex breakdown location for the isolated wing in force region *b* (see figure 3.11) could clarify why the wing downforce is limited as much by this vortex dilution. Whereas a more in depth analysis of the relationship between the geometrical parameters and the occurrence of the high wheel drag could be helpful in practical applications. Finally, hardly any PIV data is available for other configuration settings than the baseline case. With respect to the CFD, the research can also simply be continued by simulating extra ride height cases for the baseline configuration and / or by generating meshes for overlap and gap variations. Additional turbulence models can be tested and a grid sensitivity study for the combined configuration can prove useful.

**Expansion of research** Apart from continuing the research within the same parameter and condition domain, alternatively it is also possible to expand the scope of the research. In chapter 8 three additional conditions were mentioned that are of particular use to racecar aerodynamicists. First of all testing at different wing angles of attack can provide information on the aerodynamic stability of the configuration under alternative circumstances, such as acceleration (decrease in angle of attack) and braking (increase in angle of attack). The wing angle of attack has been varied by Mahon [12] for the isolated wing and this can be repeated without complications for the current configuration. Secondly, a racecar hardly ever travels forward with the wind perfectly ‘head onwards’, thus results under yaw conditions are useful as well. It would be possible to alter the wing and wheel support systems in order to incorporate a yaw angle of a few degrees, however this could be more challenging for the wind tunnel facilities and mainly for the rolling road. Finally, this research has focused on steady results, however the nature of the involved physics and geometries indicate that unsteady phenomena play an important role as well. Further examination of the instantaneous PIV and force results can give a first impression of the extent of the unsteady variations, whereas URANS or DES simulation can provide a similar idea for the computations.

The test model geometry can also easily be adapted to accommodate a number of configuration variations. The cover discs of the wheels can be removed to study the influence of flow through the hub on the outcomes. A Gurney flap can be added to the flap and / or the endplates can be modified. Flat endplate feet are available for the current model, but it is also possible to change the endplates and include features like flick-ups and vortex channels, or curvature and cuts. Finally, it would be possible to start including extra car parts to mimic the complete car conditions more accurately. Things that have to be kept in mind though, when - for example - a nose cone, undertray or suspension system are added, are that the blockage of the model in the $7 \times 5$ tunnel is currently already on the higher side (see appendix B.1) and that the wing is supported by a system that does not necessarily represent a car configuration either.

**Changes to the research approach** The last recommendations deal with potential changes to the research approach. On the experimental side it would be possible to apply new measurement methods to obtain additional data. LDA and smoke visualization could be used to determine the characteristics of the vortex breakdown in more detail. The first method can produce all three velocity components that are required to do a proper analysis of the state of the vortex, whereas a smoke visualization through the core could give an instant idea of the breakdown location and unsteady aspects. Other modifications that could benefit the results are the use of non-cambered wheels, since these do obscure some of the flow features and make it difficult to compare similar locations on the inside and outside of the wheel; even though the camber does not lead to fundamental changes of the results. Also it would be preferable to either measure the pitching moment in a different way, or to make a proper estimate of the error in the moment due to deformation and having the load cell located outside of the wing.

The computational approach can mainly be improved in two ways. Using high-quality hybrid grids, in which the non-conformal zones are replaced by unstructured zones and the cells are primarily concentrated in critical areas, such as between the wing and wheel and in the wheel wake, should improve the correlation of the wing - wheel interaction. The quality of the unstructured zones is just as important as that of the non-conformal zones with respect to the interaction phenomena, however it is expected that ultimately a higher quality overall solution can be obtained by using the hybrid approach in combination with the use of a different grid generation programme to create the unstructured mesh. Furthermore the steady RANS simulation method has its limitations when it comes to modeling the bluff body flow and vortex interactions. Obtaining averaged solutions with URANS or DES simulations should lead to an improvement in the correlation and also has the advantage that unsteady features can be analyzed and possibly hysteresis effects can be captured. For the latter the choice of initialization and boundary conditions is most likely vital to the success of the attempt.

# Bibliography

[1] Wright, P.G. The influence of aerodynamics on the design of formula one racing cars. *International journal of vehicle design*, 3(4):383–397, 1982.

[2] Agathangelou, B. and Gascoyne, M. Aerodynamic design considerations of a formula 1 racing car, 1998. SAE Publication 980399.

[3] Dominy, J.A. and Dominy, R.G. Aerodynamic influences on the performance of the Grand Prix racing car. *Proceedings of the Institution of Mechanical Engineers, Part D: Transport Engineering*, 198(7):87–93, 1984.

[4] Zhang, X., Toet, W. and Zerihan, J.D.C. Ground effect aerodynamics of race cars. *Applied Mechanics Reviews*, 59:33–49, 2006.

[5] Katz, J. Aerodynamics of race cars. *Annual Review of Fluid Mechanics*, 38:27–63, 2006.

[6] Zerihan, J.D.C. and Zhang, X. Aerodynamics of a Single Element Wing in Ground Effect. *Journal of Aircraft*, 6:1058–1064, 2000.

[7] Zhang, X. and Zerihan, J.D.C. Turbulent wake behind a single element wing in ground effect. Technical report, 10th International Symposium: Applications of laser techniques to fluid mechanics, 2000.

[8] Zerihan, J.D.C. *An investigation into the aerodynamics of wings in ground effect.* PhD thesis, University of Southampton, Southampton, UK, 2001.

[9] Zerihan, J.D.C. and Zhang, X. A single element wing in ground effect; comparisons of experiments and computation. Technical report, 2001. AIAA 2001 - 0423.

[10] Zhang, X., Zerihan, J.D.C., Ruhrmann, A. and Deviese, M. Tip vortices generated by a wing in ground effect. Technical report, 11th International Symposium: Applications of laser techniques to fluid mechanics, 2002.

[11] Mahon, S.A. and Zhang, X. Computational analysis of pressure and wake characteristics of an aerofoil in ground effect. *Journal of Fluids Engineering, Transactions of the ASME*, 127:290–298, 2005.

[12] Mahon, S.A. *The aerodynamics of multi-element wings in ground effect.* PhD thesis, University of Southampton, Southampton, U.K., 2005.

[13] Zhang, X. and Zerihan, J.D.C. Aerodynamics of a double-element wing in ground effect. *AIAA Journal*, 41:1007–1016, 2003.

[14] Senior, A.E. and Zhang, X. The force and pressure of a diffuser-equipped bluff body in ground effect. *Journal of Fluids Engineering*, 123(1):105–111, 2001.

[15] Ruhrmann, A. and Zhang, X. Influence of Diffuser Angle on a Bluff Body in Ground Effect. *Journal of Fluids Engineering*, 125(2):332–338, 2003.

[16] Zhang, X., Senior, A. and Ruhrmann, A. Vortices behind a bluff body with upswept aft section in ground effect. *International Journal of Heat and Fluid Flow*, 25:1–9, 2004.

[17] McManus, J. and Zhang, X. A computational study of the flow around an isolated wheel in contact with the ground. *Journal of Fluids Engineering, Transactions of the ASME*, 128(3):520–530, 2006.

[18] Zdravkovich, M.M. *Flow around circular cylinders. Volume 1: Fundamentals.* Oxford Science Publications, Oxford University Press, Oxford, 1997.

[19] Zdravkovich, M.M. *Flow around circular cylinders. Volume 2: Applications.* Oxford Science Publications, Oxford University Press, Oxford, 2003.

[20] Ribeiro, J.L.D. Effects of surface roughness on the two-dimensional flow past circular cylinders I: mean forces and pressures. *Journal of Wind Engineering and Industrial Aerodynamics*, 37:299–309, 1991.

[21] Ribeiro, J.L.D. Effects of surface roughness on the two-dimensional flow past circular cylinders II: fluctuating forces and pressures. *Journal of Wind Engineering and Industrial Aerodynamics*, 37:311–326, 1991.

[22] Zdravkovich, M.M., Brand V.P., Mathew G. and Weston A. Flow past short circular cylinders with two free ends. *Journal of Fluid Mechanics*, 203:557–575, 1989.

[23] Roh, S.C. and Park, S.O. Vortical flow over the free end surface of a finite circular cylinder mounted on a flat plate. *Experiments in Fluids*, 34:63–67, 2003.

[24] Ayoub, A. and Karamcheti K. An experiment on the flow past a finite circular cylinder at high subcritical and supercritical Reynolds numbers. *Journal of Fluid Mechanics*, 118:1–26, 1982.

[25] Zdravkovich, M.M., Flaherty, A.J., Pahle, M.G. and Skelhorne, I.A. Some aerodynamic aspects of coin-like cylinders. *Journal of Fluid Mechanics*, 360:73–84, 1998.

[26] Lazos, B. Surface topology on the wheels of a generic four-wheel landing gear. *AIAA Journal*, 40(12):2402–2411, 2002.

[27] Lazos, B. Mean flow around the inline wheels of four-wheel landing gear. *AIAA Journal*, 40(2):193–198, 2002.

[28] Sumer, B.M., Jensen, B.L. and Fredsoe, J. Effect of a plane boundary on oscillatory flow around a circular cylinder. *Journal of Fluid Mechanics*, 225:271–300, 1991.

[29] Bearman, W. and Zdravkovich, M.M. Flow around a circular cylinder near a plane boundary. *Journal of Fluid Mechanics*, 89(1):33–47, 1978.

[30] Zhang, X., Mahon, S., Van den Berg, M.A. and Williams, C. Aerodynamics of a Half-Cylinder in Ground Effect, 2005. Proceedings of the 6th Engineering and Turbulence Modeling and Measurements Conference ETMM6, Sardinia, Italy.

[31] Kimura, T., Tsutahara, M. and Wang, Z. Wake of a rotating circular cylinder. *AIAA Journal, Technical Notes*, 30(2):555–556, 1991.

[32] Diaz, F., Gavalda, J., Kawall, J.G., Keffer, J.F. and Giralt, F. Vortex shedding from a spinning cylinder. *Physics of Fluids*, 26(12):3454–3460, 1983.

[33] Kano, I. and Yagita, M. Flow around a rotating circular cylinder near a moving plane wall. *The Japan Society of Mechanical Engineers, International Journal, Series B*, 45(2):259–268, 2002.

[34] Fackrell, J.E. *The aerodynamics of an isolated wheel rotating in contact with the ground.* PhD thesis, University of London, London, U.K., 1974.

[35] Ulrichs, E. and Herwig, H. Between two limits: Flow separation behind a bluff body close to a wall. *Forschung im Ingenieurswesen*, 68:36–38, 2003.

[36] Morel, T. Aerodynamic drag of bluff body shapes characteristic of hatch-back cars, 1978. SAE Preprints, no. 780267.

[37] Ahmed, S.R., Ramm, G. and Faltin, G. Some salient features of the time - averaged ground vehicle wake, 1984. SAE Special Publications, 1984, p 1-31.

[38] Balachandar, S., Mittal, R. and Najjar, F.M. Properties of the mean recirculation region in the wakes of two-dimensional bluff bodies. *Journal of Fluid Mechanics*, 351:167–199, 1997.

[39] Prasad, A. and Williamson, C.H.K. A method for the reduction of bluff body drag. *Journal of Wind Engineering and Industrial Aerodynamics*, 69(71):155–167, 1997.

[40] Rathakrishnan, E. Effects of a Splitter Plate on Bluff Body Drag. *AIAA Journal*, 37(9):1125–1126, 1999.

[41] Rodi, W. Comparison of LES and RANS calculations of the flow around bluff bodies. *Journal of Wind Engineering and Industrial Aerodynamics*, 69(71):55–75, 1997.

[42] Hansen, R.P. and Forsythe, J. A grid convergence study of a highly separated turbulent flow. *Computing in Science and Engineering*, 6(6):30–37, 2004.

[43] Laurence, D. Modeling flows around bluff bodies by Reynolds averaged transport equations. *Journal of Wind Engineering and Industrial Aerodynamics*, 46, 1993.

[44] Laurence, D. and Mattei, J.D. Current state of computational bluff body aerodynamics. *Journal of Wind Engineering and Industrial Aerodynamics*, 49:23–44, 1993.

[45] Tobak, M. and Peake, D.J. Topology of three-dimensional separated flows. *Annual Review of Fluid Mechanics*, 14:61–85, 1982.

[46] Van den Berg, M.A., Proot, M.M.J. and Bakker, P.G. A topological study of the genesis of a horseshoe vortex in the symmetry plane due to an adverse pressure gradient, 2001. American Society of Mechanical Engineers, Fluids Engineering Division (Publication) FED, v 256, 2001, 17–21.

[47] Proot, M.M.J. and Bakker, P.G. Topological investigation of separation/attachment structures immediately in front of juncture, 2000. Proceedings of ASME 2000 Fluid Engineering Division Summer Meeting, FEDSM 00-11087.

[48] Mercker, E., Breuer, N., Berneburg, H. and Emmelmann, H.J. On the aerodynamic interference due to the rolling wheels of passenger cars, 1991. SAE Publication 910311.

[49] Skea, A.F., Bullen, P.R. and Qiao, J. CFD simulations and experimental measurements of the flow over a rotating wheel in a wheel arch, 2000. SAE Publication 2001-01-0487, Reprinted from Vehicle Aerodynamics (SP-1524), SAE 2000 World Congress, March 6–9, 2000, Detroit, Michigan.

[50] Basara, B., Beader, D. and Przulj, V. Numerical simulation of the air flow around a rotating wheel, 2000. 3rd MIRA International Vehicle Aerodynamics Conference, 2000, Rugby, UK.

[51] Knowles, R., Saddington, A. and Knowles, K. Simulation and experiments on an isolated racecar wheel rotating in ground contact, 2002. 4th MIRA International Vehicle Conference, 2002, Gaydon, UK.

[52] Mears, A.P., Dominy, R.G. and Sims-Williams, D.B. The flow about an isolated rotating wheel - effects of yaw on lift, drag and flow structure, 2002. 4th MIRA International Vehicle Conference, 2002, Gaydon, UK.

[53] Purvis, A.R. and Garry, K.P. The Wake Behind a Deformable Racing Tyre, 2004. 5th MIRA International Vehicle Conference, 2004, Gaydon, UK.

[54] Wäschle, A., Cyr, S., Kuthada, T. and Wiedemann, J. Flow around an isolated wheel - experimental and numerical comparison of two CFD codes. Technical Report SAE Technical Paper Series 2004-01-0445, SAE, 2004.

[55] Mears, A.P., Dominy, R.G. and Sims-Williams, D.B. The air flow about an exposed racing wheel, 2002. SAE Publication 2002-01-3290.

[56] Mears, A.P., Crossland, S.C. and Dominy, R.G. An investigation into the flow-field about an exposed racing wheel, 2004. SAE Publication 2004-01-0446.

[57] Morelli, A. Aerodynamic effects on an automobile wheel, 1969. Technical Report Translation 47/69, MIRA.

[58] Morelli, A. Aerodynamic actions on an automobile wheel, 1970. Road Vehicle Aerodynamics - Proceedings of the First Symposium on Road Vehicle Aerodynamics, City University.

[59] Stapleford, W.R. and Carr, G.W. Aerodynamic characteristics of exposed rotating wheels. Technical Report 1970/2, MIRA, 1970.

[60] Cogotti, A. Aerodynamic characteristics of car wheels, 1983. International Journal of Vehicle Design, Special Publication SP3, no. 33.

[61] Fackrell, J.E. and Harvey, J.K. The flow field and pressure distribution of an isolated road wheel, 1973. Advances in Road Vehicle Aerodynamics, BHRA Fluid Engineering.

[62] Fackrell, J.E. and Harvey, J.K. The aerodynamics of an isolated road wheel, 1975. Proceedings of the Second AIAA Symposium of Aerodynamics of Sports and Competition Automobiles.

[63] Hackett, J.E., Baker, J.B., Williams J.E. and Wallis S.B. On the influence of ground movement and wheel rotation in tests on modern car shapes, 1987. SAE Publication 870245.

[64] Oswald, L.J and Browne, A.L. The airflow field around an operating tire and its effect on tire power loss, 1981. SAE Technical Report 810166.

[65] Wickern, G., Zwicker, K. and Pfadenhauer M. Rotating wheels - their impact on windtunnel test techniques and on vehicle drag results. Technical report, 1997. SAE Publication 970133.

[66] Axon, L., Garry, K. and Howell, J. An evaluation of CFD for modeling the flow around stationary and rotating wheels. Technical report, 1998. SAE Publication 980032.

[67] Skea, A.F., Bullen, P.R. and Qiao, J. The use of CFD to predict the air flow around a rotating wheel, 1998. Proceedings of the 2nd International Conference On Vehicle Aerodynamics, UK.

[68] McManus, J.P. The aerodynamics of wheels in ground effect, 2003. MPhil, PhD Transfer Report, University of Southampton.

[69] Kellar, W.P., Pearse, S.R.G and Savill, A.M. Formula 1 car wheel aerodynamics. *Sports Engineering*, 2:203–212, 1999.

[70] Knowles, R., Saddington, A. and Knowles, K. On the near wake of rotating 40%-scale champ car wheels, 2002. SAE Publication No. 2002-01-3293, Reprinted from Proceedings of the 2002 SAE Motorsports Engineering Conference and Exhibition (P-382), December 2–5,2002, Indianapolis, Indiana.

[71] Smith, A.M.O. High-lift aerodynamics. *Journal of Aircraft*, 12(6):501–530, 1975.

[72] Petrov, A.V. Certain types of separated flow over slotted wings. *Fluid Mechanics – Soviet Research*, 7(5):80–89, 1978.

[73] Petrov, A.V. Separated flow about high-lift wings and active control, 1995. High lift and separation control, Proceedings of the conference, University of Bath, UK.

[74] Devenport, W.J., Rife, M.C., Liapis, S.I. and Follin, G.J. The structure and development of a wing-tip vortex. *Journal of Fluid Mechanics*, 312:67–106, 1996.

[75] Jasinski, W.J. and Selig, M.S. Experimental study of open-wheel race car front wings. Technical Report SAE 98–3042, SAE, 1998.

[76] Jeffrey, D., Zhang, X. and Hurst, D.W. Aerodynamics of Gurney flaps on a single-element high-lift wing. *Journal of Aircraft*, 37(2):295–301, 2000.

[77] Zerihan, J.D.C. and Zhang, X. Aerodynamics of gurney flaps on a wing in ground effect. *AIAA Journal*, 39(5):772–780, 2001.

[78] Moryossef, Y. and Levy, Y. Effect of Oscillations on Airfoils in Close Proximity to the Ground. *AIAA Journal*, 42:1755–1764, 2004.

[79] Guilmineau, E., Piquet, J. and Queutey, P. Unsteady two-dimensional turbulent viscous flow past aerofoils. *International Journal for Numerical Methods in Fluids*, 25(3):315–366, 1997.

[80] Garcia, D.L. and Katz, J. Trapped vortex in ground effect. *AIAA Journal*, 41(4):674–678, 2003.

[81] Payne, F.M., Nelson, R.C. and Schiff, L.B. Visualisation and wake surveys of vortical flow over a delta wing. *AIAA Journal*, 26(2):137–143, 1988.

[82] Jeong, J. and Hussain, F. On the identification of a vortex. *Journal of Fluid Mechanics*, 285:69–94, 1995.

[83] Dubief, Y. and Delcayre, F. On coherent-vortex identification in turbulence. *Journal of Turbulence*, 1:1–22, 2000.

[84] Levy, Y., Degani, D and Seginer, A. Graphical visualization of vortical flows by means of helicity. *AIAA Journal*, 28(8):1347–1352, 1990.

[85] Delery, J.M. Aspects of vortex breakdown. *Progress in Aerospace Science*, 30:1–59, 1994.

[86] Lucca-Negro, O. and Doherty, T.O. Vortex breakdown: a review. *Progress in Energy and Combustion Science*, 27:431–481, 2001.

[87] Harvey, J.K. and Perry, F.J. Flow field produced by trailing vortices in the vicinity of the ground. *AIAA Journal*, 9(8):1659–1660, 1971.

[88] Barker, S.J. and Crow, S.C. The motion of two-dimensional vortex pairs in a ground effect. *Journal of Fluid Mechanics*, 82(4), 1977.

[89] Puel, F. and De Saint Victor, X. Interaction of wake vortices with the ground. *Aerospace Science and Technology*, 4(4):239–247, 2000.

[90] Katz, J. and Dykstra, L. Effect of wing / body interaction on the aerodynamics of two generic racing cars. Technical Report SAE 92–0349, SAE, 1992.

[91] Soso, M.D. and Wilson, P.A. Aerodynamics of a wing in ground effect in generic racing car wake flows. *Proceedings of IMechE Part D: Journal of Automobile Engineering*, 220:1–13, 2006.

[92] Dominy, R.G., Ryan, A. and Sims-Williams, D.B. The influence of slipstreaming on sports prototype race car performance. *Proceedings of the Institution of Mechanical Engineers, Part D: Journal of Automobile Engineering*, 214(8):887–894, 2000.

[93] Zhang, H.J., Huang L. and Zhou, Y. Aerodynamic loading on a cylinder behind an airfoil. *Experiments in Fluids*, 38:588–593, 2005.

[94] Diasinos, A., Barber, T.J., Leonardi, E. and Hall, S.D. A two-dimensional analysis of the effect of a rotating cylinder on an inverted aerofoil in ground effect, 2004. 15th Australasian Fluid Mechanics Conference, The University of Sydney, Sydney, Australia.

[95] Diasinos, A., Barber, T.J., Leonardi, E. and Gatto, A. The interaction of a rotating cylinder and an inverted aerofoil in ground effect: validation and verification, 2004. 24th Applied Aerodynamics Conference, San Francisco, California, AIAA 2006-3325.

[96] Baldwin, G. 11×8 wind tunnel boundary layer test results 14th March 1999 and 7×5 wind tunnel boundary layer test results 16th July 1996, 1999. Internal report, Southampton University Wind Tunnels.

[97] Fluent Incorporated. Fluent version 6.2 manual, 2004.

[98] Czerwiec, R., Edwards J.R., Rumsey, C.L., Bertelrud, A. and Hassan, H.A. Study of high-lift configurations using k-$\zeta$ transition / turbulence model. *Journal of Aircraft*, 37(6):1008–1016, 2000.

[99] Spalart, P.R. and Allmaras, S.R. A one-equation turbulence model for aerodynamic flows, 1992. AIAA paper 92-0439.

[100] Roache, P.J. Perspective: a method for uniform reporting of grid refinement studies. *Journal of Fluids Engineering*, 116(3):405–413, 1994.

[101] Roache, P.J. Quantification of uncertainty in computational fluid dynamics. *Annual Review of Fluid Mechanics*, 29:123–160, 1997.

[102] Engineering Sciences Data Unit. Blockage corrections for bluff bodies in confined flows, 1998. ESDU Data Unit 80024.

[103] Moffat, R.J. Contributions to the theory of single-sample uncertainty analysis. *Transactions of the ASME: Journal of Fluids Engineering*, 140:250–260, 1982.

# Appendix A

# Wing Force Measurements

The wing models, used during the current study, are the same as in Mahon's work [12] in order to ensure research continuity and to limit the required work. Logically, the initial intention was therefore to re-use the wing force measurement system in a similar way as well. However during the first repeatability test in an attempt to improve on the computational correlation it was discovered that a component of the system no longer functioned. Therefore a new force measurement system had to be designed and implemented. The calibration of the load cell also had to be redone because of this and the postprocessing had to be updated. This appendix discusses the reasons for the alterations to the wing force measurement system, followed by a description of the new system, the calibration and the validation process. Finally, the consequences and implications of these changes are summarized with respect to the results and analysis presented in Mahon's work [12].

## A.1 Problem analysis

The problem with the wing force measurement system manifested itself in incorrect values of the force coefficients during a repeatability test. Further analysis of the problem revealed that either the incorporated PI (wheel drag) amplifier had failed or the wiring to or from this component. Since Mahon's system set-up had been constructed in quite an unorthodox way and none of the required expertise was available anymore, it was necessary to develop a new system. Subsequent tests showed that the load cell (Aerotech no. 0487) still functioned properly, which made it possible to base the new system on the same part. This was a major advantage, because the load cell formed a structural part of the support construction. The only aspects of the system that thus needed to be modified were the signal amplification and the subsequent steps, such as data acquisition and postprocessing.

First Mahon's approach was studied carefully to be able to re-apply his experience and to speed up the design process. This revealed that the old system had not been calibrated properly. In order to be able to determine the cross terms accurately it is essential that 'pure loadings' are applied, acting at the load cell resolution point. However the drag load had been applied to the wing itself, which was located $473mm$ below the load cell resolution point, at the end of the vertical support pillars. This induces a pitching moment relative to the load cell resolution point, resulting in a significant decoupling term in the calibration matrix. Indeed the pitching moment equation, (B.6) in Mahon's thesis [12], shows a cross term for the drag, $-0.9135 \times D_{coupled}$, which is much larger than the other cross terms and of the same order as the diagonal, direct terms. This flaw would lead to an overprediction of the pitching moment and would, via the decoupling, also have a small effect on the downforce and drag values.

A related observation seems to have even more impact on the results, however it is hard to say where this error originates from. While analyzing Mahon's calibration data it was realized that for example $10kg$ of drag applied to the wing location resulted in approximately $100Nm$ nose down pitching moment. This seems inconsistent considering that the moment arm is only $0.473m$. It could indicate that a factor 2 has been omitted somewhere during the calibration of the pitching moment component, either in the applied weights or somewhere in the subsequent scaling. A possible reason could be that this extra moment contribution is being used as a compensation for not calibrating with a pure drag force. The fact, that the recorded pitching moment during calibration of the drag component is nearly twice as high as it should be, implies that the actual moment will be about half of what is presented. However resulting errors in calibration of the cross components will reduce this effect slightly.

Apart from these interpretation mistakes during calibration, a few other small errors in the postprocessing method were discovered as well. The most important of these is in the decoupling process of the measured loads. Each of the components has to be corrected for the readings that result from applying the other two load components in a 'pure form'. Internal deformations within the load cell cause this output coupling between the three components. Instead of inverting the complete matrix consisting of the calibration trendline coefficients at once, Mahon inverted the terms independently; term by term. He also included the constant terms of the calibration trendlines into his final decoupling equations. Finally a sign typo was found in the downforce contribution to the drag as well. Nevertheless these errors in the decoupling have limited effect on the end results, because the cross terms are in general relatively small, except for the drag contribution to the pitching moment.

Mahon calibrated his system by applying loads to the wing, after which the output results would be tailored to match the input loads. These calibrated load values were subsequently decoupled into the final measured loads. Due to the improved transparency of the new force measurement system it was possible to incorporate the original calibration data provided by Aerotech. This matrix combines second order calibration and decoupling of the results. Nevertheless, at a later stage, it was found that the calibration results from 2002 were outdated and did not perform as accurately anymore as they would have initially. Therefore the calibration process had to be redone as well. Furthermore the tare measurements, which produce the correction terms for the aerodynamic loads caused by the support structure, could not be implemented in the same way as for Mahon's system and had to be retaken as well.

## A.2 New wing force measurement system

The new solution for the force measurement system consists of a splitter box to separate the three components of the load cell signal, an 8-channel Vishay external amplifier and a PC to acquire the data. Hereto a National Instruments data acquisition card and Enflow software has been used. The load cell is powered by the amplifier, which reduces the potential noise sources for the signal. The amplification factor for each channel can be set individually and the load cell signals and amplifier channels can be balanced by hand. The new system is much more conventional in set-up and has the following advantages over Mahon's system:

- The system is no longer a black box and the signals can be monitored and checked at various stages as a result.
- The sampling frequency and characteristics can now be specified and the instantaneous data can be visualized and recorded.
- The signal resolution has improved due to a better AD converter and a user-defined input range of expected values.

However, on the other hand, having to use the new system also had the following disadvantages:

- Data acquisition and wing ride height movement are no longer combined in the same system. Some steps of the previously automated process therefore now have to be operated by hand.
- Elaborate zeroing of the amplifier and load cell channels is required, instead of relying on the automatic zeroing routine of the PI system.
- Derivation of the pitching moment on the wing now relies on translation of the measured loads from the load cell resolution point to the moment point; i.e. $C_{M53mm}$. Deformation of the (support) structure therefore has more effect on the results than for the previous method in which the deformation was implicitly included in the calibration process.

The operation process of the new system as well as the postprocessing of the results has been described in section 2.3.4.

## A.3 Load cell calibration

Mahon's calibration of the wing load cell could no longer be used due to the previously discovered flaws, whereas the original second order calibration of Aerotech, which was supplied with the load cell, had lost its accuracy over time. Therefore the load cell had to be recalibrated as accurately as possible, applying only 'pure loads' that act directly at the load cell resolution point. The maximum applied calibration loads exceeded the experienced aerodynamic forces during testing for all of the components, allowing for more accurate interpolation instead of extrapolation of the results.

The downforce was applied by a hanger with weights connected to the underside of the wing support bracket along a vertical line through the load cell resolution point. During calibration the load was varied from 0 to $22kg$ in steps of $2kg$. The drag load was simulated by attaching a metal wire directly to the load cell along a horizontal line through the load cell resolution point. The direction of the wire was changed with a pulley and a hanger with weights was attached to the free end of the wire. The drag channel was calibrated from 0 to $5kg$ in steps of $0.5kg$. Finally, for the pitching moment a bar was attached to the underside of the wing support bracket. Both sides were subjected to forces by applying weights, but for one side the force direction was reversed to upwards with the help of a pulley (see figure A.1). A pure pitching moment was created by applying an equal amount of weights to both hangers simultaneously. The moment arm at each side was equal to $0.23m$ and up to $5kg$ was applied to each side in steps of $1kg$ per side.

The resulting calibration data was used to find the calibration trendline coefficients[1] for each of the component combinations. These values were put in a matrix, which was subsequently inverted into a first order calibration matrix. Multiplication of the columns with the corrected[2] lift, pitch and drag signals presents the measured loads in $kg$ and $kgm$. The calibration matrix reads:

$$\text{Calibration (lift, pitch, drag)} = \begin{pmatrix} 156.569199 & 0.698709 & 0.744715 \\ -2.361615 & 20.313815 & -0.189482 \\ -0.265788 & 0.128822 & 31.942681 \end{pmatrix} \tag{A.1}$$

The previous force measurement method immediately outputted the force coefficients relative to the $C_{M53mm}$ point on the wing, due to the unique incorporation of the load cell calibration. The new system, in contrast, produces load values relative to the load cell resolution point. The downforce and drag can be transfered to the wing point without any alterations being involved, but the pitching moment needs to be translated. The pitching moment around the $C_{M53mm}$ point can be calculated from:

$$C_{M53mm} = -C_M - 0.007/0.284 \times C_L - 0.4731/0.284 \times C_D \tag{A.2}$$

where $C_M$ is the pitching moment output by the new system. The minus signs can be explained by a difference in sign convention between the load cell and the definition proposed by Mahon. In

---

[1] The $R^2$-value of a trendline is also called the coefficient of determination, ranging between 0 and 1, with the latter representing the best correlation. The $R^2$-values of all the direct terms linear calibration trendlines were above 0.99998, whereas the cross components were above 0.995, except for the lift as a result of the drag, which was the worst term at 0.988. The RMS average of the residual, defined by the difference between the calculated load and the applied load divided by the applied load, was 0.20% for the downforce, 0.44% for the pitching moment and 0.52% for the drag.

[2] The corrected signals in $mV/V$ are calculated from the load cell output in $V$ by dividing the value by the amplification gain of 2000 and the supply voltage of $10V$ and by multiplying with 1000 to get to $mV$.

a similar way, the pitching moment around the quarter chord point can be derived from:

$$C_{M1/4c} = -C_M + 0.011/0.284 \times C_L - 0.4731/0.284 \times C_D \tag{A.3}$$

In these formulas $C_M$ is positive for a nose upwards pitching moment and $C_{M53mm}$ and $C_{M1/4c}$ for a nose downwards moment. Finally, the streamwise location of the centre of pressure, $x/c_{CoP}$ follows from:

$$\begin{aligned} x/c_{CoP} &= (C_M + 0.4731/0.284 \times C_D)/C_L + 0.06/0.284 = \\ &= -C_{M53mm}/C_L + 0.053/0.284 \end{aligned} \tag{A.4}$$

in which formula it is assumed that the $z$-position of this point is always equal to that of the $C_{M53mm}$ point, which is at the same height as the most forward point of the main element of the wing.

## A.4 Validation process

The validation process of the new force measurement system consisted of two phases. First it was checked whether the new system produced similar raw data compared to Mahon's system. This was achieved by performing a baseline repeatability force test over the complete ride height list with the use of the new system. The data was subsequently analyzed with the help of Mahon's exact postprocessing method, which was transformed into a code that could be used in conjunction with the new data format and data acquisition system. A complicating aspect in this process was that Mahon's method included unknown amplification factors for each of the signal channels, which had been set in the no longer functioning PI wheel drag amplifier. However using reversed engineering and systematical variation of the amplification factors resulted in a satisfactory match between the new results and those presented by Mahon (especially those of the long term repeatability, see figure C.3 of [12]) for a certain amplification factors combination.

The proof that the new system acquired similar data to the old one paved the way for the second phase of the validation. This consisted of verifying whether the new method provided improved, more accurate results. Because it is unknown a priori what the results should look like, it is difficult to define whether the changes in results present a real improvement or not. Nevertheless a few indications of improvements can be found in the new solutions. The main observation leading to this conclusion is that the changes of the curves are in line with the expectations. The new pitching moment (see figure A.4) features considerably smaller absolute values than that presented by Mahon[3]. This is in agreement with the conclusions about the discovered errors in calibration and postprocessing. Via the cross terms this will lead to a lower prediction of the drag value, as can be seen in figure A.3. The influence on the downforce will be less, because the downforce

---

[3] The value of the new pitching moment is almost half the original value, which confirms the conclusion that Mahon's calibration drag load returned nearly double the expected pitching moment.

values are about an order higher than the drag level and this means that the cross terms play a relatively smaller role.

Additional proof can be found in the prediction of the streamwise centre of pressure location; in Mahon's results this is at $x/c_{CoP} = 0.49$ for the isolated wing at a ride height of $h/c = 0.634$, whereas the new results give a value of $x/c_{CoP} = 0.37$. A look at the pressure distributions for the wing reveals that the centre of pressure is definitely located in front of the half chord point. This favors the new results. Furthermore, for reference, extra calibration data had been obtained for the drag component, applying the load in the same way as during Mahon's calibration. Postprocessing of this data with the new method returned the applied drag and inducing pitching moment accurately. Finally, the correlation between the new experimental force results and the CFD results has improved as well, see section 3.2.3. These results provides confidence that the new wing force measurement system returns more accurate results than the previously used one.

## A.5 Consequences of alterations

The effects of using the new force measurement system can be divided in to two categories. First of all the operational side has been influenced. Previously it has been mentioned that the data acquisition system and the wing movement system are no longer combined and that the signals and amplifier channels need to be balanced and zeroed by hand. The second category of consequences relates to the influence on the results and on the analysis of these by Mahon. This section focuses on the latter. Figures A.2, A.3 and A.4 present the new results next to those described by Mahon for respectively the downforce, drag and pitching moment. All other results shown throughout this thesis have exclusively been obtained with the new force measurement system, using the new calibration, tare measurements and postprocessing method.

The region definitions in the previously mentioned figures have been derived by Mahon. This allows a direct comparison of his regions with the new results and shows any shift or change in force behaviour. When analyzing the figures, it has to be remembered that the curves represent completely different data sets, which have been obtained with a gap of two years between them. The new results agree best with those presented as long term repeatability[4] in appendix C of Mahon's thesis [12], however the curves presented in this appendix are Mahon's baseline results from his chapter 5.

The downforce curves in figure A.2 look qualitatively quite similar. At high ride heights the new values are about 1.2% lower than the original results, but in force region *d* the downforce is slightly higher with the maximum value being 1.1% higher than in Mahon's case. The hysteresis boundary still occurs at the same ride height, $h/c = 0.81$. However the maximum downforce before vortex breakdown is now obtained at $h/c = 0.218$ instead of 0.222 and the whole of region *b* has

---

[4] This seems to indicate that the wing geometry has changed consistently over time, possibly due to wear or deformation.

shifted to lower ride heights. This is probably a result of the previously mentioned lower downforce, which induces a less severe pressure gradient and thus postpones vortex breakdown. The plateau in the downforce for region *d* has been replaced with a very moderate continuous increase with ride height reduction, which again can be traced back to the less severe pressure gradient and its effect on the bursting of the tip vortices. The values in the hysteresis zones are again slightly lower than for Mahon's data, but repeatanility of these results is the hardest to obtain in general due to the dependence on starting conditions.

The new drag values are about 2.7% to 4.0% higher than the old ones. Qualitatively the two curves look again very similar, including the ride height for which the maximum drag occurs. The main differences can be found in the hysteresis zones *e* and *f*, where the values of the increasing and decreasing branch are now very similar for the upper ride heights, but more distinguishable higher for the decreasing branch at low ride heights. The picthing moment curves ($C_{M53mm}$)have a comparable shape, but the old values are roughly 67% larger than the new ones. Again the main qualitative difference can be found in the hysteresis zones and this time the decreasing ride height values are larger. This in contrast to the old results, which showed a higher pitching moment for the increasing branch.

In summary, it can be concluded that the new downforce values are slightly lower, the drag values higher and the pitching moment values significantly reduced compared to those obtained by Mahon. The discovered calibration and coupling errors form a good explanation for this. Despite these quantitative changes, the qualitative results look still very similar though. Mahon's discussions of the flow features and physics and explanation of the behaviour are therefore still valid and do not need to be revised. The only remark worth making here is that it is difficult to draw conclusions from the presented pitching moment data around the $C_{M53mm}$ point. Discussions of the (relative) loading of the flap are hard to justify considering that both changes in the main element and in the flap loading influence the pitching moment around this arbitrary point. Therefore it is more revealing to look at the location of the centre of pressure to examine shifts in the relative loading of the elements.

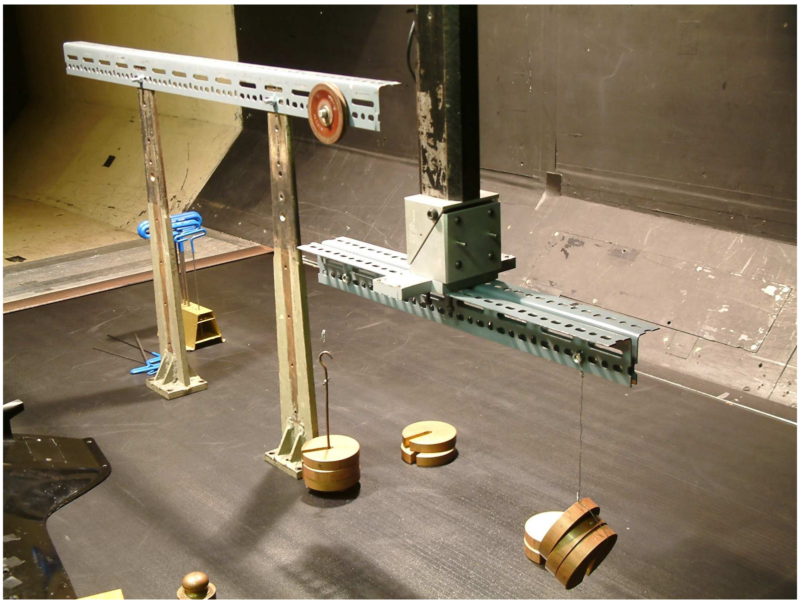

Figure A.1: Picture showing the calibration process for the pitching moment component; the lefthand side of the bar is exposed to an upwards force by using a pulley and a hangar with weights, while the righthand side experiences an equal downwards force.

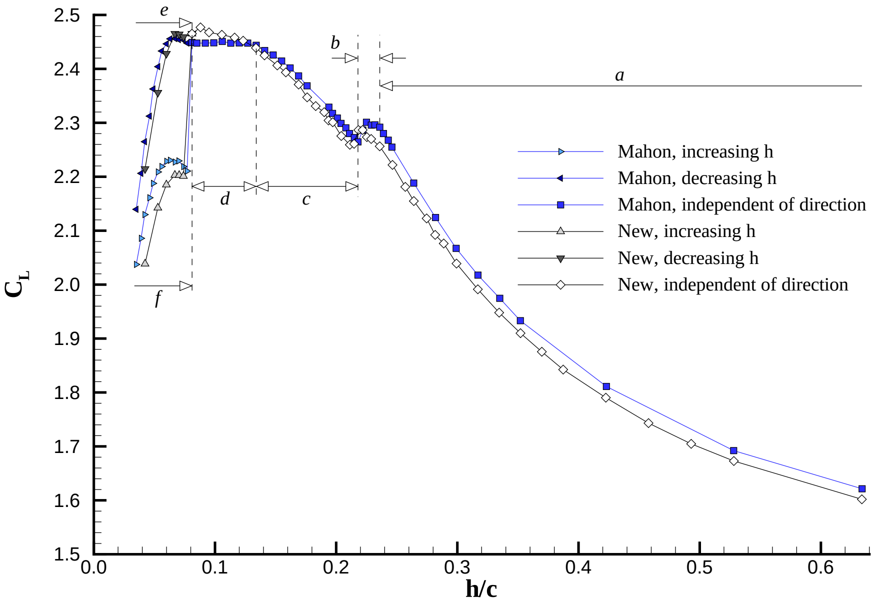

Figure A.2: Comparison of the experimental wing downforce data obtained by Mahon with that resulting from the new system.

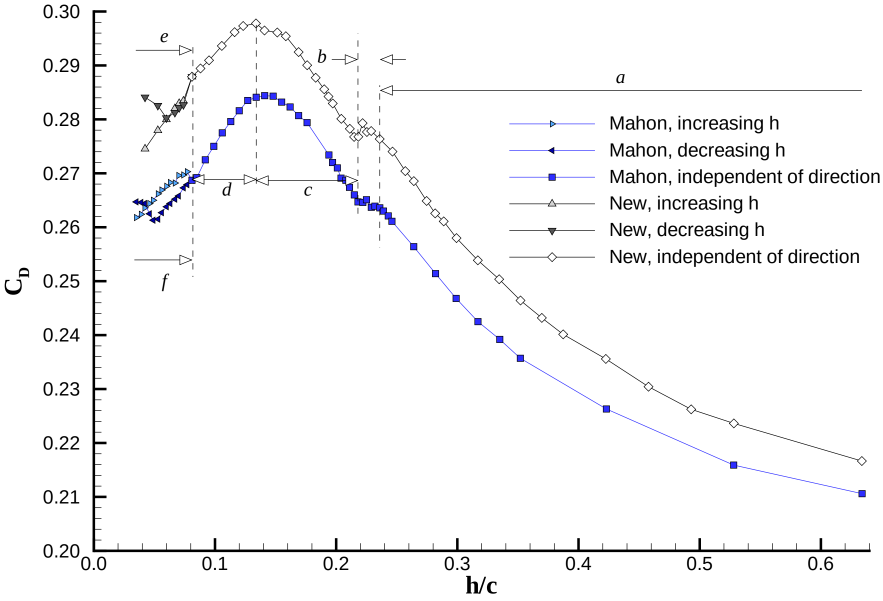

Figure A.3: Comparison of the experimental wing drag data obtained by Mahon with that resulting from the new system.

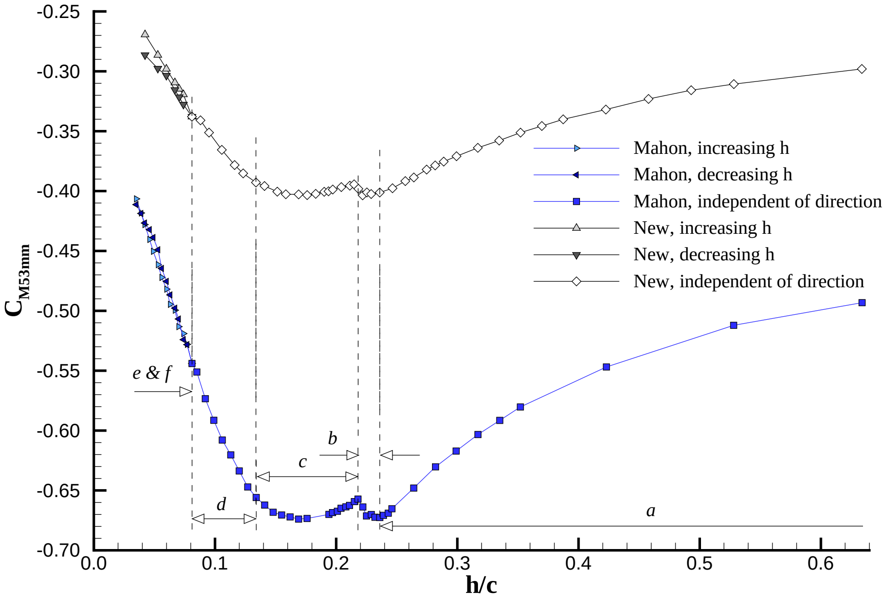

Figure A.4: Comparison of the experimental wing pitching moment data around the $C_{M53mm}$-point obtained by Mahon with that resulting from the new system.

## Appendix B

# Blockage Effects, Uncertainty and Repeatability

This appendix presents additional information about the experimental results concerning the influence of blockage effects, the uncertainty in the measurement methods and the repeatability of the experimental tests. This data can be used to assess the quality of the experimental results, but is also essential in cases when the absolute values of the quantities are required. The previously presented results have not been corrected for blockage effects and uncertainty limits have not been included in the figures and tables either, because the focus has been on deriving general trends as a result of parametrical changes, instead of showing absolute values that would correlate with ‘on-track conditions’. For continuity the same methods, which have previously been applied by Zerihan [8] and Mahon [12], have been used here as well. The force measurements form the primary subject of this appendix; the pressure and PIV results have been used in a qualitative sense and insufficient data is available for an equivalently thorough analysis of these quantities. This appendix is divided into three sections, which subsequently deal with the subjects of blockage effects, uncertainty and finally repeatability.

## B.1 Blockage effects

The results in the main body of this thesis have not been corrected for blockage effects, because the current research primarily has a comparative character and the difference in blockage effects for the various configuration settings is relatively small. However, if the results have to be used in a quantitative manner, for example to determine the exact forces that act on this specific configuration, then the data has to be corrected for blockage effects. The following part of this appendix discusses the influence of wind tunnel blockage on the experimental results, especially for the baseline CWW2020 configuration. First the blockage ratio of the test configuration relative to the wind tunnel cross section area will be determined and then the blockage correction will be discussed.

**Blockage ratio** The test configuration consists of the wing model, the wheel models and the support structures for the models. The total frontal area of these components depends on both the wing ride height and the wing - wheel overlap; the wing - wheel gap has no influence on this quantity. The frontal area of the wing support structure, $A_{fwis}$, varies with ride height $h$, whereas the frontal area of the wing, $A_{fwi}$, is dependent on the overlap $O$. The frontal wheel area, $A_{fwh}$, and the frontal area of the wheel support arms, $A_{fwhs}$, do not change with these parameters[1]. The frontal areas ($m^2$) for each of the components are given by:

$$\begin{aligned}
A_{fwi} &= 0.0475, \text{ for } O \leq 0, or: \\
A_{fwi} &= 0.0799 \cdot (0.59 - 2 \cdot O), \text{ for } O > 0 && \text{(B.1)} \\
A_{fwis} &= 0.1259 + 0.06 \cdot (0.58 - h), \text{ for all } h && \text{(B.2)} \\
A_{fwh} &= 2 \cdot 0.05201 && \text{(B.3)} \\
A_{fwhs} &= 2 \cdot 0.00725, && \text{(B.4)}
\end{aligned}$$

with $O$ and $h$ in meters.

The total frontal area of the test configuration then follows from adding the separate components, which yields:

$$A_{ftot} = A_{fwi}(O) + 0.06 \cdot (0.58 - h) + 0.24442 \tag{B.5}$$

The total cross sectional area of the $7 \times 5$ wind tunnel, $A_{WT}$, is $3.3994m^2$. With these formulas it is now possible to determine the blockage ratio for each configuration within the range of test settings. The maximum blockage ratio occurs for negative overlap and the lowest wing ride height; for $h/c = 0.053$ this results in a blockage ratio of 9.6%. The minimum blockage ratio is obtained for the maximum overlap of $50mm$ and the highest ride height of $h/c = 0.634$ at 9.0%.

**Blockage correction** A wind tunnel test model is generally chosen as large as possible to test at a Reynolds-number that is as close as possible to the real life situation. The wind tunnel cross section however limits the model size, because the walls constrain the flow, resulting in changes to the measured quantities. The confinement by the tunnel walls leads to a restriction in the expansion of the flow around the body and to a modification of the flow direction along the walls. Blockage correction is applied to wind tunnel results to predict the flow parameters, such as force coefficients and pressure distributions, that would occur in 'free air' conditions. The current blockage ratio of just under 10% is relatively high, due to the combination of the two previously used 50% scale models in a fixed dimension wind tunnel, but the results can still be corrected for this blockage.

---

[1] To simplify the calculations it has been decided to make the wing area dependent on the overlap, even though the wheels are the components that are physically positioned most downstream. The influence of the wheel camber on the variation of frontal area with ride height changes is relatively small and has been neglected.

The wing and wheel are considered as inidvidual components in the determination of the blockage correction, although the total blockage ratio of the complete model is applied to both.

The blockage correction that was applied by Mahon [12] to the isolated wing results is based on the ESDU data sheets [102]. This method calculates a force correction factor, $C_{Ff}/C_F$ for a 3D streamlined lifting body with asymmetric separation in a solid wall wind tunnel. In this method the results are corrected for solid body blockage (the increased velocity due to the blockage), lift interference (the modification of the flow direction) and for the effect of the latter on the lift induced drag for a 3D body. The force correction factor can be derived from:

$$\frac{C_{Ff}}{C_F} = 1 - \lambda_1\lambda_3\Big(1 + \frac{1}{\lambda_2}\frac{c}{v}\Big)\frac{vA_{ftot}}{{A_{WT}}^{1.5}} - 0.5(C_D - C_{Di})\frac{A_{ftot}}{A_{WT}}, \tag{B.6}$$

where $c$ is the total wing chord, $v$ the vertical dimension, $C_{Di}$ the lift induced drag and

$$\begin{aligned}
\lambda_1 &= 0.72\Big(\frac{b_{WT}}{H_{WT}} + \frac{H_{WT}}{b_{WT}}\Big) = 1.472 \\
\lambda_2 &= \frac{4}{\pi}\frac{\text{Maximum body cross sectional area}}{cv} = 1.851 \\
\lambda_3 &= \frac{\text{Body volume}}{vA_{WT}} = 0.258
\end{aligned}$$

The first parameter, $\lambda_1$, takes account of the wind tunnel design, while the last two refer to the wind tunnel model. The blockage correction factor varies with ride height as a result of the changes in $A_{ftot}$, $C_D$ and $C_{Di}$. Figure B.1 presents the wing force blockage correction factor as function of the ride height, as derived from equation (B.6) for the CWW2020 configuration. The blockage correction is at 1.3% to 1.7% higher than found by Mahon for the isolated wing, but this was expected due to the increased blockage resulting from the wheels.

The wheel results have to be corrected with a different method, because the assumption of a streamlined body does not hold for this component. The ESDU sheets [102] provide a different approach for bluff body flow, which accounts for wake blockage correction, including separation bubble effect. The force correction factor for the wheel can be determined with:

$$\frac{C_{Ff}}{C_F} = \frac{1}{1 + \varepsilon C_D A_{ftot}/A_{WT}}, \tag{B.7}$$

where $\varepsilon = -1/C_{psf}$ and $C_{psf}$ is the corrected pressure coefficient at the separation position, which can be obtained from:

$$C_{psf} = 1/2\big[(C_{ps} + C_D A_{ftot}/A_{WT}) - \sqrt{(C_{ps} + C_D A_{ftot}/A_{WT})^2 - 4C_D A_{ftot}/A_{WT}}\big]$$

The pressure coefficient at the separation position, $C_{ps}$, has been obtained from the experimental data in figure 4.3 and interpolated between the data points. The wheel blockage correction factor varies with ride height as well via $A_{ftot}$ and $C_{ps}$. The correction factor for the wheel has also been included in figure B.1 for the CWW2020 configuration. This figure shows that the correction for the wheel is much larger than for the wing, ranging from 5.4% to 8.3%. The blockage ratio for the isolated wheel[2] is 6.7%, which leads to a correction factor of 0.935. The blockage correction factor

---

[2] This set-up includes two wheels, the support arms and the wing support shroud, see figure C.6.

for the isolated wheel in CFD, where all support structures have been omitted, is still 0.940. Finally, the blockage correction for the isolated wing has been analyzed and discussed by Mahon [12].

## B.2 Uncertainty

This section assesses the uncertainty levels for the experimental results to enable a more precise judgment on the quality of the presented data. The wing force data was acquired with the same load cell as Mahon used for his research, however due to changes in the calibration, acquisition and postprocessing it is required to redo the uncertainty analysis. Wheel drag measurements have not been performed previously and therefore a full uncertainty analysis will be conducted as well. The pressure measurements are discussed in the next subsection. The following paragraphs are based on the results for the baseline combined wing - wheel configuration, the uncertainty levels for the isolated components are similar or lower since they do not depend on the additional configuration parameters of overlap and gap.

### B.2.1 Force measurements

The uncertainty analysis is split up in a number of factors that each influence the outcomes in their own way. Next, these factors are studied separately before the total uncertainty with 95% confidence level is derived from the components using the definition that is presented by Moffat [103]. With the acquired force data it is possible to estimate the effect of small deviations in ride height, overlap, gap and dynamic pressure, as well as of short term time dependence, data acquisition and calibration accuracy. Additionally, factors such as difference between road and wind speed, or set-up differences in yaw and angle of attack also affect the uncertainty level. Their influence has been estimated for as far as possible[3], but can not be derived explicitly from the available experimental data.

First of all the ride height has been set to within an accuracy of $\pm 0.05mm$ with the use of metal slip gauges. This corresponds to a maximum uncertainty with 95% confidence of $\pm 0.0018C_L$, $\pm 0.0002C_D$ wing, $\pm 0.0004C_M$ and $\pm 0.0030C_D$ wheel. Due to the more complicated procedure of overlap and gap set-up (see figure 2.4), it is estimated that both are accurate to within $\pm 0.5mm$. The resulting maximum uncertainty, derived from the results of respectively the CWW0020, CWW3520 and CWW2010, CWW2035 pairs relative to the baseline setting, are $\pm 0.0026C_L$, $\pm 0.0004C_D$ wing, $\pm 0.0022C_M$ and $\pm 0.0006C_D$ wheel for the overlap and $\pm 0.0048C_L$, $\pm 0.0008C_D$ wing, $\pm 0.0013C_M$ and $\pm 0.0040C_D$ wheel for the gap parameter. The main element and flap angle of attack have not been varied during this research, but they are dependent on the accuracy of the set-up. Hereto a digital inclinometer was used with an accuracy of $\pm 0.005°$; the resulting uncer-

---

[3] The influence of a difference in road speed relative to the wind velocity has for example been examined with a CFD simulation; a 2.5% lower road velocity led to an increase in wheel lift of 4.5% and a reduction in wheel drag of 0.4%, while having neglectable influence on the pressure distributions.

tainty values are $\pm 0.0006 C_L$, $\pm 0.0002 C_D$ and $\pm 0.0001 C_M$ for the main element and $\pm 0.0012 C_L$, $\pm 0.0002 C_D$ and $\pm 0.0004 C_M$ for the flap, according to Mahon's findings [12]. No information about the influence of these angles on the uncertainty in wheel drag is available.

The dynamic pressure is used to controll the freestream wind velocity. This variable was set to within an accuracy of $\pm 0.2 mmH_2O$, resulting in 95% confidence uncertainty levels of $\pm 0.0003 C_L$, $\pm 0.0001 C_D$ wing, $\pm 0.0001 C_M$ and $\pm 0.0005 C_D$ wheel, when the results for $24.97 mmH_2O$ are compared to those for the baseline case at $56.19 mmH_2O$. The influence of short term time dependence has been derived from measuring the forces five times in succesion without interruption of the test at a fixed ride height of $h/c = 0.264$. Using twice the standard deviation of these results to obtain a safe estimate of the uncertainty levels resulted in $\pm 0.0050 C_L$, $\pm 0.0004 C_D$ wing, $\pm 0.0001 C_M$ and $\pm 0.0010 C_D$ wheel. The influence of calibration has been derived from the standard deviation of the difference between the calculated load and the applied load for the linear calibration curves. The 95% confidence levels of uncertainty as a result of calibration are $\pm 0.0026 C_L$, $\pm 0.0010 C_D$ wing, $\pm 0.0024 C_M$ and $\pm 0.0021 C_D$ wheel.

Finally, the influence of the data acquisition method, which is related to the time dependence, was estimated from the instantaneous raw data at a fixed ride height of $h/c = 0.264$. The standard deviation calculated over the entire interval of 30,000 samples was relatively high, especially for the wheel drag. The latter varied enormously over time and the standard deviation was $0.32 C_D$. However this is the reason for the longer sampling time of 30 seconds; the average of the 30 blocks converged to a constant value during the measurement. At 2/3 of the measurement period the average had typically converged to 0.07%, 0.20%, 0.07% and 0.05% of the final value for respectively the $C_L$, $C_M$, $C_D$ wing and $C_D$ wheel. The standard deviation of the block averages is taken as an estimate of the uncertainty due to the data acquisition method. With 95% confidence level the uncertainty due to the data acquisition method is $\pm 0.0048 C_L$, $\pm 0.0008 C_D$ wing, $\pm 0.0009 C_M$ and $\pm 0.0040 C_D$ wheel.

Based on these uncertainty components the root-mean-square method of Moffat [103] predicts overall uncertainty levels of $\pm 0.0092 C_L$, $\pm 0.0018 C_D$ wing, $\pm 0.0029 C_M$ and $\pm 0.0068 C_D$ wheel with 95% confidence. This maximum value occurs at $h/c = 0.352$ for all quantities, except for $C_M$, which has a maximum at $h/c = 0.335$. To finish this analysis it needs to be mentioned that the uncertainty in pitching moment is small, however the results indicate a considerable discrepancy between experimental and CFD results. It is expected that the experimental pitching moment is affected by a bias error due to deformation of the support structure and wing model. This error depends on the deformation and thus on the aerodynamic loading. If the results are to be used for quantitative purposes, then this bias error has to be estimated by measuring the deformation under loading and by deriving a suitable correction. However for the current purposes, where the trends are most important, this has not been implemented.

### B.2.2 Pressure measurements

The wing pressures have been acquired in exactly the same way as by Mahon and for a more in depth uncertainty analysis is referred to his thesis [12]. Time constraints made it impossible to acquire a complete data set for a thorough uncertainty analysis of the wheel and wing pressure measurements. Nevertheless this should not pose any problems for the qualitative way in which the data has been used in this research. The presented uncertainty data for the pressure measurements forms a conservative estimate based on the available information.

**Wheel pressures** The wheel pressure measurement system has been designed and built by McManus to acquire accurate pressure data, using a high quality Kulite pressure sensor. This sensor has been calibrated using a digital pressure calibration device that is accurate to $\pm 0.05 mmH_2O$. The resulting uncertainty in the measured pressure is $\pm 0.0040 C_P$ under the standard test conditions[4]. Furthermore the linear calibration curve has been assessed on the difference between the calculated and the applied pressure; this yielded an average uncertainty of $\pm 0.0214 C_P$ with 95% confidence level. The pressure sensor is temperature compensated within the range of $5°C$ to $50°C$, which corrects for temperature drift at any of the encountered test conditions. The uncertainty due to the ride height set-up accuracy of $\pm 0.05 mm$ can be derived from the baseline data for CWW2020 to be $\pm 0.0006 C_P$. Based on the limited available data for different overlap (CWW3520) and gap (CWW2050) settings it is finally possible to derive uncertainty values of respectively $\pm 0.0081 C_P$ and $\pm 0.0058 C_P$ for these parameters; both accurately set to within $\pm 0.5 mm$. Moffat's root-mean-square method then estimates an overall uncertainty level for the wheel pressure measurements of $\pm 0.0239 C_P$ with 95% confidence.

**Wing pressures** The wing surface pressures have been acquired using the same measurement equipment and method as Mahon [12]. The uncertainty due to freestream velocity was estimated to be $\pm 0.0008 C_P$ by Mahon, whereas that resulting from setting the flap incidence angle was $\pm 0.0028 C_P$. The limited set of wing pressure data that was obtained during this research can be used to derive uncertainty levels resulting from the ride height and overlap set-up. The first can be derived from the baseline configuration results, which yields that the maximum uncertainty over the ride height range as a result of the $\pm 0.05 mm$ accurate height setting is $\pm 0.0017 C_P$ for the main element and $\pm 0.0021 C_P$ for the flap. From the CWW3520 results for the tip it can be calculated that the maximum uncertainty due to overlap is $\pm 0.0103 C_P$ for the main element and $\pm 0.0127 C_P$ for the flap. The uncertainty as a result of the gap setting can be estimated from that of the overlap by taking twice the worst case, yielding $\pm 0.0254 C_P$. This can be concluded from the force uncertainty data, which showed a similar relationship, and since the forces are nothing but integrated pressures this is a fair assumption. The total uncertainty with 95% confidence can once

---

[4] It needs to be remembered here that the wheel pressures are measured at a dynamic head corresponding to $20 m/s$, resulting in a higher uncertainty level than for the standard test conditions, which are equivalent to a test velocity of approximately $30 m/s$.

more be calculated with Moffat's method, resulting in a value of $\pm 0.0287 C_P$ as worst case scenario. Mahon [12] found a similar maximum uncertainty of $\pm 0.0370 C_P$ for his results, however the mean uncertainty was only $\pm 0.0087 C_P$ according to him. This shows that the given uncertainty level presents a conservative interpretation.

### B.2.3 Other methods

Finally, to conclude this uncertainty analysis, some general remarks will be made about the other methods, for which insufficient data has been acquired to conduct a thorough assessment. In particular the PIV measurements and the CFD will be discussed.

**PIV measurements** The PIV measurements have merely been used to visualize the flow field. Absolute velocity values were therefore less vital. However a few uncertainties have to be kept in mind when analyzing the data. The out-of-plane velocity component results in perspective errors that will influence the two velocity components in the plane that are being measured. Mahon [12] has quantified this error for a similar set-up, settings and characteristic distances. He found that the error was approximately 1% in the measured velocity components for a laser plane that is positioned perpendicular to the flow direction - and thus dominated by cross-flow. It is expected that the perspective errors in the current results will be of similar order and thus of limited influence on the qualitative features.

Furthermore the parallax effects have already been mentioned previously; these result in a slight distortion of the image and in blocking of certain parts of the field of view by geometries. The ratio of the distance from the camera lens to the field of view in relation to the largest dimension of the field of view is a measure for the parallax effects. This ratio was never more than 1/3 and typically around 1/5. Finally, the scale factor was based upon a dimension with a $\pm 0.1mm$ accuracy. Even for the smallest scale factor (that is the smallest field of view) this only translates into a 0.1% uncertainty in the dimensions in the plane and therefore - assuming no errors in the timing - to a similar error in velocities.

**CFD** The uncertainty in the CFD results is mainly affected by the grid and the numerical method. Chapter 3 presents the influence of grid density in the form of grid sensitivity studies. The influence of turbulence models has also been quantified in this chapter. The cross-sectional dimensions of the grid domain have been kept similar to those in the experimental research, but the streamwise dimension has been chosen to give relatively constant conditions over the inlet and outlet. Nevertheless the choice of using a steady RANS method for the simulations will have the largest influence on the results.

## B.3 Repeatability

Repeatability of experimental results is time dependent and generally deteriorates as the period between the measurements increases. The immediate repeat of the force data, by acquiring several data points in succession without interruption of the test run or change in ride height, has already been quantified and included in the uncertainty analysis. Furthermore short term repeatability is examined by comparing the data at the highest ride height - half way a test run - before and after the intermediate zero measurement. Finally the long term repeatability is studied by comparing two similar tests with a year interval between them. The repeatability analysis has been conducted with the help of force measurements for the combined configuration. These force measurements present the most comprehensive set of data and give an integral overview that is easy to compare, whereas the baseline configuration can be assumed to be representative for most of the tested cases. The repeatability of the pressure[5] and PIV data has not been checked comprehensively, because of the limited time available during the tests.

**Short term repeatability** Each force run consisted of a branch of increasing ride height followed by a branch for decreasing ride height, in order to test for the occurrence of hysteresis effects. The measurements were always interrupted at the highest point, $h/c = 0.634$, for zero measurements without wind. The data points on each side of these intermediate zeros have been assessed for short term repeatability of the experiments. Therefore the short term repeatability describes the influence of (variation in) test conditions on the results for a fixed configuration and set-up. The short term repeatability is based on 14 different runs; three for the baseline configuration and the others for various overlap and gap settings. The average difference between the data point prior to and after the zero measurement is 0.18% for the downforce, 0.27% for the wing drag, 0.53% for the pitching moment and 0.37% for the wheel drag. The respective maximum values over these 14 runs are in the same order 0.41%, 0.57%, 0.94% and 0.61%. The force coefficients outside the hysteresis zone have in the presented results been averaged over the increasing and decreasing ride height branch, because of the satisfactory short term repeatability. The repeatability of the results within the hysteresis zones was in general worse due to the governing flow phenomena and dependency on starting conditions. Especially the increasing ride height branch level varied, as can be concluded from the typical repeat shown in figure B.2.

**Long term repeatability** All the force measurements for the various overlap and gap settings have been obtained during two test sessions within a period of less than four months time.

---

[5] The short term repeatability of the on-surface wing pressures has been assessed by Mahon [12], using exactly the same method and equipment. He found a maximum variation of $\pm 0.082 C_P$ at $h/c = 0.211$ in the transition region on the flap. The average of the variation over the ride heights for the CWW2020 configuration is quantified as $\pm 0.035 C_P$, during three consecutive measurements of the centre span main element pressures, conducted as part of this research.

Additionally the baseline configuration has been tested several times and figure B.2 shows the results for the first and last measurement that were more than a year apart. The comparison of these curves does not only reveal the influence of test conditions and set-up accuracy, but also includes the effect of the deterioration of the model over time. The resolution of the data sets is not the same, but nevertheless it can still be seen that all features are present in both data sets. In general the coefficient levels are very comparable and the repeat is satisfactory.

The main differences between the two different runs are related to hysteresis, vortices and interaction. Each of these are complicated to reproduce, even in a short time span, and it is therefore not surprising to see these differences. The hysteresis zone covers the same ride height range for both runs, but the wing downforce values for the increasing branch are lower for the long term repeat. The lower wheel drag for the same branch in this region is associated with this. The vortex breakdown in force region $IV$ is captured slightly different in the wing downforce curve. While the wheel drag in region $III$ follows a different curve and reaches a lower minimum, indicating that the interaction is captured in a different way. The mean of the differences over the ride height range of the second run compared to the baseline run 1 have been quantified as $0.0076C_L$, $-0.0031C_D$ wing, $0.0059C_M$ and $-0.0027C_D$ wheel. This is of the same order as the uncertainty limits that were derived in section B.2.

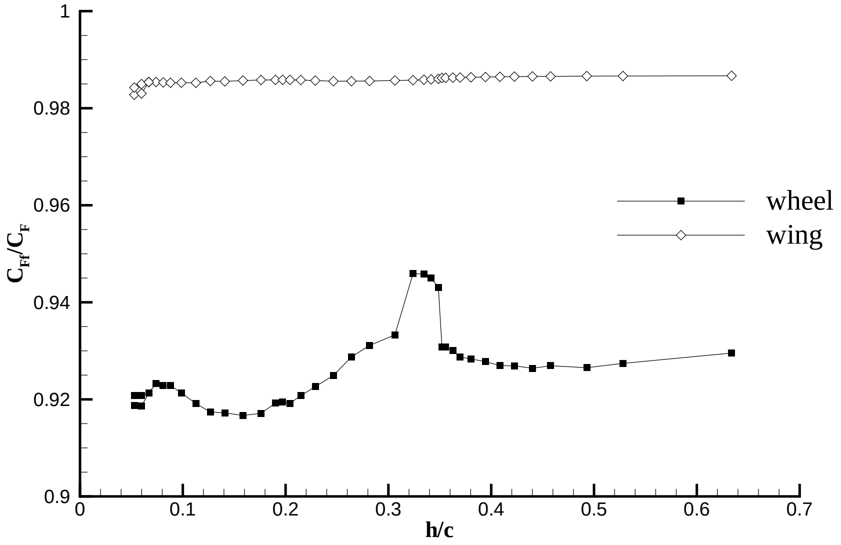

Figure B.1: Blockage correction factor, $C_{Ff}/C_F$, over the ride height range for the CWW2020 configuration, both wheel and wing.

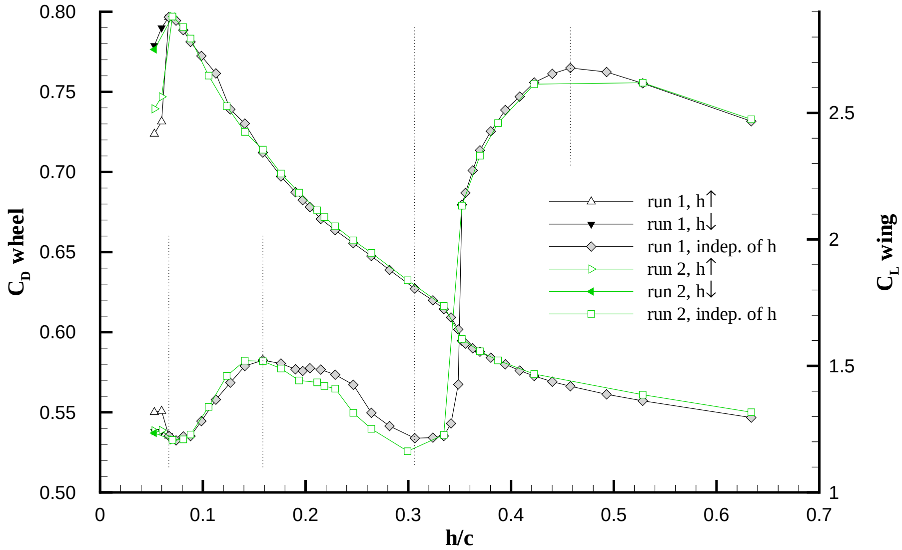

Figure B.2: Repeatability of measured force coefficients over ride height range for CWW2020 configuration; run 1 taken in 2005 and run 2 in 2006.

# Appendix C

# Influence of *Re*-number and Stationary Results

The test facilities do not allow for testing at the same *Re*-number as for the real car, because of size restrictions resulting from blockage considerations, maximum allowable test velocity and since the wind tunnel can not be pressurized. Therefore the experimental tests have been performed at 50% model scale and at roughly half the 'on track' velocity[1]. This means that the *Re*-number is apprxoimately 1/4 of that for the real car. This appendix investigates the influence of variations in *Re*-number (mainly reductions) on the force coefficients for the isolated components and for the combined baseline configuration. Furthermore a few stationary results are included as well, for reference.

## C.1 *Re*-number influence

The wheel drag for the wheels only configuration has been measured over a velocity range from 10 to $35 m/s$ for the rotating case and from 10 to $30 m/s$ for the stationary case[2]. The results are presented as function of the *Re*-number in figure C.1. The standard deviation in wheel drag over the interval is $\pm 0.0040 C_D$ and $\pm 0.0037 C_D$ for respectively the rotating and stationary case. From this it can be concluded that the *Re*-number has hardly got any influence on the wheel drag under these conditions. This is especially interesting with respect to the stationary case, since it is well known (see section 1.2.1) that the flow around a cylinder is governed by the *Re*-number. This is a clear confirmation that the end effects and ground effect have taken over the role of governing parameter for wheel geometries. For a rotating wheel the rotation effects also form a primary factor of influence.

---

[1] The average velocity over all circuits during the 2003 F1 season was approximately $60 m/s$.

[2] The reduction in upper limit of the velocity range for the stationary case was necessary because the wheel started rotating under influence of the wind for velocities above $30 m/s$.

Figure C.2 presents similar data for the isolated wing downforce and drag at three different ride heights. The influence of the $Re$-number on these force coefficients is more noticeable than for the wheel, particularly at the lower and higher end of the range. In the relevant interval from 20 to $30m/s$ the downforce is relatively constant, but the drag reduces with increasing $Re$-number due to the reduction in boundary layer thickness. A better understanding of the changes in force behaviour with $Re$-number can be obtained from figure C.4, which shows the downforce curves for three different test velocities. The main influence is an increase in hysteresis zone length with decreasing $Re$-number. The location of force region $b$, where the downforce trend is locally disrupted due to downstream lower edge wing vortex dilution, does not change from 30 to $20m/s$, but it disappears in the hysteresis region for the $10m/s$ case. The level of the curves is influenced by the $Re$-number, however it is expected that the slightly higher downforce for the $20m/s$ case compared to the $30m/s$ is within the uncertainty and repeatability levels.

Finally, figure C.3 shows the wing downforce and drag, as well as the wheel drag, as a function of the $Re$-number for the baseline combined configuration CWW2020 at a fixed ride height of $h/c = 0.264$. Once more the wing downforce is quite constant, whereas both the wing and the wheel drag reduce with increasing $Re$-number. The wing downforce and wheel drag curves as function of the ride height for $20m/s$ are compared to the standard test conditions of $30m/s$ in figure C.5. The curves for both test velocities are very similar in level and features. The main difference is again that the hysteresis zone extends to a higher ride height for the lower velocity case, which is also visible in the wheel drag. Furthermore the wheel drag follows a different curve in force region *III*, reaching a larger local maximum at a higher ride height.

In summary it can be concluded that the $Re$-number has a limited influence on the force results. The flow phenomena within the velocity range of 20 to $30m/s$ do not change fundamentally, with the exception of a small shift to lower ride height of the hysteresis zone boundary with increasing $Re$-number. The wheel drag decreases 1% for the isolated case over this interval, whereas for the combined case at $h/c = 0.264$ it decreases 4% in a constant manner. This gives a good indication that the assumption is justified that the flow field derived from the wheel pressure meassurements is similar to that for the other measuremenet methods at $30m/s$.

## C.2 Stationary results

A limited set of data for stationary conditions - without ground movement or wheel rotation - has been obtained in addition to the presented results in order to understand specific flow phenomena and features. The experimental wheel drag for the stationary isolated case has been included in figure C.1, while the CFD value can be found in table 3.1. The experimental wheel drag coefficient rises with 14% when the wheel is not rotated, whereas in CFD a 9% higher value is prediceted. This is in line with previous research from for example Fackrell [34] and confirms the effect of rotation on the force coefficients for a cylinder (see section 1.2.1).

Oil flow tests have been performed for the wheels only and for a CWW2035h60 configuration.

The figures C.6 and C.7 show pictures of the respective results. Omitting of the ground movement and wheel rotation has an unknown influence on the results, but the pictures are still interesting because of a few features. On the top of the wheel, just downstream of the crown, a bounded separation region can be recognized, which is similar in location and appearance to those described by Zdravkovich [25] for 'coin-like cylinders'[3]. At the sides of the wheel on the ground plane dead zones with small vortices inside can be distinguished, located downstream of the 'horseshoe vortex' area. From figure C.6 it can be concluded that the wheel wakes influence each other slightly, each pushing the other wake outwards, away from the symmetry plane. Finally, figure C.7 reveals a fascinating interaction pattern on the ground, including a dead zone just downstream of the wing. It is unknown whether such accelerated and retarded regions occur in similar places when the ground is moving and the wheels rotating, but the interaction between the wing and wheel flow is obvious.

---

[3] See page 7 for a discussion of these 'separation islets'.

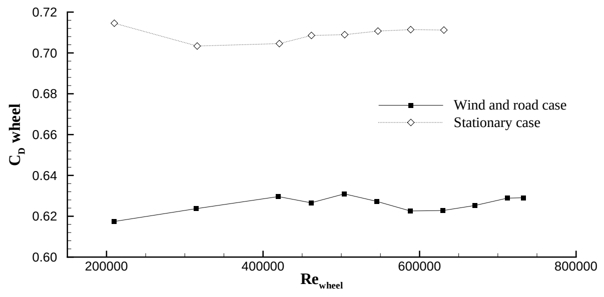

Figure C.1: Influence of *Re*-number on wheel drag; rotating and stationary case.

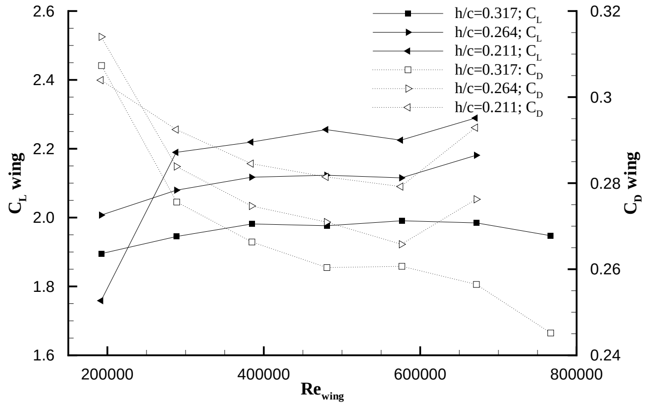

Figure C.2: Influence of *Re*-number on isolated wing force coefficients for three ride heights.

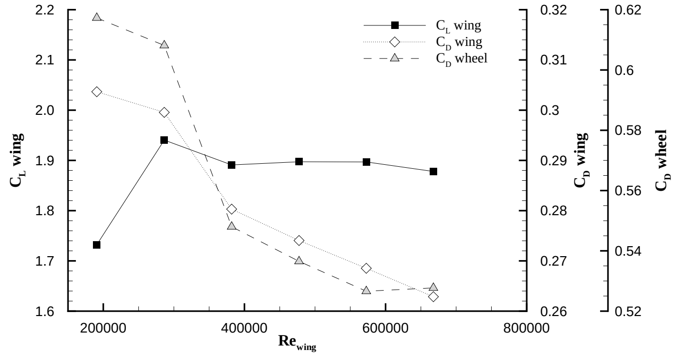

Figure C.3: Influence of *Re*-number on CWW2020 force coefficients at $h/c = 0.264$ ride height; $C_L$ wing, $C_D$ wing and $C_D$ wheel.

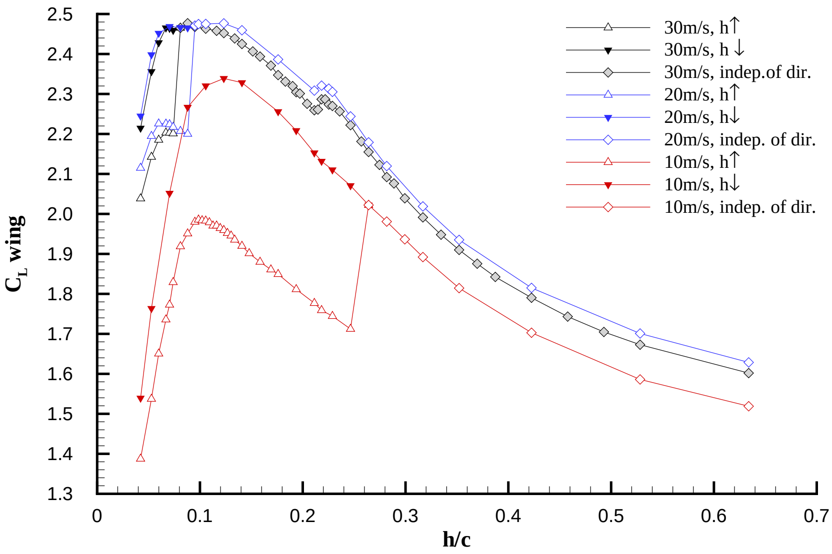

Figure C.4: Influence of freestream test velocity on measured downforce coefficients over the ride height range.

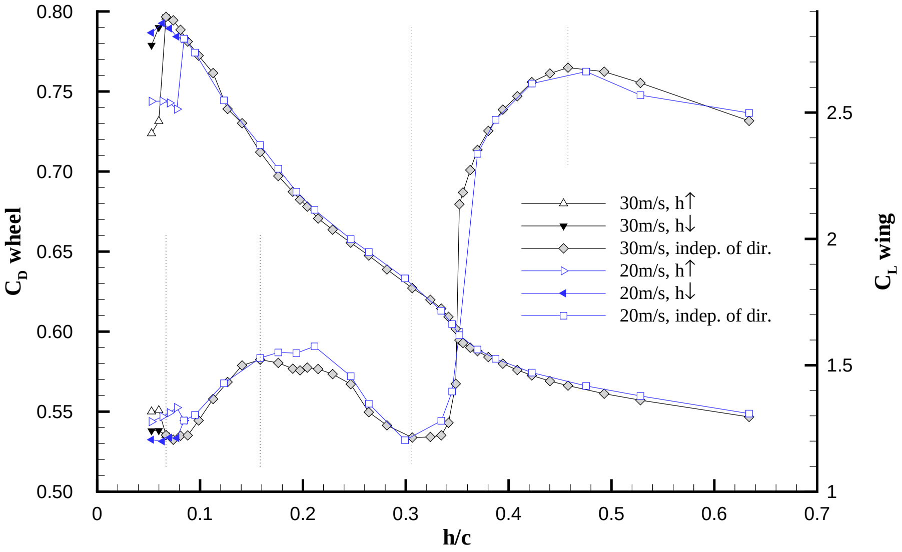

Figure C.5: Influence of freestream test velocity on measured force coefficients over the ride height range for CWW2020 configuration.

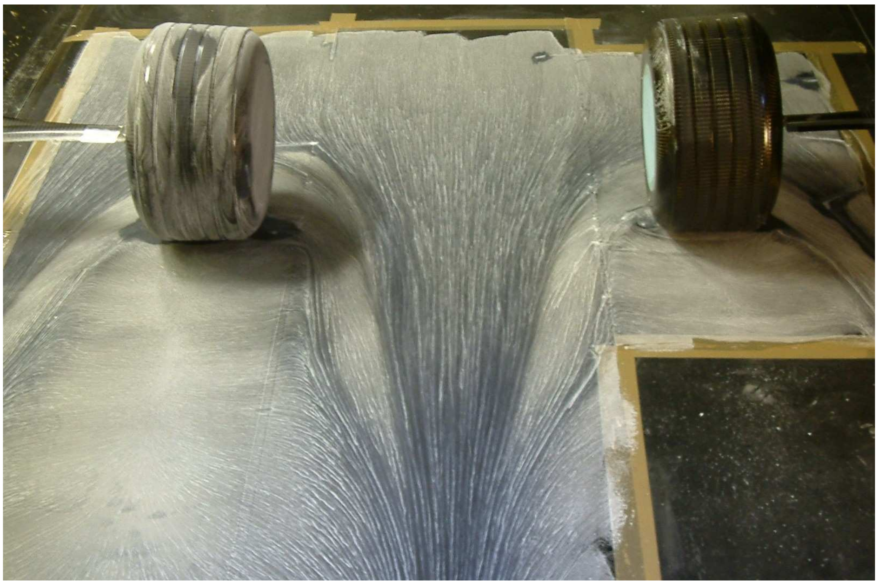

Figure C.6: Picture of oil flow results for the isolated wheel set-up as a stationary case without ground movement or wheel rotation.

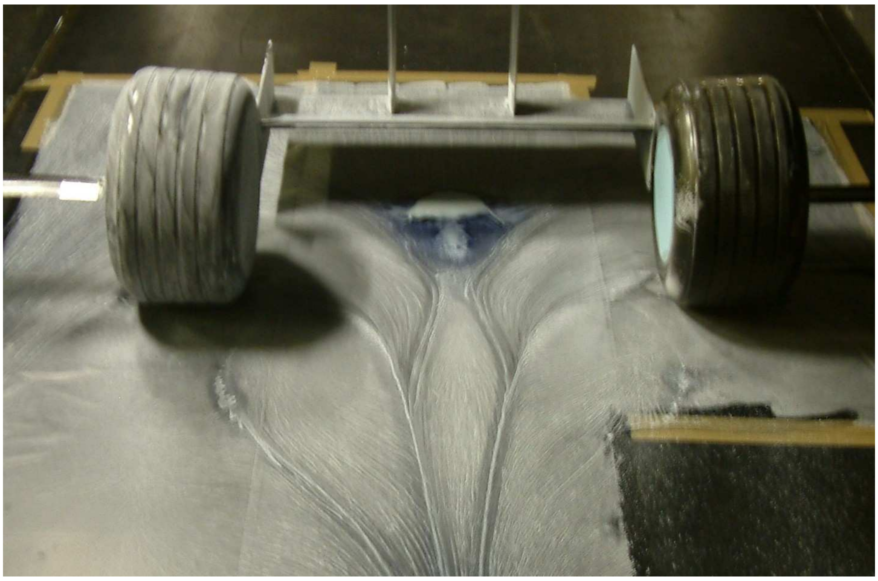

Figure C.7: Picture of oil flow results for the CWW2035 configuration at $h/c = 0.211$ as a stationary case without ground movement or wheel rotation.